University of Latvia
Faculty of Physics and Mathematics
Department of Physics

Modeling of Turbulence Properties and Particle Transport in Recirculated Flows

Maksims Kirpo
Advisor: Dr. Phys. Andris Jakovičs

A thesis submitted for the degree of

Doctor of Philosophy (Physics)

Riga, 2008

To the Family ...

Acknowledgements

I would like to acknowledge my supervisor Prof. Andris Jakovičs for his guidance, help and advices during my PhD studies. I am also indebted to all the colleagues from the Laboratory for mathematical modeling of environmental and technological processes for sharing their time and knowledge with me and for the warm working atmosphere. I am extremely grateful to Prof. Berndt Nacke and Prof. Egbert Baake from Institute of Electrotechnology, Leibniz University Hannover for the opportunity to make experimental work there and for everyday support. I also wish to express my sincere gratitude to all other colleagues from Institute of Electrotechnology, Leibniz University Hannover for sharing their experimental experience with me and for their interest in my work. I would also express my gratitude to my friends Andrejs Umbraško, Dr. Dmitrijs and Dr. Olga Docenko for their support and useful discussions. I thank my family and parents for their love, patience and understanding.

I very thankful to the Faculty of Physics and Mathematics, University of Latvia and I also acknonowledge the support from the European Social Fund (ESF). *I acknonowledge the access to the computer resources at the HLRN complex in Hannover.*

Abstract

This work is intended to the investigation of the turbulent flow properties and particle dynamics under the influence of EM and gravitational forces in induction crucible furnaces (ICF) and channel induction furnaces (CIF). The highly turbulent flow ($Re > 10^4$) is usually formed by two or more averaged recirculated vortices in these furnaces and heat and mass exchange in such flows is very significant for technological processes.

This work uses available experimental data about the Wood's metal flow in ICF and CIF to build and verify 3D large eddy simulation (LES) numerical models for heat and mass transport calculations. Additionally experimental flow velocity measurements were performed by the author in ICF in Institute of Electrotechnology, Leibniz University Hannover, which allowed to study transient and energy turbulent flow characteristics comparing both experimental and LES numerical results. Low frequency velocity oscillations, which characteristic length scale is comparable with the size of large vortices, were confirmed in the ICF melt flow. Analyzed measured and calculated turbulent flow parameters are in accordance with the turbulence theory including Kolmogorov's spectra.

The verified LES model was used to investigate transient particle behavior in the turbulent flow depending on particle density, size, boundary conditions and action of volumetric forces. It was shown that EM force and no-slip boundary conditions can dramatically improve particle accumulation in the near wall region of the crucible.

LES possibility to correctly describe heat transport in a complex 3D turbulent flow was verified using available experimental data on Wood's melt flow in CIF. This model was also applied to heat and mass transport investigation for cast iron melt flow in industrial CIF and for TiAl melt flow in induction furnace with cold crucible (IFCC). Simulation allowed to estimate melt overheat and temperature inhomogeneities inside the melt.

The thesis consists of Abstract, 8 Chapters, including Introduction and Conclusions (216 pages, 116 figures and 21 tables), and of References (110 citations). The thesis is written in English language.

Contents

List of Figures

List of Symbols and Abbreviations

Roman Symbols

A	magnetic field vector potential
B	magnetic field strength, magnetic induction
C_k	Kolmogorov constant
c_p	thermal capacity at a constant pressure
C_S	Smagorinsky constant
d	diameter
E	intensity of electric field, energy spectrum function
F	external volumetric force
f	external volumetric force density, frequency
G	filter function
g	≈ 9.81 m/s^2 acceleration due to gravity
j	current density
k	wave number, thermal diffusivity, kinetic energy
L	characteristic length scale
l_D	dissipation length
l_E	energy containing length
m_{ij}	Maxwell tensor
$\mathbf{n}$	normal vector
p	pressure
R_{ij}	covariance tensor

S_{ij}	strain rate tensor
T	absolute temperature
t	time
T_{ij}	subgrid-scale tensor
U	characteristic velocity
v	fluid velocity
$\mathbf{r}$	radius vector

Nondimensional numbers

Gr	Grashof number, $\mathrm{Gr} = \dfrac{g\alpha\Delta T L^3}{\nu^2}$
Pr	Prandtl number, $\mathrm{Pr} = \dfrac{\nu\rho c_p}{\lambda}$
Ra	Rayleigh number, $\mathrm{Ra} \equiv \mathrm{Gr} \cdot \mathrm{Pr}$
Re	Reynolds number, $\mathrm{Re} = \dfrac{UL}{\nu}$
Rm	magnetic Reynolds number, $\mathrm{Rm} = \mu_0 \sigma U L$
Sc	Schmidt number
St	Stokes number

Greek Symbols

α	thermal expansion coefficient
δ	skin layer thickness
ε	dissipation
η	Kolmogorov microscale
Γ	diffusivity
μ	dynamic viscosity of the fluid, magnetic permeability of the medium
μ_0	permeability of free space, $\mu_0 = 4\pi \cdot 10^{-7}$ Wb·A^{-1}m^{-1}
ν	kinematic viscosity of the fluid
ω	cyclic frequency
Φ	scalar potential
γ	surface tension
ρ_f	fluid density
ρ_p	particle density

λ	thermal conductivity, turbulent length scale
ϕ	passive inactive scalar
σ	electrical resistivity
ε	turbulent dissipation rate

Superscripts

$'$	pulsational component

Subscripts

$_i$	subscript index, $i = 1, 2, 3$
$_j$	subscript index, $j = 1, 2, 3$
$_m$	magnetic
$_0$	amplitude value, initial value
$_p$	particle
$_S$	on surface
$_T$	turbulent

Other Symbols

Δ	variation, LES filter width
∇	Nabla operator $\nabla = \left(\frac{\partial}{\partial x}, \frac{\partial}{\partial y}, \frac{\partial}{\partial z}\right)$

Acronyms

2D	Two-Dimensional
3D	Three-Dimensional
CIF	Channel Induction Furnace
DC	Direct Current
DNS	Direct Numerical Simulation
EM	ElectroMagnetic
FEM	Finite Element Method
FFT	Fast Fourier Transform
FVM	Finite Volume Method

ICF Induction Crucible Furnace

IFCC Induction Furnace with Cold Crucible

LES Large Eddy Simulation

MHD MagnetoHydroDynamics

PDE Partial Differential Equation

PMP Permanent Magnet Probe

RANS Reynolds Averaged Navier-Stokes equations

VOF Volume Of Fluid

1 Introduction

1.1 Melt Flow in Induction Furnaces

Turbulent heat and mass exchange including turbulent flow properties and particle transport in recirculated flows is very actual physical problem, which is closely connected to several industrial applications. Experimental and theoretical studies of this phenomena in liquid metals were intensively developed during the last few decades using mainly laboratory installations of induction furnaces with a model melt driven by electromagnetic field.

The induction furnaces are industrial equipment, which is widely used for metal alloy, oxides and glasses melting and processing. The main advantage of the induction equipment is a long-range influence of electromagnetic (EM) field, which allows to treat working materials from distance without direct mechanical contact, which can be important for pure material products. Besides, new materials with previously defined chemical components need certain physical and mechanical properties in different parts of the final product, which can be achieved by melt alloying and segregation under the influence of outer field. Induction melting is one of the ways to manufacture such materials efficiently with high production rates.

Conducting material is heated and melted by the EM field, which introduces eddy currents and Joule heat to the melt in the induction furnaces. The eddy currents and outer magnetic field interact creating Lorentz forces, which initiate flow of the liquid metal. The flow intensity can achieve several meters per second due to the large intensity of the EM field ($B \sim 0.5$ T) and typical dimensions of industrial equipment ($L \sim 1$ m), which corresponds to Reynolds numbers greater than 10^4. Therefore, liquid metal flows in the induction furnaces are usually

turbulent.

Historically the first turbulence study was performed by Reynolds in the end of the 19^{th} century [75], but till now the complete description of the turbulence is the fundamental unsolved problem of physics and the general theory, which can provide analytical or "exact" solution of the problems, is not built yet. Therefore a computer simulation of the turbulence using different approximations and assumptions is very common approach, which allows to solve complex scientific and engineering problems (e.g. [103]). The transient nature of turbulent processes and three dimensional (3D) representation of the flow introduce particular difficulties for turbulence study. Unsteady 3D computer simulations are very time and resource consuming even on modern computer systems. More simple empirical and half-empirical turbulence models, which are built using different closure schemes, are suitable for fast velocity and temperature field estimations, but these models can also produce results with the difference to observed in experiments [19] or applicable only for certain flow classes.

The turbulence can introduce positive or negative effects into the melting process depending on the desired properties of the final product and construction of melting equipment. Turbulence can improve quality of the final alloy with the effective melt mixing and temperature or admixture homogenization. From the other point of view, the turbulence is often a reason for the rigorous crucible erosion and sometimes turbulence reduction by the additional external DC magnetic field is desirable (e.g. [3, 42]). Another negative effect of the turbulent melt flow is a possible free surface instabilities which can be expresses as surface waves or oscillations and can introduce air bubbles into the melt. Turbulent velocity pulsations and heat and mass homogenization in the melt are the main topics of these thesis.

Practically turbulence is a common property of the flow and its laws are universal and can be studied using different approaches. This thesis introduces overview of the one certain flow class, i.e. the turbulent flows with several recirculating mean flow eddies in a closed volume, which can be presented by a cylindrical geometry in the simplest case, e.g. closed turbulent melt flow initiated by harmonic alternating current in a cylindrical crucible with inductor around.

Such types of the flows are observed in many metallurgical applications, e.g. induction furnaces, induction-crucible furnaces, cold crucible furnaces, continuous casting moulds, etc. The number of these applications require detailed characteristics of the flow turbulence because it has determinant effect on heat and mass transfer processes in the melt, which also can be investigated with the particle tracing.

The channel induction furnaces are widely used in steel or non-ferrous metal metallurgy for alloy melting and holding due to they high efficiency. The channel furnace consists of the large bath for liquid metal, channel and neck, which connects channel to the bath. The channel is built around EM inductor and has the highest induced current densities. Hence, the melt is generally heated there, but this heat should be transported to the bath. The channel transit flow is often developed due to thermal or geometry instabilities, which together with the flow turbulence increase heat and mass exchange between the channel and the bath. Therefore channel exit geometry is usually optimized to provide better transit flow regime and reduce channel overheat comparing to the bath.

Although CIF is well established for many years, up to now there are still open questions and room for improvements regarding the operation life time of the inductor, which is strongly limited by wear and tear damages like erosion, clogging and infiltration of the ceramic lining in the inductor channel. Practical experience in grey cast iron foundries have shown, that the operation life time of the typical used single loop channel inductors are sometimes only a few weeks due to fast growing build up formations, which lead to insufficient heat exchange and local overheating of the melt in the channel. This channel overheating, which is determined by deficit of heat transport between the channel inductor and the melt bath, significantly influence the wearing of the ceramic lining. Transit flow and structure of turbulent vortices in the channel are both affected by slag formation and channel clogging. The melt flow itself is very complex, turbulent and influenced by electromagnetic and buoyancy forces. A 3D numerical model of the flow and heat and mass exchange in the experimental induction channel furnace is developed later in the thesis.

IFCC melting or skull melting is another example of the induction melting technology, which is very perspective for the production of aggressive high tem-

perature materials. Melted material is placed in a copper crucible, which walls are splitted and cooled with water. EM field penetrates the splitted crucible and generates currents and Joule heat inside the melt. The material is melted keeping solid crust of the same material near the cold walls, which allows to get alloys without foreign inclusions of the crucible material. Al and TiAl alloy melting and remelting of radioactive waste are several examples of the cold crucible modern applications.

Figure 1.1: One loop "Otto Junker Group" channel induction furnace.

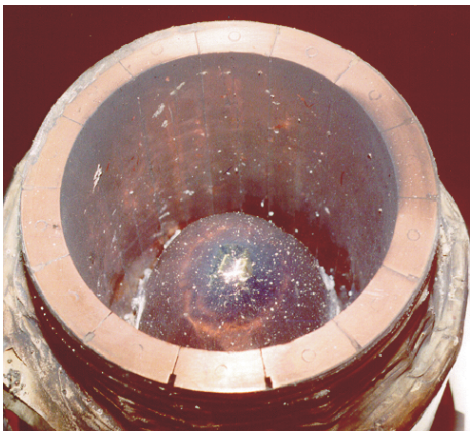

Figure 1.2: TiAl alloy in Cold Crucible furnace (property of Institute of Electrotechnology, Leibniz University Hannover).

All above mentioned examples of the recirculated turbulent flows in the liquid metals are topics of large interest. High temperatures and aggression of the melted materials prevent using of velocity measurement technics in industrial furnaces. Usually only surface temperature of the melt can be determined with pyrometers during the technological processes. Velocity estimates directly can be performed only in a liquid Al or in other metals with lower melting temperature (e.g. Zn). Such measurements have large scientific value and can provide calibration and verification data for the computer models, which are used later to estimate the melt flow in the real facilities. Therefore instantaneous two-probe measurements of the melt flow velocities were performed only in laboratory ICF for numerical

model verification in this thesis. Computer simulations of the flow structure and temperature distribution in the melt using experimentally verified numerical models are still the main scientific instrument for understanding and investigation of inner physical phenomena and optimization of industrial furnace processes.

3D transient computer simulation of the melt flow in the induction furnace can be very complex and include large number of steps:

- Determination of physical properties of used materials and their dependence on temperature, concentration etc;
- Electromagnetic analysis of induction system including estimation of power losses, distribution of eddy currents, heat sources and Lorentz forces;
- Calculations of free surface shape if necessary and recalculation of Lorentz forces and Joule heat;
- Transient 3D hydrodynamics coupled with thermal problem;
- Model verification comparing results to available experimental data or to other computational results and theoretical predictions.

Correct physical properties of the materials are very important for successful simulation. Most significant physical properties of materials for the induction melting problems are electrical conductivity (determines parameters of the furnace and melting efficiency), thermal conductivity (is very important especially for ceramic materials) and melt viscosity (determines all hydrodynamics). Density of liquid metals usually is taken to be constant, i.e. the liquid metals are treated as incompressible fluid. If initial solid material considered as powder (ceramics or glasses), then transient simulation of the entire heating and melting process is more difficult because of the sintering. Computer modeling described in the thesis states only with fully melted metallic materials and melting or solidification process itself is not investigated. The physical properties usually are temperature dependent. However, temperature gradients inside the melt seldom are greater then 10-50°C and in this work all physical properties of used materials are proposed to be constant except only density, which dependence on the

temperature should be included to the channel induction furnace model at least as Boussinesq approximation. This approach introduces buoyancy term to the Navier-Stokes equation in hydrodynamics, but the density remains function of temperature not of the pressure.

Construction of the real induction furnace still has many additional elements with different physical properties and complicated shape (crucible, support parts, magnetic core), which reduces usability of analytical methods and therefore EM field is often computed using fast 2D finite element method (FEM) models. Axial symmetry of the cylindrical crucible also is very suitable for EM field computations with 2D axis-symmetric models and is often used for EM filed calculations in ICF. But there are problems with correct estimation of the induced eddy currents and Joule heat sources in the melt if 2D models are used for EM calculations in IFCC because of influence of the slitted crucible. Often 3D EM modeling is also needed because of geometry considerations (e.g. CIF).

Deformations of the top free melt surface are result of interaction of several electrical currents: inductor, induced in the crucible (may be absent) and induced in the melt. Harmonic nature of the EM force, geometry asymmetries and intensive melt motion lead to surface instabilities, which are usually expressed as surface oscillations. For some kinds of metal processing equipment for example for Al reduction cells surface should be stabilized to decrease parasitic power losses due to such oscillations. Free surface deformations or meniscus are typical for metal melts in IFCC, where levitation melting can be implemented by a special crucible shape and configuration of several inductors. Meniscus shape is determined by EM pressure, tension and gravitational pressure balance and can be estimated with volume of fluid (VOF) model.

Hydrodynamic calculations can be performed in 2D only for initial estimation of the flow field due to possible differences between computational and experimental results. Hence, investigation of the flow phenomena together with heat and mass transport in induction furnaces should be performed using 3D transient LES method because this numerical technique seems to be appropriate for universal computer simulation of complex turbulent flows without adaptive empirical constants. However, glasses and ceramics have much smaller electrical conductiv-

ity and their flow in induction equipment is often laminar and 2D axis-symmetric models of the full meting process can be developed [34].

The Reynolds-averaged equations of motion for incompressible flows and inhomogeneous turbulence are derived by time averaging of the equations for the instantaneous flow. This procedure introduces new unknowns (Reynolds stresses) and leads to the closure problem. Therefore a special turbulence model should be used to "close" these equations. The fastest and simplest way to get simulation result is to use classic engineering 2-equation turbulence models (e.g. $k-\varepsilon$). However, comparison of $k-\varepsilon$ modeling results with the experimental temperature measurements inside the liquid Al in IFCC showed disagreement of temperature calculations with the measured temperature field [5]. The reason is low intensity of turbulent flow exchange between the averaged vortices in the calculated flow. The problem can be tried to solve increasing the turbulent Prandtl number to improve heat transport by thermal conductivity in $k-\varepsilon$ model, but this approach is not flexible because it should be performed several times for each problem comparing computational and experimental results for temperature.

Unsteady 3D simulation should be used to check out turbulence phenomena influence on heat and mass transport in the flow and perform more accurate analysis of the problem. Several turbulence models are available for transient simulations: unsteady Reynolds averaged Navier-Stokes (RANS), LES or direct numerical simulation (DNS). Detailed turbulence analysis can be performed using only the last two methods.

DNS solves Navier-Stokes equations for all spatial and temporal scales of motion present in the flow and provides very accurate results with the highest available flow description level. The smallest dissipation scales have to be resolved and therefore DNS needs very fine grids. In fact dissipation scale depends on Reynolds Number (Re). High Re corresponds to small turbulent scales and DNS usually is used only for "low" Re turbulent flows ($\mathrm{Re} < 2 \cdot 10^3$) to minimize mesh requirements and therefore computation time and costs. According to [70] computational costs increases as Re^3. DNS has specific requirements on model geometry and boundary conditions, which are the outcome of accurate high-order numerical methods. This is reason why DNS still is a perfect tool for fundamental analysis for "low" Re flows, but its usage for real problems is restricted.

Three-dimensional unsteady calculations, which are performed in this work have used LES method, which will be described in detail in section 2.4. In few words LES is the 3D turbulence modeling technique, which allows to investigate time development of turbulent flows in different geometries of a complex shapes without adjusting empirical parameters of the model. It can distinguish turbulent scales, which are comparable with the model grid size, therefore giving possibility to explore a large part of energy transferred between the turbulent vortices. In fact this exploration is limited only by the grid size and selected time step, therefore, on available time and computer resources. LES is a good compromise between the DNS and RANS turbulence models.

The discussed induction furnaces examples and physical problems demonstrate the basic features of the studied phenomena: the turbulent melt flow is closed in a rigid container (crucible or bath) with the free top surface. The flow is influenced by the EM field only near the crucible walls, which determines existence of the several recirculated vortices of the mean flow. For its part, the vortices act as effective melt "stirrers" producing intensive turbulent velocity oscillations homogenizing melt and temperature field. EM field frequency is high enough to introduce skin-effect and there is no influence of the external magnetic field on the turbulence properties inside the melt because of this. The flow structure in the central part of the crucible is determined mainly by the vortex interaction, which is presented by low-frequency velocity pulsations. These considerations introduce a new "clean" object for physical investigation, where inner physical phenomena are determined either by the problem geometry neither by external factors because there are no inflow and flow perturbations are not directly affected from outside.

Summarizing all mentioned above the one can conclude, that recirculating melt flow in the closed (cylindrical) geometry represents the large flow class, which is common in metallurgical industry and characterized by the external driving force in the absence of the mechanical obstacles in the melt. The detailed experimental and simulation data of the turbulence characteristics, mass and heat transfer processes in such flows are incomplete. Therefore, heat and mass exchange in recirculating melt flow is the subject of these thesis.

1.2 Objectives and Outline of the Present Work

Research objects of the present thesis are the turbulent flow of the incompressible liquid metal in the induction furnaces and particle transport inside the melt, which have both academic and industrial value. Induction crucible furnaces are selected for this research as a representative of recirculated flow class, which allow experimental verification of selected numerical models due to relatively simple design and operation. Channel induction furnace and cold crucible furnace models are introduced to demonstrate LES possibility to calculate transient 3D turbulent flows with heat and mass exchange in complex geometries.

The goals of this work were:

- Experimentally determine and analyze the basic properties of the recirculated turbulent flow class in the cylindrical geometry and to compare results with the available *ab initia* data;
- Numerically investigate the turbulent flow using 2D and 3D different turbulence models under the same conditions as in experiments performing verification of the numerical models;
- Study transient physical properties of the turbulent flow with recirculated vortices using LES approach;
- Study heat and mass transfer processes in induction furnaces using the particle tracing method for different kinds of particles under the influence of different volumetric forces;
- Demonstrate the possibility of LES availability for industrial applications introducing the model of Wood's melt flow in the channel induction furnace.

The thesis contains abstract, introduction, 5 chapters, conclusions and the bibliography reference. The chapters introduce topics on:

1. The first chapter introduces theoretical background of studied physical phenomena. It contains basic description of physical principles, which covers magnetic fields, hydrodynamics, turbulence and particle tracing;

2. The second chapter is dedicated to description and analysis of experiments. It introduces several sections about experimental equipment and methods and presents discussion of the measured data;

3. The third chapter introduces the numerical simulation of the Wood's metal flow in the induction crucible furnace. It shows the mathematical model description, analysis of the flow turbulence and results comparison with the *ab initio* data for hydrodynamic model verification;

4. This chapter deals with the results of Lagrangian particle tracing using the ICF model. Results of different simulations are discussed in detail;

5. The fifth chapter is mainly dedicated to the verification of heat transport in LES method using experimental results of velocity and temperature measurements in a large scale laboratory CIF.

6. The last chapter is dedicated to two examples of the LES application to heat and mass transport simulation in the IFCC and CIF furnaces.

Conclusions contain the main results, which are summarized. The references have publications and monographs from many authors and for the large time period and can be used to get more information on the subject.

2 Physics, models and calculation methods

The turbulent heat and mass exchange in ICF (figure 2.1), CIF, IFCC, etc. is a complex scientific problem, which includes coupling of several physical fields. The next sections will introduce governing equations and simplifications to the mathematical models of the induction furnace including mathematical description of the turbulence and particle transport. The resulting equations will be mainly written for the incompressible fluid motion under the influence of EM driving force. The physical description of the studied phenomena can be separated into EM and HD parts due to small magnetic Reynolds number $\mathrm{Rm} = \mu_0 \sigma U L < 10^0$ (we do not concern about influence of the conducting fluid flow on the external magnetic field).

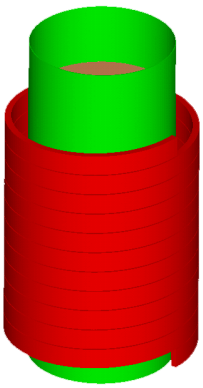

Figure 2.1: A sketch of the typical ICF, where inductor is placed around the crucible, which is filled with the melt and operation of such furnace at "Gartland Foundry".

2.1 Electromagnetic fields

All EM phenomena are described by Maxwell's equations. Let μ_0 be the permeability of free space and σ denote electrical conductivity of the material in this section. A full Maxwell's system can be simplified for magnetohydrodynamic (MHD) applications [14]. First of all, assume that liquid metal is non magnetic with large electrical conductivity (displacement currents are negligible by the comparison with the current density $\mathbf{j}$) and accumulation of the electrical charge does not occur in the medium. In this case simplified Maxwell's equations state that:

$$\nabla \cdot \mathbf{j} = 0 \qquad \text{(Charge conservation)} \tag{2.1}$$

$$\nabla \times \mathbf{B} = \mu_0 \mathbf{j} \qquad \text{(Ampere's law)} \tag{2.2}$$

$$\nabla \cdot \mathbf{B} = 0 \qquad \text{(Solenoidal nature of } \mathbf{B}\text{)} \tag{2.3}$$

$$\nabla \times \mathbf{E} = -\frac{\partial \mathbf{B}}{\partial t} \qquad \text{(Faraday's law)} \tag{2.4}$$

and in addition:

$$\mathbf{j} = \sigma(\mathbf{E} + \mathbf{v} \times \mathbf{B}) \qquad \text{(Ohm's law)} \tag{2.5}$$

Combining the Faraday's law (2.4) and the Ohm's law (2.5) together the induction equation can be obtained:

$$\frac{\partial \mathbf{B}}{\partial t} = \nabla \times (\mathbf{v} \times \mathbf{B}) + \frac{1}{\mu_0 \sigma} \nabla^2 \mathbf{B}. \tag{2.6}$$

The magnetic field induction $\mathbf{B}$ divergence is always equal to zero (2.3) and therefore a magnetic vector potential $\mathbf{A}$ can be introduced:

$$\mathbf{B} = \nabla \times \mathbf{A}. \tag{2.7}$$

Using the Faraday's law (2.4) the electrical field intensity can now be expressed as:

$$\nabla \times \mathbf{E} = -\nabla \times \frac{\partial \mathbf{A}}{\partial t}. \tag{2.8}$$

Integrating this expression leads to:

$$\mathbf{E} = -\frac{\partial \mathbf{A}}{\partial t} - \nabla\Phi, \tag{2.9}$$

where the last term from the right side represents integration constant and a new scalar is introduced — the electric potential Φ. The equation for the vector potential $\mathbf{A}$ can be obtained substituting equations (2.7), (2.9) and (2.2) into equation (2.5):

$$\frac{\partial \mathbf{A}}{\partial t} = \lambda_m \nabla^2 \mathbf{A} - \nabla\Phi + \mathbf{v} \times \nabla \times \mathbf{A}. \tag{2.10}$$

Here the magnetic vector potential was derived using the Coulomb gauge $\nabla \cdot \mathbf{A} \equiv 0$, i.e. in divergence-free form and therefore using the nabla formalism the next expression is correct: $\nabla \times \nabla \times \mathbf{A} = \nabla(\nabla \cdot \mathbf{A}) - \nabla^2 \mathbf{A} = -\nabla^2 \mathbf{A}$. Parameter $\lambda_m = 1/\mu_0 \sigma$ is called magnetic diffusivity and its sense will be clear from the next expression.

Taking the curl from the Ohm's law (2.5) and taking the current density from the Ampere's law (2.2) and combining it all together with the equation (2.4) the induction equation can be obtained:

$$\frac{\partial \mathbf{B}}{\partial t} = \lambda_m \nabla^2 \mathbf{B} + \nabla \times (\mathbf{v} \times \mathbf{B}). \tag{2.11}$$

If the last term in this equation vanishes (the conductor motion is suppressed) then the induction equation takes the form of the diffusion equation and it can be shown that a magnetic field diffuses inwards by a distance of under $(2\lambda_m t)^{1/2}$ in a time t [14].

The action of the EM field to conducting medium under the same assumptions can be expressed as:

$$\mathbf{f}_{EM} = \mathbf{j} \times \mathbf{B} \qquad \text{(Lorentz force density)} \tag{2.12}$$

$$q = \frac{j^2}{\sigma} \qquad \text{(Joule heat density).} \tag{2.13}$$

The Lorentz force density (2.12) is very important for the conducting melt convection in the crucible and therefore can be discussed more in detail. First of

all (2.12) can be written using the Ampere's law (2.2):

$$\mathbf{f}_{EM} = \frac{1}{\mu_0}(\nabla \times \mathbf{B}) \times \mathbf{B}, \tag{2.14}$$

which can be decomposed into a pressure term and a driving part:

$$\mathbf{f}_{EM} = -\nabla \left(\frac{B^2}{2\mu_0} \right) + \frac{1}{\mu_0}(\mathbf{B} \cdot \nabla)\mathbf{B}. \tag{2.15}$$

The first term from the right side in the above expression represents the electromagnetic pressure gradient, which in this form can be included into the modified pressure in Navier-Stokes equation (2.23). This electromagnetic pressure therefore can change only pressure equilibrium and modify a free surface of the melt column in this way. The latter term is the melt driving part (rotational) and can be written using index notation as $\partial m_{ij}/\partial x_j$, where $m_{ij} = (1/\mu_0)B_i B_j$ is the Maxwell tensor.

If the magnetic field is harmonic $\mathbf{B} = \mathbf{B}_c \cos(\omega t) + \mathbf{B}_s \sin(\omega t)$, then the electromagnetic force can be decomposed into a mean part and an oscillating part, where oscillating frequency is twice the electromagnetic field frequency. It can be illustrated on EM pressure term from the equation (2.15):

$$\frac{B^2}{2\mu_0} = \frac{1}{4\mu_0}\left(B_c^2 + B_s^2 + (B_c^2 - B_s^2)\cos(2\omega t) + \mathbf{B}_c \cdot \mathbf{B}_s \sin(2\omega t)\right) \tag{2.16}$$

The mean part is responsible for the meridional motion of the flow, while the oscillating part introduces surface instabilities and waves to the melt flow. However, the oscillating part should be taken into account only if the field frequency is very low (about several Hz), because of inertia impeding the melt to respond to alternating forces at higher frequencies, which are typical for induction heaters. Simulation experiment [23, 28] states, that the flow is no longer sensitive to the oscillating part of the Lorentz forces when the applied magnetic field frequency exceeds approximately $5 \div 10$ Hz.

Vector and scalar potential of the harmonic EM field can be recorded in a complex form:

$$\mathbf{A}(t) = \mathbf{A}_0 e^{i\omega t}, \quad \Phi(t) = \Phi_0 e^{i\omega t}, \tag{2.17}$$

where $\mathbf{A}_0$ is the complex vector potential amplitude, Φ_0 is the complex scalar potential amplitude, $\omega = 2\pi f$ and i is the imaginary unit. As a result equation (2.10) can be rewritten for stationary conductor as ($\nabla^2\mathbf{A} = -\nabla \times \nabla \times \mathbf{A}$):

$$\nabla \times \left(\frac{1}{\mu}\nabla \times \mathbf{A}_0\right) = \mu_0\sigma(i\omega\mathbf{A}_0 + \nabla\Phi_0). \tag{2.18}$$

Vector potential has only one component in 2D case [20], e.g. angular component A_0 for axial-symmetric problem and equation (2.18) transforms to:

$$\frac{\partial}{\partial r}\left(\frac{1}{\mu r}\frac{\partial(rA)}{\partial r}\right) + \frac{\partial}{\partial z}\left(\frac{1}{\mu}\frac{\partial A}{\partial z}\right) = \mu_0\sigma\left(i\omega A + \frac{1}{r}\frac{\partial\Phi}{\partial\varphi}\right), \tag{2.19}$$

where $A = A_0/\sqrt{2}$ and $\Phi = \Phi_0/\sqrt{2}$ are effective values of the according potentials. The Lorentz force density $\mathbf{f} = \mathbf{j} \times \mathbf{B} = \mathbf{j} \times (\nabla \times \mathbf{A})$ in axial-symmetric case can be expressed as:

$$\mathbf{f} = Re\left[j^*\left(\mathbf{e}_r\frac{1}{r}\frac{\partial(rA)}{\partial r} + \mathbf{e}_z\frac{\partial A}{\partial z}\right)\right], \tag{2.20}$$

where j and A are effective values of the current and angular component of the vector potential, symbol * represents conjugate and Re represents a real part because the force density should be a real number. It can be seen, that EM force is oriented towards reduction of the vector potential magnitude and therefore any medium in solenoidal inductor is pressed towards symmetry axis because $|\mathbf{A}|$ decreases with increasing distance to the inductor.

The material medium where EM field exists is usually characterized by parameters σ, ε and μ. The boundary conditions at the interface separating two different media 1 and 2 with parameters (σ_1, ε_1, μ_1) and (σ_2, ε_2, μ_2) can be derived from Maxwell's equations [80]:

$$E_{1t} = E_{2t} \tag{2.21}$$

$$B_{1n} = B_{2n}, \tag{2.22}$$

where subscripts $_t$ and $_n$ denote tangent and normal components of the fields with respect to interface.

In axial-symmetric case vector potential is usually taken to be zero on the symmetry axis and it also decreases away from the inductor.

2.2 Melt flow governing equations

Melt flow in the crucible is governed by the Navier-Stokes equations, which describe the principle of momentum conservation and for incompressible fluids with a constant viscosity can be written in the form (proposed summation over repeated index):

$$\frac{\partial v_i}{\partial t} + v_j \frac{\partial v_i}{\partial x_j} = -\frac{1}{\rho_f}\frac{\partial p}{\partial x_i} + \nu \frac{\partial^2 v_i}{\partial x_j \partial x_j} + f_i,\ i = 1, 2, 3 \tag{2.23}$$

where v_i is the velocity of the fluid, ρ is the fluid density, $\nu = \mu/\rho$ is the kinematic viscosity, p is the pressure and f_i denotes the total density of external volumetric forces acting on the fluid. In the following equations indices can take the values 1,2 and 3, which corresponds to x, y and z directions. The Navier-Stokes equations can also be written using the rate of strain $2S_{ij} = \partial v_i/\partial x_j + \partial v_j/\partial x_i$:

$$\frac{\partial v_i}{\partial t} + v_j \frac{\partial v_i}{\partial x_j} = -\frac{1}{\rho_f}\frac{\partial p}{\partial x_i} + 2\nu \frac{\partial S_{ij}}{\partial x_j} + f_i. \tag{2.24}$$

For melting processes typical volumetric forces acting on the fluid are gravitation and EM force. The mass conservation reduces to so-called continuity equation for incompressible fluid:

$$\frac{\partial v_i}{\partial x_i} = 0 \tag{2.25}$$

If fluid density is not constant then equation of state is usually used to close the system:

$$\rho = \rho(T, p). \tag{2.26}$$

Condition $\dfrac{d\rho}{dt} = 0$ is satisfied for melt flows in induction furnaces due to high thermal inertia of the melt [52] (the characteristic velocities of the flow are much smaller then the speed of sound). The constant density completely eliminates the buoyancy (convection) from the model, which sometimes is not desirable (specially in numerical models for CIF). However, if temperature gradients in the liquid metals are not large (several K) than density fluctuations ρ' can be thought

little: $\rho' \ll \rho$ and therefore equation of state can get pressure independent form [25, 29]:

$$\rho = \rho_0(1 - \alpha\Delta T), \tag{2.27}$$

where ρ_0 is the average density value, $\alpha = -\rho^{-1}(\partial\rho/\partial T)_p$ is the thermal expansion coefficient and ΔT is the temperature difference. Introducing (2.27) to Navier-Stokes equations (2.23) via Boussinesq approximation the buoyancy term appears:

$$\mathbf{f}_{buoyancy} = -\rho_0\alpha\Delta T\mathbf{g}. \tag{2.28}$$

From the other side the forced convection is introduced to the flow by the EM field. The electromagnetic force (2.12) can be estimated as (the Ohm's law (2.5 is used):

$$f_{em} \sim \sigma v B^2. \tag{2.29}$$

The ratio (2.29)/(2.28):

$$\frac{f_{em}}{f_{buoyancy}} = \frac{\sigma v B^2}{\rho_0\alpha\Delta T g}. \tag{2.30}$$

should be $f_{em}/f_{buoyancy} \gg 1$ to exclude buoyancy term from the equations, which is done later for ICF. Taking characteristic values for the Wood's melt flow in the induction crucible furnace (figure 2.1): $B = 0.1$ T, $v = 0.1$ m/s and $\Delta T = 10$ K the one can see that $f_{em}/f_{buoyancy} \approx 10^2 \gg 1$ for this type of induction furnaces.

The onset of convection occurs when the Rayleigh number $\mathrm{Ra} \equiv \mathrm{Gr}\cdot\mathrm{Pr}$ reaches some critical value $\mathrm{Ra_c} \gg 1$. To obtain Ra the Grashof number and the Prandtl number should be estimated:

$$\mathrm{Gr} = \frac{g\alpha\Delta T L^3}{\nu^2}, \quad \mathrm{Pr} = \frac{\mu c_p}{\lambda} \tag{2.31}$$

where L is the length scale, c_p is the specific heat capacity at constant pressure and λ is the thermal conductivity. Material properties for studied Wood's melt in ICF are given in table 2.1 and corresponding dimensionless numbers are represented in table 2.2.

Table 2.1: Physical properties of Wood's melt comparing to TiAl and Al.

	Symbol	Units	Al	TiAl	Wood's metal
Thermal conductivity (solid)	λ_{sol}	W/(m·K)	235	130	18.6
Thermal conductivity (liquid)	λ_{liq}	W/(m·K)	120	70	14.05
Specific heat capacity	c_p	J/(kg·K)	1133	1000	168
Melting temperature	T_{melt}	K	933	1773	343
Density	ρ	10^3 kg/m^3	2.30	3.75	9.40
Dynamic viscosity	μ	10^{-3} kg/(m·s)	1.29	1.10	4.2
Kinematic viscosity	ν	10^{-6} m^2/s	0.56	0.29	0.45
Electrical conductivity	σ	10^6 S/m	3.6	1.0	1.0
Surface tension	γ	N/m	0.9	1.0	0.46
Thermal expansion coeff.	α	10^{-4} 1/K	1.16	1.0	

All dimensionless numbers operate with the material physical properties and characteristic parameters of the furnace. The radius of the crucible can be selected as the characteristic length scale L and the characteristic velocity U can be estimated as the average velocity of the flow in the largest averaged eddies for induction crucible furnaces. Then the characteristic time can be estimated as the vortex circle period. The Navier-Stokes equation (2.23) can be rewritten using characteristic values in dimensionless form [44] introducing Reynolds number Re, which indicates the ratio of inertia forces to viscous forces (tildes denote dimensionless numbers):

$$\frac{\partial \tilde{v}_i}{\partial \tilde{t}} + \tilde{v}_j \frac{\partial \tilde{v}_i}{\partial \tilde{x}_j} = -\frac{\partial \tilde{p}}{\partial \tilde{x}_i} + \frac{1}{\mathrm{Re}} \frac{\partial^2 \tilde{v}_i}{\partial \tilde{x}_j \partial \tilde{x}_j} + \tilde{f}_i, \tag{2.32}$$

where Reynolds number is:

$$\mathrm{Re} = \frac{UL\rho}{\mu} = \frac{UL}{\nu}. \tag{2.33}$$

The Navier-Stokes equations (2.23) are partial differential equations and boundary and initial conditions should be included to the model. Only two types of fluid

Table 2.2: Dimensionless numbers of different melts in the studied experimental and computational models.

	Expression	Al	TiAl	Wood's metal
Crucible radius	R, m	0.080	0.080	0.158
Characteristic velocity	U, m/s	1.0	1.0	0.2
Characteristic induction	B, T	0.1	0.1	0.1
Reynolds number	$\mathrm{Re} = \frac{UL}{\nu}$	$1.4{\cdot}10^5$	$2.8{\cdot}10^5$	$0.7{\cdot}10^5$
Prandtl number	$\mathrm{Pr} = \frac{\nu\rho c_p}{\lambda}$	0.012	0.016	0.036
Grashof number	$\mathrm{Gr} = \frac{g\alpha\Delta T L^3}{\nu^2}$	$1.1{\cdot}10^7$	$3.6{\cdot}10^7$	$5.7{\cdot}10^7$
Rayleigh number	$\mathrm{Ra} \equiv \mathrm{Gr} \cdot \mathrm{Pr}$	$1.4{\cdot}10^5$	$5.6{\cdot}10^5$	$20.4{\cdot}10^5$
Magnetic Reynolds number	$\mathrm{Rm} = \mu_0\sigma UL$	0.36	0.10	0.04
Alfvén velocity	$v_a = \frac{B}{\sqrt{\rho\mu_0}}$	0.56	0.29	0.45

boundaries are examined to simplify mathematical models: a smooth solid wall and a free surface of the fluid. The wall means that no fluid may pass through it and therefore velocity component normal to the boundary must be equal to the velocity of the wall:

$$\mathbf{v} \cdot \mathbf{n} = \mathbf{V}_S \cdot \mathbf{n}, \tag{2.34}$$

where $\mathbf{V}_S$ is the velocity of the wall and $\mathbf{n}$ is the surface normal vector. Due to viscosity of the fluid tangential velocity component on the wall must be zero (no-slip boundary condition). For the free surface of the fluid next boundary condition, which allows existence of the tangential velocity component, can be used:

$$\mathbf{v} \times \mathbf{n} = \mathbf{V}_S \times \mathbf{n}. \tag{2.35}$$

Several remarks must be done about the transport of a conserved (no source or sink term) passive (does not effect material properties of the fluid) scalar

because the part of this work is intended to the heat and mass transfer processes in the flow. Let $\phi(\mathbf{x}, t)$ be the scalar. Then in a constant-property flow the next conservation equation is valid:

$$\frac{\partial \phi}{\partial t} + v_i \frac{\partial \phi}{\partial x_i} = \frac{\partial}{\partial x_i}\left(\Gamma \frac{\partial \phi}{\partial x_i}\right), \tag{2.36}$$

where Γ denotes the constant and uniform diffusivity. The scalar ϕ can represent various physical properties: small excess in temperature, which does not change physical properties; concentration of a species. For the former scalar Γ represents the thermal diffusivity and the ratio ν/Γ is the Prandtl number Pr. Equation (2.31) can be used to find the value of the thermal diffusivity: $\Gamma = \lambda/(\rho c_p)$. For the latter scalar Γ is the molecular diffusivity and ν/Γ is the Schmidt number, Sc.

Several words should be said about the boundary conditions for equation (2.36). The melt is usually surrounded by the walls where Robin boundary conditions can be applied in a general case:

$$A \cdot \phi + B \cdot \frac{\partial \phi}{\partial n} = G(\Sigma), \tag{2.37}$$

where A and B are given constants (which more generally are allowed to be given functions), $\partial\phi/\partial n$ is the normal deriviative and $G(\Sigma)$ is the given function defined on boundary Σ. For concentration c these boundary conditions on the insulating wall are usually expressed as:

$$-\Gamma c(\Sigma) + \lambda_n(\Sigma) \frac{\partial c(\Sigma)}{\partial n} = 0, \tag{2.38}$$

where λ_n is the convective constant. Thermal boundary conditions also can be recorded in the above form, but usually they are represented by fixed temperature on the wall (first type or Dirichlet): $T = T(\Sigma)$ or by specified normal heat flux (second type or Neumann): $\lambda \dfrac{\partial T}{\partial n} = q(\Sigma)$.

2.3 Turbulence and its classical description

The Navier-Stokes equation (2.23) completely describes the fluid flow. The inertia term can be neglected in this equation if Re < 1, i.e. Stokes flow. The

flow remains laminar (its perturbations are damped) till Re $\leq 10^3$. Increasing Re again, the flow becomes unstable and certainly turns turbulent when Re is of order 10^4. The turbulent flow is characterized by the chaotic vortex movements, appearance and decomposition and can be described using statistical theory, which does not produce instantaneous results, but only averaged solutions and statistical moments.

Analytical turbulence equations can be obtained from the equations (2.23) using the Reynolds averaging. Suppose that flow consists of oscillating and laminar parts. Then all physical variables can be introduced in the form:

$$p = \bar{p} + p', \quad v_i = \bar{v}_i + v_i', \tag{2.39}$$

where $\bar{p}$ and $\bar{v}_i$ represents ensemble averaged pressure and velocities and p' and v_i' are corresponding fluctuations. In general, the ensemble averaging is implemented as the time averaging for inhomogeneous turbulence. Transforming the Navier-Stokes equation (2.23) the Reynolds equation for averages is obtained:

$$\frac{\partial \bar{v}_i}{\partial t} + \bar{v}_j \frac{\partial \bar{v}_i}{\partial x_j} = -\frac{1}{\rho_f}\frac{\partial \bar{p}}{\partial x_i} + \nu \frac{\partial^2 \bar{v}_i}{\partial x_j \partial x_j} - \frac{\partial \overline{v_i' v_j'}}{\partial x_j} + \bar{f}_i, \tag{2.40}$$

$$\frac{\partial \bar{v}_i}{\partial x_i} = 0. \tag{2.41}$$

There is a new term on the right side of equation (2.40), which contains correlation $\overline{v_i' v_j'}$ – Reynolds stress. This new term is associated with a non linear nature of the Navier-Stokes equations which describe flow and in general is additional unknown, which introduces the closure problem of the turbulence – equations for 2^{nd} order correlations will have the 3^{rd} order statistical moments and so on, i.e. the number of equations is always smaller than the number of unknowns. The Reynolds stresses $\overline{v_i' v_j'}$ are the components of a second-order tensor, which is obviously symmetric $\overline{v_i' v_j'} = \overline{v_j' v_i'}$. Therefore, there are new 6 unknowns in Navier-Stokes equations. The purpose of turbulence modeling is to relate the Reynolds stresses to some quantity which is known. It is worth to mention, that half the trace of the Reynolds stress tensor defines the turbulent kinetic energy: $k = \frac{1}{2}\overline{v_i' v_i'}$. It is the mean kinetic energy per unit mass in the fluctuating velocity field.

The other approach for analytical description of turbulence is based on dimension analysis [44]. Large scale fluctuations, which scale is comparable to the dimensions of the flow region L, have the basic role in the turbulent flow. Large scale pulsation frequencies have the values of order U/L, where U is the characteristic average velocity of the flow. Small scale oscillations have much smaller intensity and spread on the basic large scale structure. Generally small scale turbulence is homogeneous and isotropic in the absence of the walls and volumetric forces. To identify particular oscillations of scale λ the pulsation Reynolds number can be defined:

$$\mathrm{Re}_\lambda = \frac{v_\lambda \lambda}{\nu}, \tag{2.42}$$

where v_λ is the change of velocity over the distance λ. This number decreases while decreasing λ but small Reynolds numbers correspond to large viscosity and therefore fluid viscosity does not effect large scale motion until some critical length scale η, which is called Kolmogorov microscale [100]. Viscosity determines energy dissipation and we can conclude that energy is transferred from large turbulence scales to small in an inertial range and it dissipates into heat when $\mathrm{Re}_\eta \sim 1$. Therefore turbulence decays without external energy source. There is only one combination of characteristic flow parameters, which establishes energy dissipation rate ε:

$$\varepsilon \sim \frac{(\Delta U)^3}{L} \sim \frac{(v_\lambda)^3}{\lambda}, \tag{2.43}$$

where ΔU is variation of U over L. Taking $\mathrm{Re}_\eta \sim 1$ the next quality expressions for the Kolmogorov scale η can be obtained:

$$\eta \sim \frac{L}{\mathrm{Re}^{\frac{3}{4}}} \sim \left(\frac{\nu^3}{\varepsilon}\right)^{\frac{1}{4}}. \tag{2.44}$$

Statistical theory of the turbulence allows to introduce the covariance tensor R_{ij}, which is defined by

$$R_{ij}(\mathbf{r}, \mathbf{x}, t) = \overline{v_i(\mathbf{x}, t) v_j(\mathbf{x} + \mathbf{r}, t)}. \tag{2.45}$$

Coefficients R_{ii} are usually called two-point, one-time autocovariance coefficients. For homogeneous turbulence the two-point correlation is independent from $\mathbf{x}$ Taking an inverse Fourier transform from the coefficient R_{ij}, the one dimensional energy spectrum $E_{ij}(k)$ can be produced, which is defined as twice R_{ij} Fourier transform [70, 100]:

$$E_{ij}(k_1) = \frac{1}{\pi} \int_{-\infty}^{\infty} e^{-ik_1 r_1} R_{ij}(\mathbf{e}_1 r_1) dr_1, \tag{2.46}$$

where subscript $_1$ shows direction ($k_1 = \mathbf{e} \cdot \mathbf{k}$), $\mathbf{e}$ is unity vector, $k = \omega/v$ is the wavenumber (Taylor's hypothesis), $\omega = 2\pi f$ is the cyclic frequency and v is the averaged velocity. For isotropic turbulence the one-dimensional spectra can be determined by energy-spectrum function $E(k)$:

$$E_{11}(k_1) = \iint_{-\infty}^{\infty} \frac{E(k)}{2\pi k^2} \left(1 - \frac{k_1^2}{k^2}\right) dk_2 dk_3. \tag{2.47}$$

Autocovariance functions are usually produced for each velocity component because the measurements producing them are usually taking in one dimension. It can be shown that one dimensional and full turbulence spectra share the same power law behavior [71].

The spectral law of turbulence in an inertial subrange (Kolmogorov law) [41], where motions are determined by inertial effects and viscous effects being negligible, can be firmulated:

$$E(k) = C_k \varepsilon^{2/3} k^{-5/3}, \tag{2.48}$$

where $C_k = 1.4 \ldots 1.5$ is the Kolmogorov constant and according to [100]:

$$\varepsilon = 2\nu \int_0^{\infty} k^2 E(k) dk. \tag{2.49}$$

Equation (2.48) in the verbal form states that in every turbulent flow with high Re the statistics of motions of scale λ in the range $\eta \ll \lambda \ll L$ have a universal form uniquely determined by ε. Another hypotheses postulated by Kolmogorov states that at sufficiently high Reynolds numbers, the small scale

turbulent motions are isotropic. It is convenient to define several scale regions of the flow [70]. Let's introduce lengthscales $l_D = 60\eta$ and $l_E = \frac{1}{6}L$. The former splits dissipation range ($\lambda < l_D$) from the inertial subrange ($l_D < \lambda < l_E$). The later is the demarcation line between the inertial range and the energy-containing range, which represents the largest eddies containing the bulk of the energy .

2.4 Turbulence models and Large Eddy Simulation

Many turbulence models were developed to close equations (2.40), i.e. to find mathematical expression for the Reynolds stresses. Historically turbulence study developed from the Reynolds pipe experiments and first closure models are similar to the boundary layer theory. For example the Prandtl mixing length theory for statistically stationary two-dimensional boundary-layer flows leads to algebraic turbulence model, where artificial turbulence viscosity ν_T is introduced:

$$\nu_T = l_{mix}^2 \left| \frac{\partial \bar{u}}{\partial y} \right|. \tag{2.50}$$

Here l_{mix} is the mixing length, $\bar{u}$ is the average velocity parallel to the boundary and y is the normal distance to the wall.

Velocity fluctuations v_i' in the turbulent flow leads to a higher energy dissipation, which can be described by the effective viscosity: $\nu_{eff} = \nu + \nu_T$. According to Boussinesq assumption Reynolds stress is equivalent to a Newtonian shear stress, which is linear function of strain, and:

$$-\rho\overline{u'v'} = \rho\nu_T \frac{\partial \bar{u}}{\partial y} = \rho l_{mix}^2 \left| \frac{\partial \bar{u}}{\partial y} \right| \frac{\partial \bar{u}}{\partial y}, \tag{2.51}$$

where v' is velocity component collinear to the boundary. The mixing length $l_{mix}(x, y)$ is a function of position and is a new variable.

To avoid modeling of the mixing length two-equation semi-empirical turbulence models can be used, e.g. $k - \varepsilon$ model, in which model transport equations are solved for the turbulent kinetic energy $k = \frac{1}{2}\overline{v_i' v_i'}$ and for its dissipation rate

$\varepsilon = 2\nu\overline{s_{ij}s_{ij}}$ ($s_{ij} = \frac{1}{2}\left(\frac{\partial v_i'}{\partial x_j} + \frac{\partial v_j'}{\partial x_i}\right)$ is fluctuating rate of strain). In place of ε another parameters can be used, e.g. $\omega = \varepsilon/k$. The $k-\varepsilon$ model is used widely and is incorporated in most commercial CFD codes. The model was developed by Launder and Spalding for fylly turbulent flow in 1972 [45] and its basic equations are [114]:

$$\nu_T = C_\mu k^2/\varepsilon \tag{2.52}$$

$$\rho\frac{\partial k}{\partial t} + \rho\bar{v}_j\frac{\partial k}{\partial x_j} = \tau_{ij}\frac{\partial \bar{v}_i}{\partial x_j} - \rho\varepsilon + \rho\frac{\partial}{\partial x_j}\left[(\nu + \nu_T/\sigma_k)\frac{\partial k}{\partial x_j}\right] \tag{2.53}$$

$$\rho\frac{\partial \varepsilon}{\partial t} + \rho\bar{v}_j\frac{\partial \varepsilon}{\partial x_j} = C_{\varepsilon 1}\frac{\varepsilon}{k}\tau_{ij}\frac{\partial \bar{v}_i}{\partial x_j} - C_{\varepsilon 2}\rho\frac{\varepsilon^2}{k} + \rho\frac{\partial}{\partial x_j}\left[(\nu + \nu_T/\sigma_\varepsilon)\frac{\partial \varepsilon}{\partial x_j}\right]. \tag{2.54}$$

The model contains five constants and in standard case:

$$C_{\varepsilon 1} = 1.44,\ C_{\varepsilon 2} = 1.92,\ C_\mu = 0.09,\ \sigma_k = 1.0,\ \sigma_\varepsilon = 1.3. \tag{2.55}$$

The turbulent stresses are computed from:

$$\overline{u'v'} = -\nu_T\left(\frac{\partial \overline{v}_i}{\partial x_j} + \frac{\partial \overline{v}_j}{\partial x_i}\right) + \frac{2}{3}k\delta_{ij}. \tag{2.56}$$

This model and $k-\omega$ are used in the work only as additional illustrations and for LES results comparison. So the author will not discuss its modifications (low-Re, RNG, SST) and special treatment for boundary region in detail. All necessary information regarding two-equation models can be found in [112, 114].

The next step is Large-eddy simulation (LES) [82], which is a good compromise between DNS and Reynolds-stress models. It combines faster computations at high Re and unsteady three-dimensional turbulence simulation in complex geometries. The idea of LES method is to directly represent large 3D unsteady turbulent motions and to model small-scale turbulent motions. The method is carried out by filtering Navier-Stokes equations (2.23) with a filter function $G(\mathbf{r}, \mathbf{x})$ and decomposing the velocity $\mathbf{v}(\mathbf{x}, t)$ into the sum of a filtered $\bar{\mathbf{v}}(\mathbf{x}, t)$ and a subgrid-scale (SGS) component $\mathbf{v}'(\mathbf{x}, t)$. This SGS component introduces the residual-stress tensor T_{ij} into the Navier-Stokes equations, which needs the closer, most simply by an eddy-viscosity model.

The LES method started to develop in the 1960's and early 1970's with the pioneering work for incompressible flows of Smagorinsky [90] and Lilly [51]. It became very popular for engineering applications since the work of Deardorff for channel flow [15]. The recent advances and strict mathematical formulation of LES can be found in [32, 49, 62] but the next paragraphs give only basic overview of LES method.

The general LES filtering is defined by [70]

$$\bar{\mathbf{v}}(\mathbf{x},t) = \int G(\mathbf{r},\mathbf{x})\mathbf{v}(\mathbf{x}-\mathbf{r})d\mathbf{r} \tag{2.57}$$

The integration takes place in the whole flow region. Filter function $G(\mathbf{r},\mathbf{x})$ must satisfy normalization condition: $\int G(\mathbf{r},\mathbf{x})d\mathbf{r} = 1$ and can be $\mathbf{x}$ independent. Therefore SGS velocity is simply

$$\mathbf{v}'(\mathbf{x},t) \equiv \mathbf{v}(\mathbf{x},t) - \bar{\mathbf{v}}(\mathbf{x},t) \tag{2.58}$$

and appears analogous to the Reynolds decomposition. The scale of the resolved eddies is determined by the specified filter width Δ (table 2.3), which is comparable to the characteristic grid spacing h.

The filtering properties can be most simply illustrated in one dimension using a random scalar (velocity) field $v(x)$. With a homogeneous filter $G(r)$ the filtered velocity field according to (2.57) is given by the convolution

$$\bar{v}(x) = \int_{-\infty}^{\infty} G(r)v(x-r)dr. \tag{2.59}$$

The most commonly used filters are the box filter, the Gaussian filter and the sharp spectral filter (table 2.3). The transfer function $\hat{G}(k)$ is 2π times the Fourier transform of the filter in the wavenumber space:

$$\hat{G}(k) = \int_{-\infty}^{\infty} G(r)e^{-ikr}dr = 2\pi\mathcal{F}\{G(r)\}. \tag{2.60}$$

Approximately 80% of the energy is resolved in 3D case with the filter of width $\Delta = l_E$. It can be shown that the energy spectrum (2.46) is attenuated by

Table 2.3: Most commonly used one dimensional filter functions and corresponding transfer functions [70]. $H(x) = 1$ if $x > 0$ and $H(x) = 0$ otherwise, is the Heaviside function

Name	Flter function	Transfer function
General	$G(r)$	$\hat{G}(k) \equiv \int_{-\infty}^{\infty} e^{-ikr} G(r) dr$
Box	$\frac{1}{\Delta} H\left(\frac{1}{2}\Delta - \lvert r\rvert\right)$	$\frac{\sin(\frac{1}{2}k\Delta)}{\frac{1}{2}k\Delta}$
Gaussian	$\left(\frac{6}{\pi\Delta^2}\right)^{1/2} \exp\left(-\frac{6r^2}{\Delta^2}\right)$	$\exp\left(-\frac{k^2\Delta^2}{24}\right)$
Sharp spectral	$\frac{\sin(\pi r/\Delta)}{\pi r}$	$H(k_C - \lvert k\rvert)$

the transfer function as

$$\bar{E}_{11}(k) = |\hat{G}(k)|^2 E_{11}(k). \tag{2.61}$$

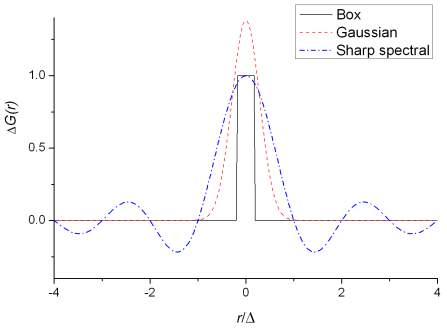

Figure 2.2: One dimensional filters $G(r)$, $\Delta = 0.35$.

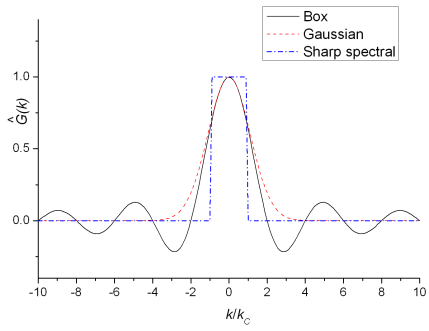

Figure 2.3: Filter transfer functions $\hat{G}(k)$, $\Delta = 0.35$.

Let's select the filter $G(\mathbf{r})$, which is independent of the position $\mathbf{x}$ and com-

mutes with spatial and temporal derivatives. Performing the filtering it can be checked that continuity equation holds for the filtered field:

$$\frac{\partial \bar{v}_i}{\partial x_i} = 0. \tag{2.62}$$

Applying the filtering to the Navier-Stokes equation (2.24) the next expression can be obtained:

$$\frac{\partial \bar{v}_i}{\partial t} + \bar{v}_j \frac{\partial \bar{v}_i}{\partial x_j} = -\frac{1}{\rho_f}\frac{\partial \bar{p}}{\partial x_i} + \frac{\partial}{\partial x_j}\left[\nu\left(\frac{\partial \bar{v}_i}{\partial x_j} + \frac{\partial \bar{v}_j}{\partial x_i}\right) + T_{ij}\right] + f_i, \tag{2.63}$$

where the subgrid-scale tensor T_{ij} is given by

$$T_{ij} = \bar{v}_i \bar{v}_j - \overline{v_i v_j}. \tag{2.64}$$

The eddy-viscosity assumption is used in most subgrid-scale models to model the subgrid-scale tensor [49]:

$$T_{ij} = 2\nu_T \bar{S}_{ij} + \frac{1}{3} T_{ll}\delta_{ij}, \tag{2.65}$$

where $\bar{S}_{i\,j}$ is the deformation tensor of the filtered field. The last term from the right side can be included into a modified pressure $\bar{P} = \bar{p} - (1/3)\rho_f T_{ll}$, which introduces the momentum equation in the form:

$$\frac{\partial \bar{v}_i}{\partial t} + \bar{v}_j \frac{\partial \bar{v}_i}{\partial x_j} = -\frac{1}{\rho_f}\frac{\partial \bar{P}}{\partial x_i} + 2\frac{\partial}{\partial x_j}[(\nu + \nu_T)\bar{S}_{ij}] + f_i.. \tag{2.66}$$

Analogically a relation for the transport of the passive scalar (2.36) can be filtered, introducing a turbulent eddy diffusivity Γ_T:

$$\frac{\partial \bar{\phi}}{\partial t} + \bar{v}_i \frac{\partial \bar{\phi}}{\partial x_i} = \frac{\partial}{\partial x_i}\left[(\Gamma + \Gamma_T)\frac{\partial \bar{\phi}}{\partial x_i}\right]. \tag{2.67}$$

The SGS viscosity is most widely modeled using the Smagorinsky model [90]. The eddy viscosity ν_T is assumed to be proportional to the subgrid-scale characteristic length scale Δ and to a characteristic turbulent velocity based on the second invariant of the filtered-field deformation tensor in this model:

$$\nu_T = (C_S\Delta)^2|\bar{S}|, \tag{2.68}$$

where the local strain rate is defined by $|\bar{S}| = (2\bar{S}_{ij}\bar{S}_{ij})^{1/2}$. Sometimes $l_S = C_S\Delta$ is called the Smagorinsky lengthscale (analogous to the mixing length). The Smagorinsky constant C_S can be adjusted so that the ensemble-averaged subgrid kinetic energy dissipation is balanced by ε. If the filter cutoff wavenumber in the Fourier space $k_C = \pi/\Delta$ is in the inertial subrange, where Kolmogorov's law (2.48) holds, then according to [51] the Smagorinsky constant can be estimated as

$$C_S \approx \frac{1}{\pi}\left(\frac{3C_k}{2}\right)^{-3/4} \approx 0.17. \tag{2.69}$$

However, this C_S value was found to cause excessive damping of large-scale fluctuations in the presence of mean shear and in transitional flows as near solid boundary, and has to be reduced in such regions. Value of around 0.1 has been found to yield the best results for a wide range of flows [49].

The number of other SGS models was developed. For example, the dynamic subgrid-scale (DSGS) model [57], which allows the Smagorinsky constant C_S vary in space and time. Here C_S is calculated locally at each time step from flow variables using two filters: test filter and grid filter.

2.5 Particle tracing Lagrangian approach

Particle motion in the fluid is a two-phase flow, which is found in many engineering systems including aerospace, biological, chemical, civil, mechanical, and nuclear applications. In particular, the interest to particle motion in a fluid is caused because many combustion and energy systems involve dilute two-phase flow, ranging from droplet sprays in high-speed gas turbine combustor flow to bubbly pipe flows of nuclear reactors. Deeper understanding of the two-phase interactions can lead to increases in performance, reduction in cost and/or improved safety for such systems. Turbulent particle transport can give additional information about mass exchange in different induction furnaces, especially for alloying and EM separation processes in ICF and for clogging and erosion in CIF.

The most simple way to model particle transport is to solve additional diffusion equation (2.36) for particle concentration. The concentration maps can be

created, however separate particle can not be distinguished. These methods are expected to have difficulties with the accurate treatment of boundary conditions.

There are two main approaches for treatment of the disperse particles: Eulerean and Lagrangian. The characteristics of the particles (e.g. velocity or temperature) are described as continuum in the Eulerian dispersed-phase description. In this way the dispersed-phase is treated with the same discretization and numerical techniques as used for the continuous-phase. This can reduce the computational costs for two-way coupling (particles are not only effected by the fluid flow, but the flow itself is effected by the particles), but this approach seems to be have more difficult realization.

Lagrangian approach means that the particle is described as a single point which moves at its own velocity. This allows direct reconstruction of the individual particle trajectories. Lagrangian technique also introduces more straightforward description of particle turbulent diffusion and particle reflection from solid boundaries. Usually the fluid velocity field is computed first and then new particle positions are computed integrating equation of the particle motion.There are also some works towards a mixed EulerianLagrangian description for the particles [39] but such approaches may not yet be developed and tested enough for general applications.

The disperse particle motion in the conducting fluid under the influence of EM field is determined by several forces: Stokes drag force, buoyancy force, EM force and Saffman lift force [81]. Besides particles are strongly affected by the flow structures and it is found experimentally and numerically that in turbulent flows without influence of EM fields preferred concentration of heavy particles can occur which is expressed as centrifuging of particles away from vortex cores and accumulation of particles in convergence zones [21].

Particle number in the flow can be expressed through the volume fraction of the dispersed phase:

$$\alpha_p = \frac{\sum_{i=1}^{N} V_p^i}{V_{tot}}, \tag{2.70}$$

where N is the total number of the particles, V_{tot} is the limiting volume, which includes both fluid and particles, V_p^i is the single particle volume. Equivalently

the volume fraction of the continuous phase α_f can be defined and a simple relation is obtained:

$$\alpha_p + \alpha_f = 1. \tag{2.71}$$

The Stokes number can be introduced to describe the intensity of the particle interaction with the fluid. It is defined as the ratio of the particle fluid response time constant to an appropriate turbulence time scale (dissipation time):

$$\mathrm{St} = \frac{\tau_p}{\tau_\eta}. \tag{2.72}$$

If the Stokes number is much less than unity then the particle and fluid velocities will be nearly equal, i.e. the particles response to the fluid velocity changes is very fast and the particles can be treated as the fluid tracers. If St$\gg$ 1, then the particle will have essentially no time to respond to the fluid velocity changes. It can be shown [12], that the ratio of the particle to fluid velocity is

$$\frac{v_p}{v} \sim \frac{1}{1+\mathrm{St}}. \tag{2.73}$$

According to [21] different estimations of τ_p corresponds to different flow Reynolds numbers. For small Re the particle response time (momentum response time) can be estimated using Stokes equation as $\tau_p = \rho_p d_p^2/(18\mu)$, where ρ_p is the particle density, μ is the dynamical viscosity of the melt and d_p is the particle diameter. Taking into account dissipation time scale $\tau_\eta = L/U$ (L and U are characteristic integral length and velocity scales) the Stokes number can be estimated as:

$$\mathrm{St} = \frac{\rho_p d_p^2 U}{18\mu L}. \tag{2.74}$$

Particles response to the vortex motion has a maximum, which lies between St $= 0.1$ and St $= 1$. Therefore, particles with corresponding St should be strongly affected by the turbulent vortices. For example, it is shown [54] that particles are excluded from the vortex centers if the particle density is much larger then the fluid density.

Detailed analysis of the motion laws for the spherical particles in the flow can be found in [58]. The Lagrangian approach was used in this work for particle tracing and the next force balance equation was solved [1, 117]:

$$\frac{d\mathbf{v}_p}{dt} = F_D(\mathbf{v} - \mathbf{v_p}) + \mathbf{g}\frac{\rho - \rho_p}{\rho} + \mathbf{F}, \tag{2.75}$$

where $\mathbf{F}$ is the possible additional volumetric force and F_D is the drag force per unit particle mass. The second term from the right side represents the lifting force. F_D can be expressed as:

$$F_D = \frac{18\mu}{\rho_p d_p^2} \cdot \frac{C_D \mathrm{Re}_p}{24}, \;\; \mathrm{Re_p} = \frac{\rho\, d_p |\mathbf{v}_p - \mathbf{v}|}{\mu}. \tag{2.76}$$

For the low Reynolds numbers, i.e. Stokes flow, the factor $C_D\mathrm{Re}_p/24$ approaches unity. The second factor $18\mu/(\rho_p d_p^2)$ is a reciprocal of the momentum response time τ_p. This allows to write a momentum equation (2.76) for the Stokes flow using the second Newton's law in the absence of the volumetric forces as:

$$\frac{d\mathbf{v}}{dt} = \frac{1}{\tau_p}(\mathbf{v} - \mathbf{v_p}). \tag{2.77}$$

This equation can be solved for a constant fluid velocity v and an initial particle velocity of zero [12]:

$$v_p = v(1 - e^{-t/\tau_p}). \tag{2.78}$$

Thus the particle response time corresponds to the time, which is needed for free released particle to reach 63% of the free stream velocity.

The drag coefficient C_D is usually calculated using [65]:

$$C_D = a_1 + \frac{a_2}{\mathrm{Re}_p} + \frac{a_3}{\mathrm{Re}_p^2}, \tag{2.79}$$

where $a1$, $a2$ and $a3$ are constants that apply to smooth spherical particles. The particular form of this expression for finite Reynolds number was derived by Oseen using a perturbation method [68]:

$$C_D = \frac{24}{\mathrm{Re}_p}\left(1 + \frac{3}{16}\mathrm{Re}_p\right). \tag{2.80}$$

It was numerically shown [59] that the Reynolds numbers Re_p of the particles that deposit does not remain small compared to unity. The effects of nonlinear drag can be accounted using an empirical relation given by [72, 83]:

$$C_D = \frac{24}{\mathrm{Re}_p}(1 + 0.15\mathrm{Re}_p^{0.687}). \tag{2.81}$$

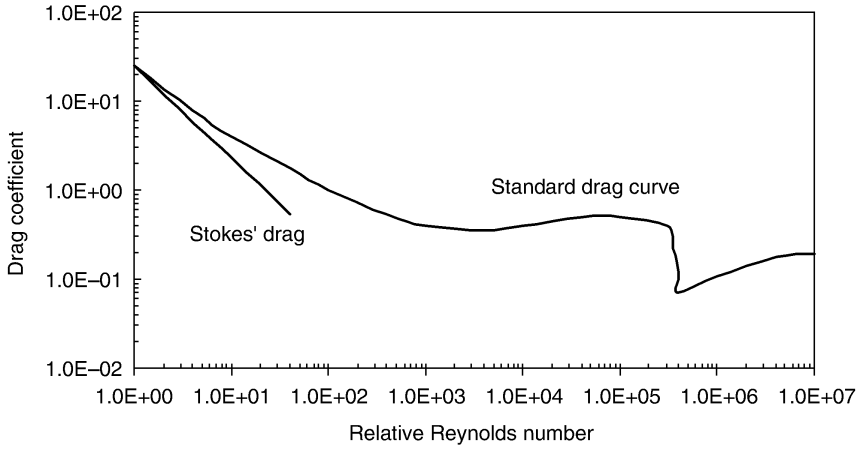

Figure 2.4: Standard drag curve [12].

The above expression is recommended to be used in the range $1 < \mathrm{Re}_p < 800$. The linear Stokes drag $C_D = 24/\mathrm{Re}_p$ can be used in the range $0 < \mathrm{Re}_p < 0.1$, which transforms to the Oseen asymptotic expression, exponentially decreases and goes to the equation (2.81) when Re_p is growing [12]. These transformations represent the standard drag curve (figure 2.4). The particle drag force (2.76) multiplied by its mass is presented on figure 2.5.

The turbulence can increase the drag coefficient of the spherical particle [72], but in general the standard drag curve is in force. However the drag coefficient can be reduced if the turbulent boundary layer is formed on the surface of the particle. We will not account on this effect because particles are represented by points and we accept that Re_p not to be very large.

The particles are influenced by the EM field if their electrical conductivity σ_p differs from conductivity of the liquid media, which can introduce inhomogeneity in locally (on the scale of particle dimensions) homogeneous EM field. The current and the magnetic induction values in the particle and in the surrounding liquid

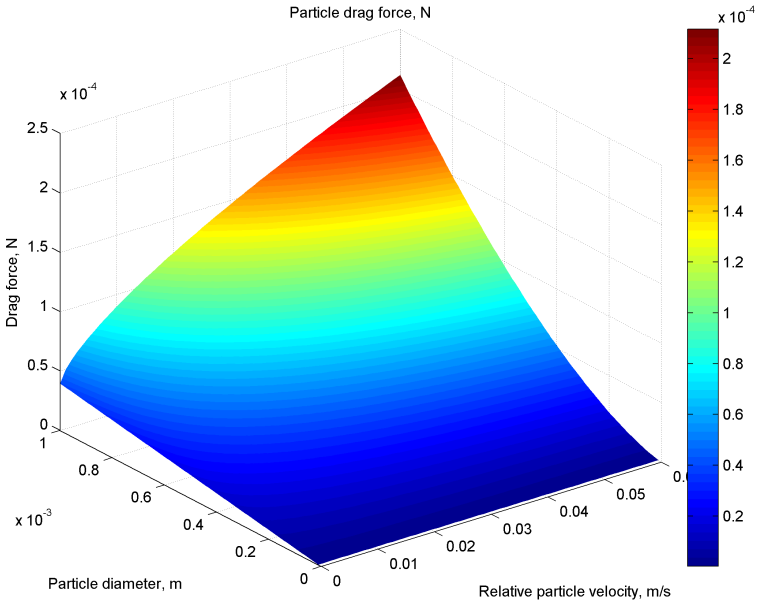

Figure 2.5: Particle drag force dependence on its diameter and relative velocity for $\rho_p = 8545$ kg/m^3, C_D is taken from (2.81).

becomes different and additional volumetric force, which acts on the particle appears. This force acting on the spherical particle can be derived solving La Place equation for current density [47]:

$$\mathbf{F}_{pEM} = -\frac{3}{2}\frac{\sigma - \sigma_p}{2\sigma + \sigma_p} V_p \mathbf{f}_{EM}, \tag{2.82}$$

where V_p is volume of the particle and the specific magnetic Lorentz force is given by (2.12). The maximal force and a simplified expression can be achieved for non-conducting particles:

$$\mathbf{F}_{pEM} = -\frac{3}{4} V_p \mathbf{f}_{EM}. \tag{2.83}$$

Particles also can be affected by lift forces. Experiments [27] have shown that neutrally buoyant particles in laminar, with radius R_t pipe flow migrate across streamlines and tend to adopt radial position of $0.6R_t$. The same phenomena in shear flow was studied [81] and it was shown that lift force is determined by

velocity gradients in the fluid:

$$F_{Saff} = 1.61\rho\nu d_p|\mathbf{v} - \mathbf{v}_p|\sqrt{\mathrm{Re}_G}, \;\; \mathrm{Re}_G = \frac{d_p^2}{nu}\frac{\partial v}{\partial x_2}, \tag{2.84}$$

where x_2 represents coordinate orthogonal to the direction of particle motion, Re_G is called shear Reynolds number. This formula is valid only for Stokes flows ($\mathrm{Re} < 1$) under the condition $\mathrm{Re}_p \ll \sqrt{\mathrm{Re}_G} \ll 1$. It has been found, that Saffman lift force is an order of magnitude smaller than the normal component of the Stokes drag force even in the viscous sublayer [59]. Furthermore, the Saffman lift force becomes less important for particles with large particlefluid density ratios or large response times.

3 Measurements of the velocity pulsations in the cylindrical container

3.1 Introduction to turbulence measurements in liquid metals

The measurement of the local flow velocity and turbulence in the industrial equipment is a topic of a great interest because knowledge about the internal flow processes in the melt is the key for successful and efficient utilization of expensive industrial equipment. From the other side such experimental measurements data are very rare due to the large difficulties of applying laboratory measuring systems to the industrial facilities. High temperatures of the most casting processes and very aggressive (hostile) nature of the liquid metals also restrict selection of possible measurement technology. Moreover, the melts are usually opaque and are enclosed in melting crucibles or other containers, which are surrounded by the thermal insulation. Besides, many industrial processes are taken in a special atmosphere, when direct access to the melt in the working facility is impossible.

Historically many methods were used for velocity measurements (e.g. [6]), but almost all of them have limitations for turbulent velocity measurements in high-temperature liquid metals. Only most interesting examples of velocity measurements are shown below.

Pitot tubes were not suitable for turbulent measurements in liquid metals at all because they give only mean velocity values and besides the tubes are troubled

by the solidification of the melt inside.

Mechanical reaction probes were based on measuring the force exerted on a submerged body by the flowing fluid. The used probes had different shapes (discs [37], plates, porous [64] or rigid spheres) and were used to measure one or two velocity components simultaneously. The inertia of the probes usually prevented the detailed measurements of the turbulence, however, turbulent intensities were measured in some experiments and compared to numerical computation. This method also was used to measure horizontal aluminium velocity using a graphite sphere in a real furnace [50]. Reaction or balance probes were the first for study of the melt flow in the induction furnace models with liquid aluminium [16, 33], where axial flow velocity distributions were measured not only on the symmetry axis of the crucible, but also near the crucible walls depending on the inductor current. These measurements introduced several important conclusions: the flow is always turbulent even for small inductor currents, the flow forms two-circuit pattern for single-phase inductor, the viscosity plays unimportant role at Re $>$ 20000.

Reaction probes had built-in strain gauges. Fibre-optic velocity sensors have been further development of this technology replacing strain transformation of the deformation to optical. They had a thin-walled glass pointer as a reacting element, which was deflected by the flow introducing different scattering to light coming from light guides to receptors. The light intensity can be measured by photocells and their signal depends on the flow velocity. The sensor was used in electrovortical mercury flow and it does not suffer from strong electromagnetic interactions [108].

Hot wire and hot film probes in mercury experiments [96] had restricted applicability to 100°C. These probes were also used in Wood's metal allowing to measure both average and pulsatile velocities. The thermal wake behind a hot wire is tracked allowing to measure the flow direction. The hot wire is supplied by sinusoidal current source allowing better determination of the wake and measurement of the flow velocity. The sensitivity of this probe starts from several cm/s [78] and a secondary recirculating flow in a n RMF-driven mercury was detected. However, the latest experiments with this method are dated back to the 80-ties.

The sphere melting technique was developed, which is able to measure not only the velocity magnitude, but also a direction of the flow [61] in any melt. The basic principle of this method is that the total melting time of a sphere is a function of the diameter, bath superheat and velocity. The uncertainty of the method for velocity magnitude is about 20% while it is below 30% for direction measurements. The mathematical model proposes the next expression for velocity estimation [60]:

$$v \sim \frac{D^3}{t_M^2 \cdot (T - T_{melt})}, \tag{3.1}$$

where D is the diameter of the sphere, t_M [s] is the sphere melting time and $(T - T_{melt})$ is the superheat. The method was applied for velocity measurements in liquid aluminium. By its definition, the method can decide only average velocity measurements.

Recent advances in ultrasound Doppler velocimetry (UDV) [98] introduce possibility to use it for the velocity measurements in hot metallic melts up to about 600-800°C using specially designed shielded sensor with high Curie temperature piezoelectric crystal [79]. However, the sensitivity of this UDV probe at high temperatures is roughly one order of magnitude less than the usual UDV method gives at 100°C. Therefore high temperature UDV also may have implementation difficulties and must be carefully tested before wide application for the measurements in high temperature liquid metals.

The idea of a contactless inductive flow tomography (CIFT) [101] is to measure perturbations in the external applied magnetic field, which are caused by the moving conducting fluid. Induced magnetic field is measured by external Hall sensors and then inverse problem is solved for velocity estimation. The method has many experimental problems but it can be used for transient resolution of 3D flow structure in steps of a few seconds.

The alternative, which is used for velocity and turbulence measurements in the liquid metals at temperatures below 720°C (for example in liquid aluminium), is the permanent magnet probe (PMP or Vives' probe) [77], which is widely used in measurements within model metals (InGaSn, Wood's metal). The working

principle of the PMP is based on the Faraday's law (2.4), i.e. if an electric conductor moves through a magnetic field the conductor has an electromotive force induced in it. This force is normal to the magnetic field and a direction of motion.

The permanent magnet probe (figure 3.1), which was used in experiments, consists of the permanent magnet, which generates high intensity constant magnetic field with B = 0.05 ÷ 0.1 T, surrounded by four steel wire electrodes. The strength of the local magnetic field is reduced by factor 2 selecting the appropriate magnetic material for the high-temperature melts. The angular distance between the electrodes is 90°. Electrodes are steel shielded and there is a ceramic insulation between the wire and the shield. The sensor is used to measure two instantaneous velocity components simultaneously, which are orthogonal to the line connecting the opposite electrodes and symmetry axis of the magnet. A voltage drop between the corresponding electrodes can be measured by a precise nano-voltmeter. In the absence of current between electrodes the Ohm's law (2.5) is also applicable. From the other side equation $\mathbf{E} = -\nabla \cdot \Phi$ can be approximated as $E \approx -\dfrac{\Delta\Phi}{\Delta x}$, where $\Delta\Phi$ and Δx are potential difference and distance between the electrodes. Therefore, for properly arranged sensor the next approximate equation should be valid:

$$\Delta\Phi = \Delta x \cdot \mathbf{VB}. \tag{3.2}$$

It can be shown that the probe works correctly in the absence of velocity gradient in the magnetic field direction, which leads to $\nabla \times \mathbf{j} = 0$, i.e. zero induced currents [3]. Similar probes without the central magnet can be successfully used in the presence of the external DC magnetic field.

It was shown, that the level of the probe signal is dependent on the size of the magnet – the larger is the magnet diameter, the better is the signal. Linearity of the probe for velocities starting from 1 cm/s is confirmed experimentally [77] and is expressed only by one constant. However the potential difference dependence on the flow velocity can be more complicated for very small flow velocities, i.e. $v <$ 1 cm/s [110]. The sensor can be modified to perform also a temperature and heat flux registration with a high rate [110] if usual electrodes are replaced by small thermocouples. The physical properties of the permanent magnets provide

stability of the measuring sensor for many hours, but this period and a signal level are reduced when melt temperature is increased. The permanent magnet probes with ALNICO magnets were successfully used for velocity measurements in liquid Al and other metals [89] and it was found, that calibration curve obtained from a crucible with a constant angular velocity is the same for different metals.

The latest trends in PMP development are their miniaturization and increasing sensitivity for small velocity measurements [4]. The geometrical size of the probe head can be reduced to only 3 mm with 70 μm copper electrodes and a rare-earth Co-Sm magnet of 2×2 mm^2 cross-section. The developed probe measures only one velocity component and it was used by [4] to measure a secondary flow in the flow drive by a rotating magnetic field. High precision of the small velocity (from 0.01 cm/s) measurements was achieved using the latest generation analog amplifies, which allowed to reconstruct non-linear part of the PMP calibration curve. However, linearity of the probe is confirmed again for $v > 0.1$ cm/s, which

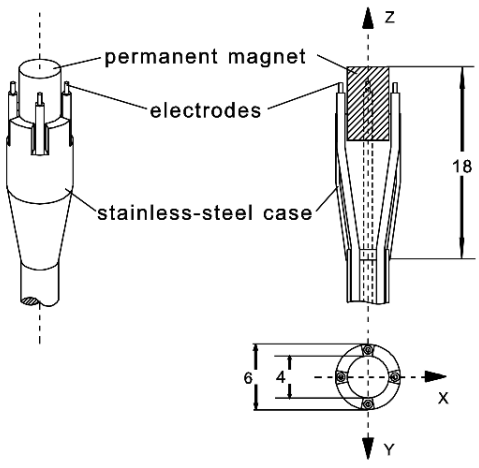

Figure 3.1: Drawing and dimensions (mm) of the permanent magnet probe used in experiments [8], with permission.

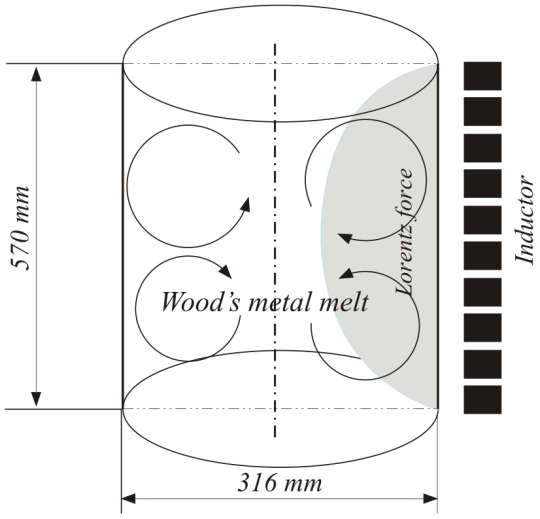

Figure 3.2: Design of the experimental crucible induction furnace with sketch of typical vortices of the mean flow.

is a working PMP range in our experiments.

3.2 Experiment setup for velocity measurements in Wood's melt

All experiments were established in the Institute of Electrotechnology, Leibniz University Hannover (Germany). The turbulent properties of the Wood's metal melt flow in the induction crucible furnace (figure 3.3) were studied. The selection of Wood's alloy as a model melt was determined by its availability.

Wood's metal is a fusible alloy. It has melting temperature about 70°C. It is a eutectic alloy of bismuth, lead, tin, and cadmium with the following percentages by weight: 50% Bi, 26.7% Pb, 13.3% Sn, 10% Cd. It is also can be called as Cerrobend, Bendalloy, and Pewtalloy. It is often used as a low-temperature casting metal in MHD experiments for prototyping. Note that the lead and cadmium components of the alloy makes it toxic. The basic physical properties of the Wood's metal are given in the table 2.1. The density of the Wood's metal is 9.4 times larger than the water density and approximately 3 times the aluminium density, but thermal conductivity of the Wood's alloy is much smaller than of the Al. Therefore, turbulent heat transfer is more determinative for temperature homogenization in the Wood's alloy than in Al.

Another fusible alloy material, which is often used for prototyping, is galinstan (68.5% Ga, 21.5% In, 10% Sn). It has very low melting temperature about 10.5°C. It was successfully used as a model material for simulation of CZ silicon crystal growth process [102] and for investigation of many other MHD processes (e.g. [2, 3]).

For turbulence measurement the non-magnetic stainless steel crucible (R = 15.8 cm, H = 57 cm) was used (figure 3.2). This steel has very high mechanical strength, which permitted to restrict the wall thickness of the melt container to 1 mm and with combination of a relatively low electrical conductivity $\sigma = 0.83 \cdot 10^6$ S·m^{-1} made it transparent for EM field of the indictor. The crucible had an electrical heating system, which could heat it till 80°C with or without

the melt inside. It allowed operations with the Wood's melt in the crucible without working AC magnetic field. However, the Wood's metal expands during the solidification and to avoid safety problems with the crucible installation the melt between the experiments was taken away from the crucible to the special vessel (figure 3.4(a)) with thicker steel walls and embedded temperature regulation system. The crucible-vessel connecting tube was made from teflon with heating elements along to allow transportation of the liquid metal to and from the crucible.

The crucible was surrounded by a high-frequency one-phase solenoidal induction coil. It had 12 or 11 turns and was placed mainly symmetrically with respect to the melt middle height. Alternating EM field was used in experiments as the driving force for melt steering. The characteristic frequency of the EM field was about 400 Hz. The influence of the AC EM field to the conducting melt is controlled by the skin effect: the ability of AC to distribute itself in a conducting medium so that the current density near the surface of the conductor is greater than that at its core [14]. For the harmonic magnetic field $\mathbf{B} = B_0 \cos(\omega t)\mathbf{e}_z$, where B_0 is a uniform field amplitude and $\omega = 2\pi f$ is the cyclic frequency the next expression for the skin-layer thickness δ can be obtained:

$$\delta = \sqrt{\frac{2}{\mu_0 \sigma \omega}}. \tag{3.3}$$

Skin-layer thickness δ characterizes thin boundary layer of the conductor (table 3.1) where the opposite induced currents are closed. These induced currents interacts with the field $\mathbf{B}$ producing the Lorentz force (2.12), which acts on the melt. The Lorentz force can be separated to the mean and oscillatory parts. The motion of the melt is mainly determined by the mean part, since the finite inertia of the fluid means that a high-frequency oscillatory part induces very little motion. It can be shown [14], that this mean repulsion force produces magnetic pressure of the order $B_0^2/4\mu_0$.

The presence of induced currents in the skin layer leads to the Joule heating of the conductor. Joule dissipation j^2/σ can be integrated across the skin depth and

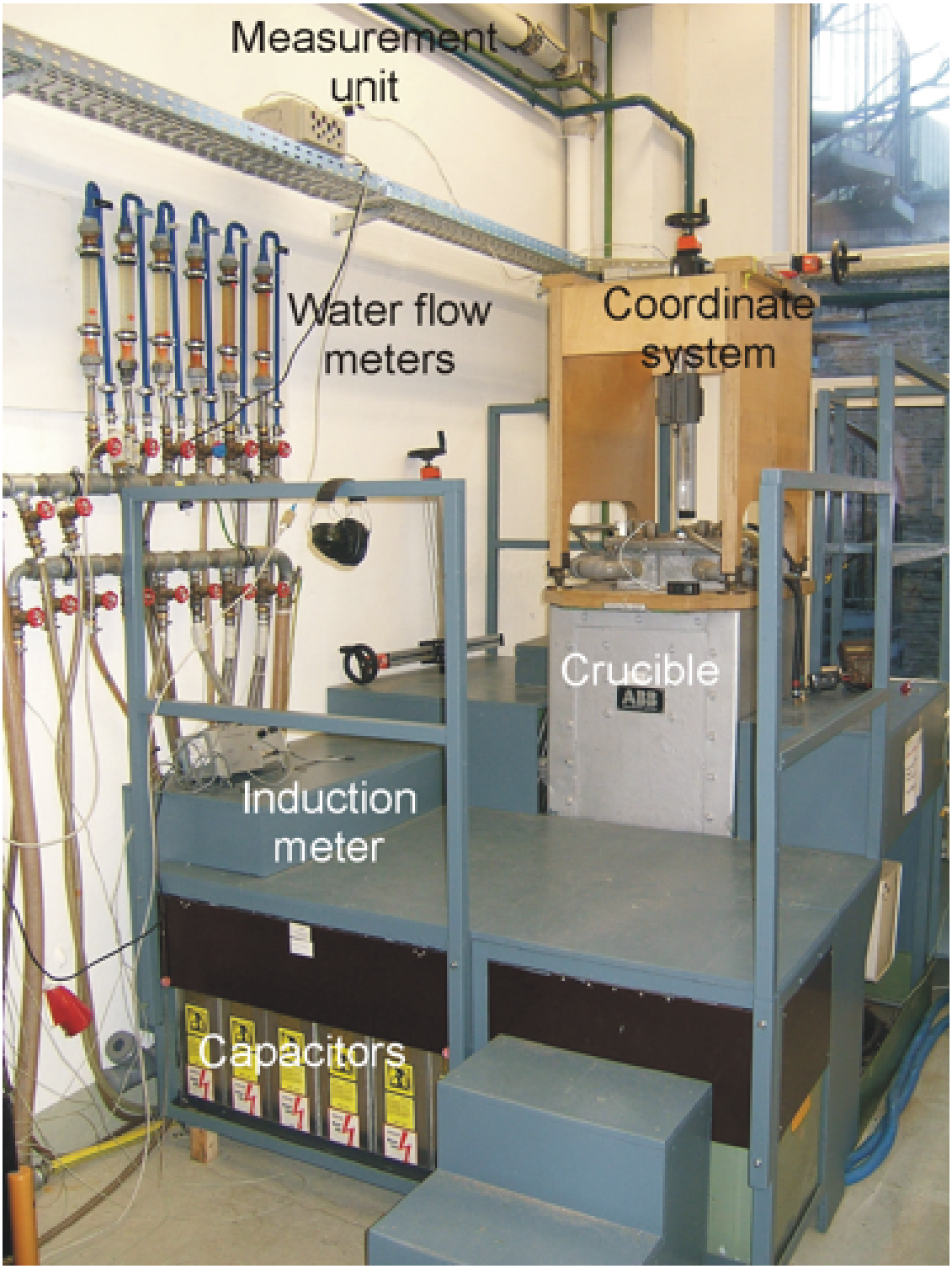

Figure 3.3: Common view of the ICF installation.

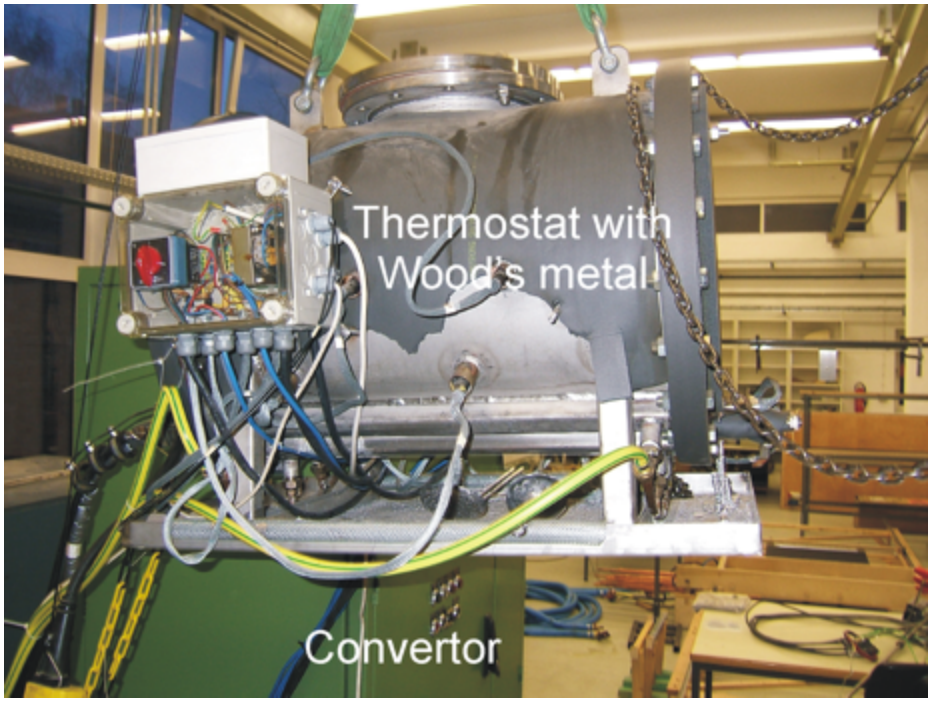

(a) Thermostat with the melt

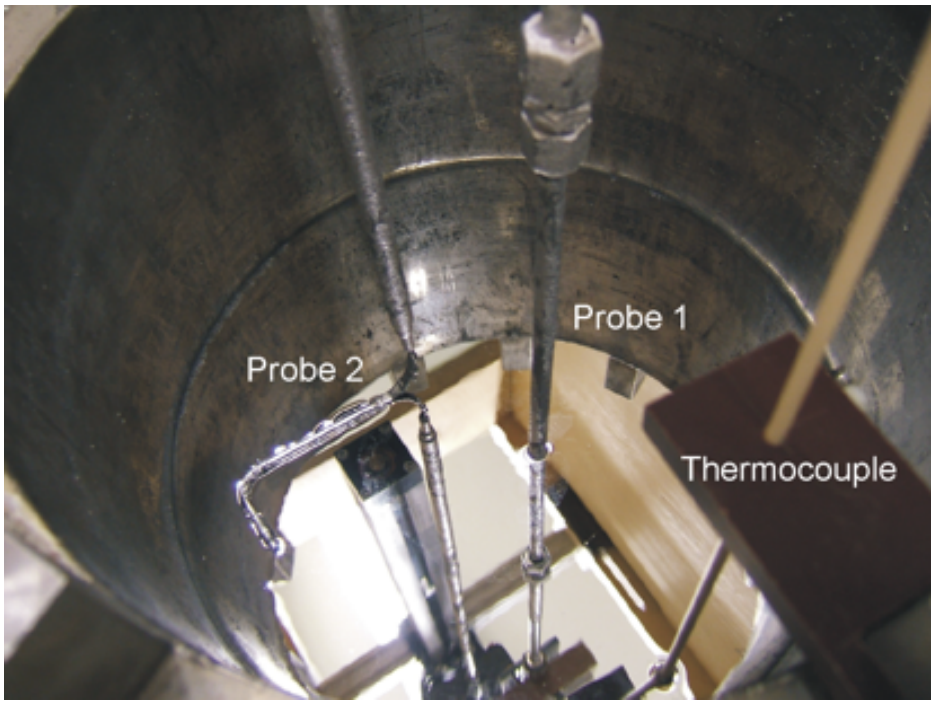

(b) Sensor installation

Figure 3.4: Thermostat with the Wood's metal and sensor installation.

Table 3.1: Calculated skin depth in centimeters for different materials and inductor frequencies.

f, Hz	Al	TiAl	Wood's metal
50	2.65	5.03	5.03
400	0.94	1.78	1.78
1000	0.59	1.13	1.13
5000	0.27	0.50	0.50
10000	0.19	0.36	0.36
20000	0.13	0.25	0.25

the expression for the net heating rate per unit surface area can be obtained [14]:

$$\dot{q} = \int_0^\infty \frac{j^2}{\sigma} dx = \frac{B_0^2}{4\mu_0} \omega \delta. \tag{3.4}$$

The melt temperature growing can introduce changes to the material properties, e.g. viscosity and density. Therefore heating and freezing of the melt should be carefully avoided to measure velocities of the same material with constant physical properties. The crucible had water cooling system, which can be regulated to obtain constant melt temperature in different experiments using flow-meters. For this reason the temperature was controlled in several points during the measurements. The crucible temperature was measured by a digital thermometer and was usually about 80°C. The melt temperature was taken by the K-type thermocouple, which was immersed into the liquid metal (10 cm from the top melt surface and 4 cm from the crucible wall, figure 3.4(b)). This temperature was approximately 114°C in average. The flow-meters were adjusted several times during the measurements to get stable temperature parameters of the crucible and of the melt. Measured temperature fluctuations were in the ±1°C range.

Velocity of the flow was measured using one or two PMP sensors. The sensors were fixed on a coordinate system (figure 3.3), which allowed independent sensor movements. Positioning precision was ±0.1 mm. The origin of the PMP

coordinate system conforms with the lowest point on central symmetry axis. Afterwards all coordinates will be translated to the center of a symmetry, which for standard filling level is shifted 0.285 m up in z direction. Careful calibration ensured that both sensors movements were limited in the one meridian plane. The banded sensor tubes allowed measurements of velocities near the crucible wall. The minimal available distance between the sensors was 20 mm because of mechanical interference.

The probes were connected to "Delphin TopMessage" 24 bit industrial measurement unit (case **A**) with 800 Hz maximal scanning rate (multiplexed channels) or to high frequency (till 2 kHz) digital data acquisition system with high precision analog amplifiers and independent (without multiplexors) signal channels (case **B**) from "*neuroConn GmbH*". For case **A** a "Mess Haus" data acquisition software was used and then data were postprocessed with our own code. For **B** Matlab interface and postprocessing was used. Due to measurement system limitations a signal only from three electrode pairs (two axial and one radial) was recorded for case **A**. The maximal theoretical scanning rate of the **A** system is 800 Hz, but due to the low signal level and constructive features, the signal was filtered and the real scanning rate was below 4 Hz in the **A** experiments. Therefore this system is not suitable for fast small-signal recording.

B measurement system had a common reference ground for all signal channels. It was connected to one wire of the probe. Velocity component signal corresponds to the opposite electrodes of the sensor. Hence, one velocity component was measured directly while for all other velocity components measurement channel subtraction was adapted (differential low-voltage measurements). This method was checked introducing another velocity component to the ground and no significant changes in signal structure or spectra were noticed comparing to the direct low-level voltage measurements. Velocity measurements were performed with 32 or 64 Hz sampling rate for each channel.

The measurements usually started from the melt and the crucible temperature regulation for selected working regime of the AC convertor. The magnetic field of the probe magnet was measured before the experiments. In most of experiments it was about 0.06 T, which is comparable with the RMS value of inductor magnetic field on symmetry axis in the empty crucible. Several test points were taken

Table 3.2: Experimental conditions.

Nr.	Inductor frequency, Hz	Inductor current, A	Total power, kW	Melt height, mm	Crucible radius, mm	Number of inductor turns	Meas. system
Exp1	384	2000	49	570	158	12	**A**
Exp2	364	2000	48	570	158	12	**A**
	370	2100	54				
	376	2200	60				
	358	1900	43				
	352	1800	39				
Exp3	376	2180	54	620	158	11	**A**, **B**
Exp4	386	2000	51	570	158	12	**B**
Exp5	386	2000	54	400	158	11	**B**

to check the probes. These points were also used for probe calibration because a rotating channel, which is usually used for PMP probe calibration, was not available during the measurements. The probes were calibrated using *ab initio* data [8] for $I = 2000$ A, $f = 394$ Hz inductor current where velocity distribution in the flow is well-known. This calibration method can introduce additional error to the measurements, which can achieve 10% according to the experiential data. Hence, absolute velocity values, provided later as experimental results are with the low reliability and it is better to use normalized velocities.

The velocity measurements were performed moving the probes in vertical direction with space resolution 20 or 30 mm. The first probe was initially placed on the symmetry axis, while the second was fixed near the crucible wall. Each measurement point was studied at least for two minutes and additional time was granted between measurements to compensate sensor movement influence on the flow. After the vertical pass had been completed, the radial position of the probes was changed by 20 mm and the next vertical velocity profiles were taken. The complete measurement cycle usually took two days.

Inductor current and frequency were also controlled during experiments and

they were found to be stable within ±1 unit. Several main series of the experiments were performed with different experimental conditions (table 3.2). First three experimental series used **A** measuring unit, while the last two series have used measurement system **B**. The **Exp1** and **Exp4** experiments used so-called standard experimental conditions, for witch *ab initio* data [8] with a good time resolution are available. Velocities were measured only on the central axis and near the wall at the second experimental set **Exp2**, but several times in a row for different inductor currents. These measurements were also repeated with the measurement unit **B**.

In the third experimental series **Exp3** the number of inductor turns was reduced by one from the bottom and additional material was added to the crucible to restore symmetrical placement of the inductor with respect to the melt. Inductor current was increased to 2180 A to compensate smaller size of the inductor. Very asymmetrical experimental setup with reduced melt level and disconnected bottom coil winding also was accomplished with the measurement unit **B**: **Exp5**. The last experimental series were performed using the fast measuring unit **B**. All velocity components including angular, which was not recorded in the previous experiments, were measured independently, each after another. Several measurements were also performed with two probes recording signal for all possible velocity components simultaneously.

3.3 Analysis of experimental data

3.3.1 Averaged velocity field

The instantaneous velocity signals were recorded for two minutes at each measurement point on the meridian plane. Recorded potential differences were translated to velocity values using calibration curves of the probes. Consecutive axial and radial velocity measurements and statistical averaging introduce an average flow pattern (figure 3.6), which illustrates the spatial structure of the mean flow. Several experiments (figures 3.6(a) and 3.6(c)) were performed under the same conditions and their results can be directly compared.

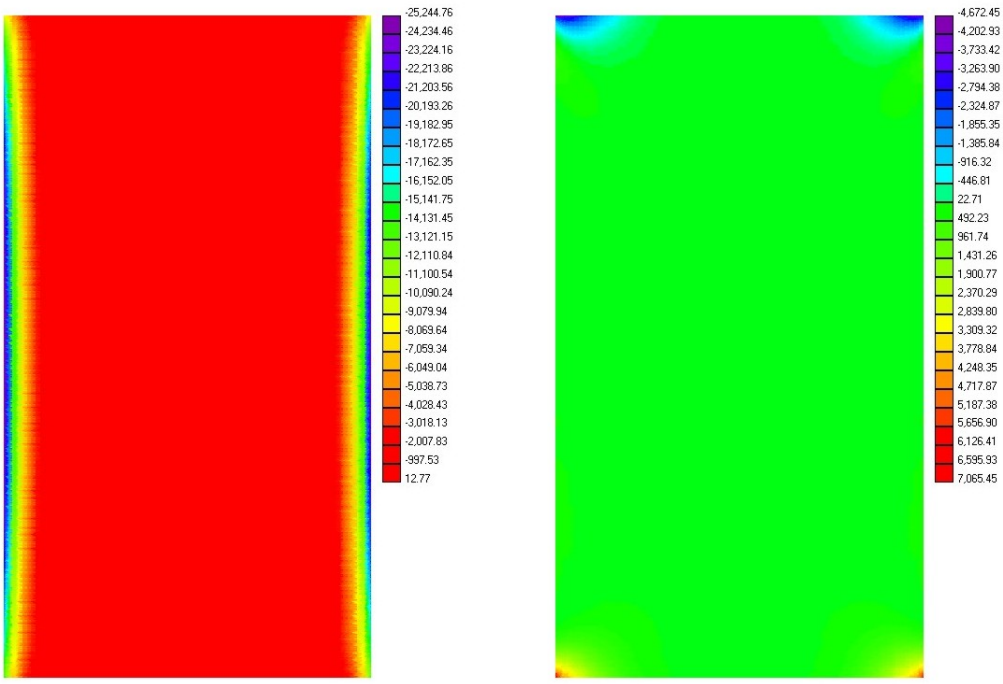

(a) Radial EM force density f_r (b) Axial EM force density f_z

Figure 3.5: Calculated Lorentz force distribution in the meridian plane $y = 0$ for $I = 2000$ A, $f = 395$ Hz, $H = 570$ mm.

Flow structure in all experiments is very similar (figure 3.6). The flow usually forms a double-torus with a common flow directed radially inwards at half the height of the melt load (e.g. figure 3.6(a)). Then the flow is carried up and down in the central region, goes radially outwards at the top and bottom lids, and closing accordingly along the sidewalls. In other words the mean flow is formed by two recirculated vortices. The inward direction of the flow in the middle region near the side wall is determined by the Lorentz force distribution in the melt (figure 3.5). The maximal radial Lorentz force density can be found in the thin border layer at the half height of the inductor, e.g. the middle part of the melt. This middle part is also characterized by the strong flow coming from the top and the bottom to the crucible center along the wall, which can be imagined as a collision of two fluid jets, which come from opposite directions. Due to the

turbulence and different boundary conditions at the top free surface and at the bottom wall the intensity of the wall jets varies in time, creating instability and secondary turbulent vortices of a considerable scale, which can annihilate later introducing low-frequency velocity oscillations in the whole melt.

The approximate positions of the centers of the mean vortices can be established. The radial distance of the centers is about 120 mm or $0.8R$ ($R = 158$ mm is the crucible radius, table 2.2), while precise identification of z coordinate for mean vortex eye is difficult. The radial center position is not equal to the half of the radius because of the cylindrical geometry and the mass conservation law $\int_0^r \bar{v}_z r dr = 0$. The maximal velocity of the melt near the crucible wall is a little higher than on the symmetry axis, but the volume of the near-wall region is smaller than the central part. It is also very difficult to analyze measured maximal flow velocities near the crucible wall because sensor size is finite and possibly maximal axial velocities are distributed closer to the wall due to small laminar shear layer thickness than it can be measured. It can be shown, that the laminar boundary layer thickness is of order $\delta \sim \mathrm{Re}^{-0.5}$ [84] and for $U = 0.2$ m/s, $L = 0.16$ m it is about $\delta \sim 3 \cdot 10^{-3}$ m, which is 5 mm closer to the wall than possible sensor position.

Similar experiment **Exp4** introduces the same flow structure (figure 3.6(c)), however flow velocities in the crucible are about 10% higher than in **Exp1**, which possibly can be explained by a little different electrical power values in these experimenters. However, difference in the power values is about 4% and possibly the measured averaged flow velocities in the crucible under the same experimental conditions can vary a little and all experiments even under the same conditions are unique.

In the experiment **Exp3** the level of the melt was increased to 620 mm ($2R/H_{melt} \approx 0.51$) and the bottom inductor turn was disconnected to obtain symmetry of the flow pattern. The velocity vectors structure (figure 3.6(b)) is very similar to the previously described, but the maximal measured velocities are higher. It can be explained with three factors: inductor is more concentrated closer to the half-height of the melt, inductor current is larger ($I = 2180$ A) and the top–bottom distance for the flow acceleration near the wall is larger. The

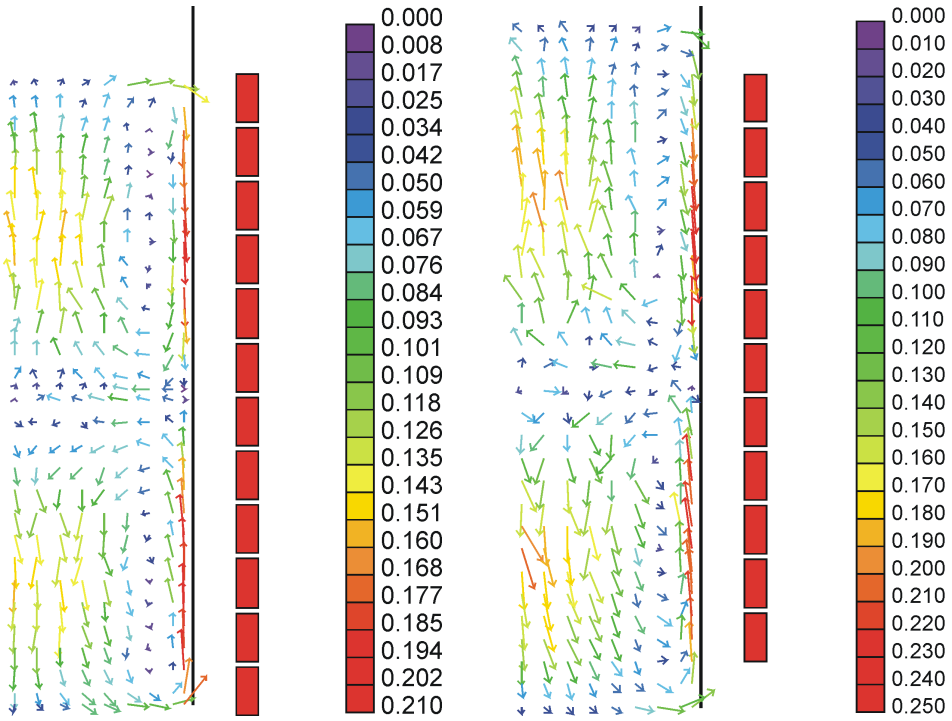

(a) **Exp1** (b) **Exp3**

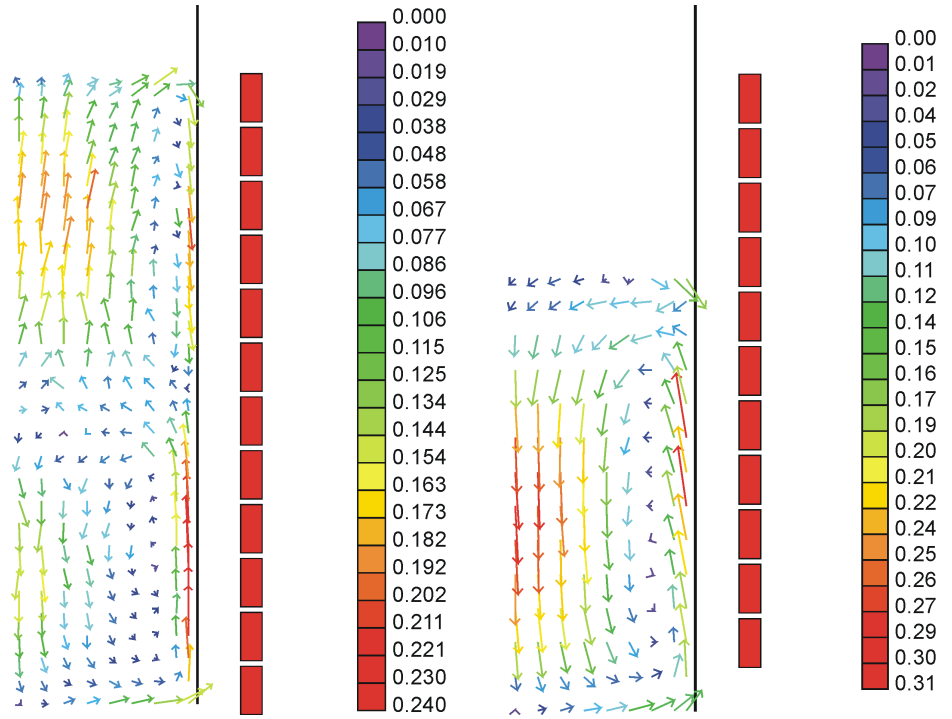

(c) **Exp4** (d) **Exp5**

Figure 3.6: Averaged velocity patterns registered by different measurement systems.

flow near the symmetry axis has also a tendency to change its direction towards the wall more early in the bottom mean vortex.

In the last experiment (figure 3.6(d)) the melt height was reduced to 400 mm ($2R/H_{melt} \approx 0.70$) and the bottom inductor turn was disconnected. As a result asymmetry over the height, which influences the flow structure, was created. In this case the averaged flow represents mainly one very large eddy, which is originated from the bottom vortex from the "standard" experiment **Exp1**. Inductor current was the same $I = 2000$ A (linear current is even higher because inductor height is smaller), but the characteristic flow velocities near the crucible wall and on the symmetry axis are almost 40-50% higher till about 30 cm/s. The second averaged vortex seems to be present on the top, but it is very compressed in the corner near the crucible wall.

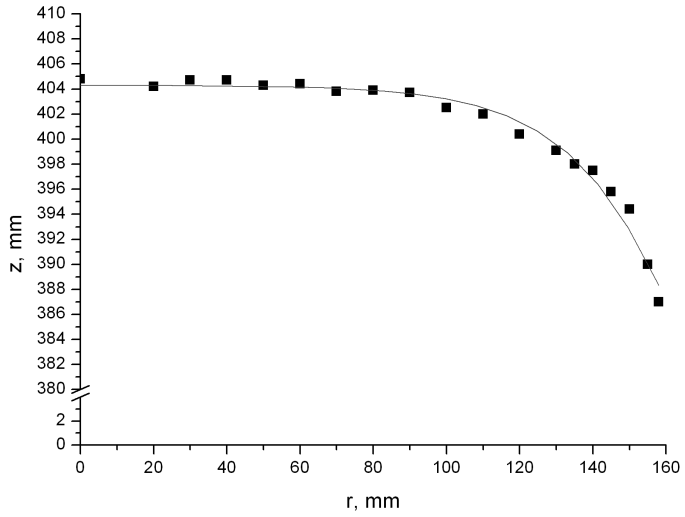

Figure 3.7: Melt free surface deformation for 400 mm ($I = 2000$ A).

Free surface of the melt was also deformed (figure 3.7) and its small oscillations were noticed. Shape deformations were measured using the contact method controlling position of the probe visually. Observed relative surface deformation was about 5% (i.e. 18÷20 mm). The approximate deformation of the free surface can be estimated using simplified equilibrium relation: $\rho g \Delta h = B^2/2\mu_0$, where

$B = \mu_0 IN/l$. Here N is the number of inductor turns, l is the length (height) of the inductor and I is effective current. Taking $I = 2000$ A, $N = 11$, $l = 0.52$ m we get $B \approx 0.053$ T. Therefore, $\Delta h \approx 12$ mm, which is of the same order like in experiment. If $B = B_0/\sqrt{2}$ is calculated using Nagaoka's formula (3.6) then Δh becomes approximately 0.021 mm, which better fits experimentally determined value.

Increasing the inductor current the magnetic field induction is increased and therefore Lorentz force acting on the melt is growing. Comparing corresponding terms in the Navier-Stokes equation 2.23 (non-linear term from the left side $v\nabla v \sim v^2$) with the Lorentz force expression (2.12) ($f \sim jB \sim j^2$) the next estimation can be derived: $v \sim I$, i.e. the fluid velocity is proportional to the inductor current.

To see, is this estimation correct, the series of measurements with the different inductor currents was performed – **Exp2** (table 3.2). Current changes during the experiment lead to small frequency variation due to the constructional features of EM convertor. Figure 3.8 shows the maximum axial velocity v_{zmax} depending on the inductor current I for different EM field frequencies at the symmetry axis point $r = 0$, $z = 13$ cm. The angle between the linear approximation line and the current I axis depends on the inductor frequency f, but to a less degree: $v_{ch} \sim \dfrac{1}{\sqrt{f}}$ [8]. Therefore this angle changes slightly in the working frequency region (table 3.2), so it can be suggested that characteristic velocities are almost frequency-independent within the accuracy of the author's experimental data.

The inductor current was changed from 1800 to 2200 A with 100 A step and velocity values were taken at two radiuses: $r = 0$ and $r = 15$ cm. The maximal velocities on corresponding radiuses can be linearly fitted as it should be (figure 3.9). Other authors also provide similar results [66, 99].

Flow velocities also can be normalized with respect to the Alfven velocity (table 3.3):

$$V_a = \frac{B_0}{\sqrt{\mu_0 \rho}}, \tag{3.5}$$

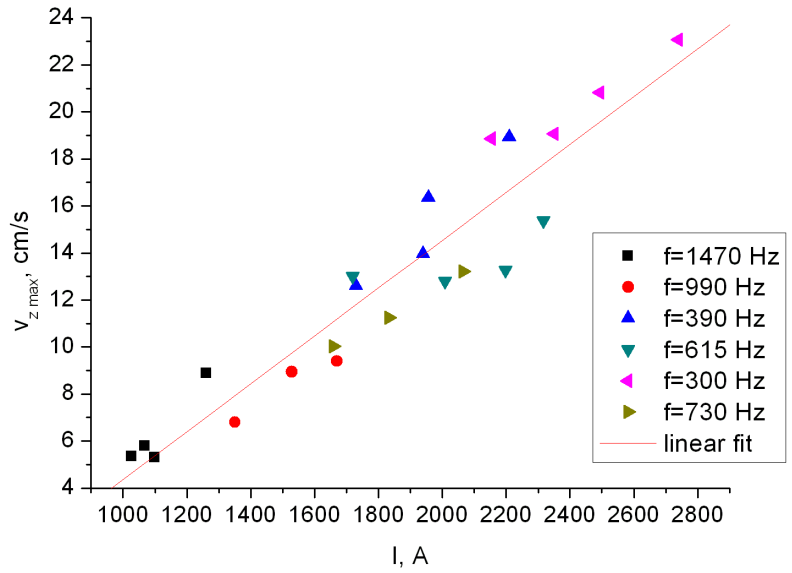

Figure 3.8: Maximum axial velocity $v_z max$ dependence on the inductor current for different frequencies at the symmetry axis point $r = 0$, $z = 13$ cm

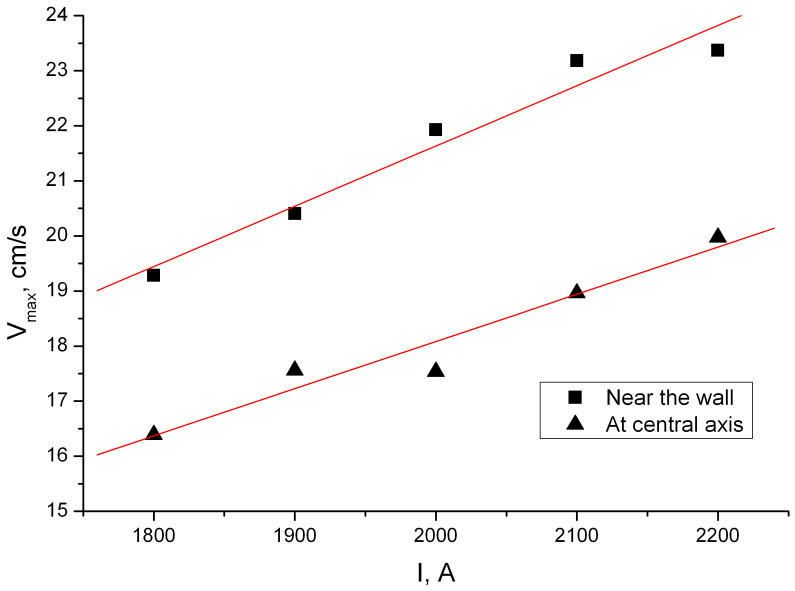

Figure 3.9: Dependence of the maximal axial velocity on the inductor current.

where induction amplitude B_0 is deduced from Nagaoka's formula [67, 96]:

$$B_0 = \sqrt{2}\frac{\mu_0 N I}{H}\left(1 + 0.88\frac{R_{coil}}{H_{coil}}\right), \tag{3.6}$$

where $H_{coil} = 0.570$ m, $R_{coil} = 0.197$ m, N and I respectively denote the height, the radius, the number of turns and the current of the coil. Taking the data for **Exp1** conditions (table 3.2) the one can get: $B_0 \approx 0.098$ T and corresponding $V_a \approx 0.90$ m/s (table 3.3).

Table 3.3: Alfven velocity values for experimental data normalization.

I, A	1600	1800	2000	2150	2200
R_{coil}, m	0.20	0.20	0.20	0.20	0.20
H_{coil}, m	0.57	0.57	0.57	0.57	0.62
N	12	12	12	12	11
B_0, T	0.078	0.088	0.098	0.105	0.111
V_a, m/s	0.72	0.81	0.90	0.97	1.02

Next figures (figures 3.10 and 3.11) introduce normalized average axial velocity on the crucible axis depending on the inductor current and radial velocity component near the melt surface respectively for 570 mm melt height. Alfven velocity increases together with the inductor current and this eliminates normalized velocity dependence on current from these charts.

3.3.2 Low-frequency velocity oscillations

The measured velocity signal introduces many harmonics from all resolved scales into velocity spectra. If the signal goes through high–frequency filter, then large amplitude low–frequency quasiperiodic oscillations (figure 3.12) are noticed in the near wall region between the mean vortices at $z = 0$, where the measured average value of the axial velocity (collinear to z direction) is close to zero in **Exp1**, **Exp3** and **Exp4**. These oscillations introduce additional imbalance to the flow. In the central part $r = 0$ intensity of the axial pulsations is much smaller than near the wall at $r = 14$ cm. The period of pulsations can be determined

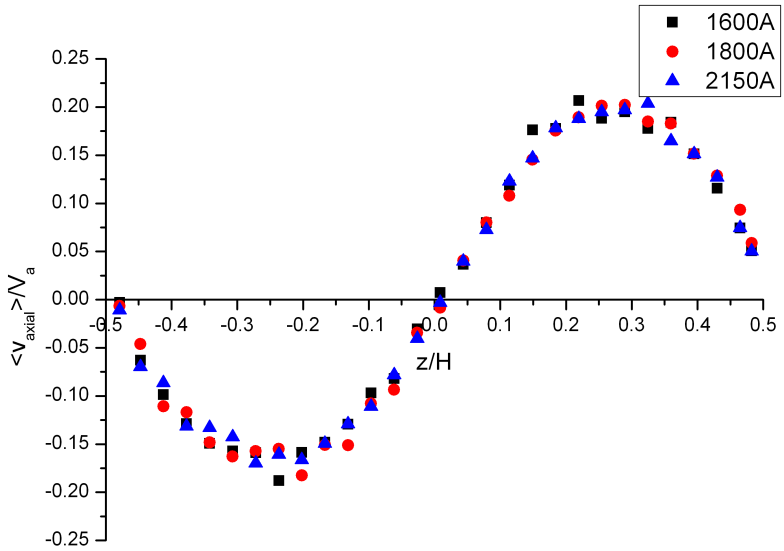

Figure 3.10: Normalized average axial velocity v_z/V_a on the symmetry axis $r = 0$ for different inductor currents (melt height is 570 mm).

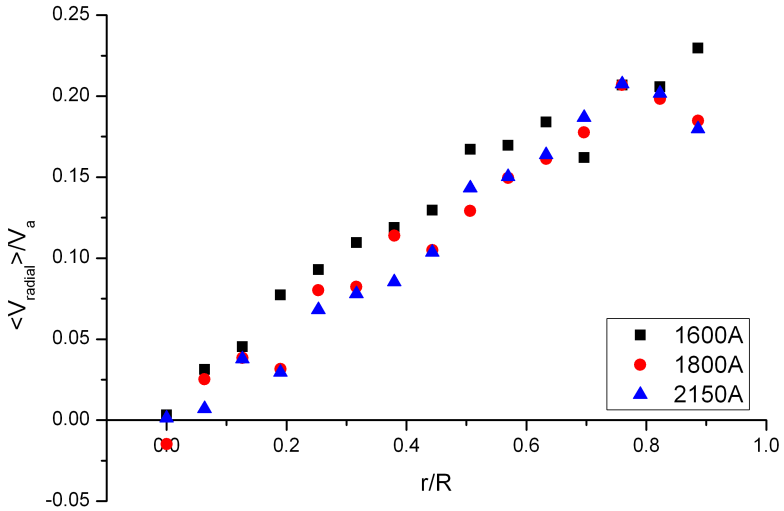

Figure 3.11: Normalized average radial velocity v_r/V_a near the top melt surface $z = 560$ mm for different inductor currents (melt height is 570 mm).

using autocorrelations (figure 3.13). These periods are estimated as $T \approx 7 \div 15$ s depending on the measurement series and selected measurement point. It can be seen, that low-frequency pulsation period in the central part of the crucible is shorter than near the crucible wall because number of "opposite jets" in the central part is larger. Higher frequency turbulent oscillations can be noticed on not filtered signal, especially in experiments where measuring system **B** was used.

The whole flow can conditionally be divided into three parts $\mathbf{v} = \bar{\mathbf{v}} + \mathbf{v_l} + \mathbf{v_t}$ depending on its behavior [10]:

1. the average flow, $\bar{\mathbf{v}}$, which forms the main toroidal vortices with velocities averaged in time;

2. the low frequency velocity oscillations, $\mathbf{v_l}$, which are defined by the interaction of vortices and the development of coherent structures;

3. the turbulent flow, $\mathbf{v_t}$, which mainly depends on the local characteristics of the flow with energy dissipation by small-scale velocity oscillations.

These low-frequency oscillations are known for a long time. The first experimental observations in the in induction-furnace-like setup were made in the middle of 80's in [96], where long-time periods lasting several minutes were reported in calculated turbulence spectra. However, the authors stated that these periods did not seem to correspond to turbulent eddies rather than to an instability of the whole flow pattern. The authors also found almost no deviations of their spectra compared to the case of homogeneous and isotropic turbulence for the higher frequencies. Experimental and numerical investigation of the problem was later reported in [18], where the flow in a cylindrical liquid metal column driven by an alternating magnetic field was studied. LES was successfully used by the authors for the numerical recognition of low frequencies. Further numerical investigation was performed in [86] using URANS method for comparable geometry. The interaction between the toroidal vortices was studied for 180 second with a time step 0.1 s and $0.15 \div 0.2$ Hz pulsations of the same kind were reported. One of the authors has continued URANS modeling [85] for the oscillating mould flow in a thin box with two nozzles and several outlet ports, where averaged flow

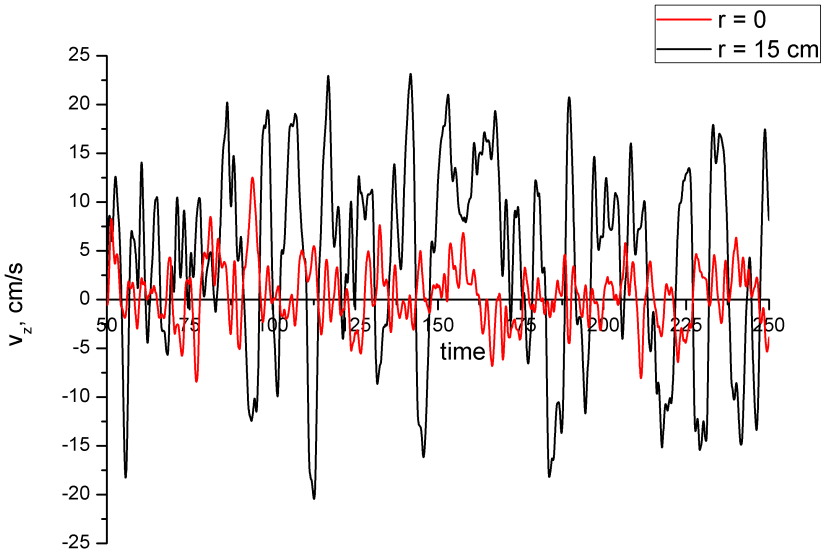

Figure 3.12: Filtered axial velocity low-frequency pulsations at $z = 0$ (experimental data, melt height is 570 mm, **Exp4**).

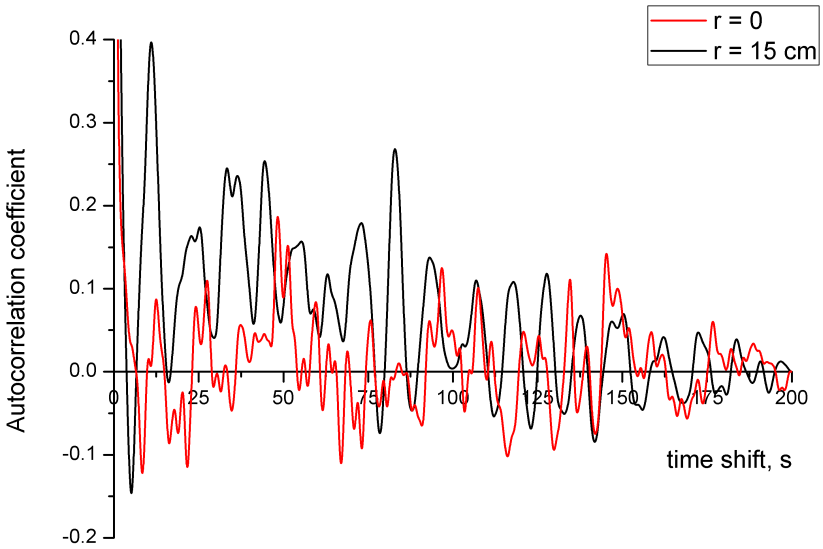

Figure 3.13: Autocorrelations of the above axial velocities at $z = 0$.

represents two toroidal vortices again. The system seems to be unstable too and oscillations with frequencies from 0.02 to 0.03 Hz are numerically found. The author has shown that the relevant low-frequency is URANS time-step dependent and states that LES can not be used for the flows with such low frequencies, because it needs more computational time.

The importance of the low-frequency velocity oscillations for the heat and mass exchange in the melt can be illustrated using turbulent specific energy ($k = v_i' v_i'/2$) charts (figure 3.14). The maximal contribution to the turbulent kinetic energy comes from the axial velocity pulsations (figure 3.14(a)) while the turbulent energy, which is contained in the remaining velocity components is about two times smaller (figures 3.14(b) and 3.14(c)). The zone of the maximal kinetic energy can be identified here like a region near the crucible wall between the averaged vortices at $z \approx 280$ mm. This maxima indicates high intensity of the characteristic vortex interaction. Decay of the axial turbulent kinetic energy is very rapid moving away from the near-wall region and the low-frequency pulsations are almost suppressed on the top and bottom surface where the energy level is defined mainly by usual small-scale turbulence. Radial and angular energy components have approximately the same level in average, however several characteristic effects are noticed:

1. the radial and tangential energy maximums are placed on line $z \approx 280$ mm, i.e. between the averaged vortices, but not so close to the crucible wall;

2. level of tangential pulsations is higher near the crucible wall and is very small in the top and bottom region of the crucible;

3. tangential pulsation intensity at $r = 0$ does not have sense because in fact it is the same radial intensity from the orthogonal direction.

For smaller filling level specific turbulent energy charts (figure 3.15) are a little different. Here again axial velocity has the highest intensity of pulsations (figure 3.15(a)), which maximal value is placed near the crucible wall at $z \approx$ 350 mm (inductor middle is 285 mm), i.e. is shifted towards the crucible top. It also can be noticed, that the local maximums of two other energy components

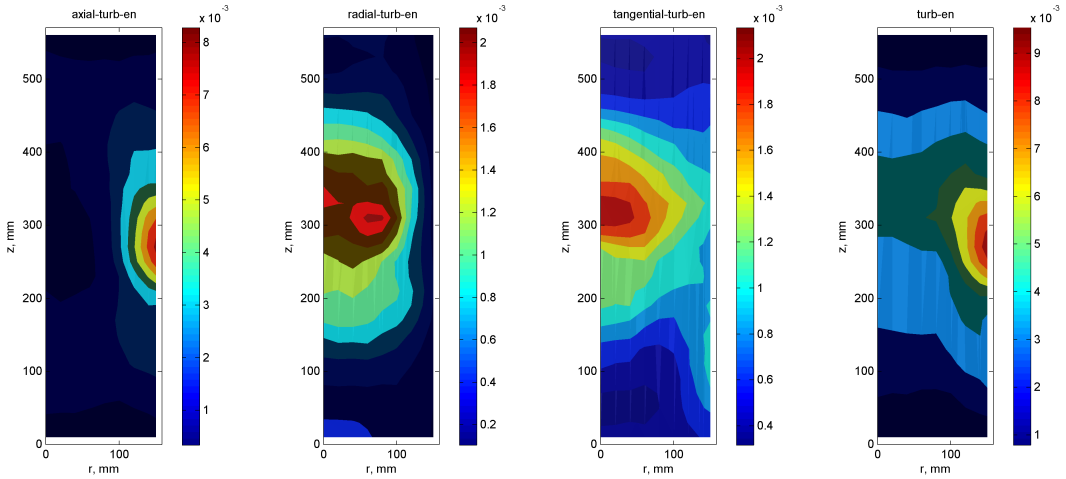

(a) Axial component (b) Radial component (c) Tangential component (d) Total

Figure 3.14: Turbulent kinetic energy in J/kg^3 for 570 mm melt height (**Exp4**).

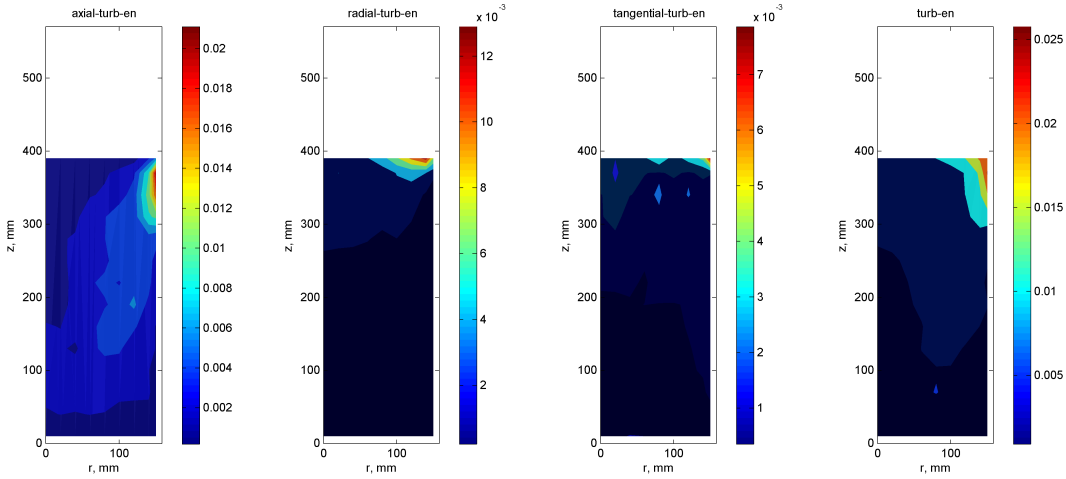

(a) Axial component (b) Radial component (c) Tangential component (d) Total

Figure 3.15: Turbulent kinetic energy in J/kg^3 for 400 mm melt height (**Exp5**).

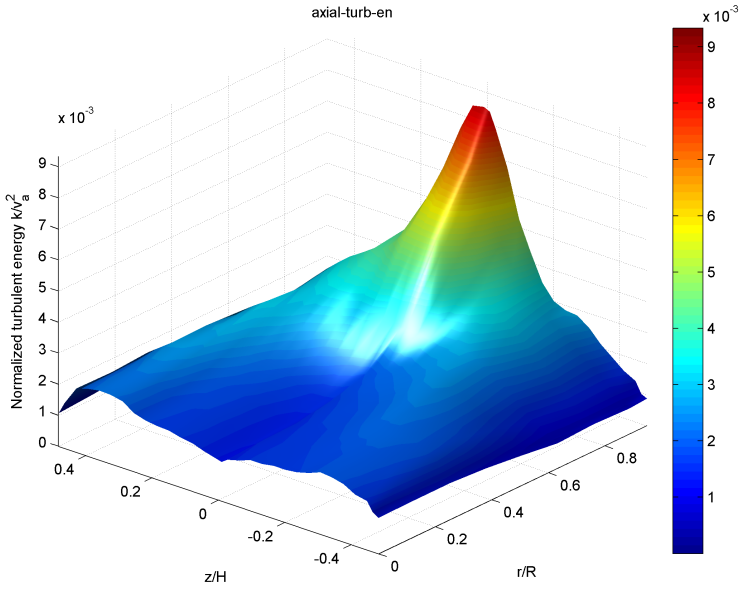

Figure 3.16: Distribution of the normalized averaged axial pulsation kinetic energy k/V_a^2 in the melt for **Exp4** (smoothed, $H = H_c = 570$ mm, $I = 2000$ A, $B_0 \approx 0.098$ T, $V_a \approx 90$ cm/s).

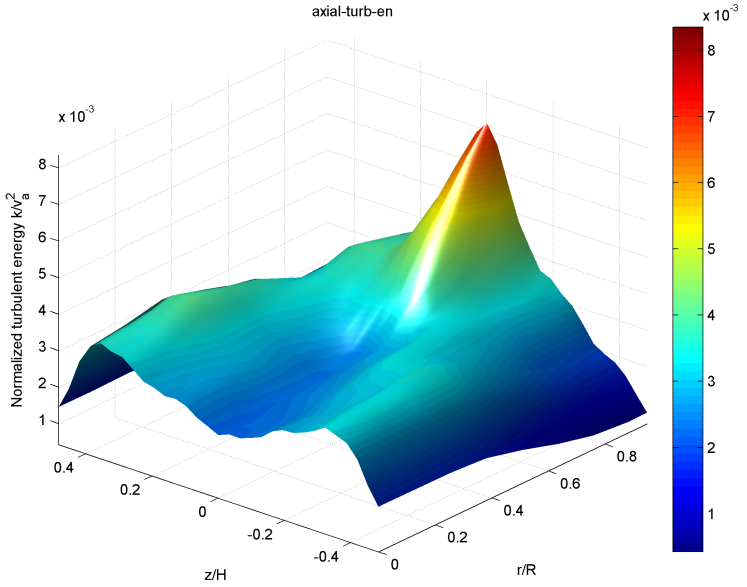

Figure 3.17: Distribution of the normalized averaged axial pulsation kinetic energy k/V_a^2 in the melt for **Exp3** (smoothed, $H = 620$ mm, $H_c = 520$ mm, $I = 2180$ A, $B_0 \approx 0.111$ T, $V_a \approx 102$ cm/s).

are placed approximately in the same region, but even closer to the free surface, producing very strong peak for the total energy (figure 3.15(d)) in the top melt corner near the crucible wall. The turbulent energy part in the remaining melt volume is much smaller (at least 4 times) and distributed more homogeneously.

Comparing normalized axial turbulent kinetic energy k/V_a^2 charts for **Exp4** (figure 3.16) and **Exp3** (figure 3.17) it can be noticed that the axial turbulent energy level in **Exp3** is higher because melt height is increased comparing to inductor here and axial velocity oscillations are less suppressed by the geometry.

3.3.3 Measured turbulent velocity spectra

Performed measurement allowed to introduce Fourier decomposition of velocity components and obtain energy power spectra (section 2.3). The basic problem is that velocity series are measured mainly as functions of time for constant radius-vectors $\mathbf{r}$: $v_i = v_i(t)|_{\mathbf{r}=const}$. All these signals are taken at different time moments, but with the constant time step Δt. Therefore, the covariance tensor $R_{ij}(\mathbf{r})$ can not be calculated directly. The proposed approach to find power spectra in wavenumber $\mathbf{k}$ space is based on autocorrelations, FFT and Taylor's hypothesis.

The autocorrelation of the discrete measured velocity signal is defined as:

$$r_{ii}^{\tau} = \frac{\sum_{t=1}^{N} (\bar{v}_i - v_i^t)(\bar{v}_i - v_i^{t+\tau})}{\sum_{t=1}^{N} (\bar{v}_i - v_i^t)^2}, \tag{3.7}$$

where bottom indices correspond to space and upper to time discretisation.

In this case a power energy spectra $E(f)$ can be calculated taking the discrete Fourier transform of the correlation coefficient r_{ii}^k:

$$E(f) = \Delta t \sum_{n=-\infty}^{\infty} r_{ii}^{\tau} e^{-i2\pi f n \Delta t}, \tag{3.8}$$

which can be transferred to the wavenumber space by means of the Taylor's hypothesis $k = 2\pi f / v_{characteristic}$ for isotropic turbulence, where $v_{characteristic} \approx 0.095$ m/s is the characteristic velocity of the flow (however, the turbulence can be

considered as isotropic only in a part of the complete flow). This value for characteristic velocity represents flow average velocity in the "main" vortex. Spectrums for all velocity components can be added together to get full power spectra of energy.

Experimental measurement frequency was $f_m = 32$ or $f_m = 64$ Hz in **Exp4** (note, that at least two measurements are needed for identification of the oscillation period), which correspond to rather high wavenumber space resolution: $k_{max} \approx 10^3$ or $k_{max} \approx 2.1 \cdot 10^3$ m^{-1}. From the other side, the size of the probe is about 6 mm, which also limits space discretisation in the measured data. This probe cut-off wavenumber, which is analogous to the characteristic grid size, can be estimated like in numerical simulation: $\frac{1}{2\delta x}$ [23]. In our case cut-off wave number k_d is about 83 m^{-1}. Therefore our experimental data should be used very carefully for predictions of turbulent structures with smaller scales then $1/83$ m (≈ 0.012 m).

All energy component spectrums have several frequencies with relatively high energy (figures 3.18 and 3.19) at wavenumbers $k < 10$ m^{-1}, which corresponds to frequencies below 0.15 Hz. Hence, it is very difficult to select only one dominating frequency in this vortical motion. Wavenumbers with $k \approx 3$ m^{-1} correspond to oscillations, which are connected with the crucible geometry. Increasing wavenumber all spectrums decay with different slopes, which can be compared with the theoretical Kolmogorov's spectrum in the inertial subrange (2.48) [100] integrating equation (2.49) for the turbulent dissipation rate from the energy spectrum $E(k)$, where $\nu = 4.5 \cdot 10^{-7}$ m^2/s and the Kolmogorov's constant is $C_k = 1.5$. Dashed lines on figures 3.18 and 3.19 represent theoretical Kolmogorov's curves calculated by these approach. It is very difficult to identify correct k zones with the slope $-5/3$, which should correspond to the inertial range, even applying the smoothing. Possibly it can be explained by the presence of turbulence anisotropy in the flow, which is caused by the wall presence and flow structure in the selected points. It can be noticed from the spectra charts (figure 3.18(b)) that the energy decay near the crucible wall is more rapid. Smaller scales, which correspond to higher wavenumbers and frequencies in the dissipation range, are below the cut-off wave number k_d. Higher sampling rate gives better spectral resolution of the

signal and together with a smaller probe size can increase k_d and make spectra more clear.

Fourier analysis are not localized in time, i.e. FFT can not say which frequencies are presented in the analyzed signal at a certain time moment. Wavelet analysis [13] introduce a decomposition of the studied signal in time and frequency scale (figure 3.21). Special functions with certain properties $\Phi(a, b)$ are used for wavelet decomposition:

$$\Phi(a, b, t) = \Phi\left(\frac{t-b}{a}\right), \tag{3.9}$$

where coefficients a and b correspond to frequency scale and time position (count). Continuous wavelet transform coefficients are expressed as:

$$C(a, b) = \int_{-\infty}^{+\infty} f(t)\Phi(a, b, t)dt. \tag{3.10}$$

There are different wavelet functions for continuous wavelet transform [91], Morlet wavelet (figure 3.20):

$$\Phi(t) = C \cdot \cos(5t)\, e^{-\frac{t^2}{2}} \tag{3.11}$$

was selected for the wavelet decomposition of the experimental data. Axial velocity signal from near-wall region ($r = 150$, $z = 290$ mm) with length about 150 s (9599 counts) was selected for the transform (figure 3.22). The top chart represents the selected signal while the bottom – coefficients $C(a, b)$ of the wavelet decomposition. High frequencies are placed in the bottom of the wavelet chart, and low frequencies are situated in the top part. The central frequency of the Morlet wavelet (global maximum of its Fourier reproduction) is $f_0 = 0.8125$ Hz. The signal sampling frequency is $f_s = 64$ Hz. The maximal frequency of wavelet decomposition is $f_{max} = f_0 \cdot f_s = 52$ Hz. This frequency corresponds to scale $a = 1$. This decomposition was performed for 1024 scales with step 4 and the minimal frequency is $f_{min} = f_{max}/1024 \approx 0.05$ Hz.

The wavelet chart (figure 3.22 (bottom)) consists of characteristic color spots and stripes, which correspond to local minimums and maximums of harmonics in the measured signal. This representation is drawn in linear scale and high

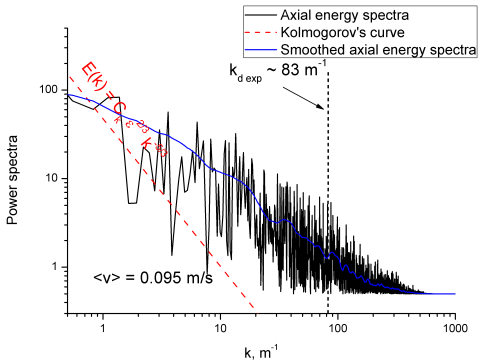

(a) axial $r = 0$, $z = 290$ mm

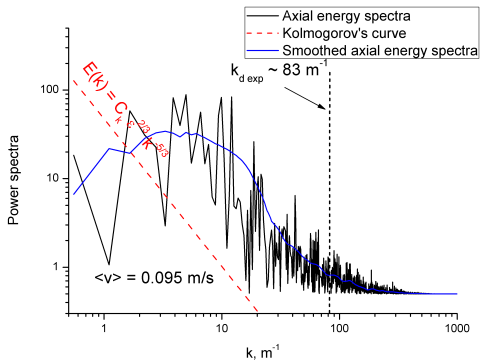

(b) axial $r = 150$, $z = 290$ mm

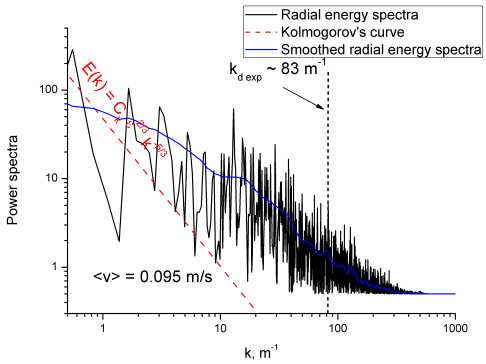

(c) radial $r = 0$, $z = 290$ mm

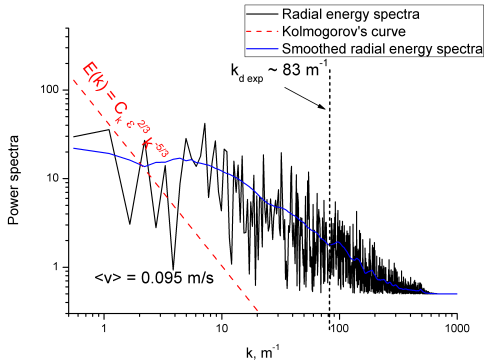

(d) radial $r = 150$, $z = 290$ mm

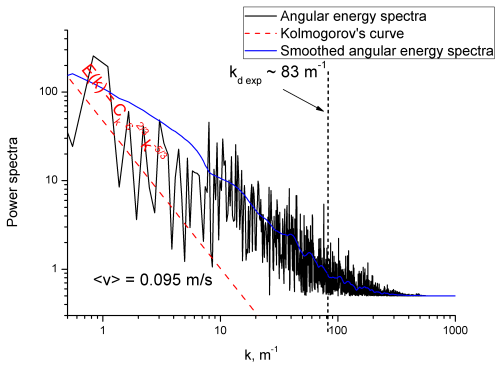

(e) angular $r = 0$, $z = 290$ mm

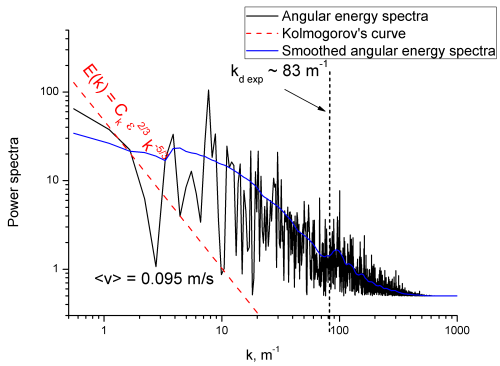

(f) angular $r = 150$, $z = 290$ mm

Figure 3.18: Experimental power spectrums of the turbulent energy calculated from different velocity components. Signals are measured independently with 32 Hz sampling frequency.

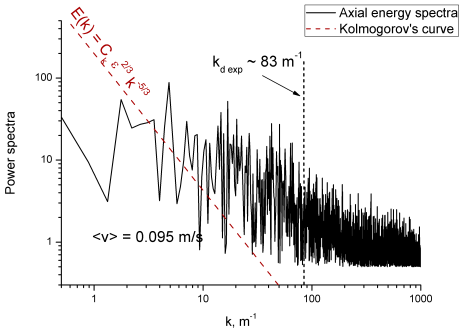

(a) axial $r = 0$, $z = 290$ mm

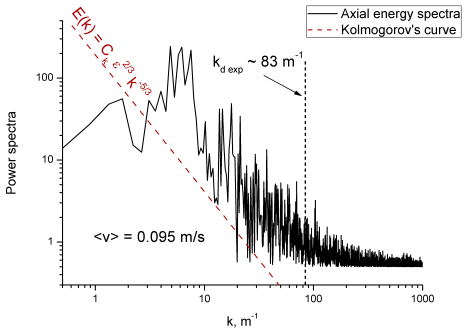

(b) axial $r = 150$, $z = 290$ mm

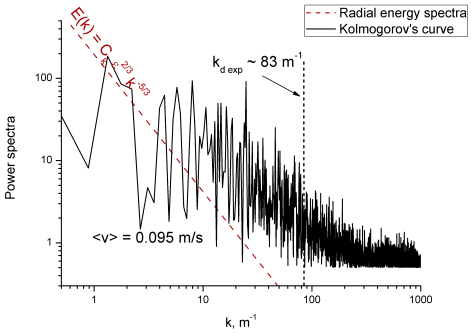

(c) radial $r = 0$, $z = 290$ mm

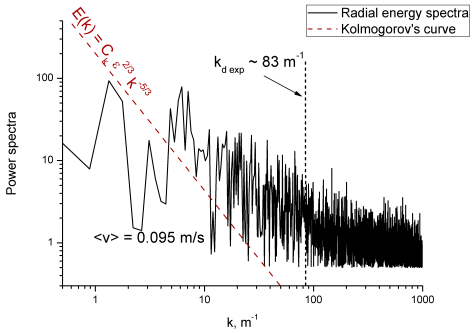

(d) radial $r = 150$, $z = 290$ mm

Figure 3.19: Experimental power spectrums of the turbulent energy calculated from different velocity components. Signals are measured together with 64 Hz sampling frequency.

frequencies are very compressed. For example, there is a group of wavelet spots for signal between $t_1 \approx 0$ and $t_2 \approx 50$ s, which corresponds to characteristic frequencies from 0.068 Hz ($T \approx 14.7$ s) to 0.081 Hz ($T \approx 12.3$ s). Then there is 10 s long transition and from $t_3 \approx 60$ s the basic low frequency has been changed to approximately 0.118 Hz ($T \approx 8.6$ s). This frequency also varies with time decreasing and increasing till $t_4 \approx 140$ s. These low-frequencies are typical for this working regime of the induction furnace. They also can be identified on Fourier spectra chart as three peaks before $k = 10$ m^{-1} (figure 3.19(b)). There

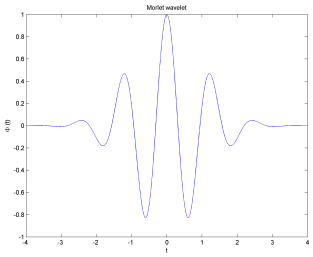

Figure 3.20: Morlet wavelet function.

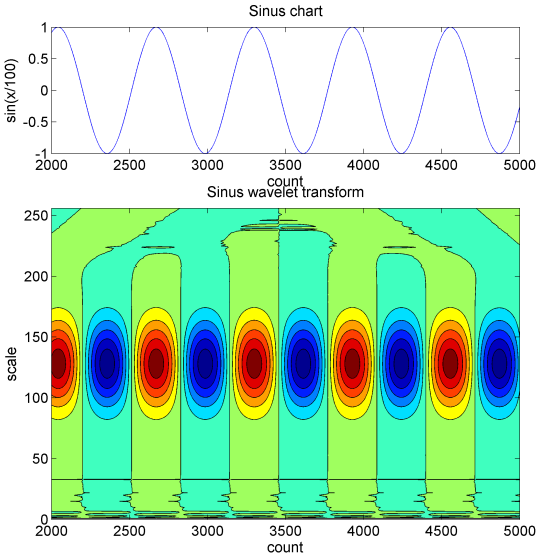

Figure 3.21: Wavelet decomposition of the sinus signal (central part).

also can be noticed several local spots at a little higher frequency at $a/4 \approx 50$, i.e. $f \approx 0.26$ Hz ($T \approx 3.84$ s), which possibly can be considered as a second harmonic.

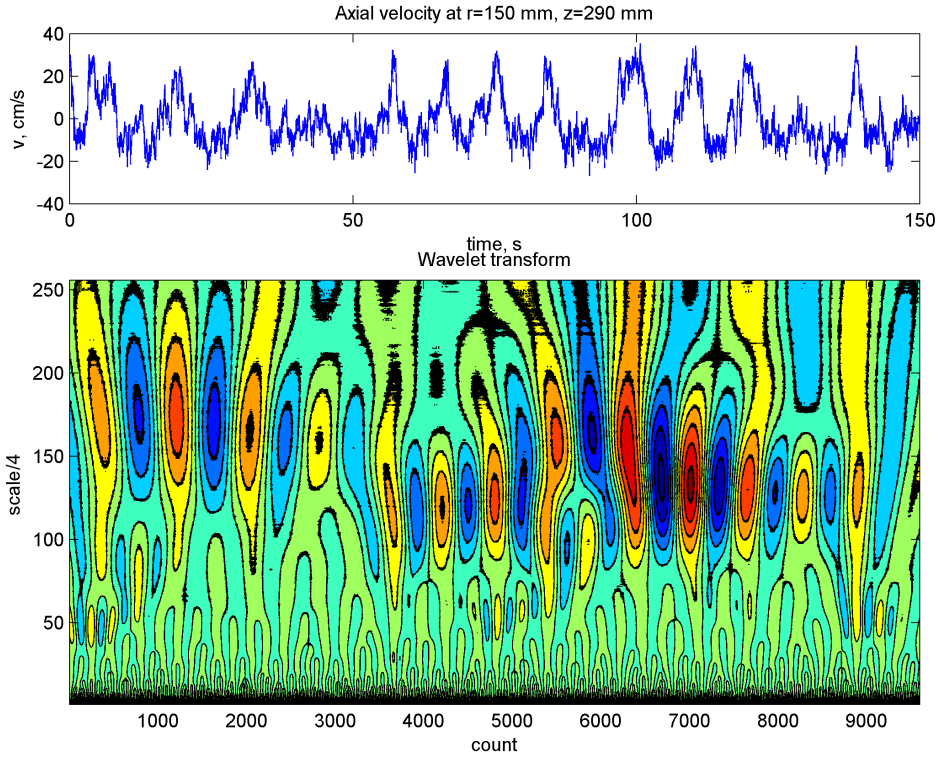

Figure 3.22: Wavelet transform of the axial velocity component at $r = 150$, $z = 290$ mm, **Exp4**. X-axis of the wavelet chart corresponds to signal counts, Y-axis to frequency scales a divided by 4 ($f = 13/Y$ [Hz]).

4 LES flow simulation

4.1 Used methods and algorithms

Commercial CFD codes, used in this work, implement finite volume method (FVM) for representing and evaluating partial differential equations (PDE) as algebraic equations. "Finite volume" refers to a small control volume surrounding each node point on a mesh, where PDE are integrated. Then volume integrals are converted to surface integrals, using the divergence theorem. These terms are then evaluated as fluxes at the surfaces of each finite volume (for incompressible fluid):

$$\int_S v_j dn_j = 0 \tag{4.1}$$

$$\rho \frac{d}{dt} \int_V v_i dV + \rho \int_S v_i v_j dn_j = - \int_S P dn_j + \mu \int_S \left(\frac{\partial v_i}{\partial x_j} + \frac{\partial v_j}{\partial x_i} \right) dn_j \tag{4.2}$$

Because the flux entering a given volume is identical to that leaving the adjacent volume, these methods are conservative. Another advantage of the finite volume method is that it is easily formulated to allow for unstructured meshes. The method is used in many computational fluid dynamics packages, like *FLUENT* or *ANSYS CFX*. More detailed FVM description can be found in [107] while only basic concepts will be introduced here.

Discretisation of the melt flow governing equations usually involves decomposition of the gradients using Taylor series. For a function $\phi(x)$:

$$\phi(x + \Delta x) = \phi(x) + \left(\frac{\partial \phi}{\partial x} \right)_x \Delta x + \left(\frac{\partial^2 \phi}{\partial x^2} \right)_x \frac{\Delta x^2}{2} + \ ... \tag{4.3}$$

Precision of the method depends on the latest truncated term, which usually is $O(\Delta x)$ if we keep only the first derivative. The second order schemes will keep also the second derivatives. The function $\phi(x - \Delta x)$ also can be decomposed in a similar way. By subtracting both Taylor series we can get a central difference formula, which is second-order accurate:

$$\left(\frac{\partial \phi}{\partial x}\right)_x = \frac{\phi(x + \Delta x) - \phi(x - \Delta x)}{2\Delta x} + O(\Delta x^2). \tag{4.4}$$

Such discretisation converts integral equations into a system of algebraic equations, which is usually solved iteratively producing solution for $\phi(x)$ at node points. Values of $\phi(x)$ in other parts of the finite volume are evaluated using shape functions and different interpolation schemes, e.g. UPWIND, which takes into account the flow direction (the convected variable at the volume face is the same as the value at upstream node) or more advanced QUICK (Quadratic Upwind Interpolation for Convective Kinematics), which uses a three point upstream-weighted quadratic interpolation for cell face values [48].

SIMPLE [69, 74] or its variation PISO [36, 76] pressure-velocity coupling algorithms are used in this work to enforce mass conservation and to obtain the pressure field from the discrete continuity equation. SIMPLE method was initially developed for steady calculations while PISO was intended for time-variable flows. However, SIMPLE algorithm is often used for transient calculations with small time steps because it also has time discretisation. The pressure field is a dependent variable which invariably forms a Poisson-type problem throughout the solution domain in all pressure-velocity coupling methods [9]. A pressure correction equation is derived by enforcing mass continuity over each computational cell. Velocities are initially predicted from the momentum equation with guessed pressure in SIMPLE method. Face flux balance corrections are substituted to the discrete continuity equation obtaining a Poisson pressure equation with source terms based on the initially predicted velocity terms. Solution of this equation introduces pressure correction, which is used to derive "more correct" velocities from the momentum equation. The PISO scheme is more complicated and has an additional corrector level for velocity that satisfies continuity.

4.2 A simple model (box model)

4.2.1 Model setup

Comparison of the experimental data with the results of 2D isotropic turbulence models (e.g. $k-\varepsilon$) shows that two-parameter models can produce wrong results on the heat-and-mass transfer between the toroidal eddies, because the two-equation model calculated turbulent energy maxima are in the vortex centers, whereas the experiments show that the maximum turbulent pulsation energy is in the zone between eddies, where the convective transfer of the averaged flow is close to zero. The reason of this may be usage of turbulence isotropy hypothesis in two-equation models, which leads to overproduction of turbulent energy by small-scale vortices, but which does not account for influence of "average" scale vortices with longer life time on momentum transport. Experimentally determined turbulent kinetic energy maximum is placed between the mean recirculating vortices in the zone of the low–frequency oscillations (figure 3.16). Therefore macroscopic pulsations significantly influence transfer processes.

The empirical approach in engineering models when the value of turbulent Prandtl number $\mathrm{Pr}_t = \dfrac{\nu_T}{\lambda_T}$ (ν_T is kinematical turbulent viscosity and λ_t is turbulent thermal diffusivity) is artificially decreased to 0.01, leads to increased heat transfer in the whole melt [17] and more homogeneous temperature distribution. But there are other differences in the values, which can not be tuned in the above way. For example, the turbulent viscosity achieves its maximum value near the center of averaged vortex in a traditionally used $k-\varepsilon$ model, but it is relatively low in the vortex interaction zone, where it should be greater. Sometimes 2D $k-\varepsilon$ models give only sophisticated results for temperature distribution [42] and LES model is proposed for 3D flow simulation.

Computational resources were limited several years ago and LES model of the Wood's melt was initially solved in a simplified geometry to obtain smaller number of elements and to perform the transient simulation on a single PC using the commercial CFD package *FLUENT*. The model, which was used in *FLUENT*, had a rectangular tank form (figure 4.1). Its sizes were similar to the experimental ones (height 57 cm, width 31.6 cm). The depth of the tank (z-direction) was

10 cm. The number of cells in the model was about 380000 (≈500 thousands nodes). The grid resolution was about $0.3 \div 0.5$ cm depending on the direction with the special refinement near the side boundaries. The front, back and upper planes had free surface boundary conditions. For the rest of walls no–slip boundary conditions were observed.

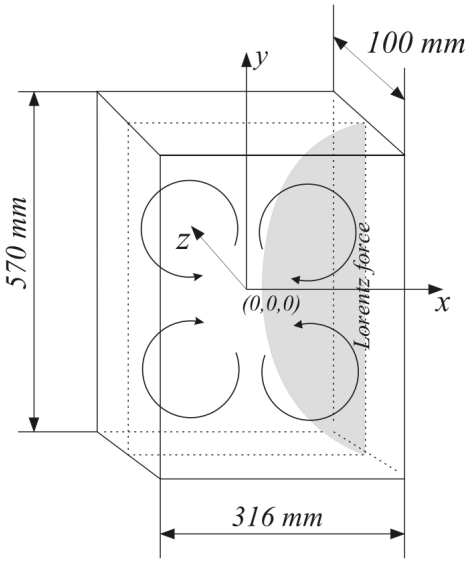

Figure 4.1: Design of the simplified geometry model.

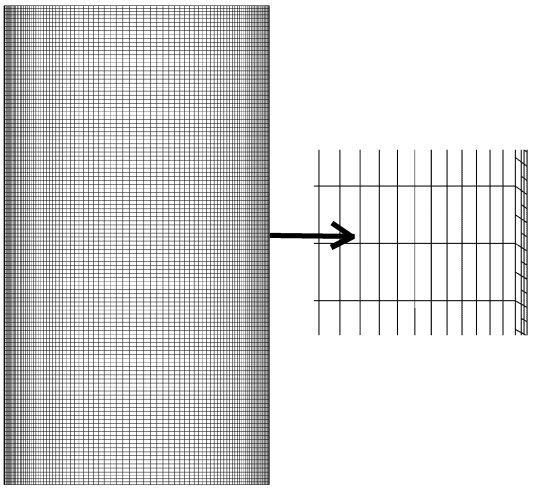

Figure 4.2: Grid projection on the symmetry plane $z = 0$ and a boundary layer adapted in *FLUENT*.

The Lorentz force for 1400 A inductor current was computed using a simple 2D axially-symmetric model in the commercial finite element package *ANSYS*, which is a common practice. The force is almost symmetric relative to the $y = 0$ plane (figure 4.3); some asymmetry in the crucible corners takes place because of the geometry. Only radial component of the averaged force was taken because this component is determinative for the flow motion in the crucible. The *ANSYS* calculated Lorentz force density was approximated by multiplication of a fourth power polynomial with a skin-layer exponent. This force was applied symmetrically to the left and the right planes of the tank using *FLUENT*'s UDF functions. The force amplitude varied for different calculation sets.

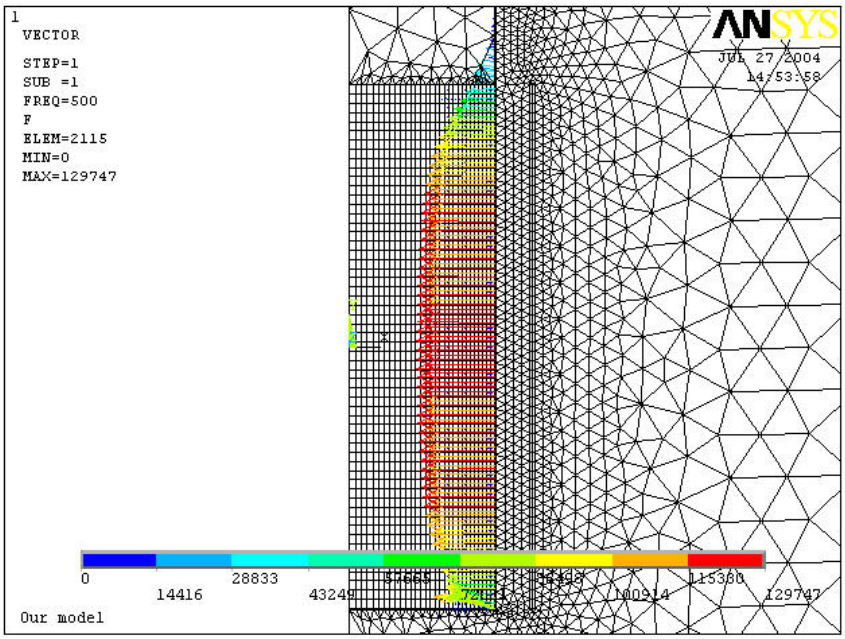

Figure 4.3: *ANSYS* calculated Lorentz force distribution.

Different numerical schemes were used for *FLUENT* (table 4.1). The $k-\varepsilon$ model was sometimes employed to obtain the initial distribution of velocity field, reducing the total time of calculations. Then a transient LES flow simulation was run. Some calculations were performed on a model, where the force was applied to the melt with zero velocity field. The time step and their number differed for each simulation and depended on the characteristic velocity of the flow or, in other words, on the period of vortex circulation. Time step values were selected between 0.01 s and 0.05 s, with their total number being about 13500 in some simulations.

The middle meridian plane was defined and the values of velocity components were saved in the profile files after each time step. A special software was developed for the correlation and Fourier analysis of the profile files.

Table 4.1: Calculated flow parameters

f/f_{nom}	Eddy period, s	Pulsation period, s	$\langle v \rangle$, cm/s (calc)	Approximation scheme	$\langle v \rangle$, cm/s (exp)
0.16	115.0	40	0.6	First order	
0.80	20.9	20	3.3	Centr. dif.	5.92
1.00	13.8	17	5.0	First order	8.36
1.00	14.7	10	4.7	Centr. dif.	8.36

4.2.2 Results of computations

A model with a small Lorentz force (16% of the rated, the rated force corresponds to the 1400 A inductor current) was implemented to see how the flow is developed in time. Nine minutes of the real flow were calculated with the time step of 0.04 s. The characteristic velocities of such flow were below 1 cm/s (with Re about 3400) and the period of vortex circulation was about 40 s, which means that the selected time step was fully appropriate. The maximal number of iterations per time step was set equal to 30 and the total count of time steps was 13500. The melt was in the rest at zero time and the motion of the melt began when force was applied. The velocity values were growing, achieving their maximum after about 70 flow seconds (figure 4.4). Then the melt flow stabilized and approximately after 240 s low-frequency oscillations began. These calculations were done using first-order upwind approximation for momentum equations.

The Fourier analysis was performed for each stage of flow development. The first stage **I** of the flow (figure 4.4), when the velocities are growing, does not contain characteristic frequencies. The spectrum covering the time of flowing from 82 to 245 s (**II**) contains some low frequencies, which can be explained as instabilities of vortex development (figure 4.5). This flow is not explicitly turbulent, since Fourier's spectra do not contain high harmonics and the oscillation energy is small. The flow fully develops to turbulent after about 240 s of the run (**III**) and the spectra of the last stage are typical to turbulent flow containing lots of high frequencies. The intensity of this turbulent spectrum is at least one order greater than that in the stage (**II**). This spectrum also has low frequency part,

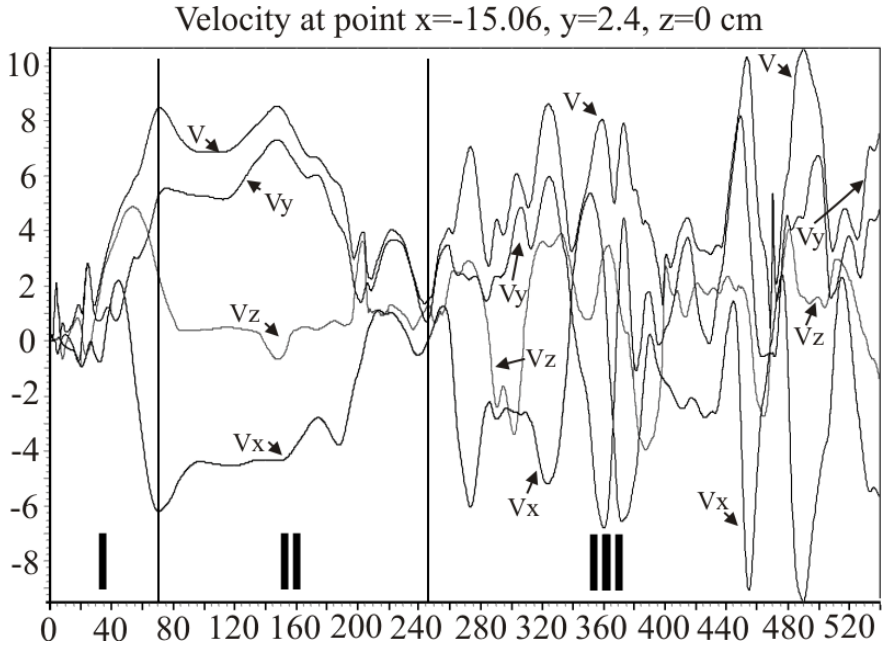

Figure 4.4: Time dependence of the flow velocity between eddies near the wall for small Lorentz force (16% of rated).

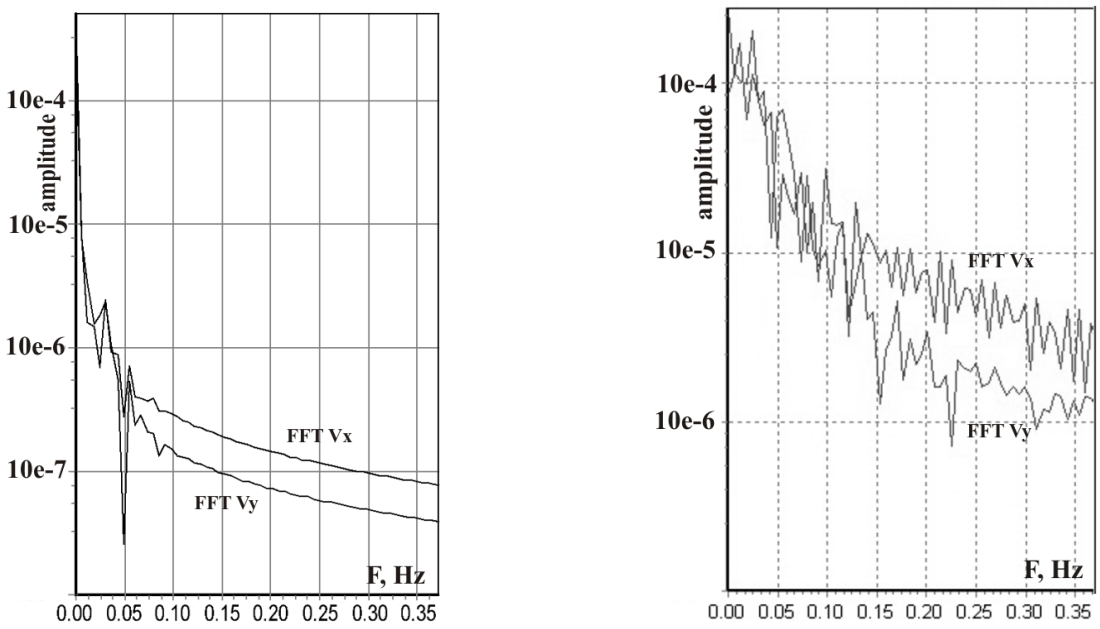

Figure 4.5: Fourier velocity spectra at the beginning of the flow (80-240 s, left) and in the fully developed flow (right), force is 16% of rated

in which the largest part of energy is found.

The flow development is laminar until the Reynolds number reaches values above 2000 (the corresponding velocity is about 0.8 cm/s). Then some instability develops so that z–velocity component, which is not influenced by the Lorentz force and which should be zero in laminar flow, also starts to oscillate. This velocity component corresponds to angular in the full cylindrical geometry. LES numerical approach gives a qualitative pattern of the flow development for simplified geometry model.

The following calculations were performed with the force, which is 80% of the rated value. The maximum flow velocity near the wall is about 7.5 cm/s in this case (Re$\sim$25000). The mesh was the same and the stationary $k-\varepsilon$ solution was selected as the initial state for the LES model. No calculations of the rest state were performed since they need a smaller time-step to obtain solution convergence at high force values. In the present calculations the central difference scheme for momentum equations was applied, which is recommended for LES calculations. The time step was the same and two minutes of the flow were computed (figure 4.6). The flow pattern at every time step is not symmetric because of the high turbulence, but averaged flow is almost fully symmetrical. The computed averaged flow shows a zone near the middle of the tank wall, between vortices where flow intensity is low. The height of this zone is about 10 cm. The velocity vectors change their values and direction depending on the "strength" of interacting eddies at every time moment.

A typical Fourier's spectrum and the correlation spectrum are shown on figure 4.7. There are several frequencies in Fourier's spectrum, at which the energy values are large. Autocorrelation analysis also give the basic frequencies of pulsations (for example, the basic frequency of pulsations on figure 4.7(right) is about 7 s).

Two series of calculations were made with the rated force corresponding to the 1400 A current. The time step in both calculations was 0.05 s. The only difference was the scheme used for the momentum equation approximation: first-order upwind or central-difference scheme. The FFT analysis for both calculations show that the difference in the spectra at using the first-order upwind and central differences approximation schemes is about 5-10 times at the region of low frequencies

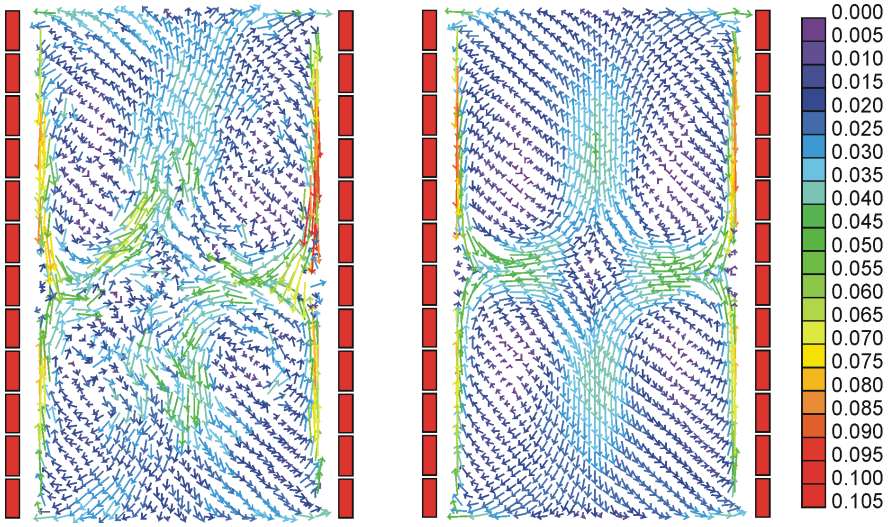

Figure 4.6: Flow pattern in the middle plane (instantaneous and averaged, force is rated and corresponds to current 1400 A).

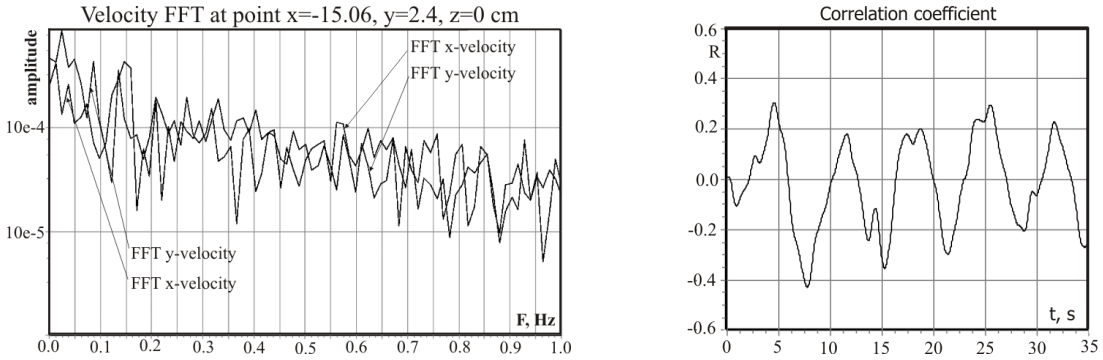

Figure 4.7: FFT velocity and v_z autocorrelation at the point near the wall between vortices. Force is 80% of rated (central differences approximation).

(figure 4.8). Here again we have several frequencies of equal energies in the spectrum in the model based on the central-difference scheme (figure 4.8 right). The one can conclude from these figures that the first-order upwind approximation of momentum equations reduce the intensity (energy) of pulsations.

The smallest frequency we have found was about 0.025 Hz, which gives a

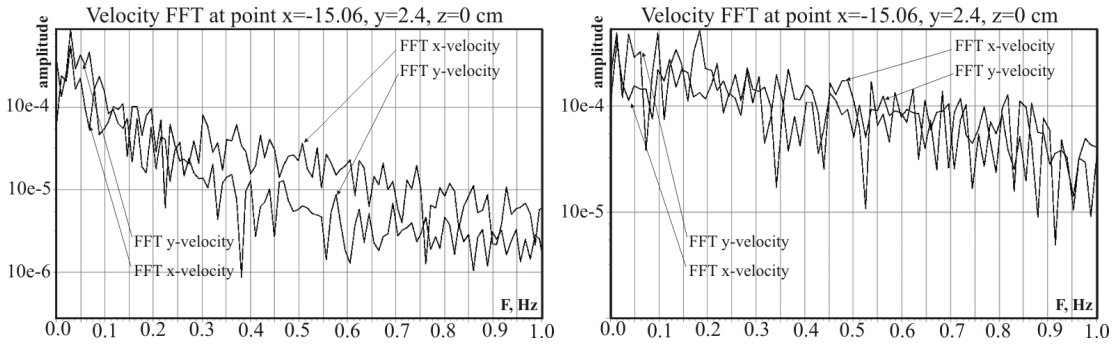

Figure 4.8: FFT velocity corresponds to calculations performed with the first-order (left) and with the central-difference scheme (right) for the momentum equations

period of 40 s. That is why such a long calculation time is needed. This frequency is characteristic of all the models, so it can be defined by the model geometry.

The calculated flow parameters are shown in table 4.1. The pulsation period is of the same order as the eddy circulation period. More precise comparison is difficult to make since different methods for calculation of averaged velocity can be applied. The calculated averaged velocities are smaller than the equivalent velocities from the experiments because of different model geometry. The maximum flow velocities are in the by-wall region. They are of the same order as the measured averaged velocities at the symmetry axis.

This model gives only qualitative description of the flow. Produced velocity patterns and turbulent spectra in general are in accordance with the experimental in respect of structure. However, absolute values of the velocities or energies are much smaller than in experiments and usage of this approach is very limited and not needed since high performance computer clusters are available.

4.3 Full 3D model for 570 mm filling level

3D transient LES simulation was used to investigate turbulent flow phenomena in ICF quantitatively. All calculations were mainly performed in commercial CFD

packages *FLUENT* and *ANSYS CFX*. The model setup was mainly like in the simple model (section 4.2), but several things were different. This model had full 3D cylindrical form and all solid walls had no-slip boundary conditions. No shear stress (free-slip) boundary condition was used for the top surface of the melt. The motion of the melt was controlled by 2D axis-symmetric electromagnetic *ANSYS* model calculated Lorentz force for "standard" case of the melt-crucible-inductor system (**Exp1**, figure 3.5). Because the inductor frequency is much larger then 5 Hz, there is no need to consider oscillating nature of Lorentz forces and tangential force component [23]. EM forces were directly transferred to every finite volume in *FLUENT* by UDF during the model initialization (transfer error is less then 1%). *ANSYS CFX* had forces interpolated from a text file.

FLUENT and *CFX* numerical grids were built in Gambit and had about 2 million elements. Typical mesh resolution in the middle zone was about 3 mm. Solid boundary layers had refinement with the first layer 0.5 mm. High precision second-order numerical schemes with central-difference momentum discretisation were used for transient simulation. Time step was selected to be 0.005 s for the full LES model. Performed LES test with larger time step $\Delta t = 0.01$ s have shown that the averaged results do not depend on concirn about such time step change. Smaller time step is more convenient for spectral analysis of calculated velocities, larger time step can be used to get fast averaged results. About 60 s of the flow development were calculated starting from the zero velocity field. Calculations were performed on a Linux cluster iteratively until each variable change is less than 10^{-3} for a time step.

ANSYS CFX and *FLUENT* CFD software packages were used for LES simulation and results of the computations will be presented in parallel. Calculated velocity patterns introduce well-developed turbulent flow consisting of different size vortices (figures 4.9 and 4.10). The flow develops from the zero velocity field very fast. The typical two-vortex structure presents in the flow already after 5 s of the flow development as a small turned flow in the middle of the crucible (figures 4.9(a) and 4.10(a)). The flow velocities are already relatively high, even above 10 cm/s, but there are still regions, where the melt is almost calm: central parts near the crucible bottom and near the top surface.

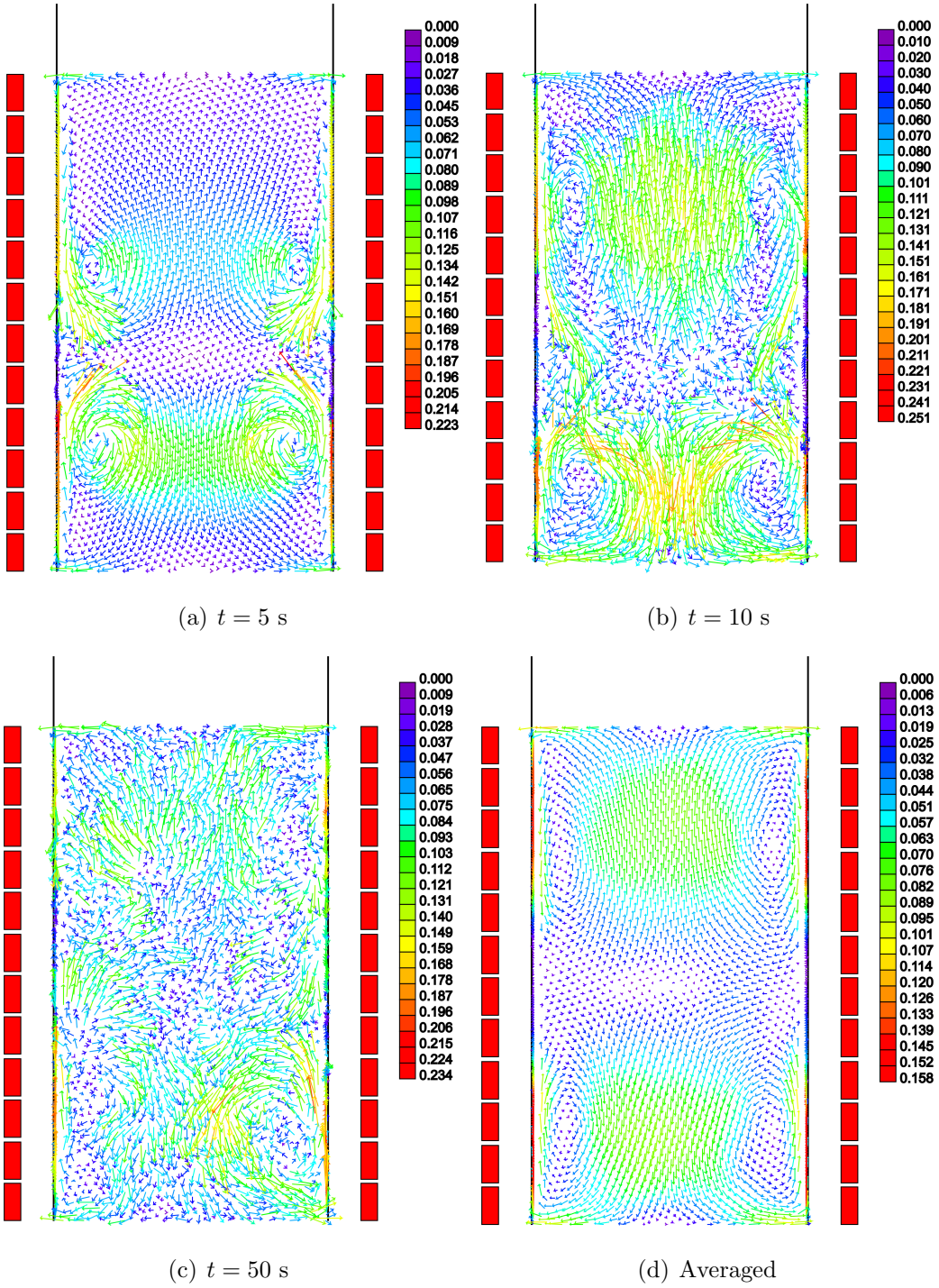

(a) $t = 5$ s (b) $t = 10$ s

(c) $t = 50$ s (d) Averaged

Figure 4.9: LES calculated flow patterns at different time moments and the averaged flow from *ANSYS CFX* (simulation starts from the zero velocity).

The typical "main" vortices also can be clearly identified at $t = 10$ s (figures 4.9(b) and 4.10(b)), but their shape is already disturbed by starting velocity oscillations and already full melt volume is under the motion. All velocity components increase and angular velocity component starts to oscillate. The calculated flow pattern in *ANSYS CFX* is different from corresponding *FLUENT* velocity pattern. *CFX* has instantaneous solution where the bottom "main" vortex is locked near the bottom crucible corner and it is smaller comparing to the upper vortex. The same vortices in *FLUENT* seems to be equivalent. Instantaneous velocities are a little higher in *CFX*. Different FVM realization in CFD code and transient nature of the flow development process can be possible reasons of these differences, because in general all boundary and numerical conditions were the same for both used packages.

The fully developed turbulent flow (figures 4.9(c) and 4.10(c)) has more local vortices and its structure is completely three dimensional with intensive angular velocity oscillations. The flow is presented by many vortices, several vortices have considerable size, which is comparable to the size of the "main" eddies. The maximal flow velocities are achieved near the crucible wall where permanent upward and downward flow jets are located.

Flow averaging was performed from $t = 10$ s to the end of simulation. The averaged patterns (figures 4.9(d) and 4.10(d)) introduce experimentally determined two-loop flow structure. The averaged "main" flow vortices are very similar to each other, however a little asymmetry can be noticed on the figures, which can arise due to insufficient time of the 3D transient simulation. Maximal averaged velocities are less than maximal instantaneous and also calculated averaged velocities are 12-25% far from the experimentally determined values (figures 3.6(a) and 3.6(c)). Here again a question about the correct PMP probe calibration in experiments appears. In general the computational error seems to be relatively large comparing to experimental data, LES simulations under-predict absolute velocity values in the averaged flow, however its main advantage comparing to half-empirical turbulence models is its ability to get more realistic heat and mass exchange between the turbulent eddies.

Two parameter models ($k - \varepsilon$ and $k - \omega$) also accurately predict structure of averaged flow, which corresponds to seen in experiments - two dominating vortices

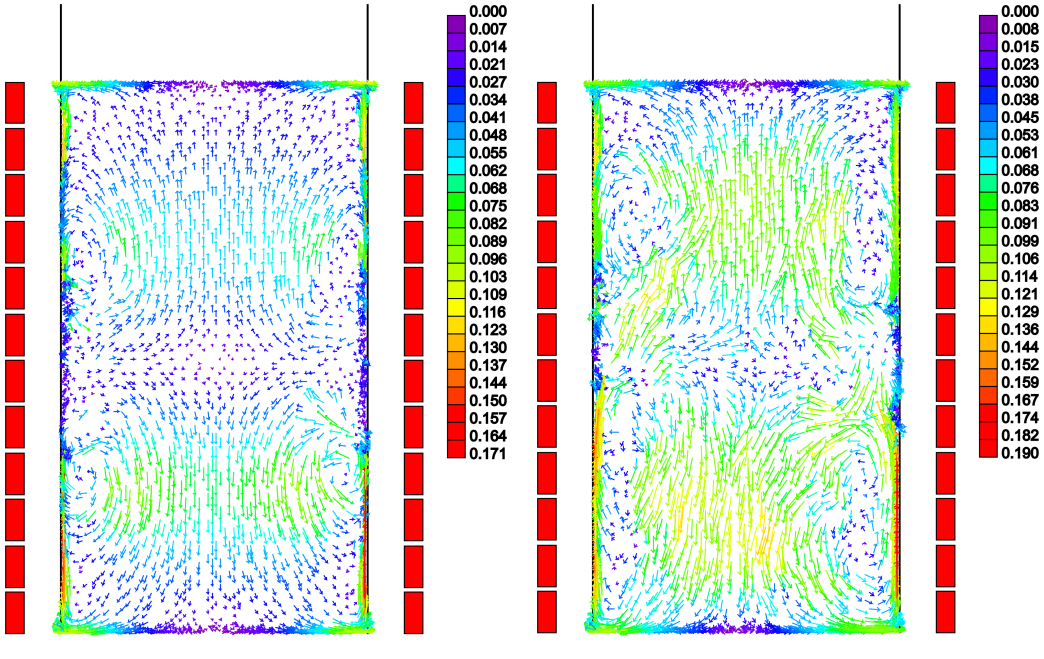

(a) $t = 5$ s (b) $t = 10$ s

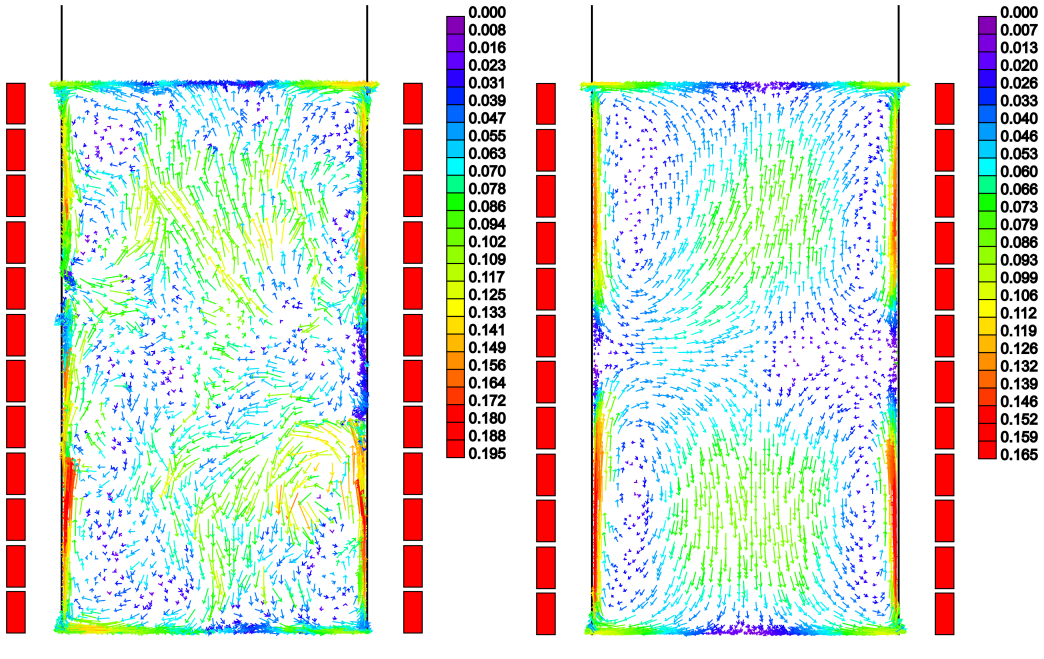

(c) $t = 50$ s (d) Averaged

Figure 4.10: LES calculated flow patterns at different time moments and the averaged flow from *FLUENT* (simulation starts from the zero velocity).

with approximately equal size and intensity (lower vortex intensity is a little larger). Smaller intensity of the upper vortex can be explained with corner effects: inductor height is equal to the crucible filling level, but HD boundary conditions on the top and near the bottom are different. Motion of the melt is initiated by the azimuthal component of Lorentz force rotor: $(\mathrm{rot}\mathbf{f_{EM}})_z = \partial f_{EM_z}/\partial r - \partial f_{EM_r}/\partial z$. Absolute value of axial Lorentz force component f_{EM_z} near the bottom crucible corner is larger then near the top corner because the geometry (figure 3.5(b)) and $\partial f_{EM_z}/\partial r$ is also larger near the bottom corner of the crucible.

Axial velocity profiles at selected time moments are introduced on figure 4.11 on the vertical line $r = 0.15$ m and on figure 4.12 on the diameter at $z = 0.285$ m. These figures show how axial velocity changes upon the time: instantaneous flow vortices keep the basic structure of the flow, however smaller vortices are also important for turbulent mass transport. There are local (concurrent to the "main" eddies) vortices with characteristic scales between $0.01 \div 0.05$ m. The instantaneous flow is very unstable in the middle zone of the crucible ($z = 0.285$ m), where $\partial f_{EM_r}/\partial z \approx 0$. Two opposite flow jets come parallel to the crucible wall into collision and are drown away from the wall. The axial velocity intensity oscillates along the wall under the influence of local vortices (figure 4.11) in the studied flow. Interchanging streams of different instantaneous axial velocity intensities are observed. Vortices of different sizes are drawn away from the wall to the regions of opposite averaged vortices. In this way effective impulse and scalar (temperature, concentration) value transfer is ensured between the upper and the lower eddy. However, the axial velocity of the averaged flow near the wall and in the symmetry central point ($r = 0$, $z = 0.285$ m) must be close to zero in an ideal case ($v_z \to 0$). Radial velocity of the flow has its maximal value between the near-wall region and the symmetry point at radii $z = 0.285$ m.

Experimental and modeling results are compared for radius at $z = 0.13$ m (lower vortex, figure 4.13). The best fit is achieved using 2D $k - \omega$ model [114], but all models introduce results in relatively good accordance with experimental data on the selected radii. Some difference from experimental results is observed mainly near the symmetry axis. Calculation results for $r > 0.4$ m and also near the wall fit experimental data very well, however, it was expected that

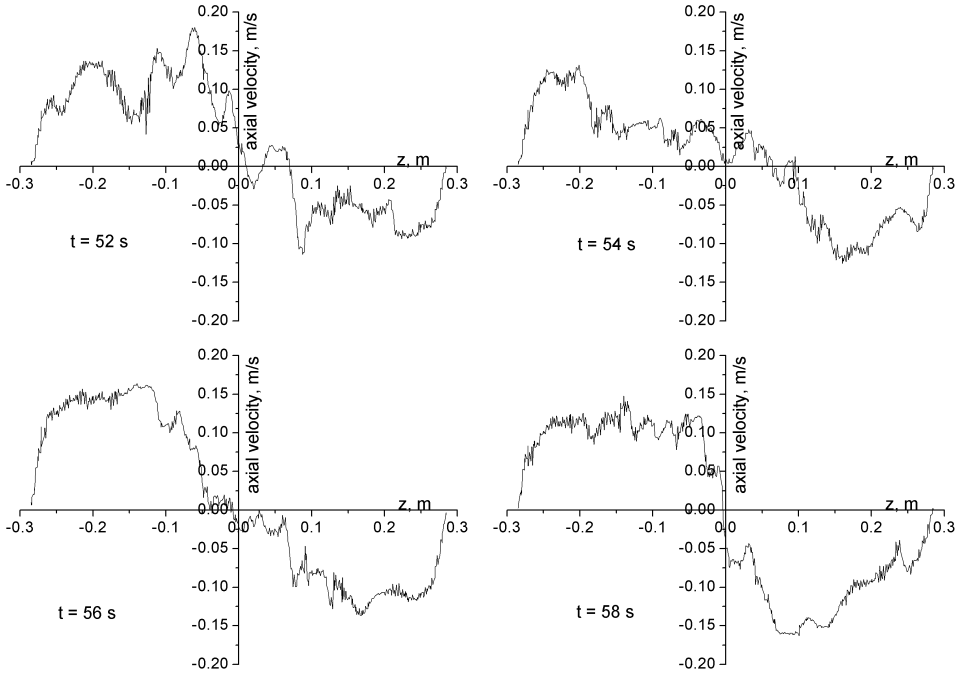

Figure 4.11: *FLUENT* full 3D model calculated axial velocity $v_z(z)$ at $r = 0.15$ m for different time moments.

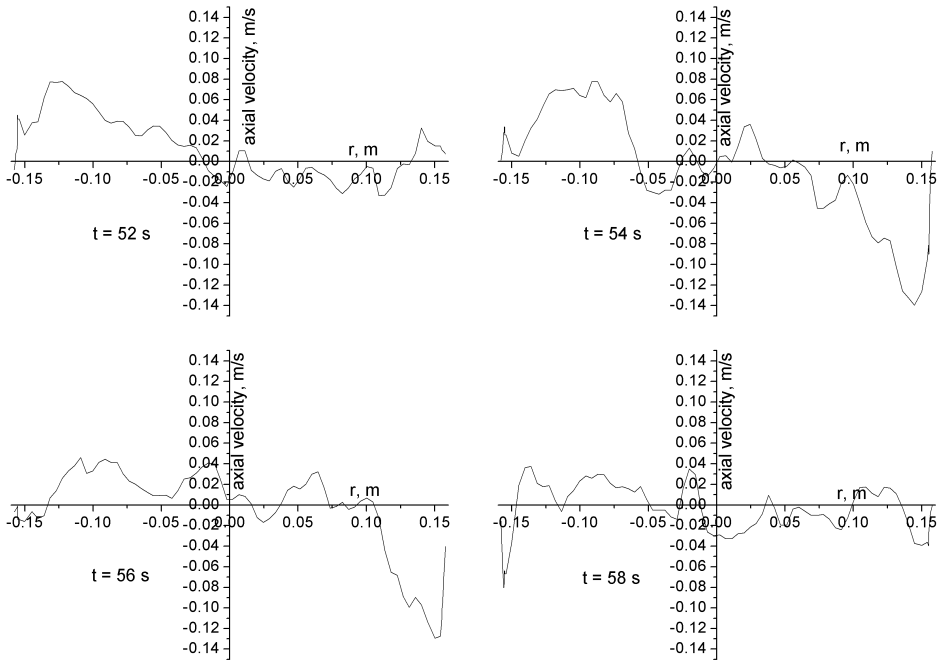

Figure 4.12: *FLUENT* full 3D model calculated axial velocity $v_z(r)$ at at $z = 0.285$ m for different time moments.

experimental results can suffer from the outer EM field. Full 3D LES model results are comparable with 2D model results in *FLUENT*.

Figure 4.14 shows axial velocity distribution on symmetry axis for 2D models and averaged LES models. Simple (box) LES model (section 4.2) maximal axial velocity value is smaller then in other models because this model has rectangular form and due to the mass conservation low flow velocity in the middle zone should be smaller than in the near-wall region (vortex centers are closer to the crucible walls), but the flow regime for this model is still turbulent ($\mathrm{Re} > 10^4$). Models, which account for axial symmetry (2D and full 3D models), have axial velocity maximums near the crucible wall and on symmetry axis approximately in the middle of top or bottom vortex height while the simplified geometry box model has velocity maximum, which is closer to the diameter $z = 0.285$ m (figure 4.14).

Transient flow development from the zero velocity field (figure 4.15) is very similar to calculated with the simple (box) model. The radial velocity component grows very fast near the crucible wall at a half-height of the melt. Flow accelerates and transition to turbulence occurs. Velocity oscillations present in the flow already at $t = 5$ s, when tangential velocity fluctuations start. The low-frequency velocity oscillations can be seen after 10 s, but their frequency seems to be lower than in experiment.

Correlation analysis (figure 4.16(a)) does not show existence of regular velocity fluctuations because local maximums and minimums of the velocity autocorrelation are not very large, i.e. there is no linear dependence of the signal on itself for 60 s. The same correlations were used to get power spectrum of the velocity components (figures 4.16(b) and 4.17). All power spectrums have characteristic wavenumber ranges (approximately $40 \div 200$ m^{-1}), which correspond to the Kolmogorov's inertial subrange. Smaller wavenumbers have characteristic peaks at interval $2 < k < 4$, which fits to geometry size of the crucible and height of the characteristic vortices.

Wavelet transformations of the calculated velocities need more input data (longer simulation time) because in this case very large oscillation periods seems to present in the flow. Longer simulated time allows to have better low-frequency resolution on a wavelet charts (figures 4.18 and 4.19). Both calculated axial velocity wavelet patterns near the crucible wall seems to have 8 s expressed period

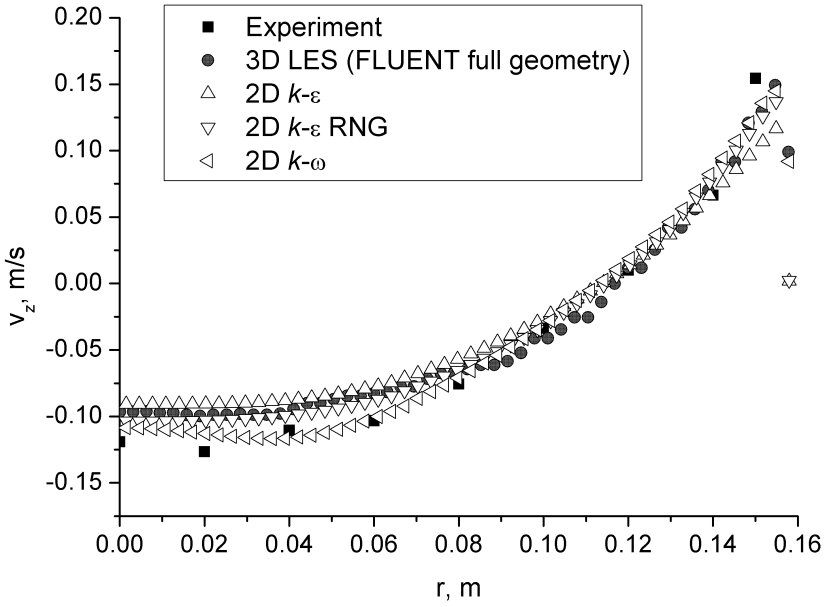

Figure 4.13: Axial velocity profile at $z = 0.13$ m.

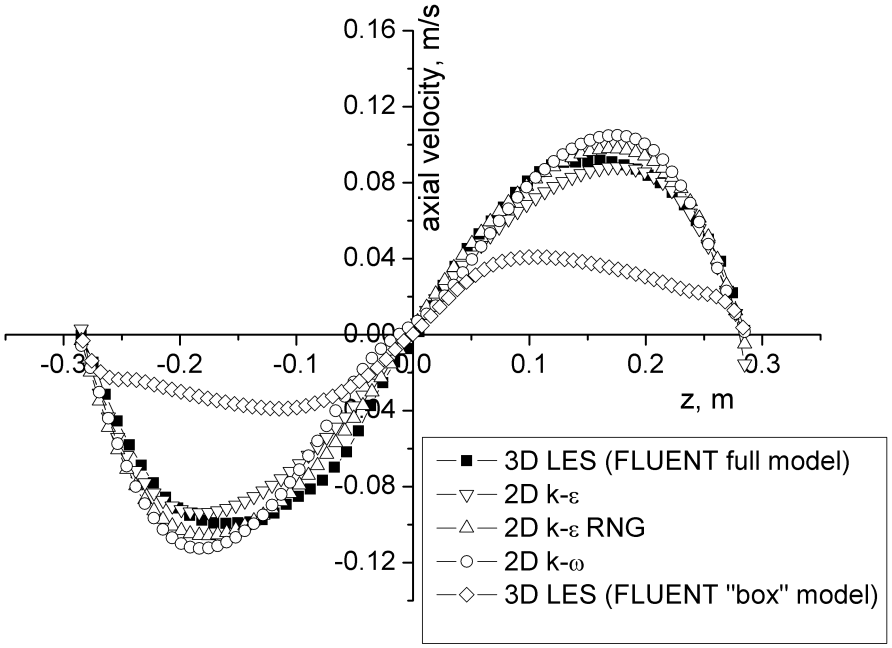

Figure 4.14: Axial velocity profile at $r = 0$ (coordinate system origin is in the symmetry point of the melt).

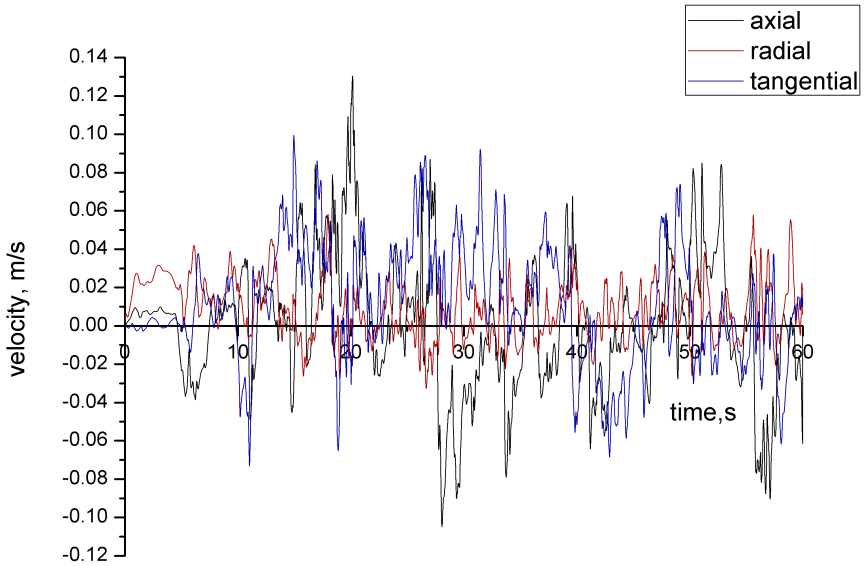

Figure 4.15: Flow velocities near the crucible wall $r = 150$, $z = 290$ mm (*FLUENT*).

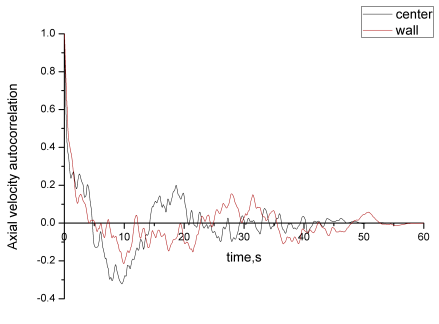

(a) axial autocorrelations, $z = 290$ mm

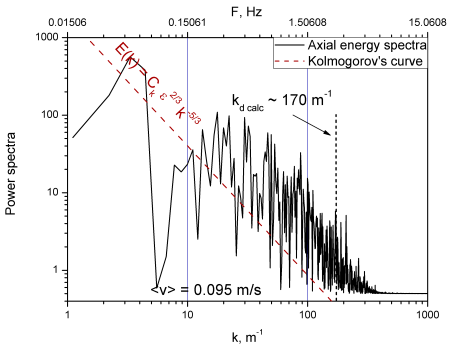

(b) axial spectra $r = 0$, $z = 290$ mm

Figure 4.16: Axial velocity autocorrelations and power spectra at $r = 0$ (*FLUENT*).

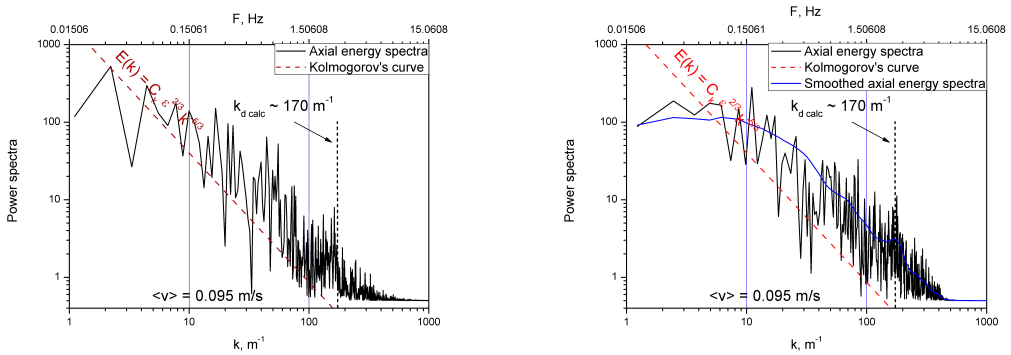

(a) *FLUENT* (b) *CFX*

Figure 4.17: Axial velocity power spectrums at $r = 150$ mm.

(see page 64 for description of the used wavelets). Spectra charts from *CFX* (figure 4.17(b)) also seems very close to *FLUENT* result.

Anisotropy analysis of the flow can be performed using the results from the numerical computation in *FLUENT*. Coefficients $G_{ij,kl}$ were selected as anisotropy measure of the flow [70]:

$$G_{ij,kl} = \frac{\langle (\partial u_j/\partial x_i)^2 \rangle}{\langle (\partial u_l/\partial x_k)^2 \rangle}, \; i,j,k,l = x,y,z \tag{4.5}$$

Anisotropy coefficient calculations should be performed only with signal fluctuations (averages should be removed) [92] for correct analysis. A point at the center of the crucible (on symmetry axis between upper and lower averaged vortices) has zero averaged velocity and isotropy analysis can be made directly on velocity gradients. Example $G_{ij,kl}$ values are presented in table 4.2, where they can be compared with theoretical values for isotropic turbulence [70]. Computed coefficients shows that the turbulence in the flow is anisotropic even in the middle of the crucible where wall effects are neglected. This anisotropy is caused by the different preferential directions of the flow near the central point of the symmetry. Coefficient values in other parts of the flow are even larger, so we can conclude that isotropic laws generally can not be applied for such types of the flows.

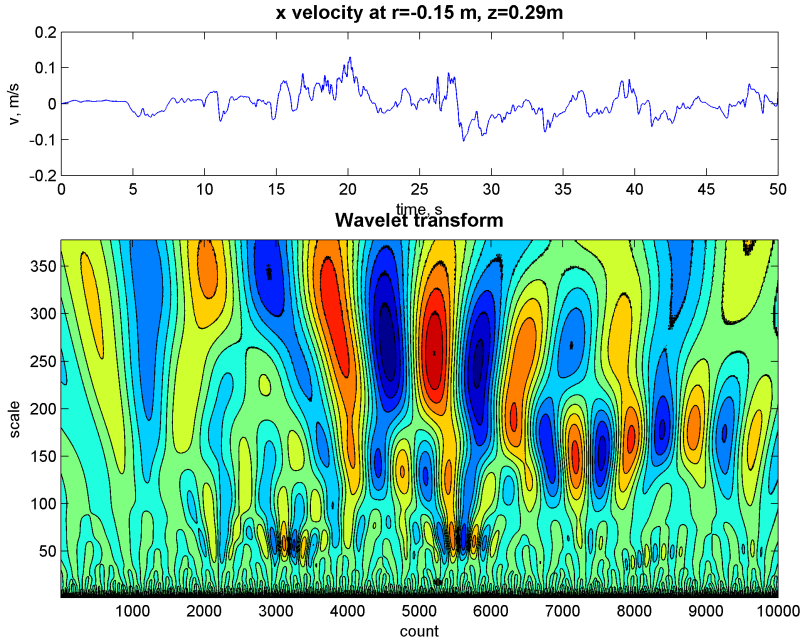

Figure 4.18: Wavelet transform of the near-wall axial velocity from *FLUENT*.

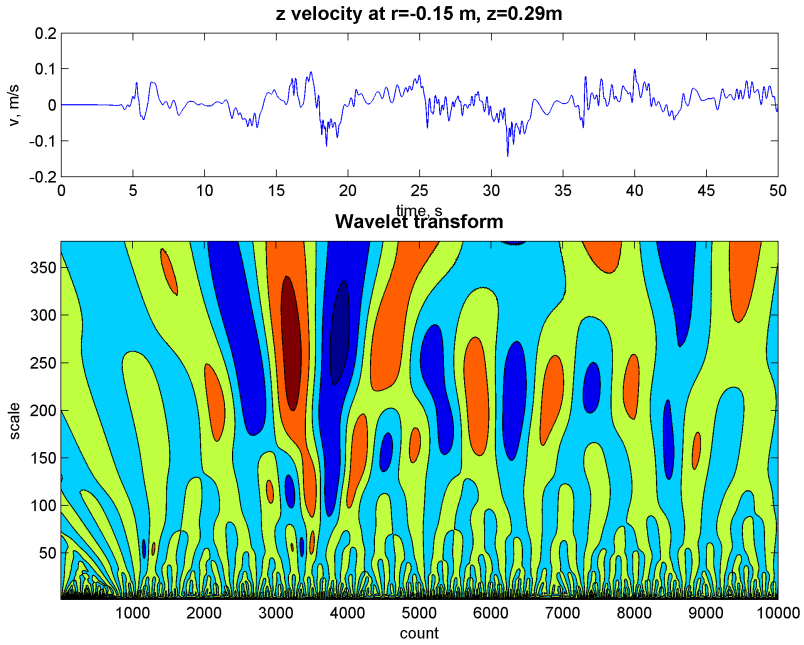

Figure 4.19: Wavelet transform of the near-wall axial velocity from *CFX*.

Point	$G_{xx,yx}$	$G_{xx,zx}$	$G_{xy,yy}$	$G_{xz,zz}$	$G_{xy,zy}$	$G_{xz,yz}$
isotropic [70]	0.5	0.5	2	2	1	1
$r = 0$, $z = 290$ mm	6.4	24.9	1.2	1.5	4.7	1.2

Table 4.2: Relative strength of velocity gradients in different directions.

4.4 Full 3D model for 620 mm filling level

A complete 3D numerical unsteady model was also used for simulation of the crucible with 620 mm filling of the melt under **Exp 3** conditions. This simulation was performed only in *ANSYS CFX* with characteristic grid size 3 mm like in all previous simulations (the total number of elements is approximately 2 millions). 2D axis-symmetric electromagnetic *ANSYS* model was adapted to include increased melt height, shortened inductor and higher inductor current ($I = 2180$ A). Axial and radial EM forces were interpolated to hydrodynamic grid from a text file (figure 4.20).

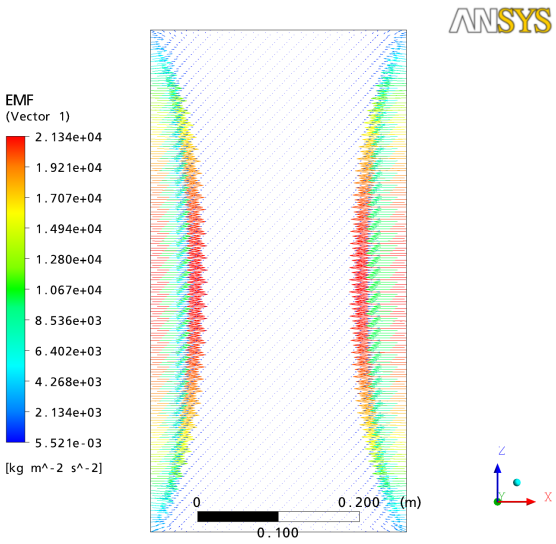

Figure 4.20: Lorentz force transferred to HD model ($H = 620$ mm).

High precision second-order numerical schemes with central-difference momentum discretisation were used for transient simulation. Initial velocity field

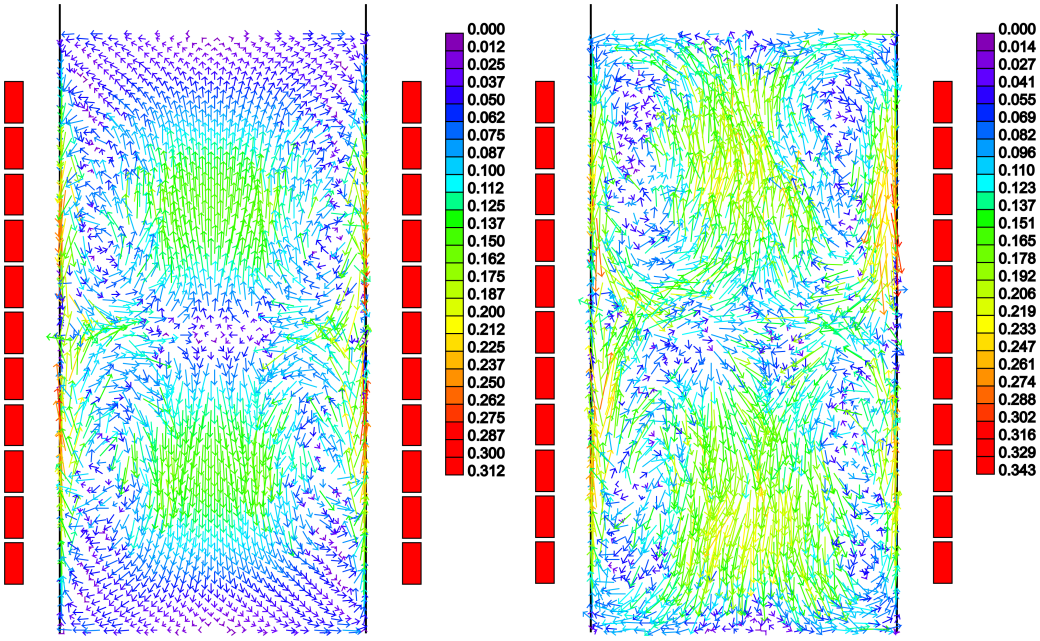

(a) $t = 5$ s (b) $t = 10$ s

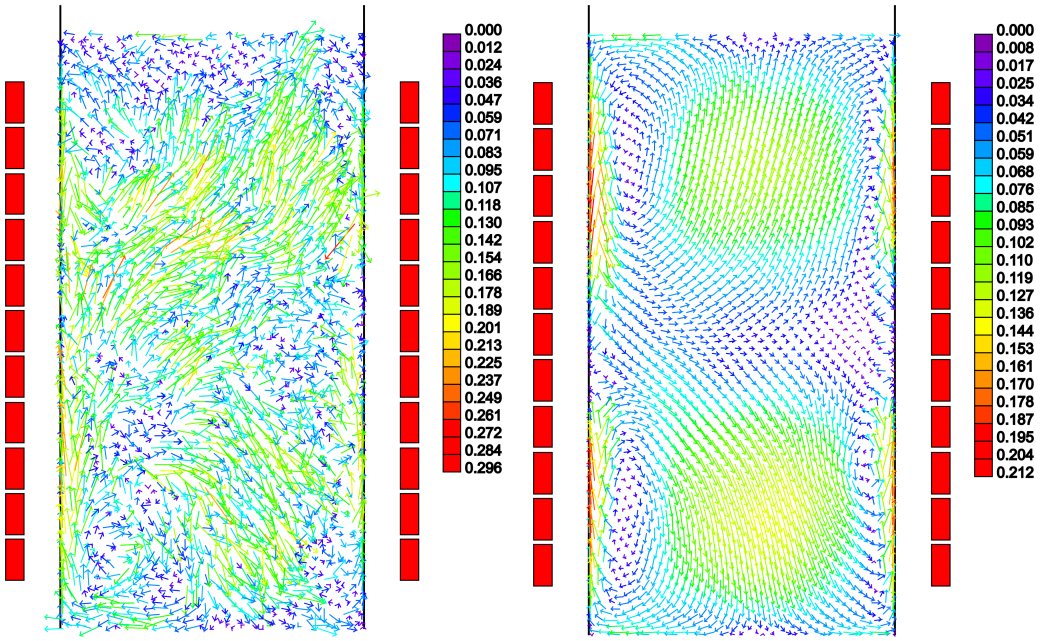

(c) $t = 50$ s (d) Averaged

Figure 4.21: LES calculated flow patterns at different time moments and the averaged flow from *ANSYS CFX* (**Exp3** conditions, simulation starts from the zero velocity).

was set to zeroes. Time step was selected to be 0.005 s for the full LES model and 52 s of the flow development were calculated starting from the zero velocity field. Calculations were performed on a Linux cluster iteratively until each variable change is less than 10^{-3} for a time step.

The inductor is shorter than the melt height and it is placed symmetrically in respect to the melt. Such geometry setup reduces corner effects of the EM field. As a result EM force is more localized in the central part of the melt and the the flow has only geometrical limits when closing loops in the top and bottom crucible corners. The flow also have more place to accelerate near the crucible wall. Above mentioned effects and increased inductor current (linear inductor current is also increased) lead to faster melt velocities and faster development of the turbulence than it was for 570 mm (figure 4.21). The first velocity oscillations are seen already at $t = 5$ s. The flow still have the typical two-vortex structure at $t = 10$ s, but these vortices are already deformed by the turbulent velocity oscillations (figure 4.21(b)). The axial large scale motion is more expressed in the developed turbulence than radial or angular (figure 4.21(c)). The maximal flow velocities are localized mainly near the crucible wall and can achieve 30 cm/s in instantaneous flow and 22 cm/s or even more in averaged (figure 4.21(d)) due to higher induced current densities and therefore Lorentz forces.

The turbulent flow develops very fast (figure 4.22) and tangential velocity oscillations are presented in the flow almost at once after power on switching. Radial velocity also oscillate in the vicinity of the crucible wall, but there are time range ($21 < t < 49$ s) where it keeps its sign. Axial velocity starts to oscillate at $t \approx 2$ s and these oscillations have full amplitude already at $t = 5$ s. Axial velocity achieves relatively large values till ± 15 cm/s. Radial velocity oscillations have the largest amplitude, which is comparable to the maximal flow velocities in the melt $\pm 25 \div 30$ cm/s.

Fourier power spectrums in wavenumber space (figure 4.23) were created using the same characteristic flow velocity $v_c = 0.095$ m/s. The spectra from the near-wall region has a little larger energy in the low-frequency region. Both spectrums have parts, which can be approximated with the Kolmogorov's slope $E(k)\ k^{-5/3}$.

Wavelet transform of the axial velocity near the crucible wall (figure 4.24) does not present low-frequency oscillations with a quasi constant period. Several

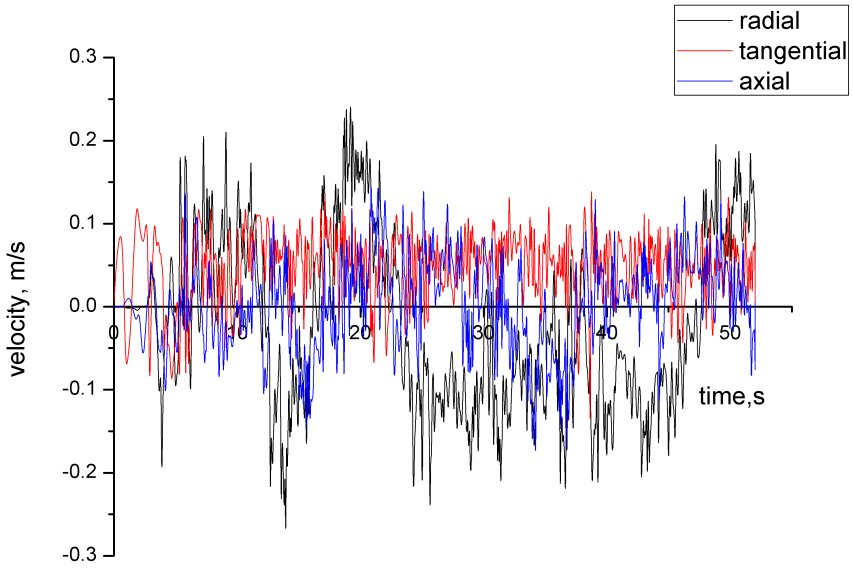

Figure 4.22: Flow velocities near the crucible wall $r = 140$, $z = 310$ mm (CFX).

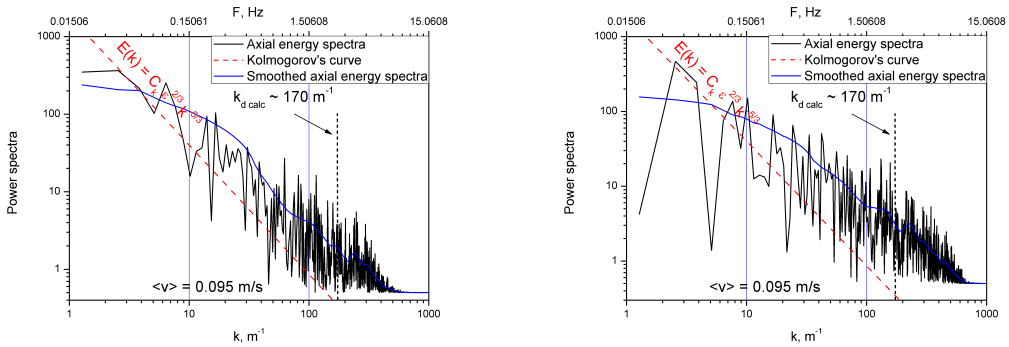

(a) $r = 0$, $z = 310$ mm

(b) $r = 150$, $z = 310$ mm

Figure 4.23: Axial velocity power spectra (CFX).

unstable periods can be found for signal at $5 < t < 25$ s: $T_1 \approx 3.8$ s, $T_2 \approx 9.6$ s and $T_2 \approx 19.2$ s.

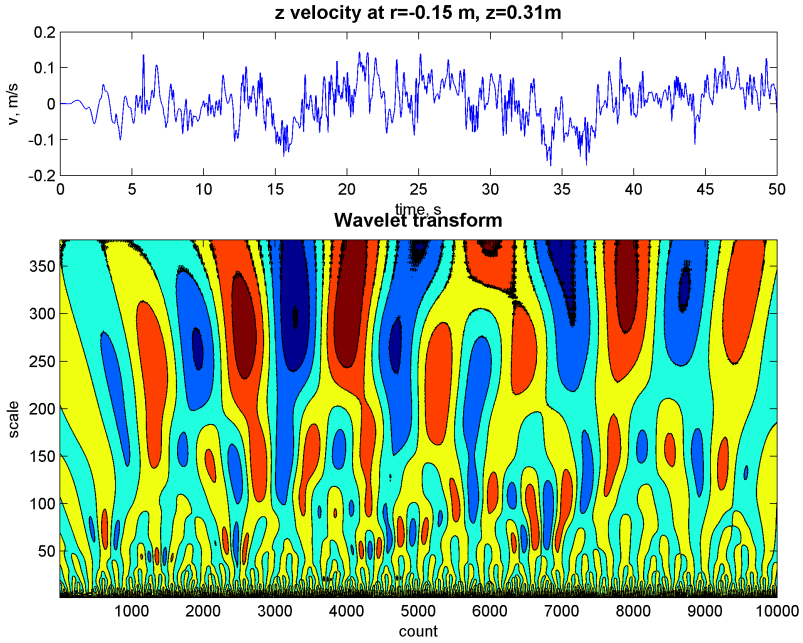

Figure 4.24: Axial velocity wavelet transform near the crucible wall $r = 150$, $z = 290$ mm (CFX).

4.5 VOF calculation of free surface deformation for 400 mm

Experiments have shown, that the flow in the ICF is more intensive if the melt height is reduced. However, the free surface of the melt is deformed and oscillates in this case. Metal free surfaces deformation by the strong EM field is known for a long time and is especially actual in the TiAl or Al cold crucible melters and levitation [115]. Therefore, numerical methods for estimating a shape of the deformed free surface (meniscus) of the melt have been developed. The developed methods were mainly 2D finite or boundary element with ignorance of the melt stirring [46, 88, 93, 94]. Later 2D and 3D simulations with fluid motion also were introduced using VOF [26, 38]. All developed methods had good results comparing to experimentally determined meniscus shapes (usually

by contact probes or mirrors). Selected here VOF method allows to determine melt–air interface with influence of all incorporated phenomena, such as gravity, EM pressure, surface tension and melt stirring.

Strong deformation of the free surface, which is noticed in experiment **Exp5** (I = 2000 A, $H_{melt}/H_{coil} \approx 0.75$), is mainly caused by the EM pressure $p_M = B^2/(2\mu_0)$ from the inductor. Free surface oscillations are mainly caused by the turbulent melt motion, especially by a small turbulent vortex in the top corner of the melt. It was decided to try 2D VOF analysis of the above problem in *ANSYS CFX*. VOF method means that two-fluid model is used. The volume of the melt can vary in each computational element from 1, which means, that this cell is completely filled with the melt, to 0, which means that this cell is filled with air. Interface between the air and the melt is presented by the isoline where volume of the melt is equal to one half. The top wall of the model is left as opening with the air fraction equal to one. This method requests larger geometry region to model. 570 mm high cylindrical sector was selected for VOF calculations.

The problem can be solved iteratively decoupling EM and HD parts to independent tasks because we can exclude influence of the moving conducting fluid on the external magnetic field like before (magnetic Reynolds number is low). In this case we can select initial approximation for the free surface shape (horizontal, not deformed) and then calculate EM force distribution in the melt with this initial surface (figure 4.25). After that Lorentz forces can be transferred to HD calculations and new surface shape can be estimated after 100 iterations. This iteration limit is selected for speed up of calculations. EM calculations are performed again for this new shape and the process loop will continue until convergence criteria is fulfilled. Convergence criteria can be selected in two ways: 1 – HD error is below some limit; 2 – surface change between loop steps is minimal.

This process was fully automated. *ANSYS Classic* and *ANSYS CFX* were launched in batch mode using command files from special program, which was also designed to process *CFX* results automatically. *ANSYS* scripts were written for EM analysis and HD grid generation. 2D axis-symmetric steady case file with $k-\varepsilon$ turbulence model was created for *CFX* input for 100 iterations. *CFX* posprocessing was obtained using *cfx5post* journal file, which produced new calculated shape, which was later smoothed for better migration to *ANSYS Classic*. Grids

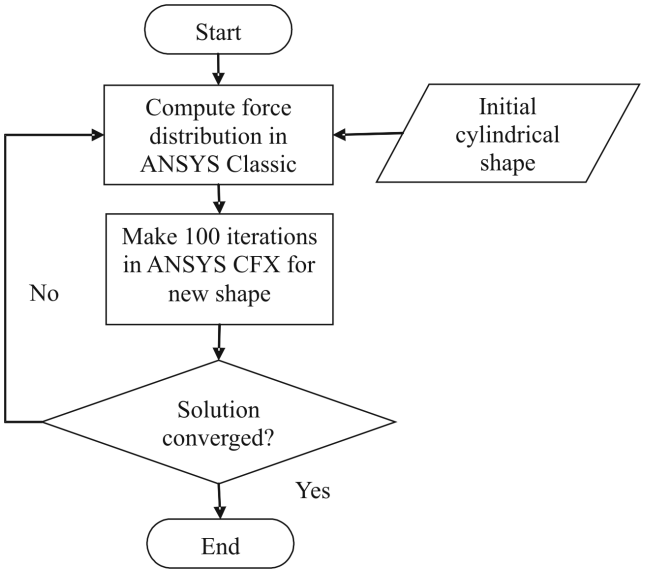

Figure 4.25: Computational algorithm for free surface calculations.

for EM and HD calculations are shown accordingly on figures 4.26(a) and 4.26(b). Typical element size for melt in EM analysis is only 2 mm. HD grid has refined zones in the fluid-air interface region and near the crucible wall.

Two major issues are found when setup two fluid VOF in *CFX*. The model is also very sensitive to mesh quality near the interface. Mesh there should be very fine to get stable numerical solution and also it should not contain rapid element size changes. There is an example of mesh adaptation in *CFX* free surface tutorial, but it crashed *CFX* during our problem tests.

Simulation showed that after approximately 10 calculation loops there were no significant changes in the interface shape. All residuals also were small enough to except this solution. Resulting Lorentz force distribution in the melt (figure 4.27) is very smooth without any anomalies. Force density has maximum in the corner between the top surface and the crucible wall, which is shifted up comparing to the inductor middle.

Simulated flow in the melt has two typical main recirculated vortices (figure 4.28). The bottom vortex is much bigger than the top vortex and characteristic flow velocities in the bottom part are higher. Vortex interaction zone is also a little shifted up in respect to the middle. Calculated flow velocities (figure 4.28(a))

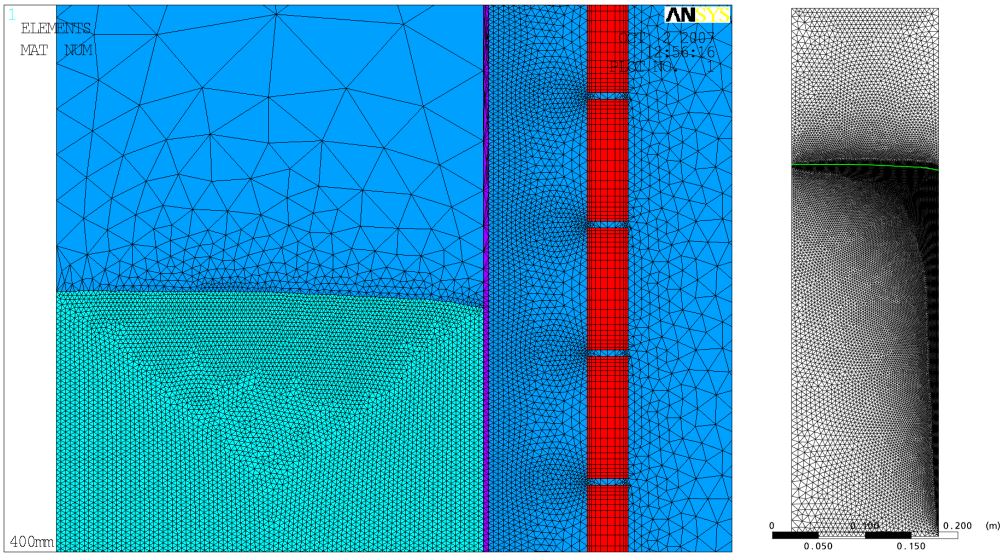

(a) *ANSYS Classic* (b) *ANSYS CFX*

Figure 4.26: Automatically generated grids for EM and HD analysis.

are with in 10% difference comparing to experimental data (figure 4.28(b)). The upper vortex also seems to be a little larger than in experiment.

Calculated surface shapes (figure 4.29) are wavy even after smoothing especially near the crucible wall. They are almost equivalent for the last calculation loops. However, experimentally measured surface has at least twice larger Δh comparing to calculated surfaces. Only one explanation, which can be found, is seen on calculated velocity chart (figure 4.28(a)). There is a zone of zero flow in the corner between the upper vortex and the crucible wall, which was never noticed in experiments and which removing should help the surface shape better correspond to experimental. Usually the assumption about small influence of the flow to the meniscus shape is made for the free surface calculations under EM field action and the same result was expected here. Such "bad" result possibly can be explained only with mistake in the model formulation in according CFD software.

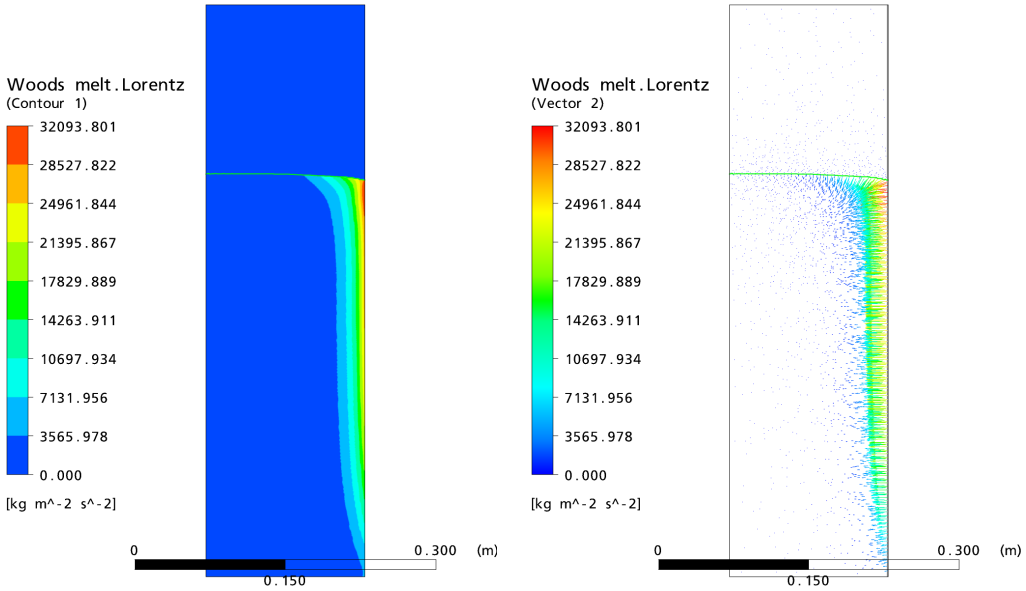

(a) Contours (b) Vectors

Figure 4.27: Lorentz force distribution in the melt for final shape.

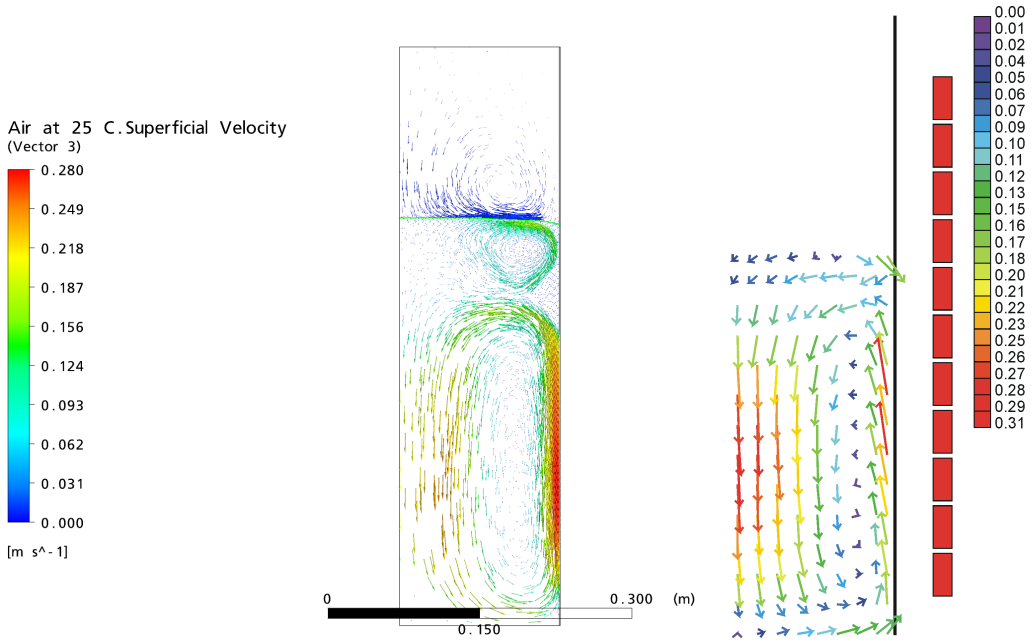

(a) Calculated (b) Measured

Figure 4.28: Calculated and measured velocity distributions in 400 mm high Wood's melt.

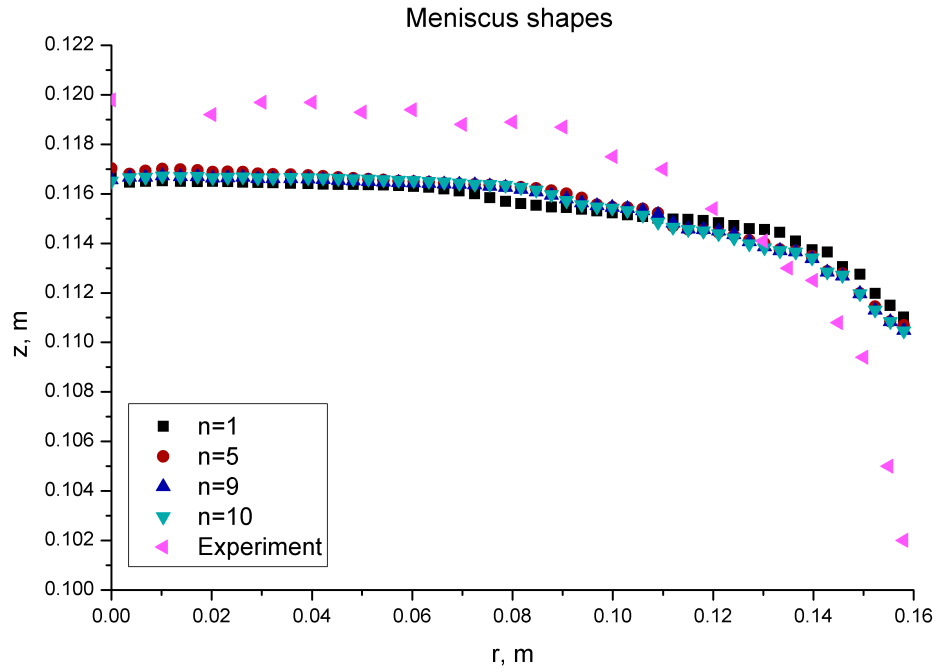

Figure 4.29: Surface shapes after calculation loops comparing to experimentally measured.

5 Study of particle distribution in the ICF

5.1 Model simplifications

Particle tracking is very useful modeling technique for additional analysis of the flow properties and mass transport estimation. Particle motion in the flow is directly utilized in separation and coagulation processes. In this thesis particle tracking is used to additionally investigate vortex structures and to find zones of particle preferential concentration depending on acting forces and different boundary conditions.

Generally this simulation is intended to particle EM separation process, which can be used to remove impurities from the melt or to accumulate certain particles near the working boundary of a final product. This method is very promising, but is often limited by other acting forces (fluid drag, lift force). Theoretical background for EM separation was established in [47]. Later the movement of a spherical particle in a gradient force field was discussed in [105] and a stronger interaction was found [104]. However, most work are based on equation (2.82) from [47]. Works Takahashi and Taniguchi [97] and Y. Kanno and Yoshikawa [116] can be mentioned as examples of successful EM separation experiments of non-metallic particles in conducting melt, in which a particle accumulation layer is comparable to the EM skin layer thickness $\delta = \sqrt{\frac{2}{\mu_0 \sigma \omega}}$, where $\mu_0 = 4\pi \cdot 10^{-7}$ H/m is the magnetic constant and $\omega = 2\pi f$ is the frequency. However, the size of inclusion particles in this works is about 20 μm and negative role of the flow, which disturbs separation can be increased due to small particle relaxation time. Therefore, Kanno Y. Kanno and Yoshikawa [116] propose an intermittent

imposition of the separation magnetic field to enhance the effect. The particle movements in the fluid are also influenced by the presence of a solid boundary. Detailed analysis of particle behavior near the wall can be found in a recent work [87], which accounts for the particle translation and also rotation.

The calculations of particle trajectories and concentrations were performed using Lagrangian approach integrating equation (2.75) after fluid flow is known at each time step with several assumptions made:

- particle-particle interaction is negligible,
- all particles are rigid spheres,
- particles do not affect the structure and velocities of the flow.

The latest statement can be wrong for turbulence study because it is shown that particles introduce non-uniform distortion of turbulent energy spectra $E(k)$, which increases in small scales [55].

In other words one-way fluid-particle coupling was applied with a point-volume particle representation. The first of the above considerations is true if the next relation is valid ([53]):

$$\frac{N d_p^2}{LH\sqrt{(\gamma^2+1)}} \ll 1, \tag{5.1}$$

where N is the total number of the particles in the fluid volume $V = \pi R^2 H$, $\gamma = v_{term}/v'_{f,rms}$ is the ratio of the particle terminal velocity to the R.M.S. velocity of turbulent pulsations. The particle terminal velocity under the influence of buoyancy and drag force can be expressed as:

$$v_{term} = \sqrt{\frac{4 g d_p}{3 C_d} \frac{\rho_p - \rho}{\rho}}, \tag{5.2}$$

where C_d is the drag coefficient. For the Stokes flow the above equation simplifies to $v_{term} = \frac{g d_p^2}{18\nu} \frac{\rho_p - \rho}{\rho}$. Taking the extremal parameter values for $N \approx 3 \cdot 10^4$, $d_p = 10^{-3}$ m, $L = R = 0.158$ m and $H = 0.57$ m the left side ratio of expression (5.1) is below one.

The particle volume fraction $\varepsilon_p = NV_p/V = Nd_p^3/(6R^2H) \approx 3.5 \cdot 10^{-4}$, which is much less than 1, is another criteria for estimation of particle-particle interaction. The numerical and experimental results show, that particle spacing exceeding $5d_p$ have only secondary effects with respect to fluid dynamics forces and for negligible particle-particle interactions. Therefore, the next restrictive relation is applied $\varepsilon_p < 0.001$, which also is satisfied in this work.

The last made assumption also has a validity criteria ([53]), which is mean flow momentum-coupling parameter:

$$\Pi_{\mathrm{L}} = \varepsilon_p \frac{gL\left|\frac{\rho_p}{\rho}\right|}{U^2} \tag{5.3}$$

For our simulation and homogeneous particle distribution $\Pi_{\mathrm{L}} \approx 0.05 \ll 1$, hence, particle coupling on the mean flow is also be neglected.

The mentioned criteria possibly can not be accomplished in the zones of larger particle concentration. In this case the total number of particles and/or their diameter can be reduced.

The simulation of particle deposition in the induction crucible furnace is also simplified in respect to Saffman shear lift force (2.84), which intend to pull particles away from the boundary wall due to logarithmic velocity profile near the solid boundary, however, it is planned to introduce this force to the model in further calculations.

5.2 Numerical setup

Particle tracing was performed in the commercial CFD package FLUENT using ICF model (section 4.3). There are used two ways to introduce particles into the flow: single particle injection and surface injection. For the first case individual injection must be created for each particle. Therefore, particles can have different initial coordinates and velocities, injection time and physical properties (density and diameters). The injected particles can be marked with a little different density and can be distinguished at each time step, so particle trajectories can be easily reconstructed. The later method can be used to put large amount of

particles to the flow. All particles will have the same physical properties. Their initial positions are determined by the position of initial injection plane and numerical mesh because particles are placed into each grid element in the plane at zero time moment. This does not distinguish separate tracks, but produces results for transient particle distribution statistics.

Single injections were placed at a central axis point, which is close to the top free surface of the melt. Surface injections of 1 mm particles ($d_p = 1$ mm) were placed on two orthogonal meridian planes ($x = 0$ and $y = 0$ in Cartesian coordinates). All particles (table 5.1) were injected at $t = 0$ (i.e. at the start of transient simulation) and about 60 s of the flow were computed.

Table 5.1: Physical properties of the particles.

Parameter	Symbol	Units	Value
Diameter	d_p	mm	from 0.02 to 1.0
Density	ρ_p	kg/m^3	8545, 9400, 10340
Electrical conductivity	σ_p	1/(Ω·m)	0.0 or σ
Number of injected particles	N		1, $\approx 3 \cdot 10^4$
Stokes number	St		from $3 \cdot 10^{-5}$ to 0.09
Particle Reynolds number	Re_p		< 200

In most simulations the difference between the particle and fluid densities was 1.1 times. The Stokes number for all 1 mm large particles is close to 0.08 with small variations depending on density.

5.3 Modeling results for particles without EM interaction

5.3.1 Particle density is equal to the fluid's density

The absence of the EM interaction means that $\sigma_p = \sigma$. Buoyancy is also excluded if particle and fluid densities are equal. In this case particle motion is

determined mainly by the fluid drag and top and bottom directions are equivalent for the particles.

Initially injected particles form cross-like figure on the top view (figure 5.1(a)). Particles are distributed uniformly on the surfaces $y = 0$ and $x = 0$ in the central part of the melt. The initial particle distribution density is higher in the boundary region near the side crucible wall because mesh is finer there. A homogenization of particle concentration occurs (figures 5.1(b) and 5.1(c)) during the transition from $k - \varepsilon$ solution to fully developed transient LES flow and approximately after 10 seconds the initial angular distribution of the injected particles is fully eliminated, i.e. the angular particle concentration inside the melt is homogenized.

The initial flow structure computed by $k-\varepsilon$ model is very close to the averaged LES solution (figure 4.10(d)). There is no angular velocity component in a fully converged $k - \varepsilon$ solution. 3D transient simulation introduces angular turbulent oscillations of the flow velocity and the particle concentration equalizes over the angle. The percent numbers in the chart captions and on the right side of each chart represent a relative number of particles in the layer and a relative number of particles over the height respectively.

Changes in particle concentration can also be observed selecting thin boundary layer near the crucible wall and expanding this cylindrical layer over the angle (figure 5.2). Angular and height distributions of the particles are easily catched with this projection.

The initial particle distribution forms four vertical stripes in the chosen angle-height plane. This is illustrated on figure 5.2(a), which corresponds to $t = 2$ s and where these stripes are already disturbed a little by the angular flow perturbations. Flow perturbations start especially in the middle, but also in the top and in the bottom parts of the crucible, where the melt flow is forced to change its direction by the geometry. The middle zone of the near-wall boundary is also characterized by the presence of relatively large scale vortices ($5 \div 10$ cm), which are created by interaction of two near-wall jets coming from the opposite directions. The flow breaks here and changes its direction towards the center of the crucible and therefore this near wall region has much smaller average velocity magnitudes. Thus, these large scale vortices are collinear to the wall and can accumulate particles inside, forming particle clusters. As a result, a zone of a

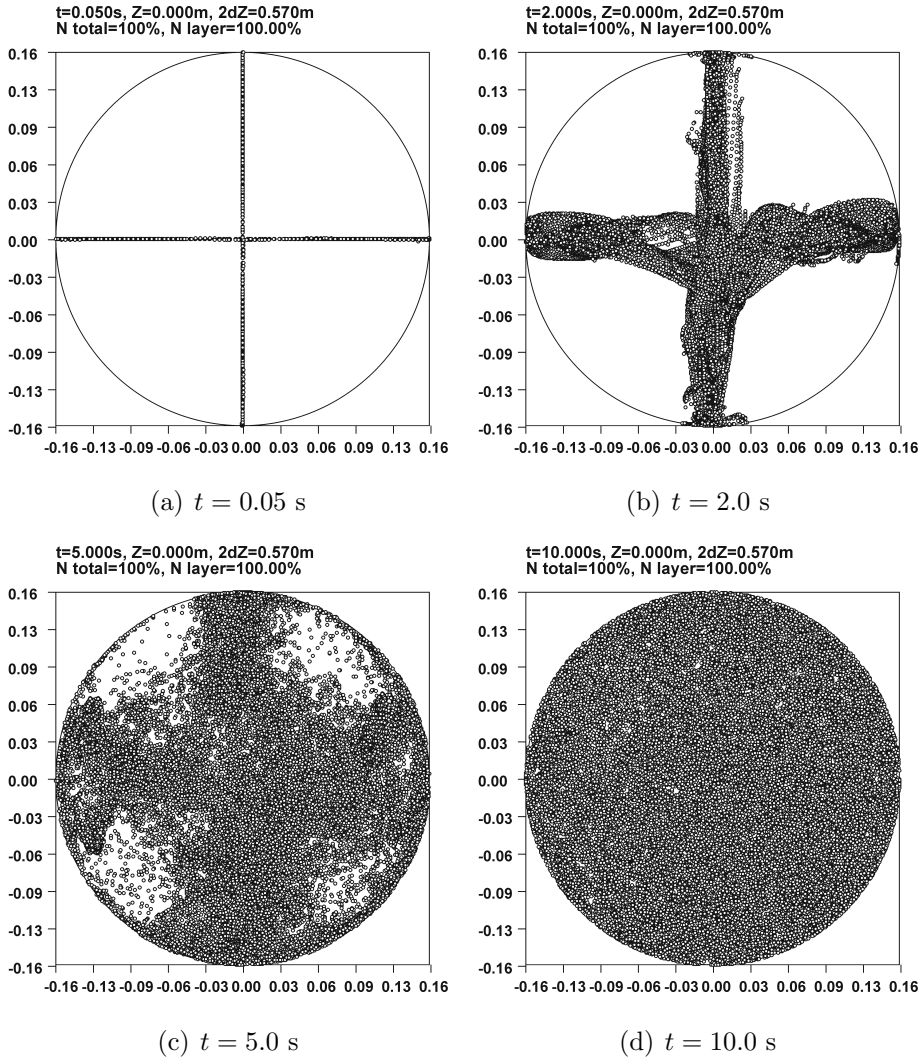

(a) $t = 0.05$ s (b) $t = 2.0$ s

(c) $t = 5.0$ s (d) $t = 10.0$ s

Figure 5.1: Particle positions in the flow at different time moments, $\rho_p = \rho = 9400$ kg/m^3. View from the top through the full crucible. Time is calculated from the particle injection. Particle tracking is performed starting from $k-\varepsilon$ solution.

slightly larger concentration can be located between the main vortices at a later time (figure 5.2(b)), while the particle distribution over the height and over the angle in other parts of the layer is more or less uniform. The presence of large scale vortices is also determined by free-slip boundary conditions which reduce shear stresses in the near-wall region.

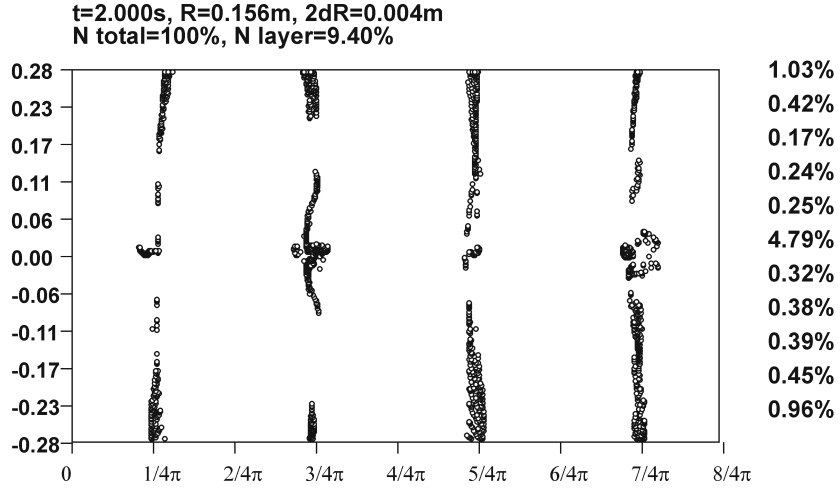

(a) $t = 2.0$ s

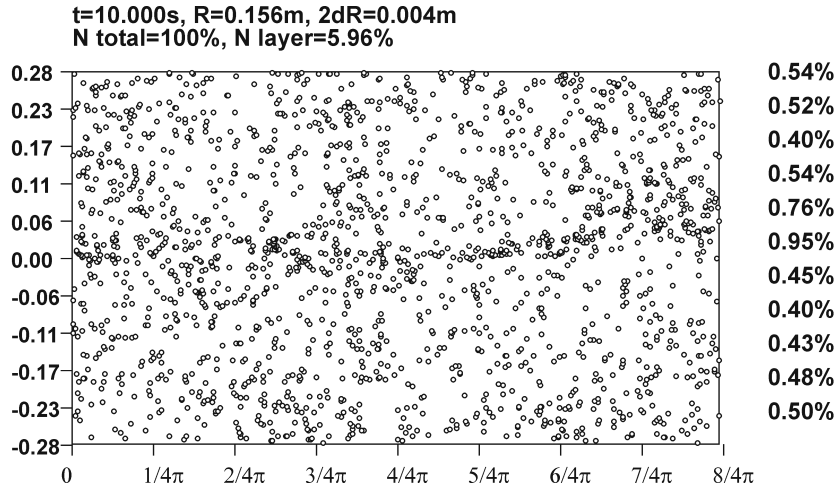

(b) $t = 10.0$ s

Figure 5.2: Angular particle distribution in 4 mm thick layer near the side crucible wall, $\rho_p = \rho = 9400$ kg/m^3. View from the outside of the crucible. Particle tracking is performed starting from $k - \varepsilon$ solution.

A particle volume fraction $\varepsilon_p = \dfrac{NV_p}{V}$ maps can be studied to get more quantitative data for analysis. These maps (figures 5.3 and 5.4) represent evolution of the local particle volume fraction in time over the radial distance and angle accordingly (data from the full crucible are taken into account in this case).

The volume fraction peaks at $t = 0$ represent initial particle distribution. These peaks disappear due to angular velocity oscillations, when the flow develops in time. For radial distance – time chart (figure 5.3) the largest peak is connected with the uncertainty $1/r$ at $r = 0$. Initially there is a smaller local fraction maximum near the crucible wall, where the mesh is refined. The particle distribution becomes almost uniform (except the layer near the side boundary) and quasi-stationary after approximately 10 s of the real time.

Angular particle distribution (figure 5.4) does not have a preferred direction for $\sigma_p = \sigma$ and $\rho_p = \rho$. The volume fraction peaks are visible again only during the transition. Homogenization of the particle distribution over the angle takes roughly the same 10 s.

This homogenization time of the flow is an important parameter for many industrial processes and its reduction sometimes is needed. The test with injection of the same configuration particles (injected particle count, initial positions and particle physical properties) was performed for fully developed turbulent flow. Simulation showed, that the particle concentration homogenization time is shorter by a factor of two (≈ 5 s) in the fully developed turbulent flow (figure 5.5) than in the transitional flow from $k - \varepsilon$ solution. Here the angular disturbance of the particles can be noticed almost at once after their injection. The homogenization time can be compared to the turnover period of the main flow eddy, which is about $6 \div 7$ s for 0.1 m/s average flow velocity. The minimal homogenization time is smaller, but several turnover periods are needed for perfect mixing of the particles.

5.3.2 Particle density is 1.1 times the fluid's density

Numerical setup of the model was the same as in the previous subsection, only the density of the particles was changed to $\rho_p = 1.1 \cdot \rho = 10340$ kg/m^3. Hence, in normal situation in steady fluid the particles should be drawn with the Stokes velocity $U_S \approx 13$ cm/s, which gives the drawing time to be about 4.4 s.

Higher particle density has changed distribution of the particles in the 4 mm near wall region, where the particles are concentrated now mainly in the middle and the bottom parts of the layer (figure 5.6). Particle accumulation in these

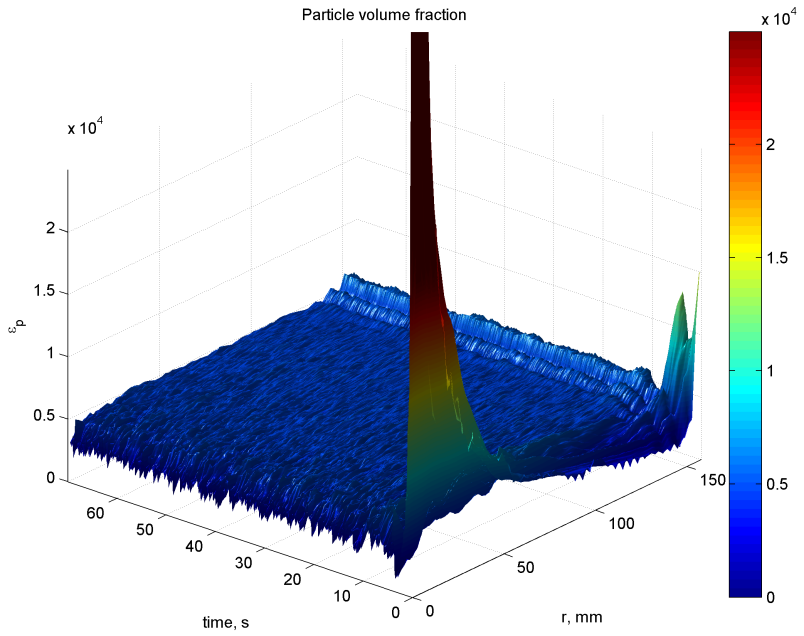

Figure 5.3: Surface map of particle volume fraction $\varepsilon_p = \varepsilon_p(r,t)$, $\rho_p = \rho = 9400$ kg/m^3. The maximal volume fraction value is limited for better readability.

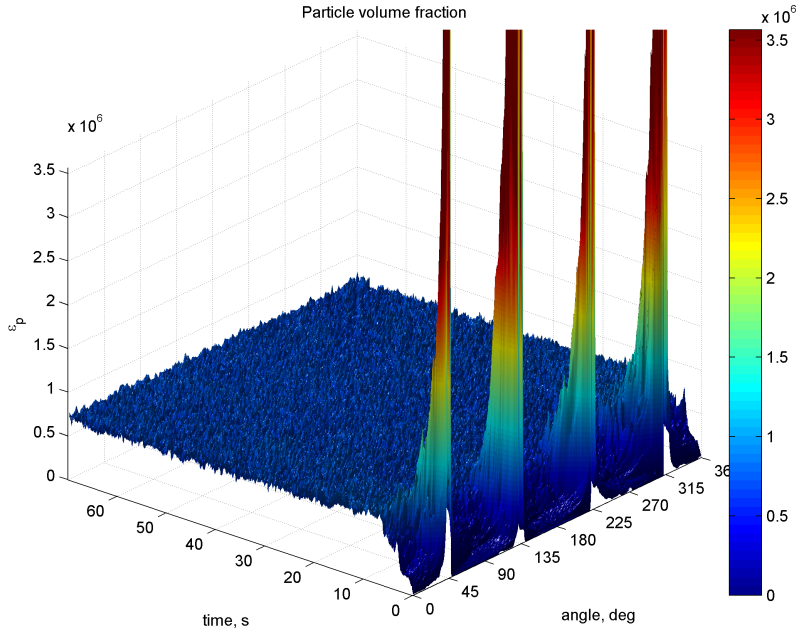

Figure 5.4: Surface map of particle volume fraction $\varepsilon_p = \varepsilon_p(angle,t)$, $\rho_p = \rho = 9400$ kg/m^3. The maximal volume fraction value is limited for better readability.

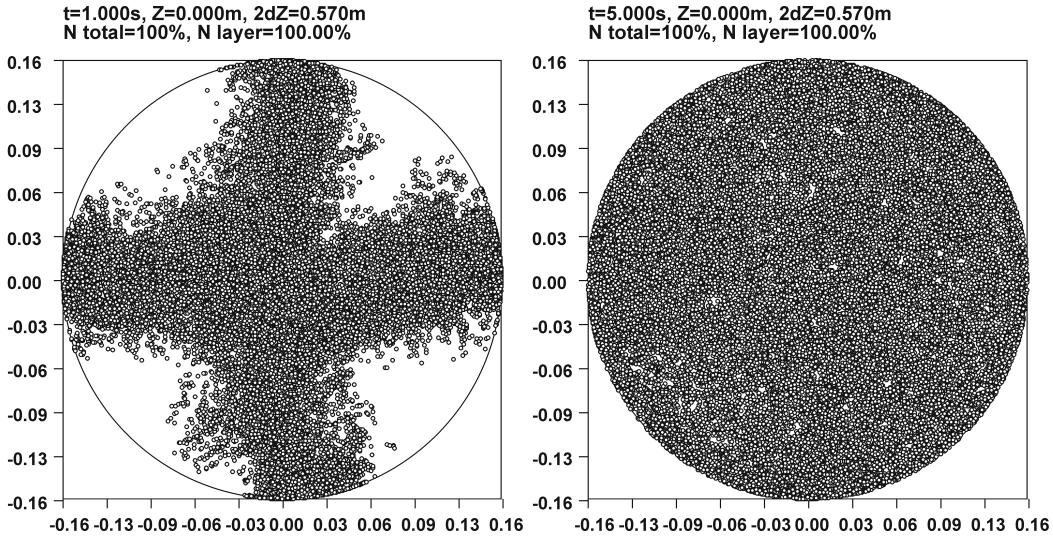

(a) $t = 1.0$ s (b) $t = 5.0$ s

Figure 5.5: Particle positions in the flow, when injection is performed into the developed turbulent flow, $\rho_p = \rho = 9400$ kg/m^3. View from the top.

parts of the crucible is also noticed in industrial ceramic crucibles, where oxide slag sediments are observed. Such particles distribution in the melt is developed during the first 10 s and almost does not vary over the time later. Particles in the bottom part near the wall move together with the melt upward and their trajectories are close to vertical lines. Particles in the middle are affected by the smaller vortices, which form round particle clusters, and can influence particle distribution over the angle. Such particle clustering can lead to more complicated mathematical models, which should include particle – particle interaction.

Disappearing of the particles from the top part of the near-wall region can be explained by the forces, which are acting on particles. If the particle density is higher then a particle has a tendency to drown, which corresponds to the downward flow on the symmetry axis in the bottom half of the crucible. The melt flow tries to drag the particle upward near the symmetry axis in the top part of the crucible. Therefore, if the particle is placed near the crucible middle than its probability to flow up is smaller than to drown down. If the particle is near the crucible top, it is directed to the side boundary by the flow and

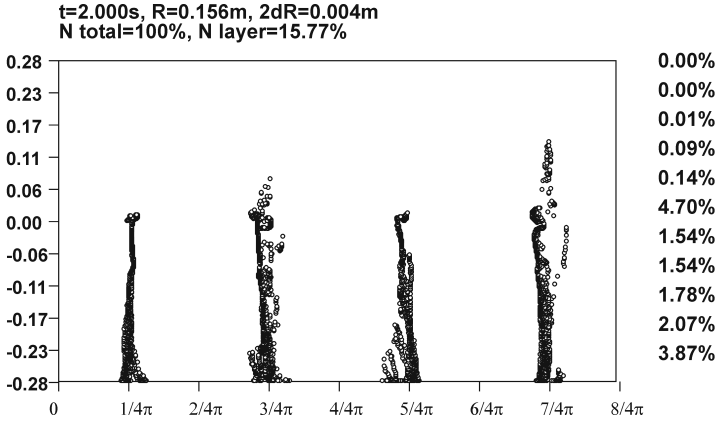

(a) $t = 2.0$ s, $r = 156 \pm 2$ mm

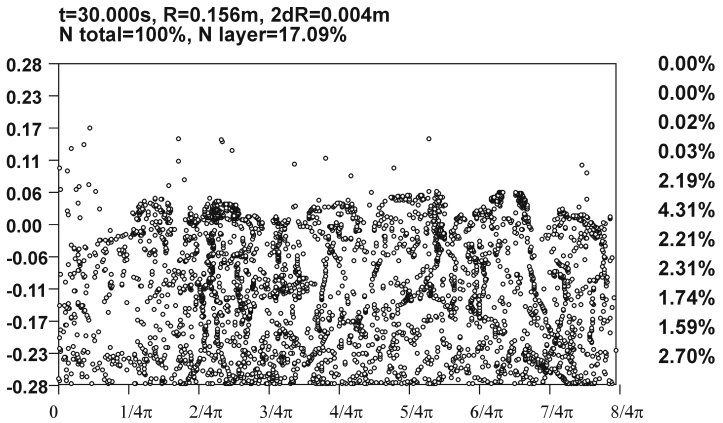

(b) $t = 30.0$ s, $r = 156 \pm 2$ mm

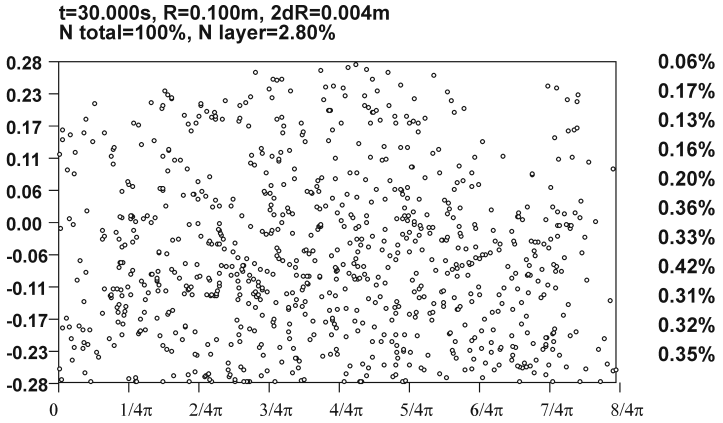

(c) $t = 30.0$ s, $r = 100 \pm 2$ mm

Figure 5.6: Angular particle distribution in 4 mm thick layer near the side crucible wall and inside the melt, $\rho_p = 1.1\rho = 10340$ kg/m^3. View from the outside of the crucible. Particle tracking is performed starting from $k - \varepsilon$ solution.

goes down at a first chance due to gravity and flow direction. In the bottom part particle goes up only when they are constrained by the geometry and large drag. This hypothesis possibly is confirmed by the particle distribution inside the melt (figure 5.6(c)), where the particles are placed much more uniformly over the height comparing to the near-wall region.

Homogenization of the angular particle concentration takes roughly the same time as it was for $\rho_p = \rho$.

Volume fraction charts are given later in a section 5.4.

5.3.3 Particle density is 1.1 times less then the fluid's density

Modeling results in this case are contrary to the results, which were discussed in the previous subsection. Particles are lighter and try to flow upward at the first possibility (figure 5.7). Their concentration in the side boundary layer is a little smaller comparing to the previous case at $t = 30$ s, but it is still growing. Particle distribution is more homogenous in the interior of the melt.

The top (melt surface) and the middle near-wall zones are prospective for the sediment accumulation, which is similar to the previous case, where $\rho_p > \rho$.

5.4 Summary on $\sigma = \sigma_p$ calculations

Presented results demonstrate several tendencies, which are characteristic to the studied particle laden flow. First of all the preferred particle concentration changes dramatically in the side boundary region depending on the particle density for equal sizes and conductivity $\sigma = \sigma_p$. Near-wall concentration of the particles is more expressed if $\rho_p \neq \rho$. Corresponding particle accumulation region for $\sigma = \sigma_p$ is smaller then the EM skin depth thickness $\delta = 18$ mm.

Particle behavior in the whole melt is also determined by its velocity (figure 5.8). If the particle density and fluid density are not equal, then the local Re_p can achieve values up to 200. Therefore, the drag term in the equation (2.75) becomes determinative for the particle motion.

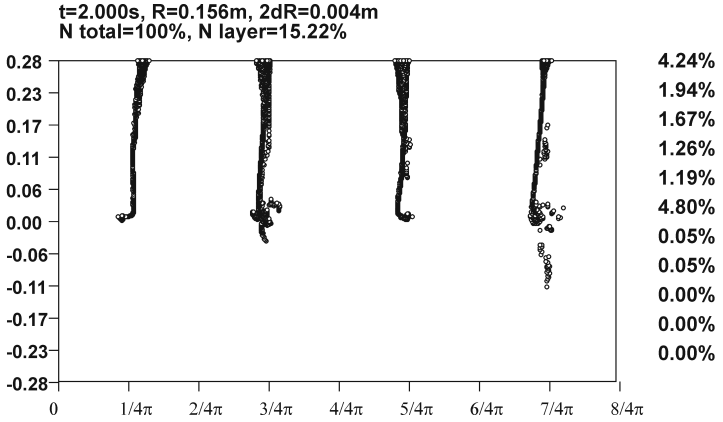

(a) $t = 2.0$ s, $r = 156 \pm 2$ mm

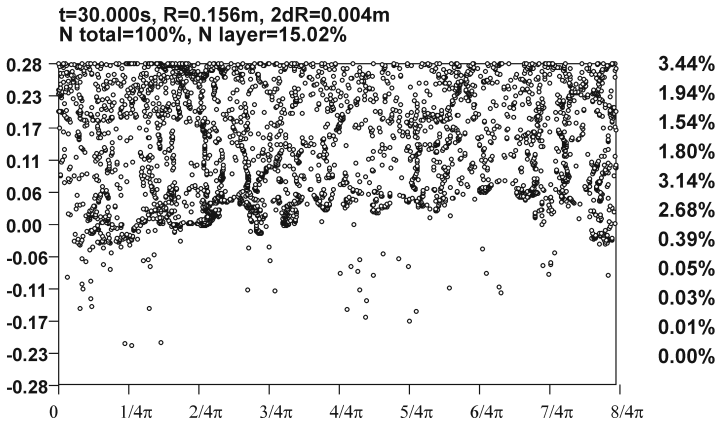

(b) $t = 30.0$ s, $r = 156 \pm 2$ mm

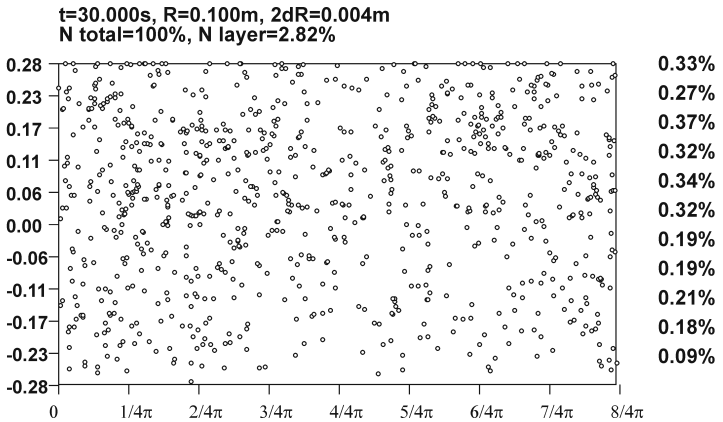

(c) $t = 30.0$ s, $r = 100 \pm 2$ mm

Figure 5.7: Angular particle distribution in 4 mm thick layer near the side crucible wall and inside the melt, $\rho_p = 0.9\rho = 8545$ kg/m^3. View from the outside of the crucible. Particle tracking is performed starting from $k - \varepsilon$ solution, free-shear boundary conditions.

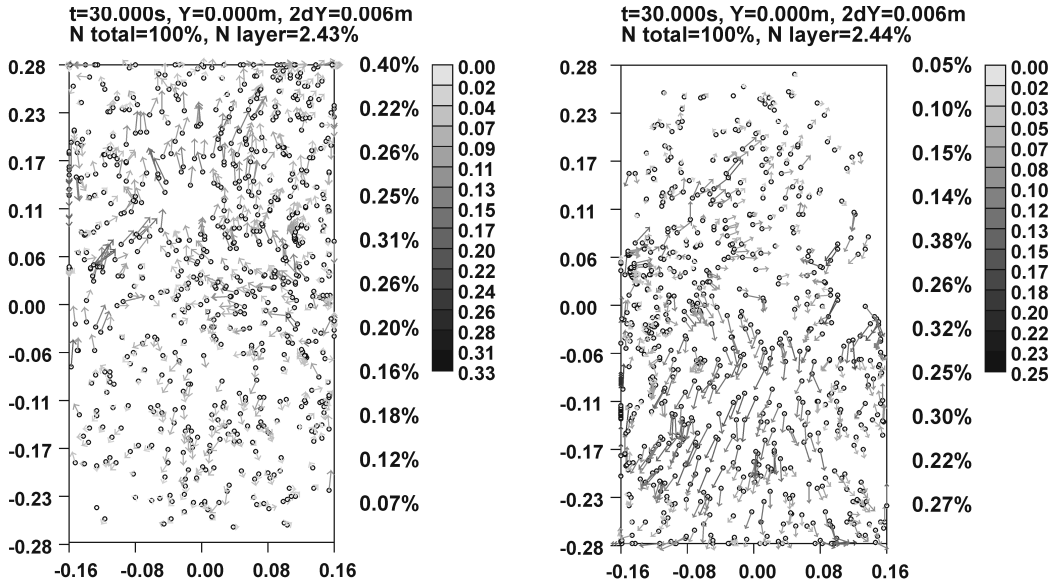

(a) $\rho_p = 8545$ kg/m^3 (b) $\rho_p = 10340$ kg/m^3

Figure 5.8: Particle velocity pattern (m/s) in 6 mm thin meridional layer for $\rho_p = 8545$ kg/m^3 and $\rho_p = 10340$ kg/m^3.

If $\rho_p < \rho$, then the velocities of the particles in downward flow can be several times smaller than in the upward flow (figure 5.8(a)) and large count of particles is placed on the top free surface, but the crucible bottom is free from the particles.

The velocity magnitude of the heavier particles in the central region is a little higher (figure 5.8(b)), because the downward flow direction and gravity direction are the same near the symmetry axis in the bottom part of the crucible.

Evolution of the particle volume fraction in time (figure 5.9) presents its fast homogenization ($t < 10$ s) in the interior of the melt, while the initial particle concentration near the crucible wall increases only if $\rho_p \neq \rho$. Initial peaks in the particle volume fraction are connected to the transfer of the large number of boundary particles to the middle part of the boundary region after the model release at $t = 0$. Later these peaks becomes less explicit and the volume fraction tends to its saturation. However, during the flow transition the particle concentration can have strong oscillations in the near-wall region (e.g. figure 5.9(e)),

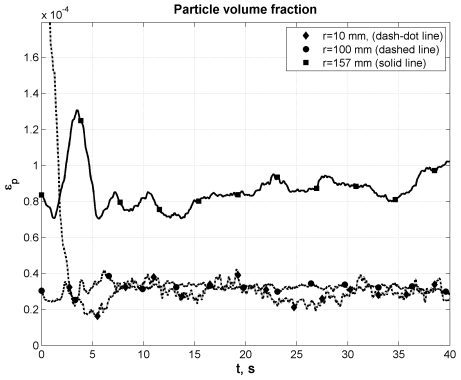

(a) $\rho_p = 0.9\rho = 8545$ kg/m^3, r is fixed

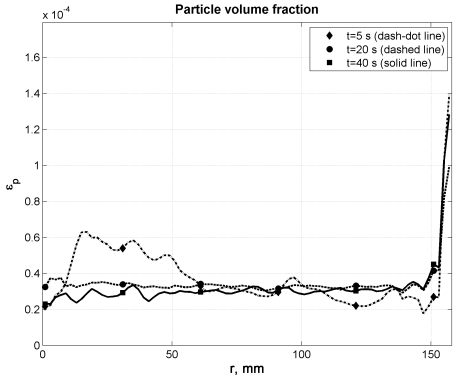

(b) $\rho_p = 0.9\rho = 8545$ kg/m^3, t is fixed

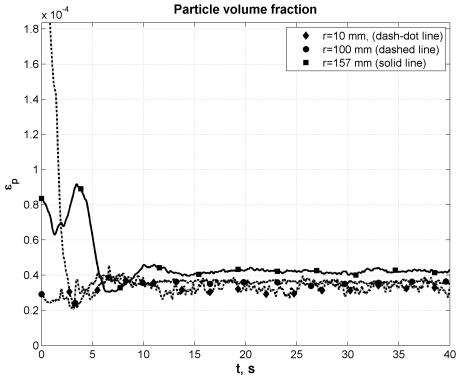

(c) $\rho_p = \rho = 9400$ kg/m^3, r is fixed

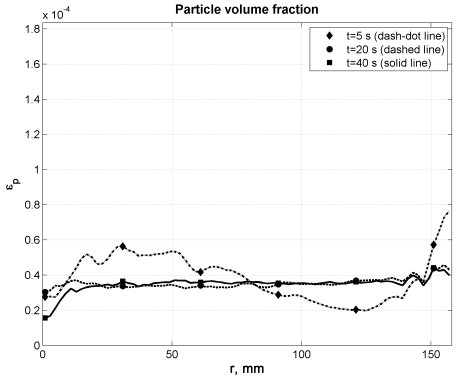

(d) $\rho_p = \rho = 9400$ kg/m^3, t is fixed

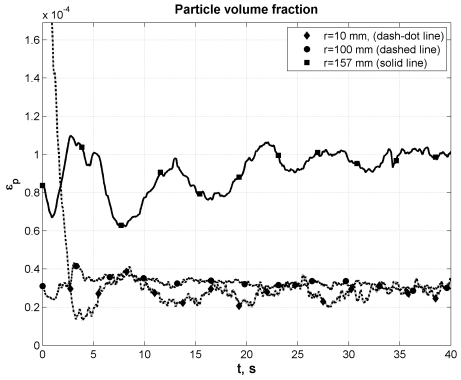

(e) $\rho_p = 1.1\rho = 10340$ kg/m^3, r is fixed

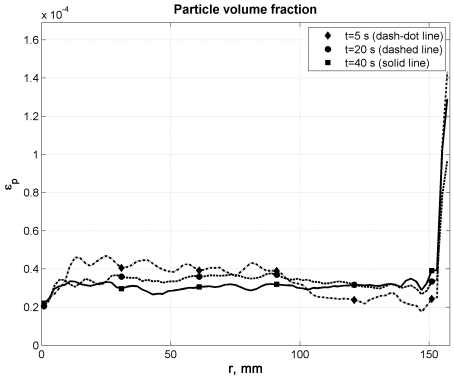

(f) $\rho_p = 1.1\rho = 10340$ kg/m^3, t is fixed

Figure 5.9: Particle volume fraction ε_p evolution in time at different radiuses (left) and at different time moments (right), $\sigma_p = \sigma$.

which period is comparable to the averaged eddy turn-over period.

5.4.1 Influence of the free-slip boundary condition

All above mentioned results are produced from the flow model with free-slip boundary condition on the side walls, which has small practical interest for the real world. Therefore, the question about the influence of the free-slip boundary conditions arises and the particles with $\rho_p = 0.9 \cdot \rho = 8545$ kg/m^3 were selected for the test study. The closest to the side wall element of the boundary region was additionally refined for more accurate resolution of the viscous sublayer.

The boundary conditions on the side wall of the crucible were only changed to no-slip in this simulation, while all other model parameters were left intact. Particle behavior at once after the injection (figure 5.10(a)) is very similar to free-slip cases. The stripes of the initial particle distribution are still seen as usual at $t = 2$ s and some angular deposition already is seen. The higher relative accumulation of the particles in the boundary layer at initial is caused by the larger number of elements in the boundary layer.

The particle distribution in the developed flow (figures 5.10(b) and 5.10(c)) introduces much higher accumulation of the particles in the near-wall region than it was for the free-slip boundary conditions. Almost half of the all particles is accumulated near the crucible boundary just after 30 s of the flow development. Particle clustering also occurs, but it is shifted to approximately 3/4 height of the melt and these clusters are not round, but more elongated in z direction, which is explained with the absence of angular velocity component near the wall. These elongated clusters are not longer than 1/4 of the melt height, and particles mostly are accumulated here. Middle part of the near-wall region is almost free from particles also like the bottom. From the other side there are still some particles inside the melt with relatively homogeneous distribution.

Formation of stripe particle clusters in the top part of the crucible can be explained by the fact, that with no-slip boundary condition the downward flow has smaller velocity near the wall and lighter particles tend to rise without angular velocity oscillations. The second possible reason is the model start from $k - \varepsilon$ solution where angular velocity is near zero and particles initially get acceleration

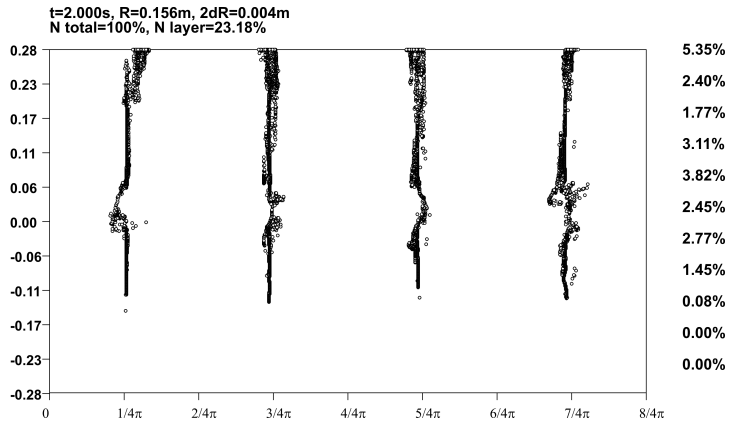

(a) $t = 2.0$ s, $r = 156 \pm 2$ mm

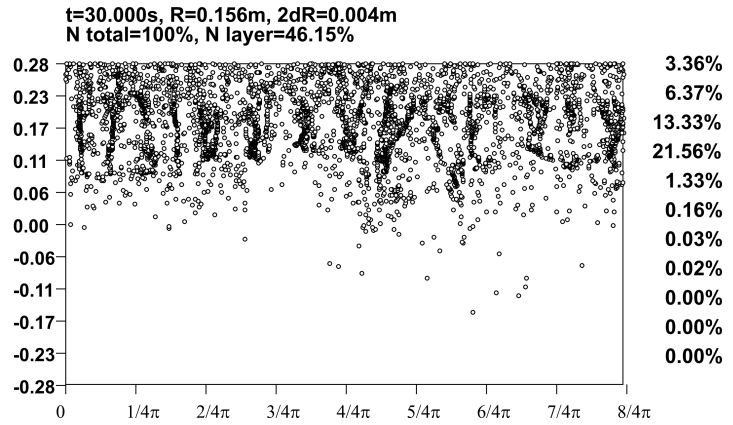

(b) $t = 30.0$ s, $r = 156 \pm 2$ mm

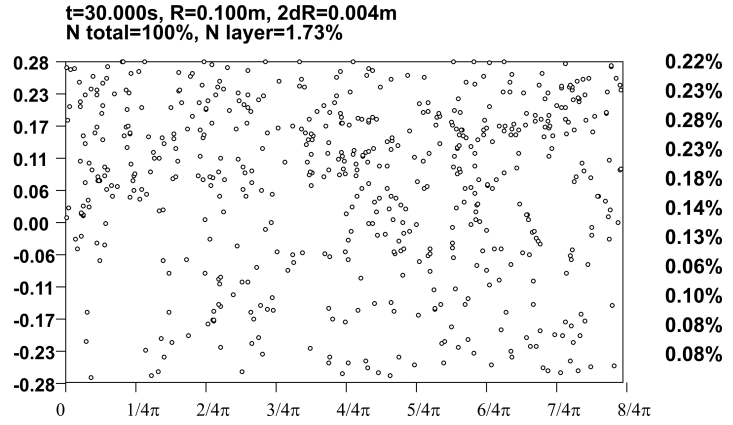

(c) $t = 30.0$ s, $r = 100 \pm 2$ mm

Figure 5.10: Angular particle distribution in 4 mm thick layer near the side crucible wall and inside the melt, $\rho_p = 0.9\rho = 8545$ kg/m^3. View from the outside of the crucible. Particle tracking is performed starting from $k - \varepsilon$ solution.

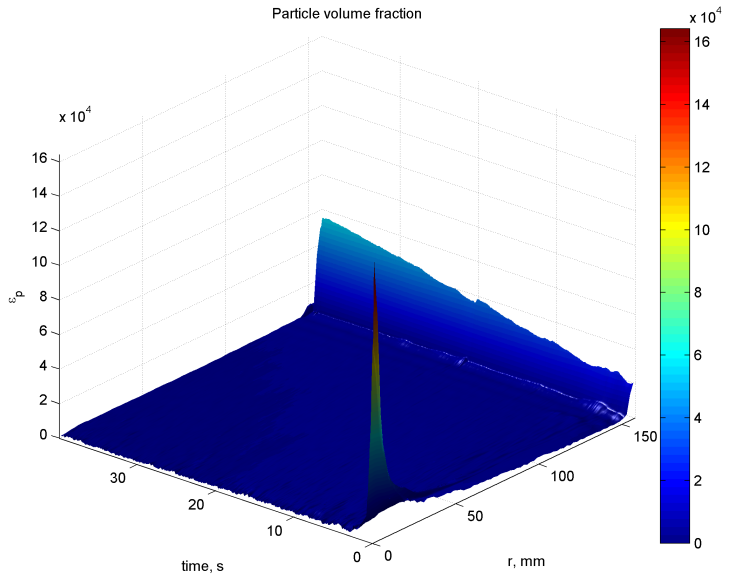

Figure 5.11: Surface map of particle volume fraction $\varepsilon_p = \varepsilon_p(r,t)$, $\rho_p = \rho = 8545$ kg/m^3 with no-slip boundary conditions. The maximal volume fraction value is limited for better readability.

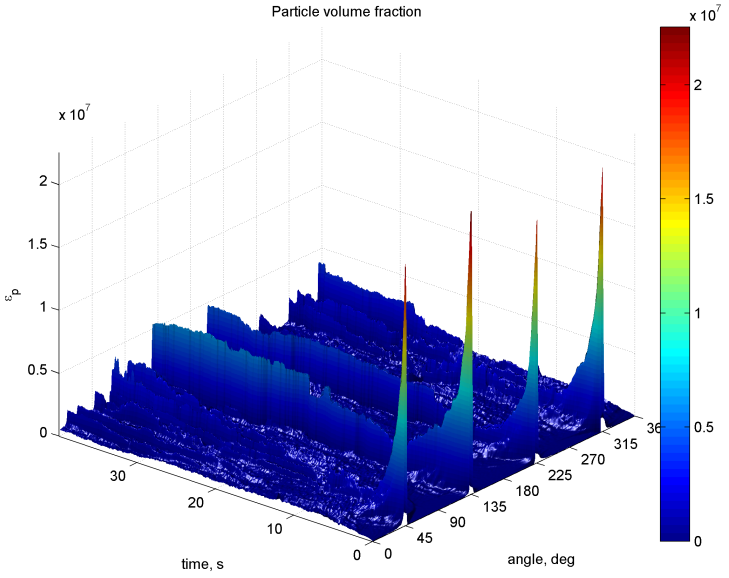

Figure 5.12: Surface map of particle volume fraction $\varepsilon_p = \varepsilon_p(angle,t)$, $\rho_p = \rho = 8545$ kg/m^3 with no-slip boundary conditions. The maximal volume fraction value is limited for better readability.

only from axial and radial flow velocity components. The particle concentration near the wall grows also because small velocity of the flow can not take particles away to the inner crucible region effectively.

The particle volume fraction charts clearly show these effects: a lot of particles are accumulated in the near wall region (figure 5.11) and their concentration there seems to be still growing. Vertically oriented particle clusters introduce angular inhomogeneity to the particle concentration distribution (figure 5.12) showing stripes with large number of particles which distribution only slightly changes in time.

5.4.2 Separate tracks

Nine particles with different densities ($\rho_p = 8545, 9400, 10340$ kg/m^3) and sizes ($d_p = 0.02, 0.2, 1$ mm) were injected to the Wood's metal at $t = 0$ at one point near the top surface. Corresponding Stokes numbers varies form $3 \cdot 10^{-5}$ to approximately 0.08 (table 5.2). The particle trajectories are strongly affected by $\mathbf{g}$ and the fluid drag.

For small particle size ($d_p = 0.02$ mm (figure 5.13) and respectively small Stokes numbers density role is neglected. Both "light" and "heavy" particles are freely moving between the top and bottom crucible parts and are staying near the boundary wall for a very short time.

If d_p becomes larger, then density role increases (figure 5.14) and several interesting effects can be noticed. If $\rho_p \neq \rho$ then the particle can be entrapped in the top half of the crucible (figure 5.14(a)) or in the near-wall region for a considerable time (figure 5.14(c)). This is noticed mainly for particles with large sizes $d_p = 1$ mm and is repeated in several computational runs. Near-wall entrapping can be explained by the particle catching by sufficiently large vortices ($l \sim 10$ cm), which are formed at the middle height of the melt when the opposite flows collapse. These vortices can stay alive up to $5 \div 10$ seconds and the author think them to be between reasons of the experimentally noticed low-frequency velocity oscillations.

The distance, which is passed during 60 s by the separate particles is 5.0 ± 0.5 m, which corresponds to 8.3 cm/s average particle velocity. This distance

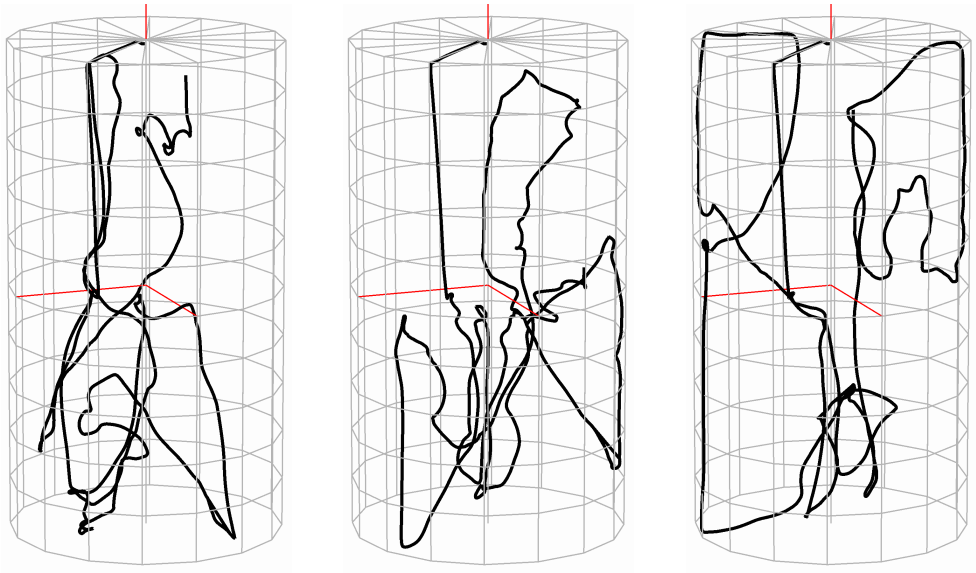

(a) $\rho_p = 0.9\rho = 8545$ kg/m^3, $d_p = 0.02$ mm

(b) $\rho_p = \rho = 9400$ kg/m^3, $d_p = 0.02$ mm

(c) $\rho_p = 1.1\rho = 10340$ kg/m^3, $d_p = 0.02$ mm

Figure 5.13: $d_p = 0.02$ mm particle tracks, which are injected from the top at t=0 after $k - \varepsilon$ solution. Track length corresponds to 60 s.

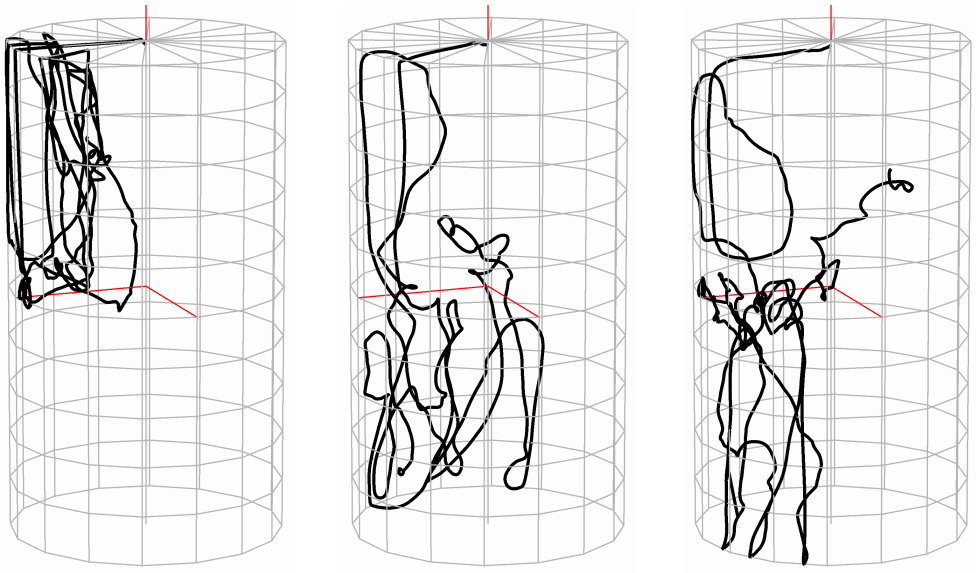

(a) $\rho_p = 0.9\rho = 8545$ kg/m^3, $d_p = 1$ mm

(b) $\rho_p = \rho = 9400$ kg/m^3, $d_p = 1$ mm

(c) $\rho_p = 1.1\rho = 10340$ kg/m^3, $d_p = 1$ mm

Figure 5.14: $d_p = 1$ mm particle tracks, which are injected from the top at t=0 after $k - \varepsilon$ solution. Track length corresponds to 60 s.

Table 5.2: Separate particle track parameters after 60 s of the flow.

Nr.	Density, kg/m^3	Diameter, mm	St	Track length, m	Average velocity, cm/s	Points in bottom
1	8545	0.02	$2.9 \cdot 10^{-5}$	4.58	7.6	72.1%
2	9400		$3.1 \cdot 10^{-5}$	4.94	8.2	76.5%
3	10340		$3.5 \cdot 10^{-5}$	5.20	8.7	57.6%
4	8545	0.20	$2.9 \cdot 10^{-3}$	5.22	8.7	49.5%
5	9400		$3.1 \cdot 10^{-3}$	4.82	8.0	66.1%
6	10340		$3.5 \cdot 10^{-3}$	5.31	8.9	93.2%
7	8545	1.00	$7.2 \cdot 10^{-2}$	4.89	8.2	25.8%
8	9400		$7.9 \cdot 10^{-2}$	5.00	8.3	83.0%
9	10340		$8.7 \cdot 10^{-2}$	4.91	8.2	73.4%

depends on the particle path in the fluid, which is theoretically defined by the Stokes number. However the presented results do not show such clear dependence (table 5.2) without the influence of EM forces on the particles. Comparing averaged particle velocities (table 5.2) one can say, that the entrapped large particles have the lowest average velocity, which can be 30% less than average velocity of the flow.

The time of particle separation after the injection depends on the particle size. "Heavy" 1 mm particle tries to go down after the injection and notices the opposite flow drag after some distance from the injection point, i.e. closer to the crucible bottom. The distance, when particles of equal sizes are separated depends again on the Stokes number. For small St particles can go together for a relatively long time (for 0.02 mm particles this time is larger than 5 s). For larger St all the particles are separated immediately.

These results should be taken into account very carefully, because they represent the behavior of separate particles and does not have statistical certainty.

5.5 Modeling results for particles with EM interaction

5.5.1 Particle density is less than the fluid's density (free-slip boundary conditions on the side crucible walls)

EM field influence on the preferential particle concentration should be expressed as additional particle accumulation in the boundary region, which thickness is comparable to appropriate skin-depth (3.3). A special function was implemented in FLUENT to take into account EM influence (2.82) for particles. These models were implemented only for particle clouds where $\rho_p = 8545$ kg/m^3 $< \rho$. The first studied case for particles, which electrical conductivity is zero ($\sigma_p = 0$), also had free-slip boundary conditions on the side crucible wall. All model parameters and model initial conditions were exactly like in simulations without EM influence on the particles. Only the closest to the wall layer of the computational grid was adapted by FLUENT for better resolution of logarithmic velocity profile near the wall.

Free-slip boundary conditions mean that vortices of considerable scale can be created in the middle of near wall region and as it was shown previously the large particles can be entrapped there forming particle clusters (in this way the influence of buoyancy is decreased). The presence of EM field increases particle concentration near the wall dramatically for large particles (figure 5.15). The particle concentration in the thin near-wall region is growing all the time and it is already about 70% after 5 s of the flow development. Particles just do not go inside the melt together with the flow in the middle. They are staying approximately in the half height of the melt forming almost straight large concentration line, but this straight line breaks and goes a little up after several more seconds. Particle concentration becomes greater than 90% after 30 s of the flow and it is difficult to say that it will not increase in the future. There are more particles going to the middle from the top part of the crucible than from the bottom. Entrapped particles are moving but with very low velocities.

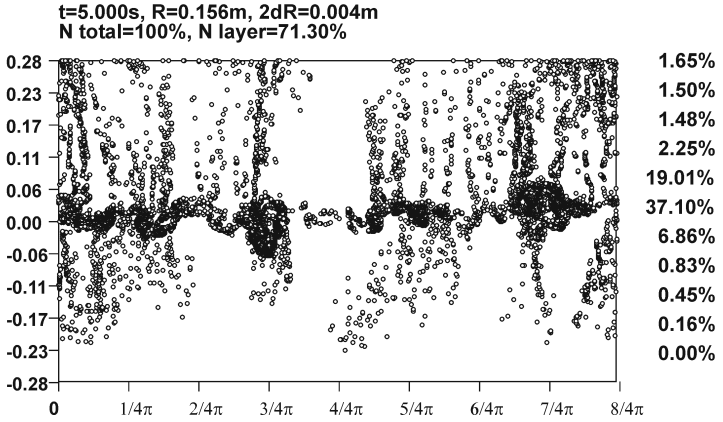

(a) $t = 5.0$ s, $r = 156 \pm 2$ mm

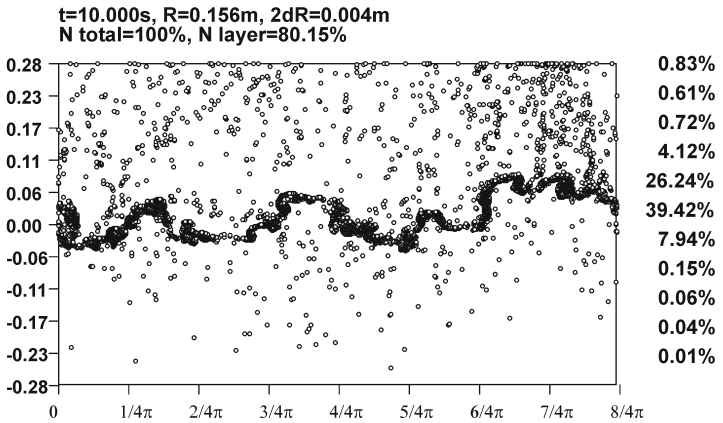

(b) $t = 10.0$ s, $r = 156 \pm 2$ mm

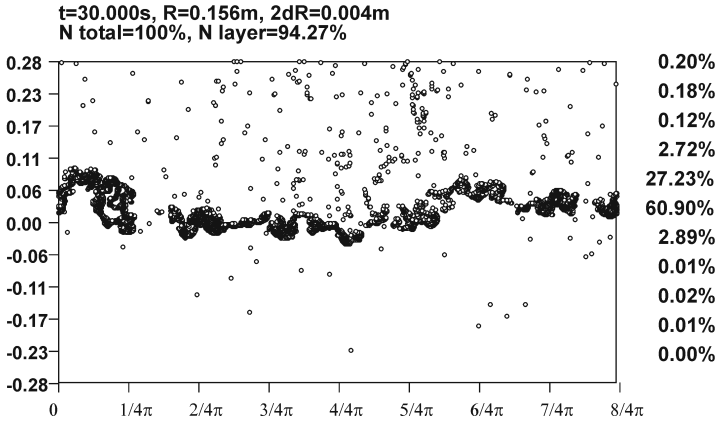

(c) $t = 30.0$ s, $r = 156 \pm 2$ mm

Figure 5.15: Angular particle distribution with EM interaction in 4 mm thick layer near the side crucible wall with free-shear boundary conditions, $\rho_p = 0.9\rho = 8545$ kg/m^3. View from the outside of the crucible. Particle tracking is performed starting from $k - \varepsilon$ solution.

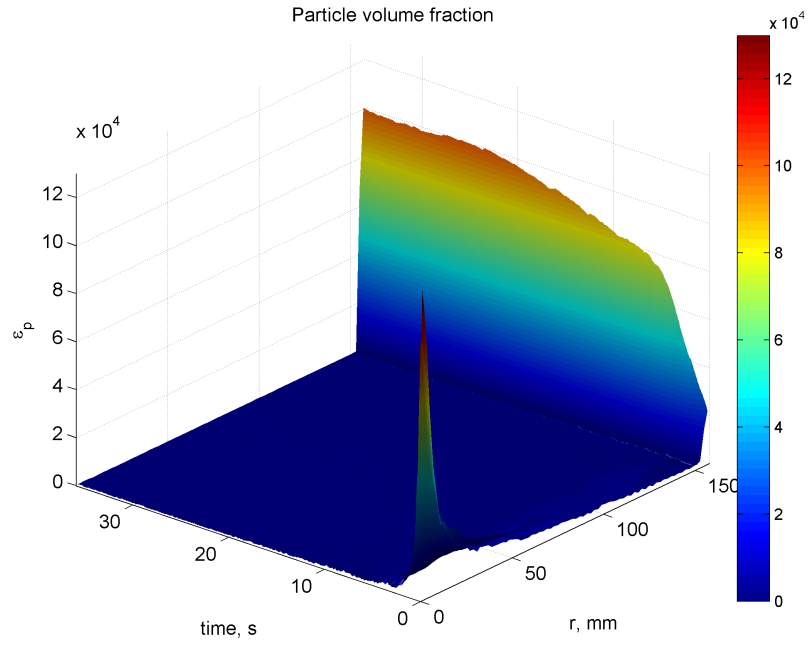

Figure 5.16: Surface map of particle volume fraction $\varepsilon_p = \varepsilon_p(r,t)$, $\rho_p = \rho = 8545$ kg/m^3.

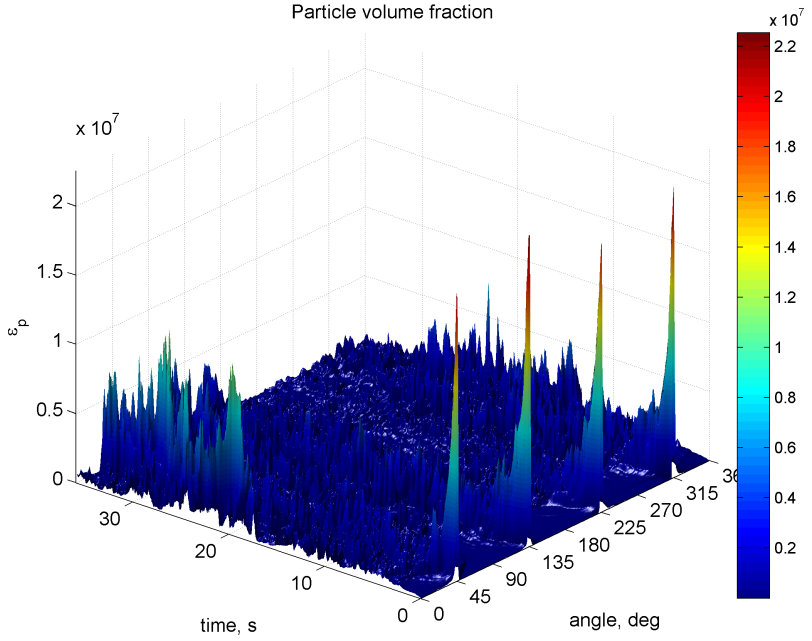

Figure 5.17: Surface map of particle volume fraction $\varepsilon_p = \varepsilon_p(angle,t)$, $\rho_p = \rho = 8545$ kg/m^3.

Surface charts of particle concentration introduce very homogeneous particle distribution inside the melt, which is very small (figure 5.16). From the other side, particle distribution near the crucible wall starts to grow immediately after particle release and reaches some constant value after 25 s. Three regions can be detected on this figure:

1. Fast particle volume fraction growing region, $\frac{\partial \varepsilon_p}{\partial t} \approx 5000\ \mathrm{s}^{-1}$. The particles initially have zero velocities and if they feel EM field, then they are attracted to the wall. Initially there are more particle placed closer to the wall due to problem setup. Fluid motion also brings particle to the near-wall region from the top and bottom parts of the crucible, clustering starts;

2. Moderate particle volume fraction growing region, $\frac{\partial \varepsilon_p}{\partial t} \approx 1300\ \mathrm{s}^{-1}$. The particles, which were deeper inside the melt are catched by the EM force in the near-wall region;

3. Constant particle volume fraction, $\frac{\partial \varepsilon_p}{\partial t} \approx 0$. Only separate particle are moving inside the melt, while all other particles are concentrated in the near-wall region. The melt has relatively high velocities near the wall because is not influenced by the boundary shear and sometimes can take away single particles.

The distribution of the particle volume fraction over the angle is not homogeneous (figure 5.17). Particle angular distribution is disturbed, but initial particle volume fraction structures and zones with higher particle concentration can be noticed. Almost all particles are in the side wall boundary region and therefore the peaks in angular distribution of the volume fraction are caused mainly by the wall collinear vortices with entrapped particles.

5.5.2 Particle density is less than the fluid's density (no-slip boundary conditions on the side crucible walls)

Here only boundary conditions were changed to no-slip comparing with the former problem setup. Particle conductivity was set to zero again.

Initially particles distribution over the height is homogeneous, but the particle count near the top surface becomes larger after several seconds from simulation start (figure 5.18(a)). Angular homogenization of the particle concentration also starts, but with less intensity comparing to the previous results for free-slip side boundary conditions. Angular concentration changes depending on the particle position, i.e. there are height regions where particles distribution is presented by clear vertical stripes, but also there are regions where particle angular distribution is more spread. The formation of the characteristic wall-collinear vortices in the middle zone is decreased and particle clustering here is minimal. There are no particles near the wall at the bottom of the melt.

Angular concentration becomes more equalized at the free surface and bottom half of the crucible, while here are vertical clusters of particles at the top half after 10 s of the flow (figure 5.18(b)). The zone of the highest particle concentration is shifted approximately to 75% height of the melt filling level and particle accumulation here runs very intensively because almost 90% of all particles are already in the layer. Particle accumulation continue to grow up and is very close to 100% after 30 s (figure 5.18(c)). Here almost all particles are concentrated in thin about 100 mm high near-wall region forming mainly vertically oriented clusters and keeping angular anisotropy of the particle volume fraction.

The dependence of the particle volume fraction on the radial coordinate and time $\varepsilon_p = \varepsilon_p(r, t)$ (figure 5.19) is very similar to the case with free-slip boundary conditions and the same zones with approximately the same particle accumulation rates can be found. Here only the borders between zones are more rounded. Angular dependence (figure 5.20) introduces large anisotropy to the particle volume fraction distribution and several preferential angles of particle concentration can be noticed. Initial angular concentration peaks are decreased anywhere as usual after simulation starts, but particle volume fraction grows faster for one angular direction approximately after $t = 20$ s of the flow development. It is seen, that particles can change their angular position, but the reason why they go to the other selected angle keeping the zones of significantly higher angular concentration is not clear. Possibly separate particles can be affected and arrested by the vertically shaped particle clusters. Particles can be accumulated in the near-wall region by the EM forces, but their concentration is not homogeneous

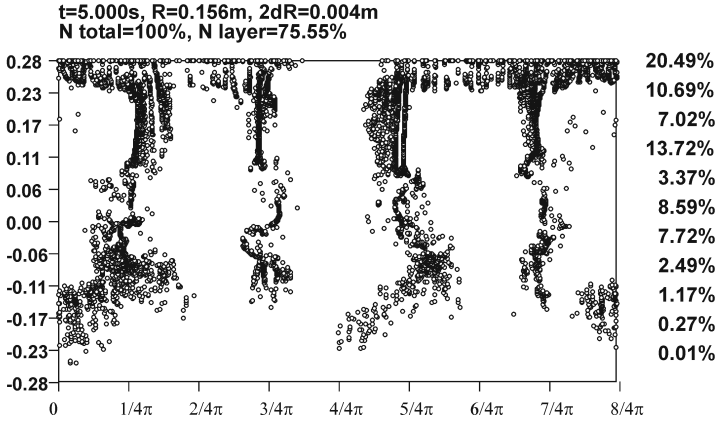

(a) $t = 5.0$ s, $r = 156 \pm 2$ mm

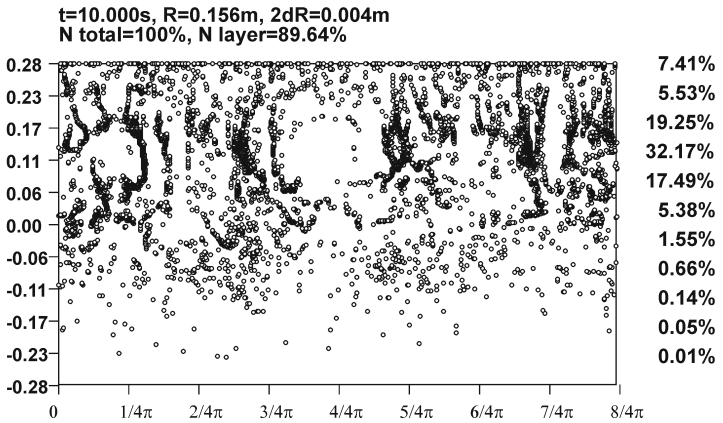

(b) $t = 10.0$ s, $r = 156 \pm 2$ mm

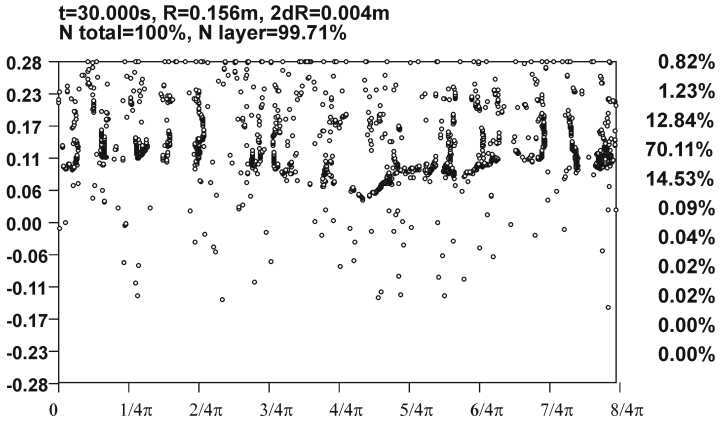

(c) $t = 30.0$ s, $r = 156 \pm 2$ mm

Figure 5.18: Angular particle distribution with EM interaction in 4 mm thick layer near the side crucible wall with no-slip boundary conditions, $\rho_p = 0.9\rho = 8545$ kg/m^3. View from the outside of the crucible. Particle tracking is performed starting from $k - \varepsilon$ solution.

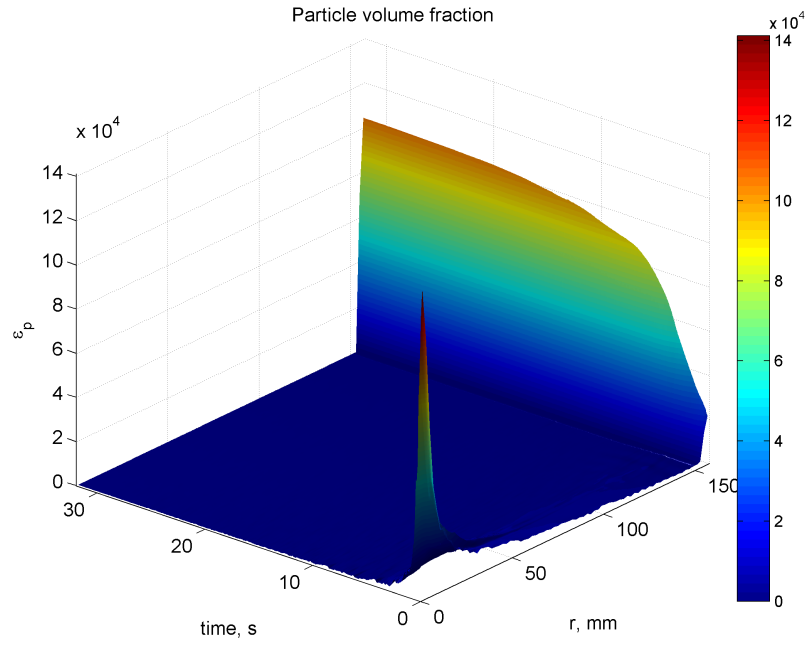

Figure 5.19: Surface map of particle volume fraction $\varepsilon_p = \varepsilon_p(r,t)$, $\rho_p = 0.9\rho = 8545$ kg/m^3.

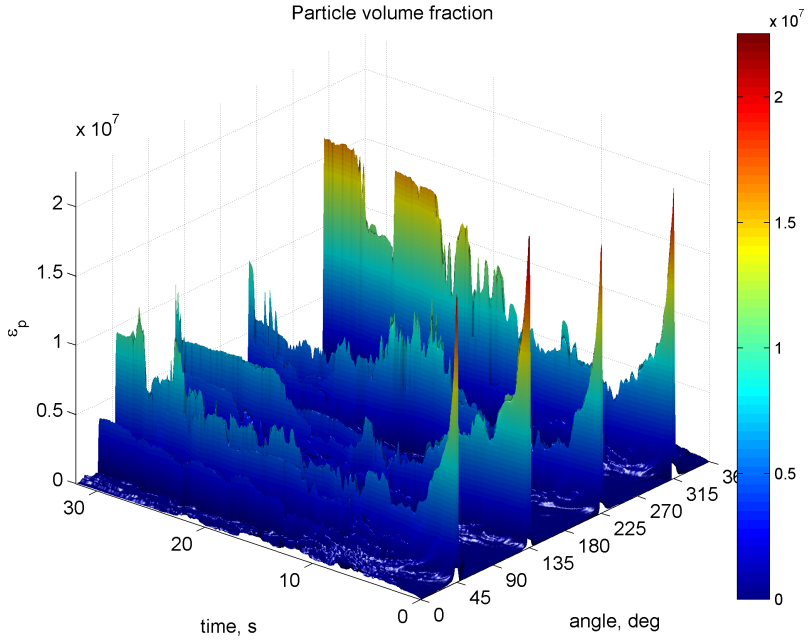

Figure 5.20: Surface map of particle volume fraction $\varepsilon_p = \varepsilon_p(angle,t)$, $\rho_p = 0.9\rho = 8545$ kg/m^3.

over the height and over the angle in this case. Such situation in a real life should be very seldom because the particles have a finite dimensions and therefore they will have more spread distribution in the near wall region both in angle and radial distance.

5.5.3 Separate tracks with EM field interaction

Lagrangian particle tracing of several sets of the inertial particles of different masses was performed under the influence of EM field for different boundary conditions and σ_p/σ ratios (table 5.3) like in the previous calculations. Three sizes and three characteristic densities were selected for separate particles as usual, which gave nine possible trajectory variations for each simulation. Forty seconds of the flow were computed starting from $k-\varepsilon$ solution.

Table 5.3: Parameters of the particle trajectories (total flow time is 40 s).

Model setup	Density, kg/m^3	d_p, m	V_p, m^3	St	N_{bot}, %	Track len., m	Average vel., m/s
	8545	$1{\cdot}10^{-3}$	$5.24{\cdot}10^{-10}$	$7.15{\cdot}10^{-2}$	35.6	3.18	0.079
	8545	$2{\cdot}10^{-4}$	$4.19{\cdot}10^{-12}$	$2.86{\cdot}10^{-3}$	0.0	2.62	0.066
	8545	$2{\cdot}10^{-5}$	$4.19{\cdot}10^{-15}$	$2.86{\cdot}10^{-5}$	68.4	3.35	0.084
free-slip	9400	$1{\cdot}10^{-3}$	$5.24{\cdot}10^{-10}$	$7.87{\cdot}10^{-2}$	50.4	3.88	0.097
$\sigma_p = 0$	9400	$2{\cdot}10^{-4}$	$4.19{\cdot}10^{-12}$	$3.15{\cdot}10^{-3}$	6.5	2.98	0.075
	9400	$2{\cdot}10^{-5}$	$4.19{\cdot}10^{-15}$	$3.15{\cdot}10^{-5}$	78.9	2.67	0.067
	10340	$1{\cdot}10^{-3}$	$5.24{\cdot}10^{-10}$	$8.66{\cdot}10^{-2}$	26.3	2.91	0.073
	10340	$2{\cdot}10^{-4}$	$4.19{\cdot}10^{-12}$	$3.46{\cdot}10^{-3}$	59.3	3.36	0.084
	10340	$2{\cdot}10^{-5}$	$4.19{\cdot}10^{-15}$	$3.46{\cdot}10^{-5}$	70.4	3.02	0.075
	8545	$1{\cdot}10^{-3}$	$5.24{\cdot}10^{-10}$	$7.15{\cdot}10^{-2}$	0	0.91	0.023
	8545	$2{\cdot}10^{-4}$	$4.19{\cdot}10^{-12}$	$2.86{\cdot}10^{-3}$	0	0.63	0.016
	8545	$2{\cdot}10^{-5}$	$4.19{\cdot}10^{-15}$	$2.86{\cdot}10^{-5}$	44,3	3.00	0.075
no-slip	9400	$1{\cdot}10^{-3}$	$5.24{\cdot}10^{-10}$	$7.87{\cdot}10^{-2}$	15.9	0.95	0.024
$\sigma_p = 0$	9400	$2{\cdot}10^{-4}$	$4.19{\cdot}10^{-12}$	$3.15{\cdot}10^{-3}$	4.7	0.64	0.016
	9400	$2{\cdot}10^{-5}$	$4.19{\cdot}10^{-15}$	$3.15{\cdot}10^{-5}$	76.7	2.93	0.073
	10340	$1{\cdot}10^{-3}$	$5.24{\cdot}10^{-10}$	$8.66{\cdot}10^{-2}$	63.2	1.15	0.029
	10340	$2{\cdot}10^{-4}$	$4.19{\cdot}10^{-12}$	$3.46{\cdot}10^{-3}$	64.4	2.45	0.061

Continued on next page...

Model setup	Density, kg/m^3	d_p, m	V_p, m^3	St	N_{bot}, %	Track len., m	Average vel., m/s
	10340	$2{\cdot}10^{-5}$	$4.19{\cdot}10^{-15}$	$3.46{\cdot}10^{-5}$	51	3.01	0.075
	8545	$1{\cdot}10^{-3}$	$5.24{\cdot}10^{-10}$	$7.15{\cdot}10^{-2}$	18.0	3.45	0.086
	8545	$2{\cdot}10^{-4}$	$4.19{\cdot}10^{-12}$	$2.86{\cdot}10^{-3}$	38.1	3.05	0.076
	8545	$2{\cdot}10^{-5}$	$4.19{\cdot}10^{-15}$	$2.86{\cdot}10^{-5}$	29.2	3.10	0.078
no-slip	9400	$1{\cdot}10^{-3}$	$5.24{\cdot}10^{-10}$	$7.87{\cdot}10^{-2}$	51.8	3.01	0.075
$\sigma_p = \sigma$	9400	$2{\cdot}10^{-4}$	$4.19{\cdot}10^{-12}$	$3.15{\cdot}10^{-3}$	52.2	0.91	0.023
	9400	$2{\cdot}10^{-5}$	$4.19{\cdot}10^{-15}$	$3.15{\cdot}10^{-5}$	82.9	2.27	0.057
	10340	$1{\cdot}10^{-3}$	$5.24{\cdot}10^{-10}$	$8.66{\cdot}10^{-2}$	50.3	1.20	0.030
	10340	$2{\cdot}10^{-4}$	$4.19{\cdot}10^{-12}$	$3.46{\cdot}10^{-3}$	59.4	2.65	0.066
	10340	$2{\cdot}10^{-5}$	$4.19{\cdot}10^{-15}$	$3.46{\cdot}10^{-5}$	18.8	2.00	0.050
	8545	$1{\cdot}10^{-3}$	$5.24{\cdot}10^{-10}$	$7.15{\cdot}10^{-2}$	0	0.92	0.023
	8545	$2{\cdot}10^{-4}$	$4.19{\cdot}10^{-12}$	$2.86{\cdot}10^{-3}$	60.0	1.88	0.047
	8545	$2{\cdot}10^{-5}$	$4.19{\cdot}10^{-15}$	$2.86{\cdot}10^{-5}$	77.3	4.15	0.104
no-slip	9400	$1{\cdot}10^{-3}$	$5.24{\cdot}10^{-10}$	$7.87{\cdot}10^{-2}$	20.4	0.97	0.024
$\sigma_p = 0.5\sigma$	9400	$2{\cdot}10^{-4}$	$4.19{\cdot}10^{-12}$	$3.15{\cdot}10^{-3}$	5.9	0.67	0.017
	9400	$2{\cdot}10^{-5}$	$4.19{\cdot}10^{-15}$	$3.15{\cdot}10^{-5}$	48.1	3.22	0.081
	10340	$1{\cdot}10^{-3}$	$5.24{\cdot}10^{-10}$	$8.66{\cdot}10^{-2}$	55.6	1.39	0.035
	10340	$2{\cdot}10^{-4}$	$4.19{\cdot}10^{-12}$	$3.46{\cdot}10^{-3}$	32.3	0.71	0.018
	10340	$2{\cdot}10^{-5}$	$4.19{\cdot}10^{-15}$	$3.46{\cdot}10^{-5}$	33.3	3.04	0.076

No-slip boundary conditions have small influence on the particle accumulation near the wall (figure 5.21) and particle behavior is similar to the case with the free-slip boundary even for the largest particles. However, particle trajectories are less angular dispersion with the no-slip boundary conditions. The particles also can be catched near the boundary.

EM force influences particles if $\sigma_p \neq \sigma$ and traps them near the crucible boundary almost immediately after their release (figure 5.22). It also can be seen from table 5.3, where almost all particles with the sizes 0.2 and 2 mm have very low velocities in the presence of EM interaction. No-slip boundary conditions is the second factor, which reduces average particle velocity in the melt. With zero shear on the boundary angular flow intensity is larger and particles can move in tangential direction near the wall together with the flow eddies forming long tracks with larger trajectory loops (figure 5.23(a)). No-slip boundary conditions

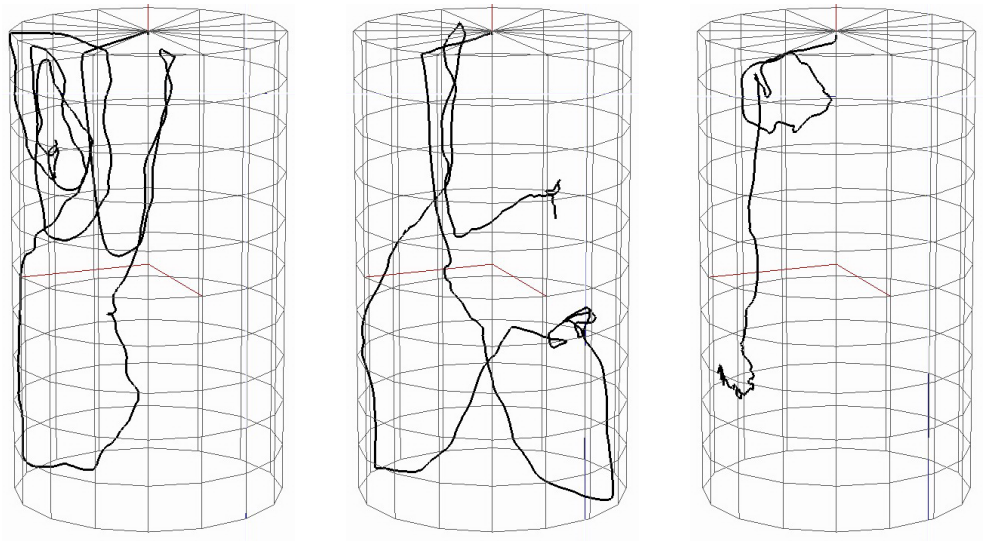

(a) $\rho_p = 0.9\rho = 8545$ kg/m^3, $d_p = 1$ mm

(b) $\rho_p = \rho = 9400$ kg/m^3, $d_p = 1$ mm

(c) $\rho_p = 1.1\rho = 10340$ kg/m^3, $d_p = 1$ mm

Figure 5.21: $d_p = 1$ mm particle tracks, which are injected from the top at t=0 after $k - \varepsilon$ solution. Track length corresponds to 40 s. No-slip boundary conditions with $\sigma_p = \sigma$.

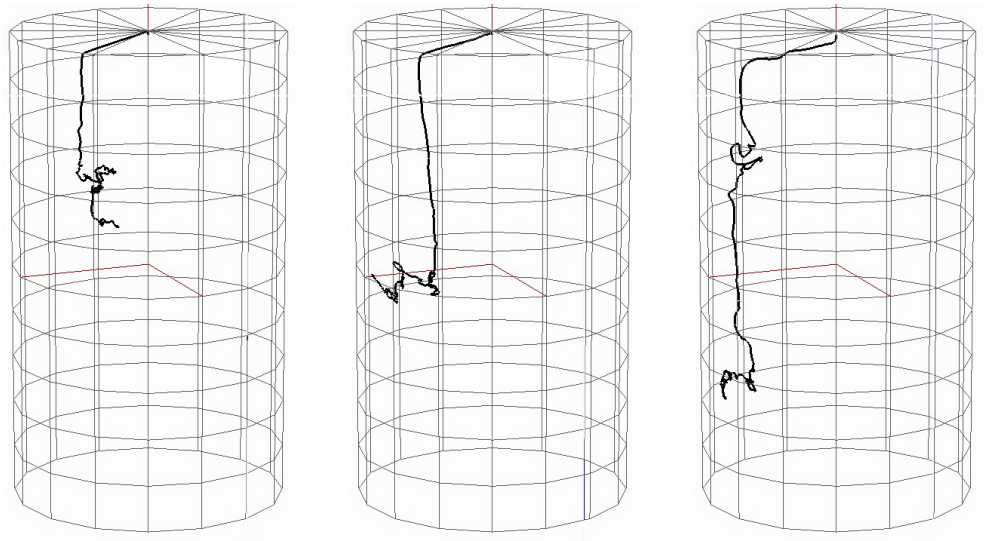

(a) $\rho_p = 0.9\rho = 8545$ kg/m^3, $d_p = 1$ mm

(b) $\rho_p = \rho = 9400$ kg/m^3, $d_p = 1$ mm

(c) $\rho_p = 1.1\rho = 10340$ kg/m^3, $d_p = 1$ mm

Figure 5.22: $d_p = 1$ mm particle tracks, which are injected from the top at t=0 after $k - \varepsilon$ solution. Track length corresponds to 40 s. No-slip boundary conditions with $\sigma_p = 0$.

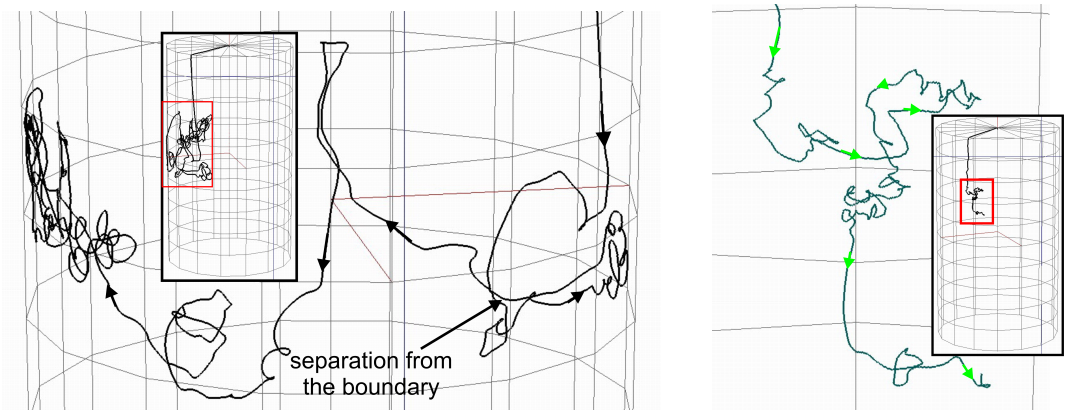

(a) free-slip (b) no-slip

Figure 5.23: Close view on 1 mm particle tracks under the influence of EM field with different boundary conditions.

reduce size of these angular flow loops and the particle angular dispersion becomes smaller and particle velocity reduces. It means, that particles inhabit near-wall region of the melt larger time, than the inner melt parts when no-slip boundary conditions are applied to the model. Particle separation according to their density also can be seen on figure 5.22.

6 Verifiction of LES method for heat and mass exchange in channel induction furnaces

6.1 Introduction to channel induction furnaces

Channel induction furnaces (CIF) are widely used for melting and holding of iron and nonferrous metals (mainly zinc, copper and its alloys) because they have high thermal efficiency usually above 80% [35] and have simple construction.

CIF is build like transformer with the iron core where the melt channel acts as a secondary coil. The iron core has large magnetic permeability and therefore reduces magnetic flux leakage increasing electrical efficiency. Primary coil or inductor is usually orthogonal to the symmetry plane of the channel. The channel is surrounded by the thermal insulating ceramics with outer metallic shield, which can be easily replaced when necessary. This part of the furnace represents heating element or induction unit and is called channel induction unit, because main ohmic power losses occur here. Melt bath is connected to the channel through the neck and can have any shape. Usually the bath is cylindrical with rounded bottom surface, which reduces surface (round shapes have minimal surface area for a constant volume) to minimize thermal losses. Magnetic field almost not penetrate to the bath and the bath also has thermal insulation around to reduce heat losses through ceramic walls.

Power range of the industrial channel furnaces starts at about 300 kW and extends to 1200 kW and above for each induction heating unit. Maximal channel

furnace power is limited by maximal melt overheat, which leads to technological problems (higher thermal losses, infiltration into ceramics and possible leakage). This overheat T_M can reach 200°C, however nobody knows exact values for industrial furnaces because precise temperature measurements in the channel are not yet implemented. The overheat can be reduced by transit flow of the melt through the channel, which intensifies heat exchange in the bath-channel system and improves heating efficiency. Transit melt flow through the channel can be influenced by the channel design, which rearrange distribution of Lorentz forces in the melt. There are possible many designs of the channel in respect to the shape of its cross-section (round, oval, rectangular) and channel connection to the bath (symmetry, shape of channel exits, exit angles) and the basic aim of this LES research is to determine proper overheat of the melt and create some preconditions for channel shape optimization for stronger transit flow.

The primary melt flow in the channel is introduced by the local vortices, which are formed under the influence of Lorentz forces. Lorentz forces are distributed radially from the inductor having the largest intensity near the inner channel wall. The melt flow in the channel cross-section can easily achieve 10 times higher velocities comparing to the transit flow. Therefore, fast channel erosion can be observed. As a result channel geometry changes, which influences transit flow stability and existence and introduces ceramics inclusions to the flow. Channel erosion reduces the working time of the induction unit and sometimes the unit should be replaced already after one month of operation. Refractory inclusions in the flow not only influence the chemical purity of the final product but also can participate in chemical reaction with oxygen and melt components creating compounds with higher melting temperatures. These compounds can form sediments on furnace walls especially in colder wall regions near the channel exits (channel clogging). This also decreases efficiency of heat and mass exchange between the channel and the bath. Flow velocities in the bath are much smaller than in the channel because the flow there is determined mainly by thermal convection. The flow circulation in the bath region is also entailed by the transit channel flow.

CIF constructions are different and can contain several heating induction units to increase total power, however the furnaces with one or two induction units are more common. Very detailed theoretical and experimental investigation of the

physical processes in CIF was performed in [7, 35], where theoretical estimations of transit flow velocities in the adiabatic channel with the one and two metal loops were performed. Adiabatic boundary conditions for the channel means that $\partial^2 T/\partial l^2 = 0$ (or $T = T_M \cdot l/L$), where l is a coordinate along the channel for one induction unit. The temperature maximum T_M is shifted to the channel side due to some initial fluctuation by the transit flow and temperature changes along the channel assumed to be are linear. With these considerations the next expression is provided for the channel transit velocity estimation:

$$V_0 = \frac{1}{\sqrt{2}} \sqrt[3]{\frac{dg\beta L j^2}{2\rho c_p \lambda \sigma}}, \tag{6.1}$$

where g is the gravity acceleration, c_p is the heat capacity, L is the channel length, d is the channel diameter, λ is the turbulent resistance, β is the thermal expansion coefficient. For the overheat estimation the next expression is proposed:

$$T_M = \sqrt{2} \cdot \sqrt[3]{\frac{2\lambda L^2 j^4}{dg\beta c_p^2 \rho^2 \sigma^2}}, \tag{6.2}$$

or if the channel transit velocity V_0 is known:

$$T_M = \frac{1}{2^{1/3}} \frac{L j^2}{V_0 \rho c_p \sigma}. \tag{6.3}$$

Several dimensionless numbers define flow regime and heat and mass transfer processes in the channel furnace [35] (table 6.1): Prandtl number (2.31); electrically induced flow number $S = \mu_0 I^2/(\rho\nu^2)$, which describes EM force influence on the fluid motion; shield parameter $R_\omega = \mu_0 \sigma R^2 \omega$, which describes EM force inhomogeneity due to skin effect; specific Joule power losses $\bar{Q} = I^2/\rho c_p \sigma \nu R^2 \Delta T$, which describes relative power of the Joule heat sources; Grashof number (2.31), which describes thermal convection.

Experimental study of horizontal channel furnace models [7], where buoyancy influence on the transit flow is excluded, showed presence of many transversal vortices in the channel, which should also present in vertical channel, because they are created by EM force. The authors stated that temperature distribution is determined mainly by the turbulent mixing in the horizontal channel while

Table 6.1: Dimensionless numbers and characteristic parameters for studied CIF with Wood's melt.

Parameter	Expression	Value
Channel radius	R, m	0.065
Channel length	L, m	2
Inductor frequency	f, Hz	50
Characteristic current	I, A	10^3
Characteristic velocity in the channel	U, m/s	0.5
Characteristic temperature difference	ΔT, K	30
Characteristic induction	B, T	0.1
Reynolds number	$\mathrm{Re} = \frac{UR}{\nu}$	$0.7{\cdot}10^5$
Prandtl number	$\mathrm{Pr} = \frac{\nu\rho c_p}{\lambda}$	0.05
Electrically induced flow number	$S = \frac{\mu_0 I^2}{\rho\nu^2}$	$6.6 \cdot 10^8$
Grashof number	$\mathrm{Gr} = \frac{g\alpha\Delta T L^3}{\nu^2}$	$4.1 \cdot 10^7$
Shield parameter	$R_\omega = \mu_0\sigma R^2\omega$	1.7
Specific Joule power losses	$\bar{Q} = \frac{I^2}{\rho c_p\sigma\nu R^2\Delta T}$	11.1
Rayleigh number	$\mathrm{Ra} \equiv \mathrm{Gr} \cdot \mathrm{Pr}$	$2.1{\cdot}10^6$
Magnetic Reynolds number	$\mathrm{Rm} = \mu_0\sigma UR$	0.4

thermal conductivity effects and therefore Prandtl number can be excluded. The transit flow existence was not found in the horizontal model for several symmetrical channel furnaces (one loop) with Wood's melt, however it was proposed that concentric (to inductor) channel with straight exits is the most efficient channel design for optimal heat transport to the bath. The transit flow should develop in vertical furnace because of thermal convection due to some initial fluctuation, which can make symmetric flow pattern unstable.

The further development of the one-dimensional channel model described bath as a part of the channel to close hydrodynamic equation integrals and exclude pressure [43]. The model had a usual temperature equation with the effective

thermal diffusivity and momentum equation in integral form:

$$L\frac{d\dot{V}}{dt} = \frac{1}{\rho_0}\left(\int_\Omega \rho_0\beta\mathbf{g}T\sin\varphi d\Omega - \int_\Omega (f_r - f_e)d\Omega\right), \tag{6.4}$$

where $\dot{V}$ is the volumetric expenditure, the latest integral represents the friction force and is replaced by the $\int_\Omega (f_r - f_e)d\Omega = \rho_0 L\frac{k}{2Ad\mathrm{Re}^n}\dot{V}|\dot{V}|$, where $\mathrm{Re} = \frac{\dot{V}d\rho_0}{A\eta}$, d is the channel hydraulic diameter, A is the channel cross-section area and $k, n = const$. The model also includes equation with unknown constant α for estimation of the power losses $q(\mathbf{x}, t)$ in the bath:

$$q(l,t) = \alpha_b(T(l,t) - T_w), \tag{6.5}$$

where α_b is the effective heat transfer coefficient from the channel to the bath, l is the channel coordinate and T_w is the temperature of the cooling water.

The model constants were power dependent and they were determined from experimental results accounting for the channel maximal temperature location and its value. Model equations were also solved with the finite-difference method and temperature difference and transit flow velocity have been approximated with expressions

$$\Delta T \sim P^{\varepsilon_1} \;\; v \sim P^{\varepsilon_2}, \tag{6.6}$$

where experimentally and theoretically determined coefficients ε_1 and ε_2 are in the range $0.57 \div 0.78$ and $0.27 \div 0.34$ correspondingly, which are in accordance with equations (6.1) and (6.2). The authors also have made several important conclusions: the transit flow in the channel is a result of action of the EM force together with the buoyancy; the turbulent oscillations are very important for heat and mass transport between the channel and the bath, where $\alpha_b \sim \sqrt{P}$; the stability of the transit flow becomes better when the power increases.

An interesting theoretical model of CIF is presented in [63], where EM field equations are exactly solved for circular cross-section torus channel and circular cross-section iron core. The model operates with important simplifications: only channel is taken into account and it is formed by the closed metal loop; the iron

core was closed to infinity. A primary flow-field in the channel's circular cross-section was studied using the finite-difference method for Navier-Stokes equations with constant viscosity and without thermal dependence. The transit flow was later estimated introducing some perturbations into the primary field.

Industrial channel furnaces were studied experimentally using similarity theory in [109], where a fourth-tenth scale physical model of 1300 kW inductor unit was described. The authors made experimental setup with a mercury and water-cooled design (mercury temperature was homogeneous within 1°C) of two-loop induction unit with a small bath. They have made very detailed measurements of induced electrical currents, external magnetic field and flow velocities in the bath but without thermal convection. They have found that flow pattern in the bath and in the channel is not stable and it is difficult to find an averaged flow pattern. Transit flow through the channel legs was found to change its direction and magnitude several times during a test of 1 minute duration and possibly here is an analogy for low-frequency vortices oscillations in the induction crucible furnaces. Electrical power of this furnace was only 2.55 kW and heat and mass exchanged between the channel and the bath was not efficiently promoted. Finally the shielding parameter R_ω of the laboratory furnace was only 0.63, which is at least one orders of magnitude smaller than in industrial CIF.

Very intensive experimental and numerical study of the vertical channel furnaces with one induction unit [22, 73] and two induction units [22, 113] were performed in the beginning of $90^t h$. These experimental data have large scientific value and will be used for LES model calibration, thus more details on experiment setup on the one-induction unit setup will be given here and in further sections.

Experiments were performed on the large scale CIF with Wood's melt [22] (figure 6.1). The channel was made from refractory ceramics but the bath walls were made from stainless steel with built-in water cooling for better control of thermal regime. Different cross-section shapes (round, square, rectangular) were studied. Flow velocities were measured using permanent magnet probes [77] with 18 Hz sampling rate and with maximal spatial resolution 0.01 m. The measured maximal velocities in the channel were in the range 20–35 cm/s depending on the channel cross-section shape and on the furnace power, which had range 27–74 kW.

Computer simulations of described experiments were performed using finite-difference method and modified $k - \varepsilon$ model to include low-frequency velocity oscillation influence on turbulent kinetic energy [73]. Proposed numerical method showed the presence of double vortex structure in the channel cross-section with high values of turbulent viscosity and heat and mass exchange coefficients.

All mentioned authors conclude that 3D EM field and correct heat and mass transfer simulations in CIF are extremely difficult due to complicated geometry and 3D nature of inner physical processes. Besides it is practically impossible to carry out a comprehensive temperature and velocity measurements on an actual channel furnace. The most recent development in 3D simulation of channel induction furnace was made utilizing coupled EM and thermal analysis [31] for zinc, which were combined with steady HD calculations [30] for aluminium. The first of these works is dedicated to thermal analysis of twin-channel design of the induction unit where current in the central channel is equal to the sum of currents in side channels. The transit flow velocity was initially estimated from thermodynamics laws and its dependence on furnace power Q and overheat temperature was found:

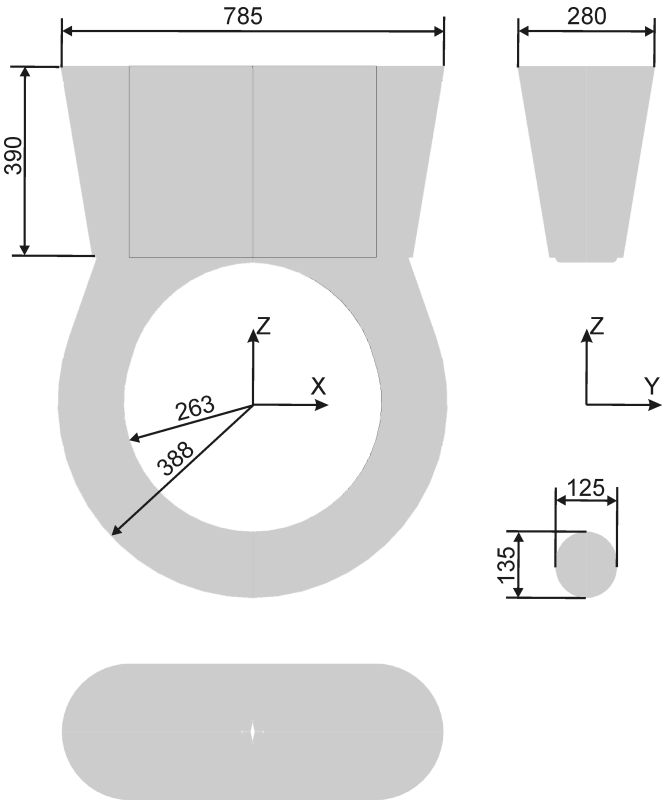

Figure 6.1: Dimensions in mm of the melt region in experimental CIF with local coordinate system for EM and LES simulation.

$$V_0 = k_1 \frac{Q}{T_M}, \tag{6.7}$$

where k_1 is a constant for a given system and is dependent on the geometry of the inductor side channel and properties of the melt. Computer simulation has shown 50°C temperature difference between side and central channels for 300 kW input power and proposed 27 cm/s flow velocity.

The later work [30] includes also 3D steady flow calculations of twin-loop channel furnace for aluminium melting with several turbulence models. The simulation couples EM, thermal and HD calculations in a loop using *ANSYS Multiphysics*. Furnace geometry was presented by one quarter part because of symmetry. It included inductor with cooling shield, magnetic steel core, channel with throat and melt bath, refractory and thermal insulation. Simulation showed that all selected turbulence models provide similar results for flow velocity and temperature fields without presence of transit flow in the channels. Flow intensities in the bath are much smaller than in the channels and temperature gradients in the melt are about 12 K.

All above mentioned examples include almost full review of available experimental data and models of channel furnaces and proposed 3D LES simulation of such device can be a breakthrough to complete understanding of internal flow processes and heat exchange in the melt.

6.2 EM model of the experimental induction furnace

Experimental channel furnace geometry (model 1 [22], table 6.1) with the Wood's melt was selected for hydrodynamic and thermal verification of LES computer simulation. Electromagnetic simulation of CIF was performed in *ANSYS Classic* FEM package using APDL script. The script was fully parametric and allowed easy modifications of model geometry and mesh. Taking into account symmetry of geometry, only a half of the full furnace is EM modeled (figure 6.2) utilizing symmetry of the channel furnace geometry. The model has several regions defined, where electrical properties (table 6.2) are important:

1. channel itself and a bath with the Wood's metal (figure 6.1);

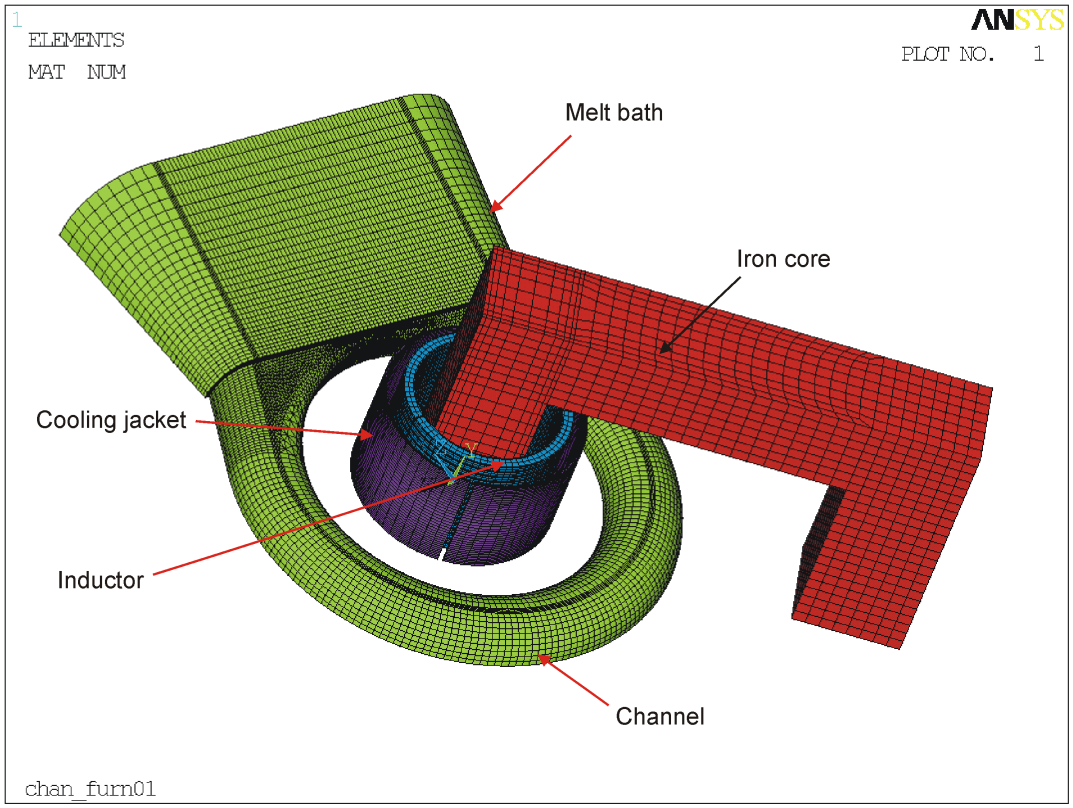

Figure 6.2: Geometry and mesh of channel furnace EM model.

2. cylindrical cooling jacket from copper between the inductor and the channel;
3. copper inductor with ;
4. iron core for EM field amplification;
5. surrounding air with infinite boundary.

It can be noticed that channel has very complex neck geometry without rapid face connections on its side, which is close to the inductor. Channel shape changes from round to rectangular smoothly in the throat. Introducing laminated iron core to the model, the one can take its electrical conductivity to be zero, because core construction should eliminate eddy currents and prevent Joule dissipation here. Refractory resistivity is very large as for ceramics and thus it is transparent for EM field at such low frequencies (skin depth is very large).

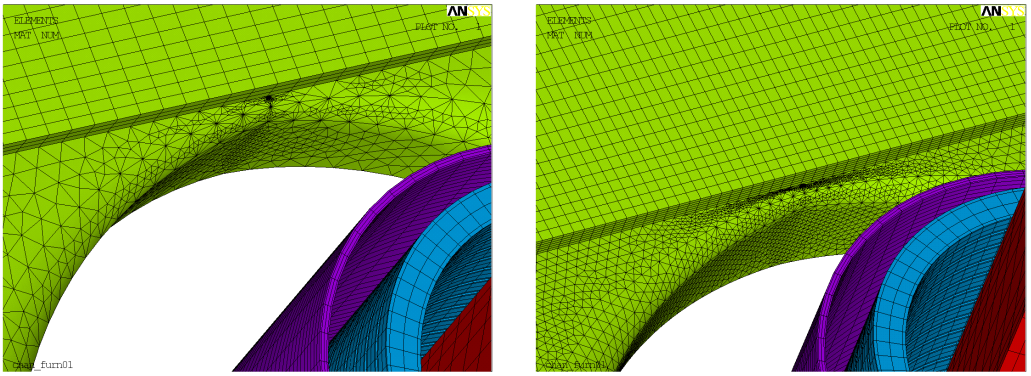

(a) Coarse model (b) Fine model

Figure 6.3: Two different meshes used in EM simulation.

Each model region is constructed from several primitive volumes for easier model creation and brick mapped meshing of important regions. As a result free tetrahedral mesh can be found only in two transition volumes of very complex geometry in the channel neck and in the air. Special infinite elements are created in the outer shell of the air for correct description of EM field damping far from the inductor. Flux parallel EM boundary conditions can be applied on a far model boundary as alternative. Total number of elements in the model is above 1 million and for direct solution of this problems multi-core SMP Linux workstation is used. Degrees of freedom (magnetic vector potential and scalar potential) were associated with the element nodes, i.e. low-frequency node-based harmonic analysis were applied. All other magnetic field properties are derived from these potentials.

For this model inductor frequency 50 Hz and the total EM power were initially known. For correct model formulation inductor current should be chosen. The model inductor has one turn less than the real inductor because the total number of inductor turns is 33 but only 16 were included to the half-model. Electrical current is applied only to one node for each inductor turn and therefore eddy current distribution is calculated like in massive conductors.

A coarse grid (table 6.3) was initially created to estimate inductor current – power curve (figure 6.4), which illustrates quadratic dependence of the power

Table 6.2: Electrical properties of the model regions and materials.

Type	Region	Electrical resistivity, Ω·m	Magnetic permeability
900	Wood's melt	$1{\cdot}10^{-6}$	1
400, 200	Cooper inductor and cooling jacket	$0.16949{\cdot}10^{-7}$	1
300	Iron core		1000
100	Air		1

Table 6.3: Grid size comparison between the coarse and the fine models.

	Total number of elements	Number of elements in the melt
Coarse model	450000	45000
Fine model	765000	124000

losses in the system on inductor current ($P \sim I^2$). The coarse mesh model precision was verified with a finer grid (figure 6.3(b)) for one selected current value $I_{ampl} = 1200$ A. Calculated total electrical power and Joule dissipation in the melt were almost equal for two different grids. The amplitude current 1200 A, which corresponds to 62 kW total power, was also selected to be a model current for EM force and Joule heat calculation on the large grid.

Induced current distribution in the melt is not uniform (figure 6.5). The current forms a closed anticlockwise loop along the channel, which direction is opposite to inductor current. Skin depth is large (table 6.4) and the electromagnetic skin effect can be neglected. Current density has the largest values near the inner channel surface below the inductor. Current densities in the bath are much smaller and the influence of EM force on the melt flow there should be negligible.

Magnetic field distribution in the melt (figures 6.7 and 6.8) is determined by superposition of the magnetic field which is produced by the induced currents in the melt and by leakage magnetic field from the primary inductor coils [109].

Simulation results show very symmetrical heat source (figure 6.6) and Lorentz force (figure 6.9) distribution in the channel in respect to YZ and XZ planes (fig-

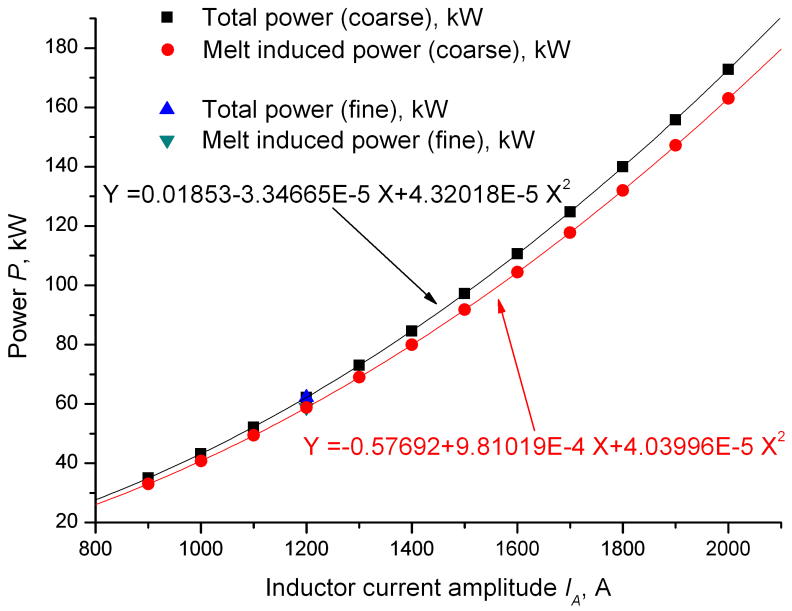

Figure 6.4: Current power curve for model 1 (current values are amplitude).

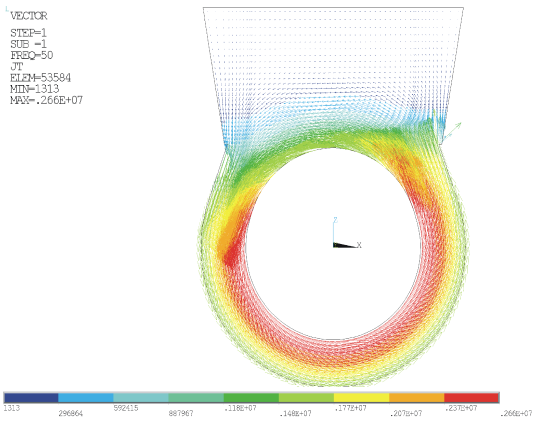

Figure 6.5: Current density distribution in the symmetry plane for $I_A = 1200$ A.

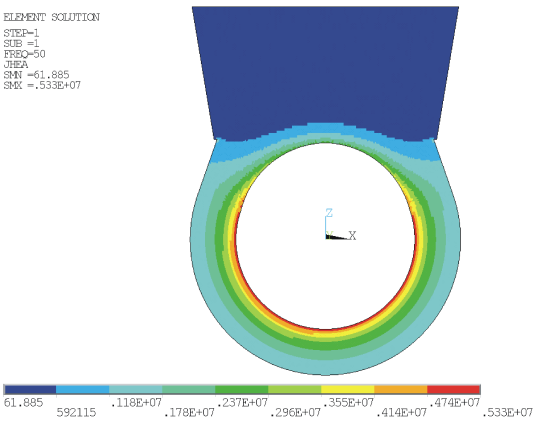

Figure 6.6: Joule heat sources in the symmetry plane for $I_A = 1200$ A.

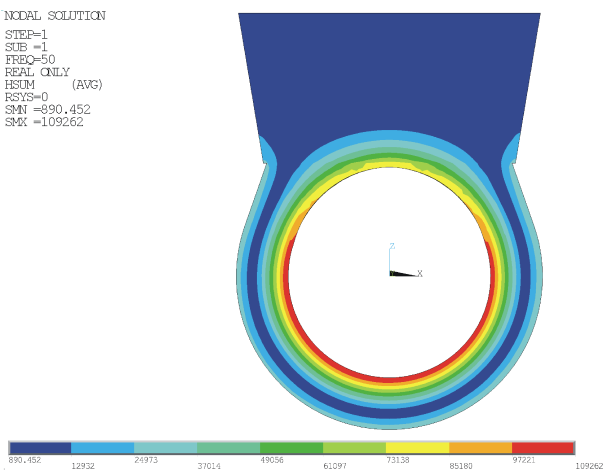

Figure 6.7: Magnetic field intensity in the symmetry plane for $I_A = 1200$ A.

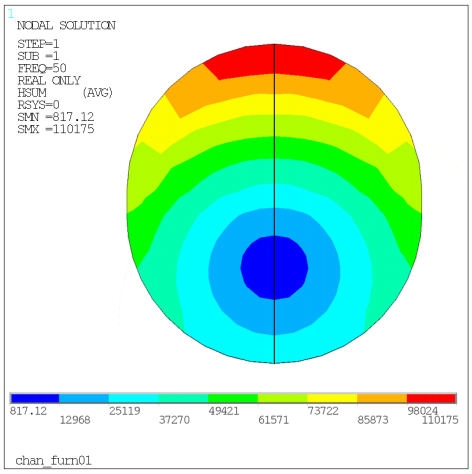

Figure 6.8: Magnetic field intensity in the bottom cross-section of the channel for $I_A = 1200$ A.

ure 6.1). The maximal values of Lorentz forces and heat sources are noticed on the inner bottom surface of the channel, which is closest to the inductor and where maximal values of current density can be found. Lorentz force direction is collinear to the radii direction in the symmetry plane and force intensity in the bath is mach lower than in the channel. EM force distribution in the channel cross-sections (figure 6.9(b)) should lead to two-vortex structure inside the channel because there is dominant radial direction. It also should ensure upward flow directly above the channel in the XZ symmetry plane.

6.3 HD model of the experimental induction furnace

Hydrodynamic simulations were fully decoupled from EM calculations due to small Rm $= \mu_0 \mu \sigma U L << 1$. Free surface oscillations also were not taken into account because here they are mainly determined by the Wood's melt flow (EM inductor is far below the free surface) and are suppressed by the high melt

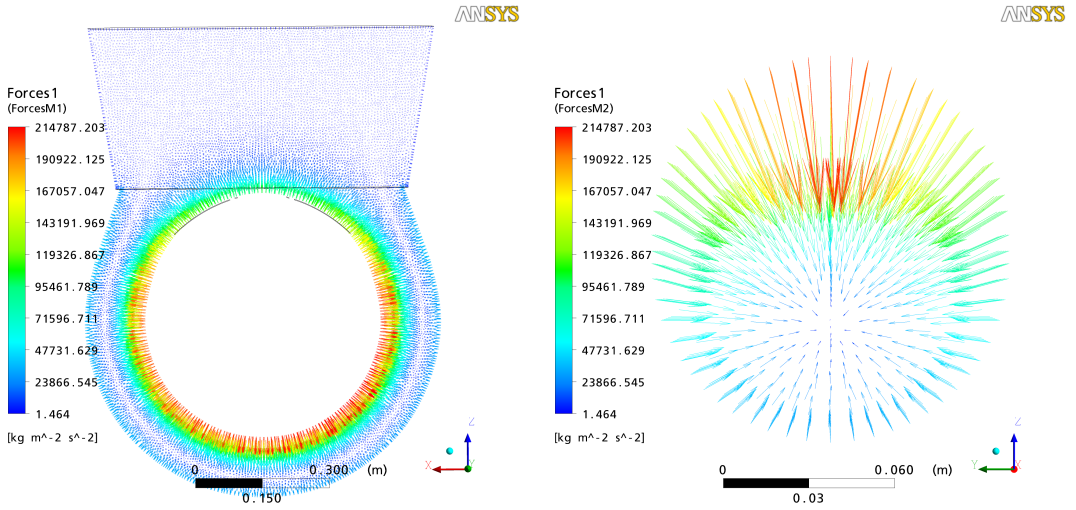

(a) Symmetry plane

(b) Channel cross-section

Figure 6.9: Distribution of Lorentz force density in the melt.

density and relatively small melt velocities near the free surface. *ANSYS CFX* 10 or 11 commercial CFD package was available for HD simulations. This software package is highly valued in CFD community allowing solution of complex physical problems. All meshes for *ANSYS CFX* were created in *ANSYS ICEM CFD* software using IGES format export from *ANSYS Classic*.

Several turbulence and geometry models have been tried in HD simulations. SST and $k-\varepsilon$ turbulence models were compared on one half symmetrical 3D and on full 3D models, while transient LES included only full geometry.

6.3.1 Steady simulations

Steady simulations were performed initially to verify model setup and to get initial numerical solution for LES. Two equation SST (modified $k-\omega$) and $k-\varepsilon$ models were used. Shear Stress Transport or SST is also a kind of two-equation turbulence models and "CFX-Berlin Gmbh" recommends it for use in steady calculations. $k-\varepsilon$ and $k-\omega$ turbulence models do not account for the transport of turbulent shear stresses. This results in an overprediction of the eddy-viscosity

Table 6.4: Physical properties used for CIF simulation of the Wood's melt comparing to the cast iron.

	Symbol	Units	Cast iron	Wood's metal
Thermal conductivity	λ	W/(m·K)	18.5	14.05
Specific heat capacity	c_p	J/(kg·K)	775	168
Melting temperature	T_{melt}	K	1880	343
Density at melt. temp.	ρ_0	10^3 kg/m^3	6.8	9.40
Dynamic viscosity	μ	10^{-3} kg/(m·s)	5.6	4.2
Electrical conductivity	σ	10^6 1/(Ω·m)	1.8	1.0
Thermal expansion coeff.	α	10^{-6} 1/K	180	100
EM skin depth at 50 Hz	$\delta_{50\ \mathrm{Hz}}$	m	3.8	5.0

in the boundary layer near the solid wall. The proper transport behavior can be obtained by a limiter to the formulation of the eddy-viscosity.

A **half CIF geometry** model had about 1.3 million tetrahedral elements (unstructured mesh) created in ICEM CFD. An outer boundary region was refined everywhere except symmetry plane and a free surface. The model had applied loads from the fine mesh EM model. No-slip boundary conditions were used for hydrodynamics on channel and bath walls, top surface had no shear condition. The channel had adiabatic walls while wall temperature of the metal bath was fixed to 80°C and thermal convection was applied (the heat transfer coefficient $k = 20$ W/(m^2·K)) for the free top surface. The model also included buoyancy with temperature dependent melt density, which should be very important for creation of the channel transit flow: $\rho = \rho_0 (1 - \alpha(T - T_0))$. Gravity vector was directed to negative z. High resolution numerical schemes were selected for precise calculations.

Results of the half geometry 3D steady models are presented below. $k - \varepsilon$ model calculated velocity distribution in the symmetry plane (figure 6.10(a)) satisfies EM force distribution in the melt. Flow is directed radially outwards in the channel in this cross-section and there is an upward flow just above the

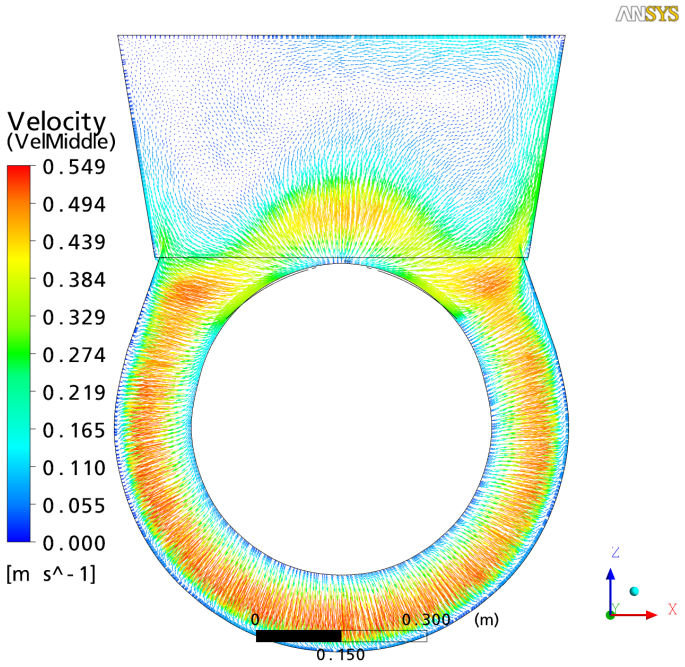

(a) $k - \varepsilon$

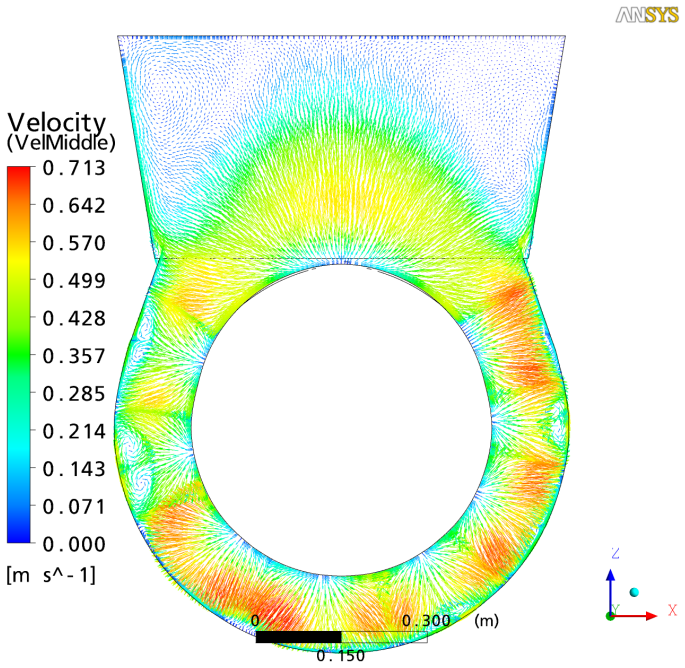

(b) SST

Figure 6.10: Velocity vectors on symmetry plane from the half geometry 3D model.

channel forming two vortex loops in the bath with smaller flow velocity comparing to the channel. These loops have complex 3D structure and are closed at the side walls of the bath. There is also less intensive upward flow near the left and right sides of the bath. Different intensity of this side flow can be explained by the buoyancy.

SST model (figure 6.10(b)) produces similar results for flow structure in the bath, but there is completely different flow pattern in the channel, where flow is represented by complex 3D vortices, which looks like Bénard cells. There are about 8 such structures with characteristic sizes $1.2 \sim 1.5$ channel diameters along the channel length. The flow intensity calculated by SST model is about 30% higher especially in the bath where the upward flow in the central part above the channel is more expressed.

Velocity distribution in the channel is represented by the two-vortex structure (figure 6.11) due to strong symmetry condition. Characteristic velocity magnitudes in the channel are approximately the same for both models (~ 0.5 m/s in maximum). The distance between the vortex centers is about one channel radius.

Table 6.5: Thermal balance of the experimental CIF from different turbulence models.

Turbulence models	Geometry	Induced power, W	Crucible walls, W	Free surface, W	Disbalance
$k-\varepsilon$	3D half	58396	62066	237.506	-6.7%
SST	3D half	58396	55844.6	236.85	4.0%
SST	3D full	58396	55585.8	243.103	4.4%
LES (at 77.15 s)	3D full	58396	48996.8	257.6	15.7%

Temperature distribution in the melt is completely coupled with the flow, because the melt density is temperature dependent. Very strong turbulent heat exchange is expectable in the furnace while thermal conductivity effects should be smaller. Temperature plots (figure 6.12) show that melt temperature in the bath is smaller than melt temperature in the channel (remember, that channel is adiabatic). Both calculated temperature distributions are in accordance with the

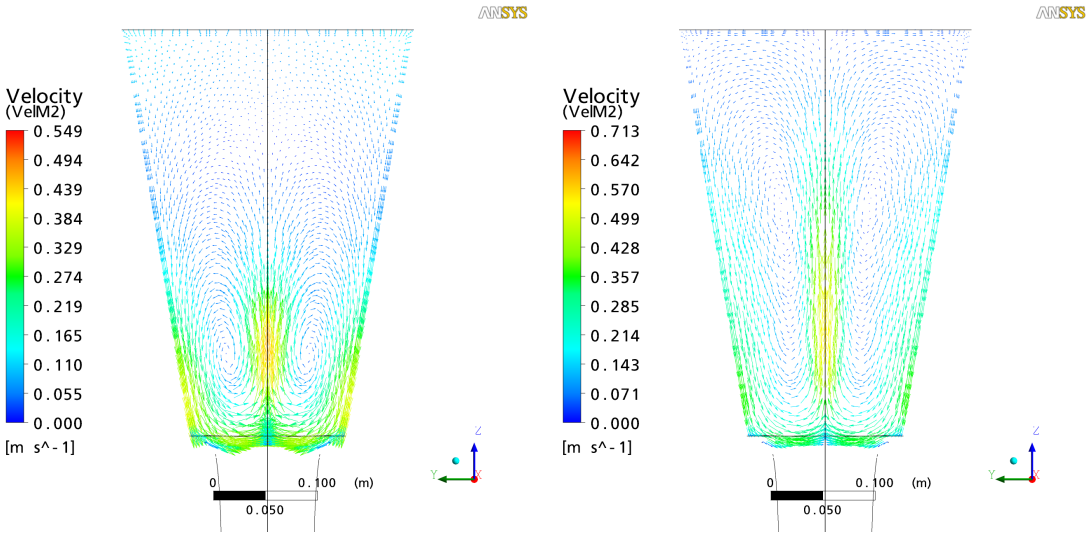

(a) $k-\varepsilon$

(b) SST

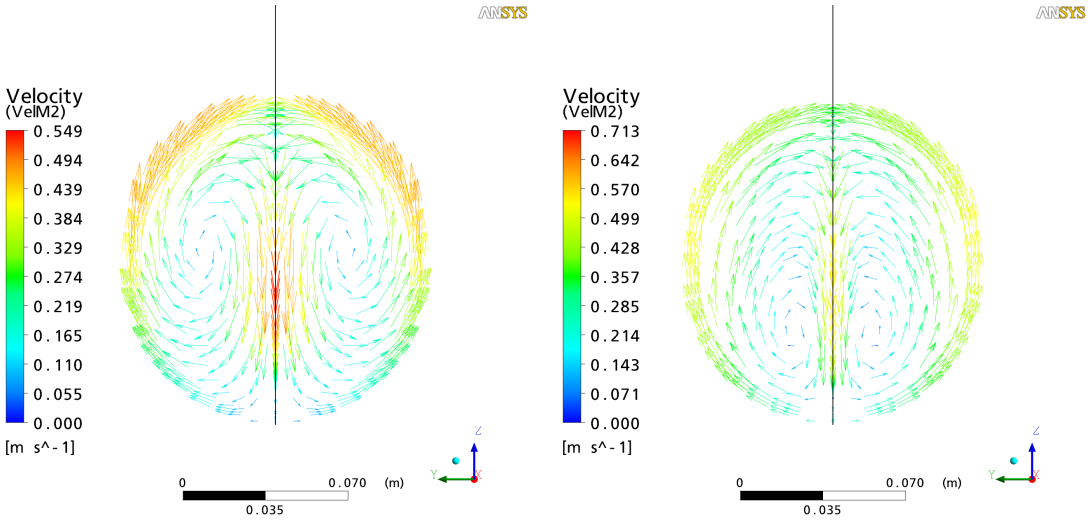

(c) $k-\varepsilon$

(d) SST

Figure 6.11: Velocity distribution in the bath and in the channel, $x = 0$.

thermal balance (table 6.5), which is given with in 10% accuracy for all steady models. It can be seen that corresponding to thermal balances $k-\varepsilon$ temperatures are a little higher, than should be while SST model produces smaller temperature magnitudes.

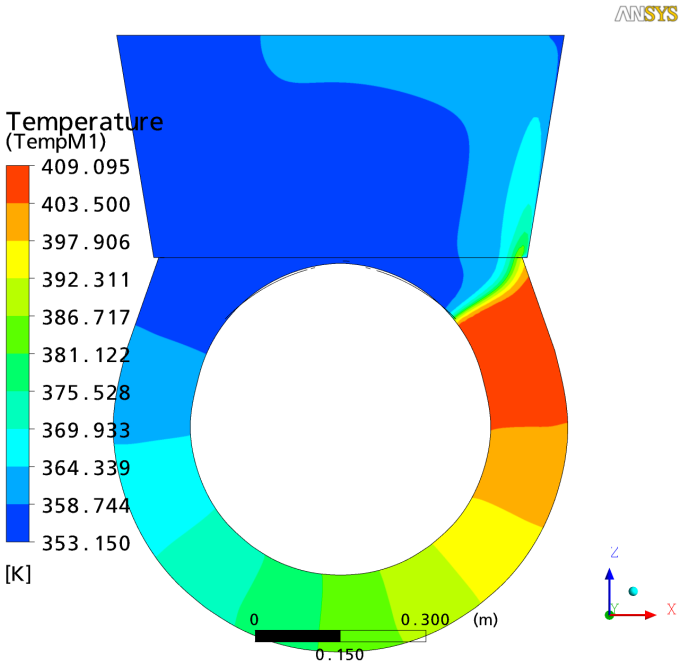

(a) $k - \varepsilon$

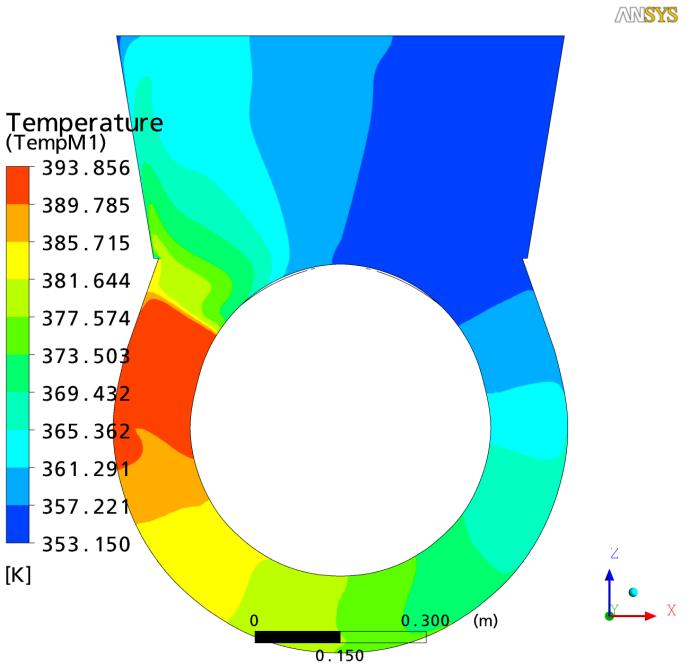

(b) SST

Figure 6.12: Temperature distribution on symmetry plane $y = 0$ for the half geometry 3D models.

Melt temperature in the bath is only several Kelvins higher than the wall temperature, which can be explained by the reduced heat exchange between the turbulent vortices in a standard $k-\varepsilon$ model. Temperature distribution in the channel is not symmetric having local maximum at one channel side with temperature difference about 45 K comparing to the bath. SST calculated temperature distribution (figure 6.12(b)) is a little different from the $k-\varepsilon$ model result. The maximal temperature is almost 15 K (3.75%) less than in $k-\varepsilon$ simulation and is placed in the other half of the channel. It means that transit flow in the channel has changed its direction. Temperature gradients channel–bath are also less expressed and therefore temperature distribution in the bath is less homogeneous again comparing to $k-\varepsilon$.

Full 3D steady calculations were performed only with SST turbulence model. Simulated region is represented by the symmetrical channel with the metal bath above, which represents channel neck. The mesh was recreated from a forth part of the geometry by mirroring and had about 3.2 million elements in total. The same mesh was later used in LES. All boundary conditions and material properties were the same.

Simulation results are oscillating because the strong symmetry condition is removed and CFX solver can not find stable flow pattern in the furnace. Transient simulation with further averaging of results can be used in such situation to get stable flow pattern, but due to planned LES calculations, transient SST simulation was not performed.

Resulting flow structure (figure 6.13(a)) introduces the same tendencies like in the half geometry models: flow in the channel forms vortex structures, flow in the bath is less intensive comparing to the channel. The maximal flow velocities became smaller than in the half geometry SST model, but they are still higher than in $k-\varepsilon$ model. The flow in the bath also became less intensive with higher count of smaller vortices and this projection on $y=0$ surface does not introduce upward flow in the bath center.

Side projection $x=0$ (figure 6.14(a)), however, shows such upward flow near the bath bottom, which has large velocities and forms two interacting recirculated vortices with different sizes. Flow in the channel crossection (figure 6.14(b)) is also represented by two vortices with different sizes and varies along the channel.

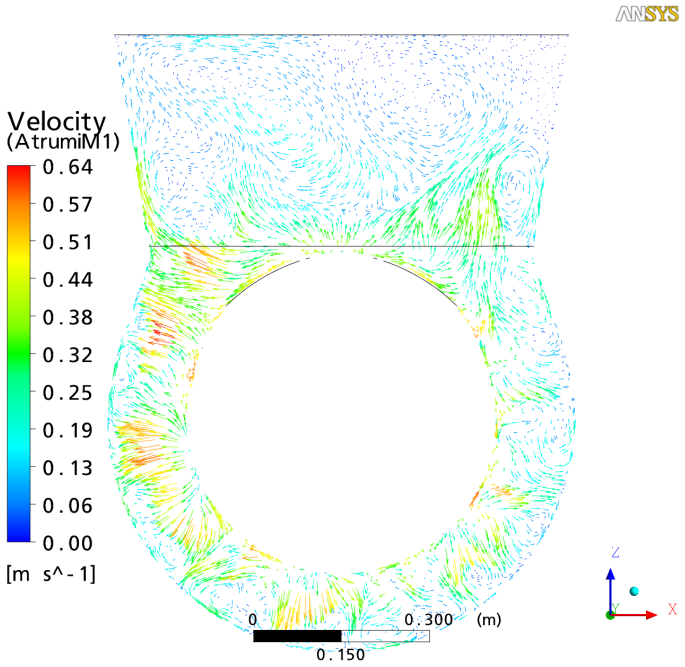

(a) velocities

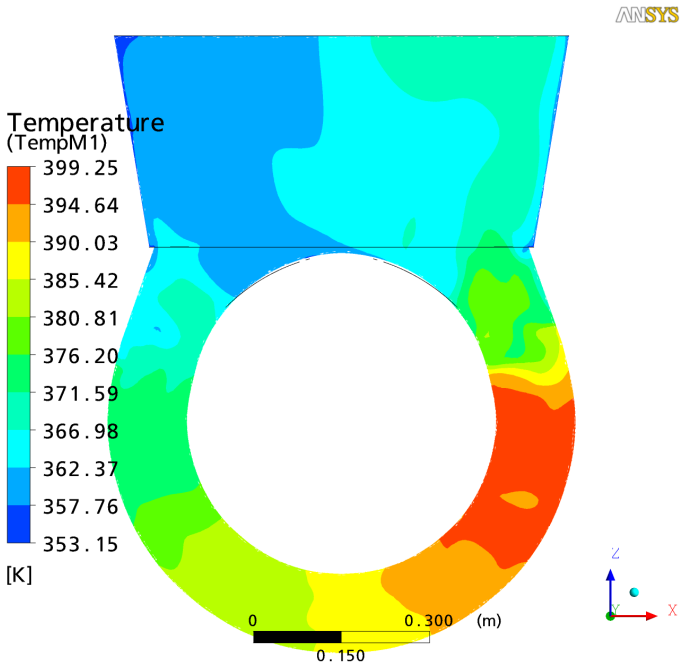

(b) temperatures

Figure 6.13: Velocity and temperature distributions on symmetry plane $y = 0$ for the full 3D SST model.

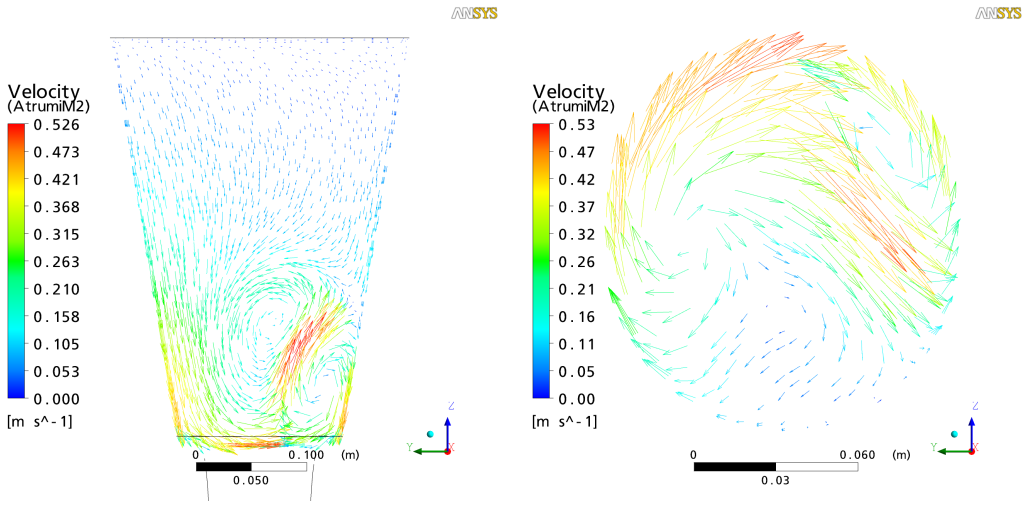

(a) bath (b) channel

Figure 6.14: Velocity distribution in the bath and in the channel, $x = 0$.

Temperature distribution (figure 6.13(a)) shows the shifted to the right side temperature maximum with overheat about 47 K. The shift position of the temperature maximum has changed its side comparing to the half geometry results. It seems that for symmetrical geometry channel furnaces the maximal temperature position can not be determined exactly, so it has equal probability to select one or another channel side. It means that the direction of the transit flow velocity is determined by random fluctuations or disturbances in the flow itself neither on mesh and geometry factors. Temperature contour borders are disturbed by the intensive turbulence and larger vortices.

6.3.2 Transient LES simulation

Transient LES simulation under the same conditions like described was started from zero velocity field and uniform $T = 80°\text{C}$ temperature distribution with $\Delta t = 0.01$ s time step. The flow development was modeled for approximately 77 s, but variable averaging was started from $t = 10$ s.

Instantaneous flow pattern in the CIF is very chaotic (figure 6.15(a)) with characteristic velocities in the channel from 30 to 50 cm/s and in the bath from

10 to 30 cm/s. Identification of the large scale vortices is very difficult due to high turbulence intensity, but some part of the vortex can be located near the channel exits forming upward flow along the left and right walls of the bath.

Averaged velocity pattern (figure 6.15(b)) introduces similarity to all steady models introduced above. The melt flow is directed radially outwards on the symmetry plane in the channel mostly like in $k - \varepsilon$ model, but also there are several vortices, which were introduced in SST simulations. Flow in the bath is mainly formed by two large vortices, which take melt away from the channel exits.

Upward flow in the bath middle above the channel (figure 6.16) is shifted to the back wall of the bath and again typical vortices are of different sizes. This flow is formed by the presence of Lorentz forces and its intensity reduced over the height. It is already can not be distinguished at approximately half height of the bath (20 cm). Flow in the top half of the bath is relatively slow, only $5 \div 10$ cm/s, but characteristic Re 10^5, hence, the flow is still turbulent.

Flow in the orthogonal channel cross-sections is introduced by two typical vortices, which have velocity components along the channel (figure 6.17). Instantaneous flow velocities can easily reach 70 cm/s, while in average maximal flow velocities here are about 50 cm/s.

Temperature contours (figure 6.18) introduce overall heat and mass circulation in counterclockwise direction. The temperature maximum is shifted to the left side and heated melt comes up to the bath, then it goes to the other bath side, is cooled by the cold walls and pumped back to the channel.

6.3.3 Comparison to the experimental results and discussion

All above mentioned turbulent models have shown ability to simulate velocity field in the channel furnace. Some models have produced smaller or higher velocities comparing to experimental data (figure 6.19), but the difference between the characteristic velocities from simulation or experiment is not more thane 20%

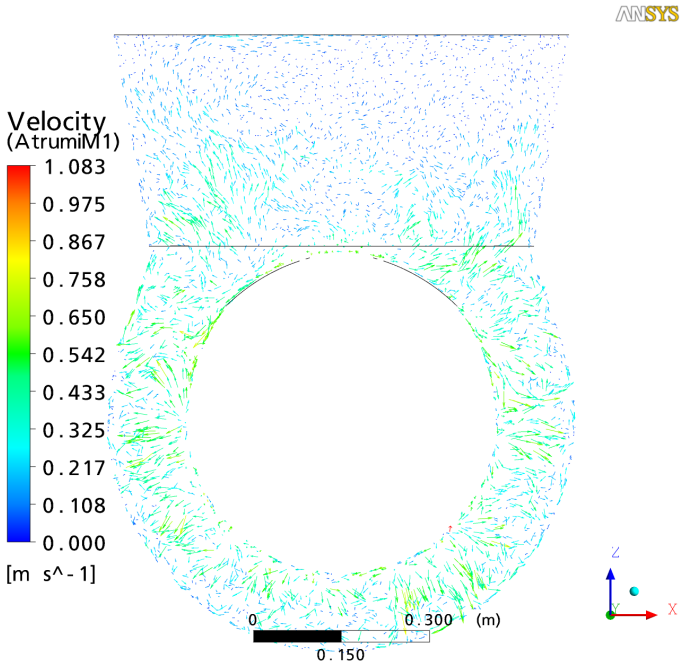

(a) $t = 77$ s

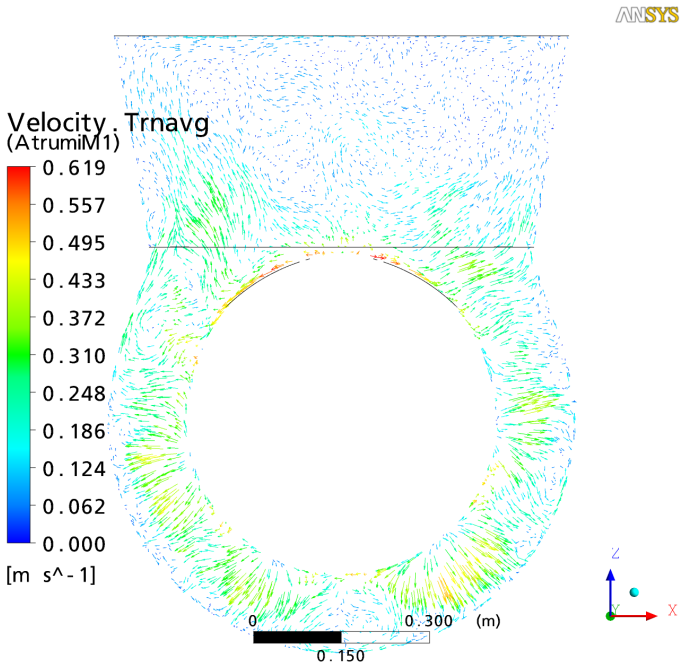

(b) average

Figure 6.15: LES instantaneous $t = 77$ s and averaged velocity distribution on symmetry plane $y = 0$.

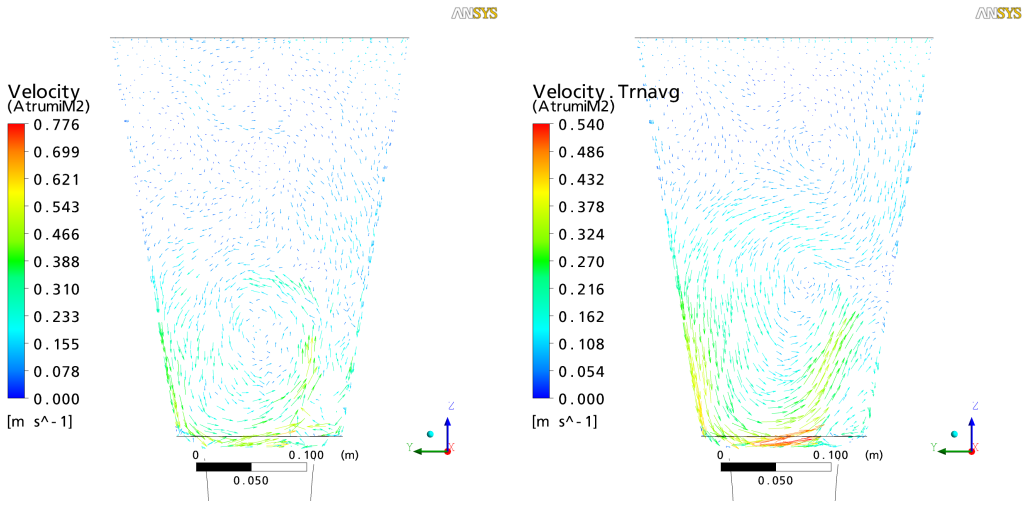

(a) $t = 77$ s (b) average

Figure 6.16: LES instantaneous $t = 77$ s and averaged velocity distribution on symmetry plane $x = 0$ (bath).

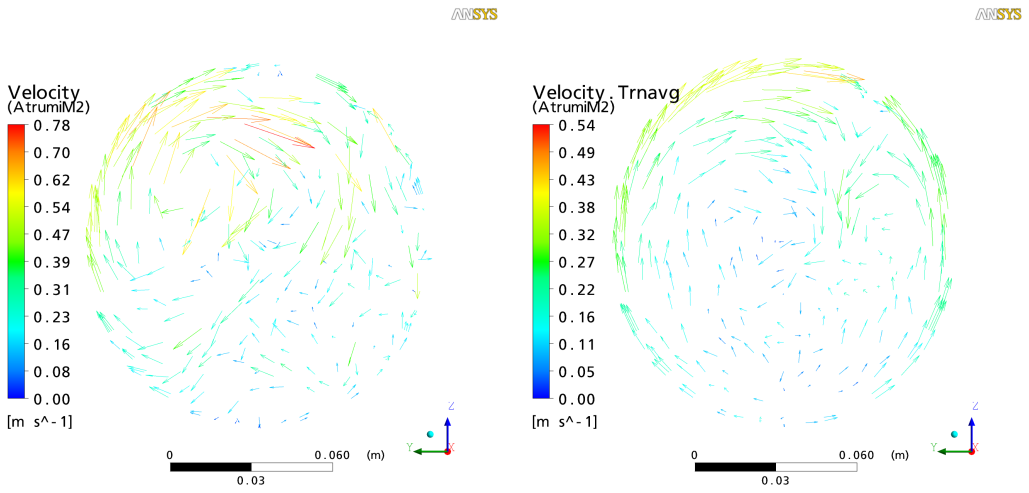

(a) $t = 77$ s (b) average

Figure 6.17: LES instantaneous $t = 77$ s and averaged velocity distribution on symmetry plane $x = 0$ (channel).

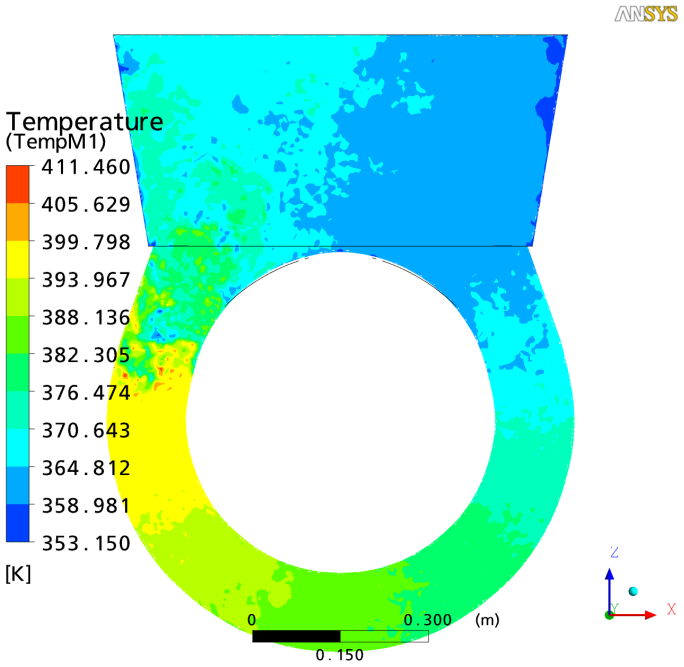

(a) $t = 77$ s

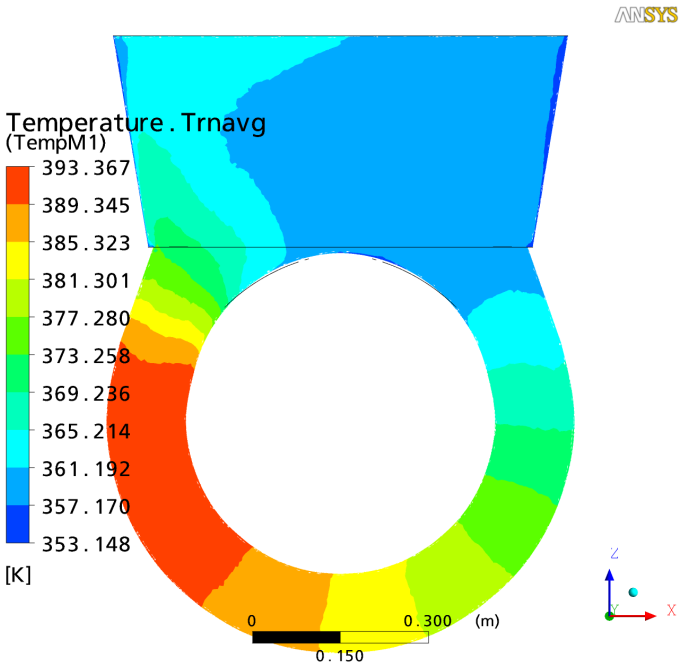

(b) average

Figure 6.18: LES instantaneous $t = 77$ s and averaged temperature distribution on symmetry plane $y = 0$.

and all simulation results are considerable. Half geometry 3D steady models (especially $k-\varepsilon$) seems to be more accurate determining average velocity pattern because it was found to be very symmetrical also in the experiments.

However, the main goal of channel furnace simulation is to determine the channel overheat temperature T_M, which for the 64 kW total power is 33.5 K. The closest result is achieved with the LES model (table 6.6), while the $k-\varepsilon$ solution introduces error above 50%.

The transit flow velocity can be denoted from the mass flow rate or integrating transit velocity component, which lies along the channel through the channel crossection S. The channel crossection at $x = 0$ is the most convenient for such calculations due to symmetry and the structure of the numerical grid. For instance, if $Q|_{x=0} = \iint_S V_x \; dS$ than $V_{trans} = Q/S$ is the transit flow velocity (table 6.6). However, this method is not very precise because Q can have another value in other crossection due to vortical flow structure in the channel. Therefore, some theoretical estimations can be made.

The method proposed in [35] is based on a stationary scalar transport equation (2.36) with added source therm for Joule heat:

$$v_i \frac{\partial T}{\partial x_i} = \frac{\partial}{\partial x_i}\left(\frac{\lambda}{\rho c_p}\frac{\partial T}{\partial x_i}\right) + \frac{1}{\rho c_p}\frac{j^2}{\sigma}. \tag{6.8}$$

The above expression can be simplified taking into account only components, which are collinear to the channel. We also can assume that $T = T_M \dfrac{l}{L}$ due to adiabatic boundary conditions and express current density through the induced Joule heat power $\dfrac{j^2}{\sigma} = \dfrac{P_{Joule}}{V}$. Linear variation of the temperature along the channel is confirmed by numerical calculations (figure 6.20(c)). Finally the next expression is derived for approximate estimation of the transit flow velocity:

$$V_{trans} = \frac{2}{\rho c_p}\frac{LP}{T_M V} \approx \frac{1}{\rho c_p}\frac{P}{T_M S}. \tag{6.9}$$

It can be noticed that $V_{trans} \sim T_M^{-1}$ or $V_{trans} \sim \Delta T$. Calculated V_{trans} values are shown in the table 6.6. These theoretical values of the transit flow velocity are below $V_{trans}^{theor} < 1.5$ cm/s.

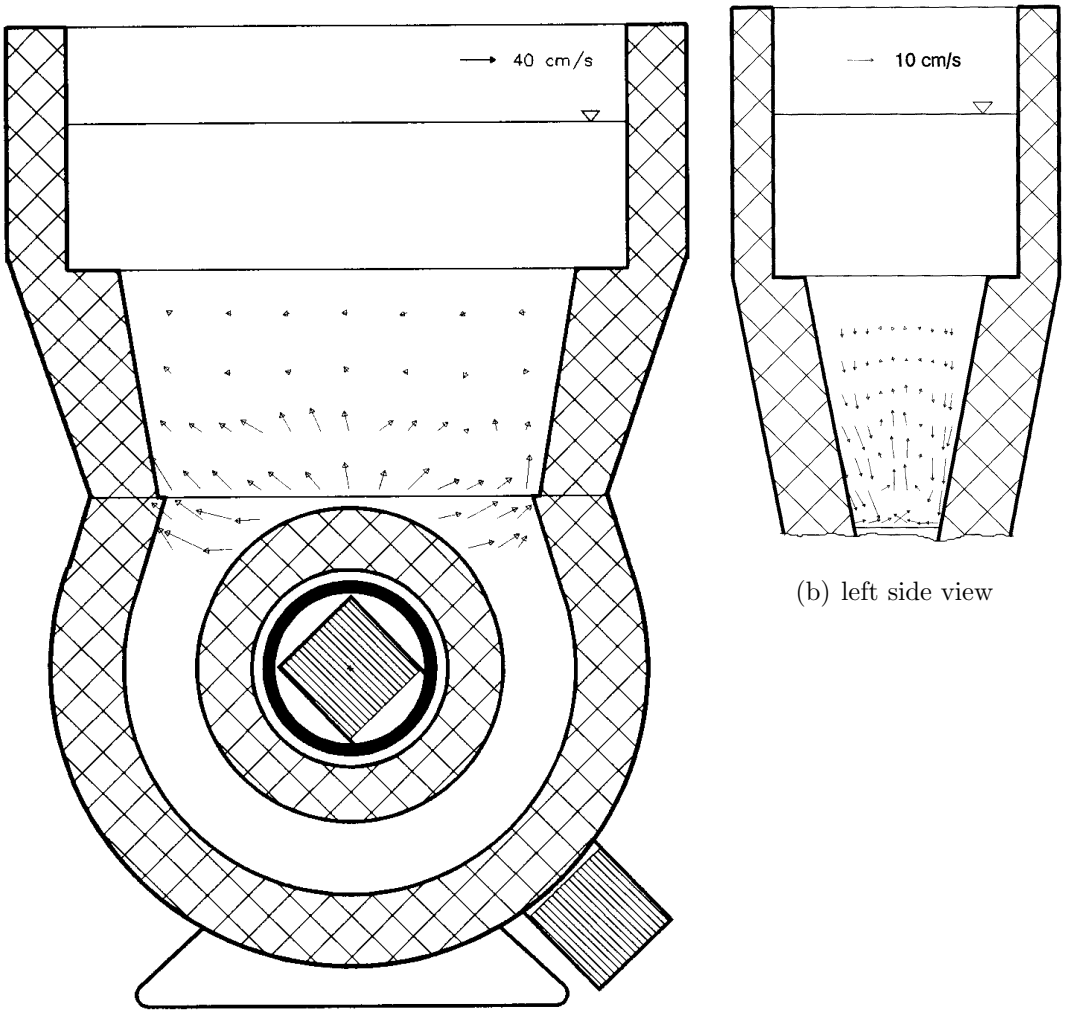

(a) front side view

(b) left side view

(c) horizontal plane above the throat

(d) horizontal plane in the channel

Figure 6.19: Experimentally captured averaged velocity distribution in the channel furnace [22].

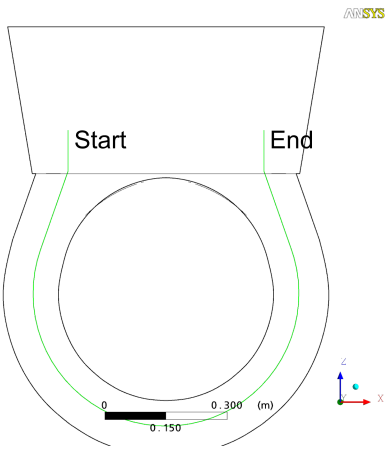

(a) path definition

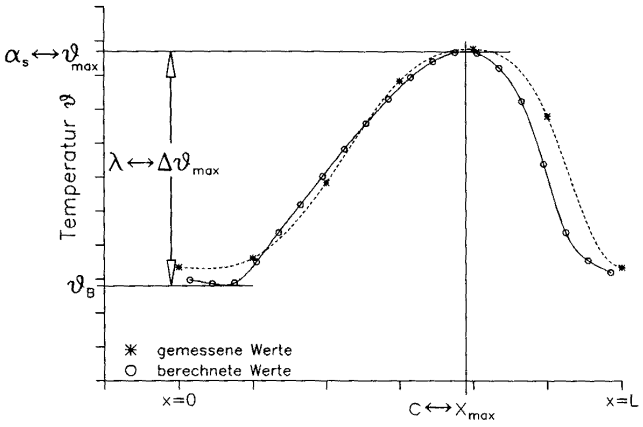

(b) experimental data

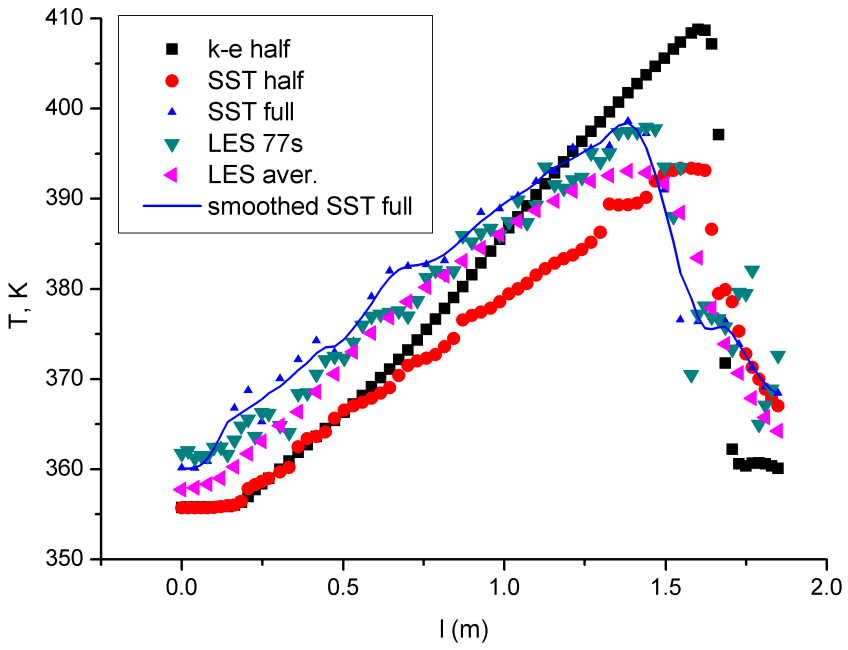

(c) computational results

Figure 6.20: Measured [22] and calculated distribution of the temperature in the channel.

Table 6.6: Transit flow velocities estimated on surface $x = 0$ and temperature differences along the path.

Model	S, m^2	$\iint_S V_x \, dS$, $\mathrm{m}^3{\cdot}\mathrm{s}^{-1}$	V_{trans}, $\mathrm{cm}{\cdot}\mathrm{s}^{-1}$	V_{trans}^{theor}, $\mathrm{cm}{\cdot}\mathrm{s}^{-1}$	ΔT, K	T_M, K	T maximum location
$k-\omega$ SST half	6.75E-03	-3.6E-04	-5.4	1.42	37.7	393.4	left
$k-\varepsilon$ half	6.75E-03	3.5E-04	5.2	1.36	53.0	408.8	right
$k-\omega$ SST full	1.35E-02	3.4E-05	0.3	1.40	38.5	398.6	right
LES $t = 77$ s	1.35E-02	-2.4E-04	-1.8	1.40	36.6	397.2	left
LES av.	1.35E-02	-3.0E-04	-2.2	1.42	35.5	393.2	left
experiment [22]					33.5		

7 Examples of industrial applications

Simulation of the physical processes in the industrial induction equipment demands very fast and precise calculations of the involved physical phenomena (e.g., coupled EM, HD and thermal field). However, recent developments in computer technics and numerical algorithms allow using the most advanced computational technics also for heat and mass transport simulation in liquid metal flows for industrial applications. There are two examples of the LES method application for solving industrial problems in induction furnace with the cold crucible and in large industrial induction channel furnace.

7.1 Induction furnace with the cold crucible

Cold crucible melting [111] is usually performed in a water cooled copper crucible, which allows producing of clean melts of aggressive materials, because the melt is surrounded by skull made of the same material due to the contact with the cold crucible walls. In special cases with the help of a special inductor design and location a levitating melting can be achieved [56, 106].

The working frequencies of IFCC are very different depending on the melted material. For metals frequencies are in kHz range while for oxides their are within MHz. A water cooled AC coil surrounds the crucible with slitted walls causing EM field to penetrate the walls and create induction currents, melt the alloy and partially suspend it against gravity away from water-cooled surfaces (figure 7.1). Strong stirring occurs in the melt due to the induced EM Lorentz forces and very high temperatures can be achieved under the right conditions

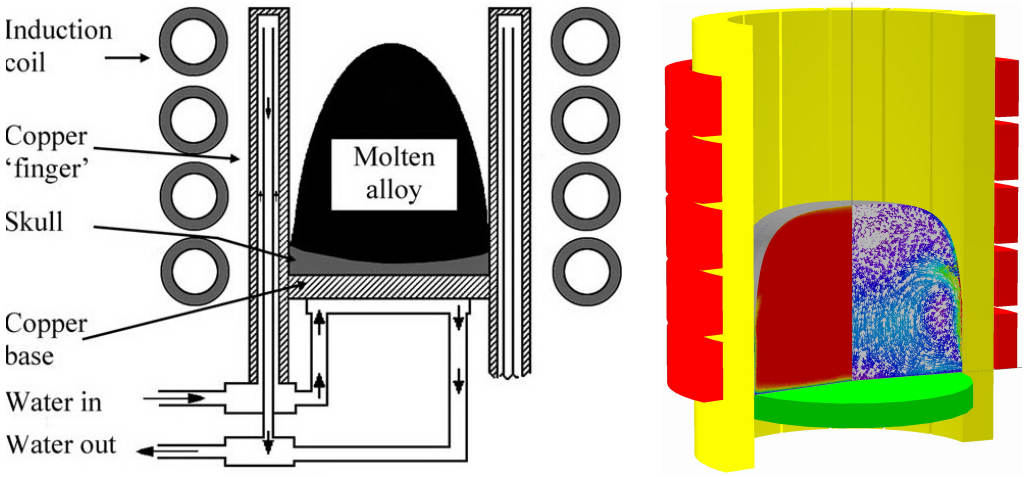

(a) IFCC design [40] (b) 3D view

Figure 7.1: Construction and 3D sketch of IFCC.

(i.e., provided contact with water cooled walls is minimised) allowing melting of TiAl and Ti6Al4V alloys for Aerospace [40].

The same simulation approach was used for TiAl melt flow simulation in IFCC. EM and HD calculations were decoupled as usually. EM simulation was performed iteratively using 3D *ANSYS* model of a half wall slit with melt inside (figure 7.2). These computations were performed in cooperation with M. Sc. A. Umbrashko, which was created a program for estimation of TiAl free surface and EM calculations using 3D *ANSYS* and also performed a part of HD calculations in collaboration with Institute of Electrotechnology, Leibniz University of Hannover. The EM model allows direct computations of the induced currents (figure 7.3) and therefore of 3D EM field distribution. 3D simulation of the cold crucible system was necessary because non-homogeneous due to the slitted crucible Lorentz force distribution could influence 3D transient flow of the melt and 2D axis-symmetrical model with effective magnetic permeability of the crucible walls [11] can provide only approximate EM field distribution in the liquid metal.

Heat and mass transport simulation for 7 kg TiAl flow with amplitude inductor current 3100 A and current frequency 20 kHz in 8 cm IFFC is presented below. This is only one simulation result from the performed parameter study on TiAl

overheat temperature depending on the crucible radii, melt mass and inductor current parameters.

Iterating approach is used to find a correct meniscus shape of the molten TiAl. The next balance equation should be satisfied in 43 control points on the free surface of the melt [24]:

$$\gamma\left(\frac{1}{R_1}+\frac{1}{R_2}\right)+\frac{B^2}{2\mu_0}=\rho g z, \tag{7.1}$$

where γ is the surface tension coefficient, R_1 and R_2 are the main curvature radiuses. This approach does not account for the melt flow influence on the melt meniscus shape because it will make calculations more complicated and possibly introduce additional instability into the model. Such simplification can be applied, if the shield parameter $\mathrm{R}_\omega = \mu\sigma\omega R^2$ is larger than 10 [95], where μ is the magnetic permeability of the medium and R is the radii of the crucible. For the studied IFCC: $\mu = 1$, $\sigma \approx 10^6$ S/m, $R \approx 0.1$ m, $\omega = 2\pi f = 2 \cdot 3.14 \cdot 2 \cdot 10^4 \approx 1.26 \cdot 10^5$ 1/s and $R_\omega \approx 1.3 \cdot 10^9 \gg 10$.

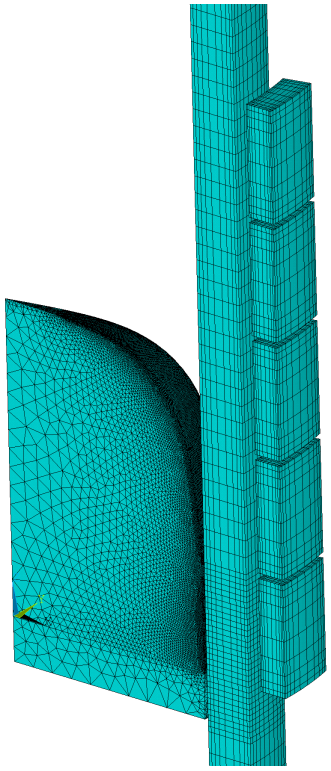

Figure 7.2: The final TiAl shape meshed for EM calculations in ANSYS (20 kHz, 3100 A).

7.1.1 EM analysis

Distribution of power losses in 3D ANSYS EM model (table 7.1) shows that major amount of EM energy (at least 55%) is accepted by the slit walls of the crucible. Amount of energy accepted by the melt (efficiency factor) is between 20 and 25% for all frequencies and currents. Relative power losses distribution in the melt is almost constant for the selected currents and frequencies and is small influenced

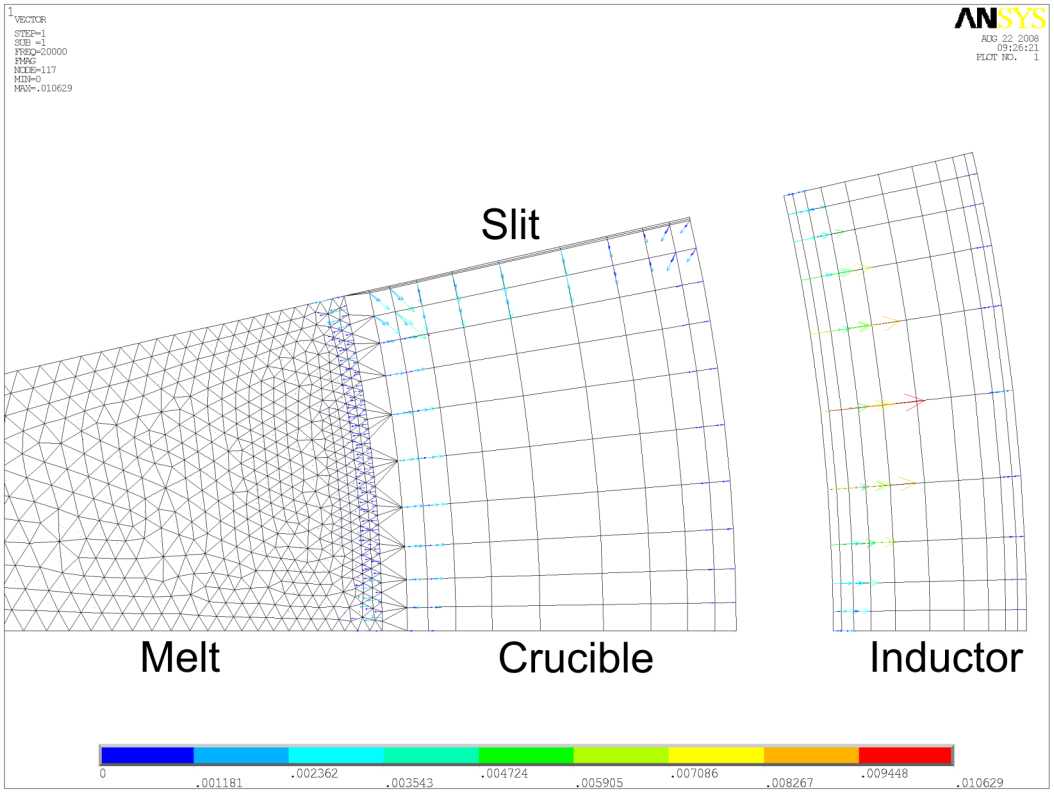

Figure 7.3: Current density distribution at the bottom of the melt (1/28 part of the full 3D).

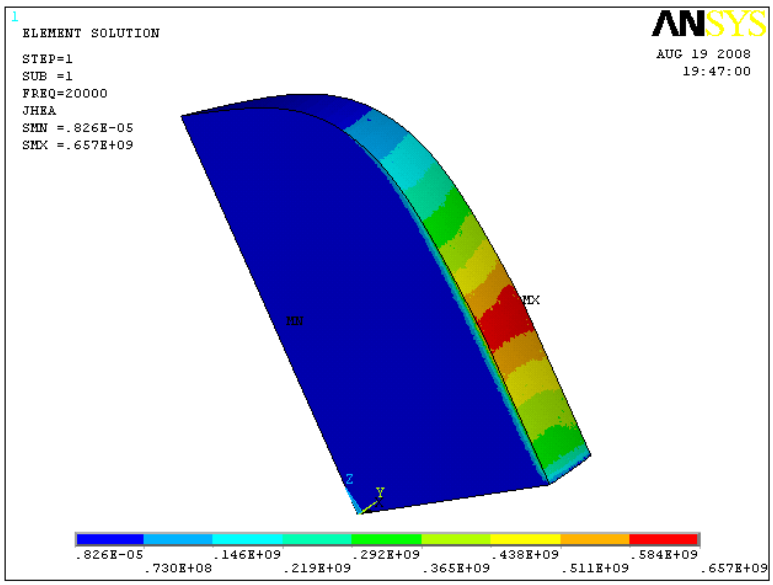

Figure 7.4: 3D Joule heat source distribution on the surface of the melt (20 kHz, 3100 A).

by the shape of the TiAl load. Quantitative value of EM power losses in the melt depends on the total generator power and on the coupling between the melt, the crucible and the inductor. For example, total power of the system is about 186 kW for 20 kHz 4 kA current (table 7.1). The height of 7 kg melt in this case is about 12 cm therefore melt is closer to the crucible walls comparing to higher currents and power losses in the melt increases, therefore increasing efficiency of melting.

Table 7.1: EM power losses in different regions of the 3D IFCC model depending on inductor current.

f, kHz	I, A	Melt height, cm	Inductor losses, kW	Crucible walls, kW	Crucible base, kW	Melt, kW	Total losses, kW
5	6500	15.34	27.5	97.1	9.8	36.3	170.7
10	5000	13.12	23.9	104.5	11.6	38.5	179.0
20	4000	11.89	21.5	109.8	11.0	44.6	186.5
20	3100	11.25	13.2	66.2	5.1	35.4	119.9

IFCC TiAl (table 2.1) flow calculations included 3D distribution of radial (figure 7.5(a)) and axial (figure 7.5(b)) Lorentz force components and Joule heat sources (figure 7.4) for correct description of the EM field penetration through the crucible slits. 3D simulation introduce maximal Joule heat and Lorentz force density on the melt surface between the wall slits. Maximal radial Lorentz force density can be found at the point where melt is pressed away from the crucible walls. Axial component maximal modulus is placed somewhere near the side of free surface and is twice less than the radial force maximal modulus.

7.1.2 HD simulation

FLUENT HD mesh had about 3 million elements with refined boundary regions. Characteristic size of the element in the middle was about 1.3 mm, near the border – $0.2 \div 0.4$ mm. The model had no slip boundary conditions for all melt surfaces, fixed temperature $T_{melting} = 1773$ K on all contact surfaces with

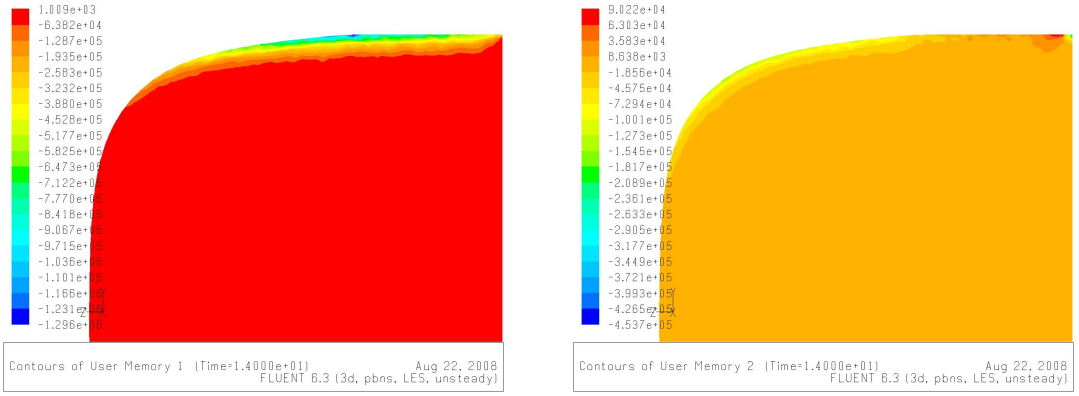

(a) radial Lorentz force F_r (b) axial Lorentz force F_z

Figure 7.5: Lorentz force distribution in the melt (20 kHz, 3100 A).

the cooled crucible and radiation from the upper free surface (T_{ref} = 300 K, k_r = 0.3). Converged steady $k-\varepsilon$ model results (figures 7.6(b), 7.6(b), 7.7(a)) were used as initial conditions for transient LES calculations with 0.01 s time step.

$K-\varepsilon$ model calculated velocity pattern (figure 7.6(b)) introduce the typical two vortex flow structure on the meridian plane. Although flow intensity in the bottom vortex is larger, upper vortex is still present. Maximal velocities near 0.8 m/s are observed in the side boundary region of the melt. Bottom vortex velocity values at the symmetry axis are at least twice smaller. Such vortical flow structure provide very rigorous TiAl stirring as it can be seen from figure 7.6(d) where instantaneous velocity distribution is shown. Averaged LES velocity distribution (figure 7.6(f)) introduce larger maximal velocities in the flow. Smaller vortex can be identified with difficulties, but all upper half of the melt has small average velocities comparing to $k-\varepsilon$ results. However, instantaneous flow pattern (figure 7.6(d)) shows many small turbulent vortices there.

Upper views of velocity distribution between the vortices (figures 7.6(a), 7.6(c), 7.6(e)) introduce periodical zones of higher and lower radial velocities, which are created due to the periodical distribution of the Lorentz forces.

LES calculated average temperature distribution (figure 7.7(b)) is more homogeneous comparing to $k-\varepsilon$ model result (figure 7.7(a)), which has well pro-

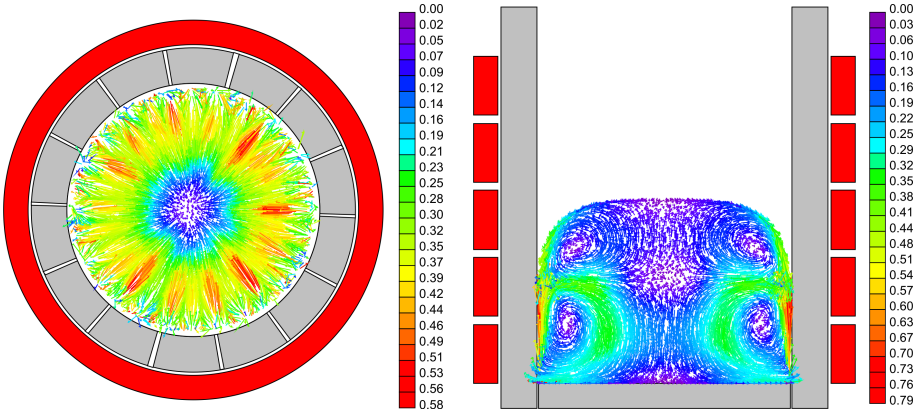

(a) $k - \varepsilon$, $z = 0.06$ m (b) $k - \varepsilon$, $x = 0$

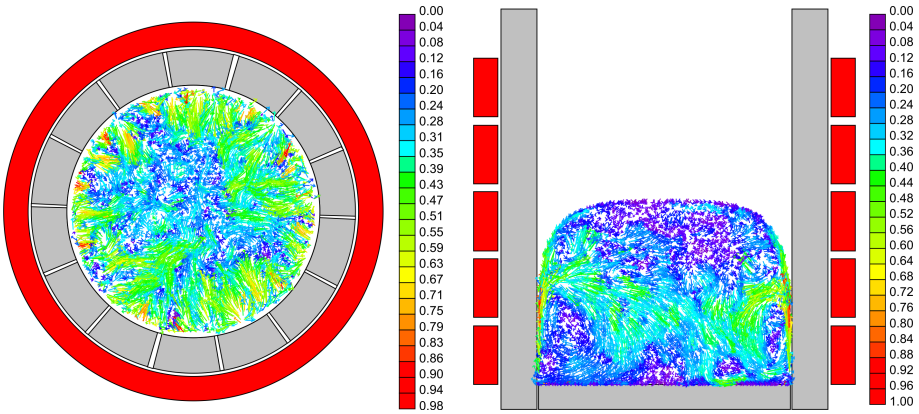

(c) LES, $t = 30$ s, $z = 0.06$ m (d) LES, $t = 30$ s, $x = 0$

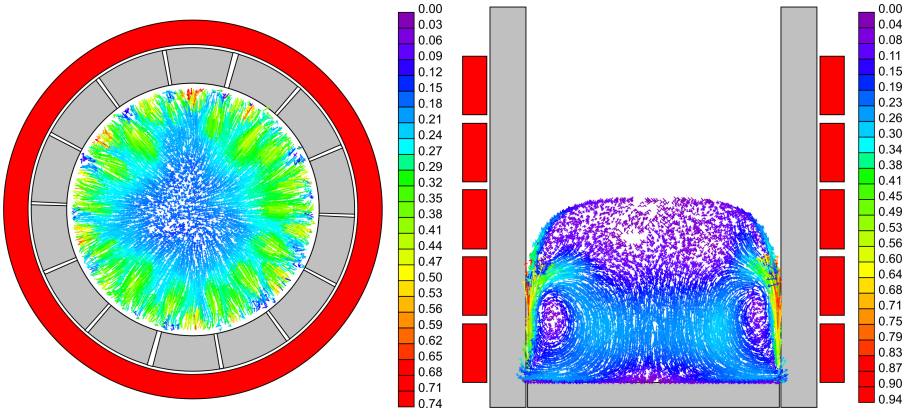

(e) LES averaged, $z = 0.06$ m (f) LES averaged, $x = 0$

Figure 7.6: Velocity vectors in TiAl melt (20 kHz, 3100 A).

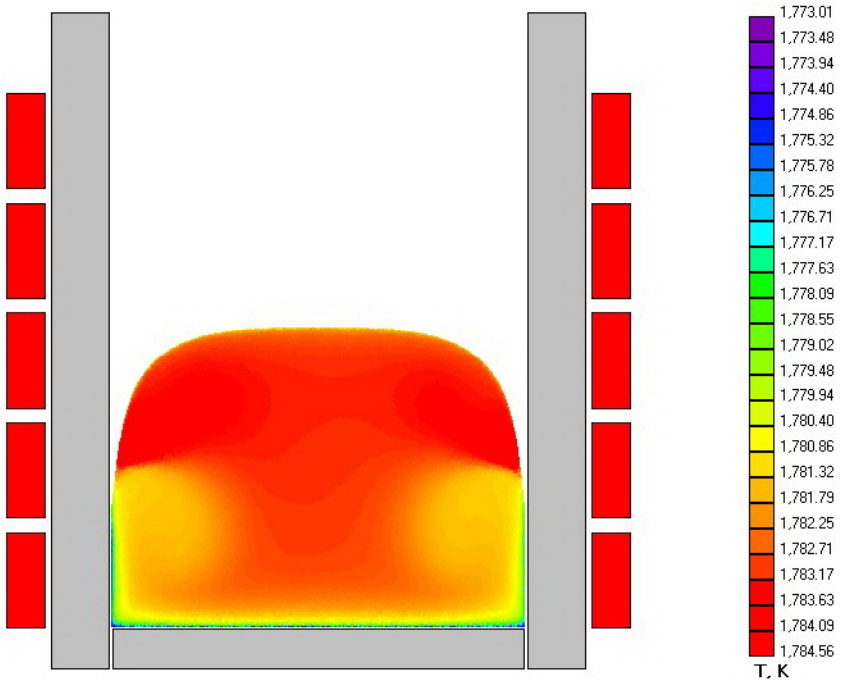

(a) $k - \varepsilon$, $x = 0$

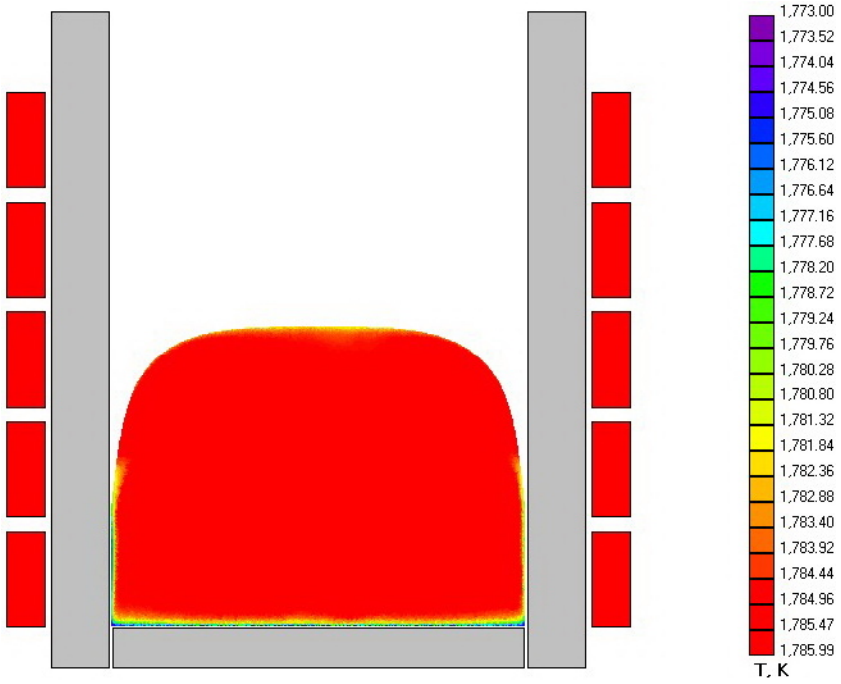

(b) LES averaged, $x = 0$

Figure 7.7: Temperature distributions in TiAl melt (20 kHz, 3100 A).

nounced $4 \div 5$ K temperature difference on the border between upper and lower vortices. Temperature homogenization in the melt is guarantied by high intensity turbulent steering, which is also observed in experiments with Al [5].

7.1.3 Results discussion

Result analysis have introduced that higher melt overheat can be achieved with the smaller coil current if its frequency is increased (table 7.2). Therefore, common power losses in the IFCC system can be reduced. For example maximal overheat temperature in the melt is about 34 K for 4 kA current at 20 kHz. Two vortex averaged flow structure was seen in all calculations. Maximal velocities in the flow are observed in the lower vortex in the near crucible surface region. Maximal velocity values decreases when EM field frequency becomes larger.

Table 7.2: Calculated characteristic velocities and temperatures in 7 kg TiAl melt depending on inductor current and frequency.

Melt height, cm	I, kA	f, kHz	P_{melt} kW	$k-\varepsilon$ v_m, m/s	$k-\varepsilon$ T_m, K	LES v_m, m/s	LES T_m, K	Overheat, ΔT K
15.3	6.5	5	36.3	1.41	1791	1.33	1795	22
13.1	5.0	10	38.5	1.16	1796	1.16	1800	27
11.9	4.0	20	44.5	1.11	1801	1.14	1807	34
11.3	3.1	20	35.4	0.79	1785	0.94	1786	13

7.2 Industrial channel furnaces

The total electrical power of the chosen one-loop industrial channel furnace for cast iron (table 6.4) was just 240 kW. Geometry of this furnace has many right angles and the neck contains only flat surfaces. This furnace is also characterized by several possible symmetries. The full furnace geometry can be constructed by reflection $y = 0$ and this symmetry is used for EM model. HD simulation

theoretically can be performed on a quarter model with reflection $x = 0$, but such model will remove some degree of freedom even in steady solution.

7.2.1 EM simulation

The model had only electrically important regions (figure 7.8(a)) with the standard material properties, however the iron core had applied electrical resistivity $\rho_{core} = 10^4 \cdot 9.579 \cdot 10^{-8} = 9.579 \cdot 10^{-4}$ Ω·m (10^4 times the iron resistivity), which was excluded from the experimental furnace model due to high electrical losses. As a result induced heat in the iron core is about 5% of the total electrical power (table 7.3). The furnace efficiency therefore is 90.5%, which is comparable to the experimental furnace where it was 93.6%.

Table 7.3: EM power losses in different regions of the model.

Inductor current amplitude	Melt	Inductor	Cooling Shield	Iron Core	Total
1074.8 A	219.0 kW	8.8 kW	8.1 kW	5.8 kW	241.8 kW

EM model had half of the geometry due to symmetry conditions. The furnace AC inductor had two layers and different distances between the turns, which were combined in blocks by 4. The total number of turns was $7 \times 4 = 28$ for the half geometry model. All geometry parts except the neck and air were meshed with hexahedral elements. The total element count was about 1.2 million.

The EM model has produced a text file with the forces (figure 7.8(b)) and heat sources for HD simulation.

7.2.2 HD simulation

Hydrodynamic simulation was performed in *FLUENT 6.3.26* CFD package. The model mesh was built in *GAMBIT* using *ANSYS* IGES export of the full melt geometry. Final mesh from *GAMBIT* was additionally adapted in *FLUENT* to refine boundary regions and the mesh had 3.7 million nodes.

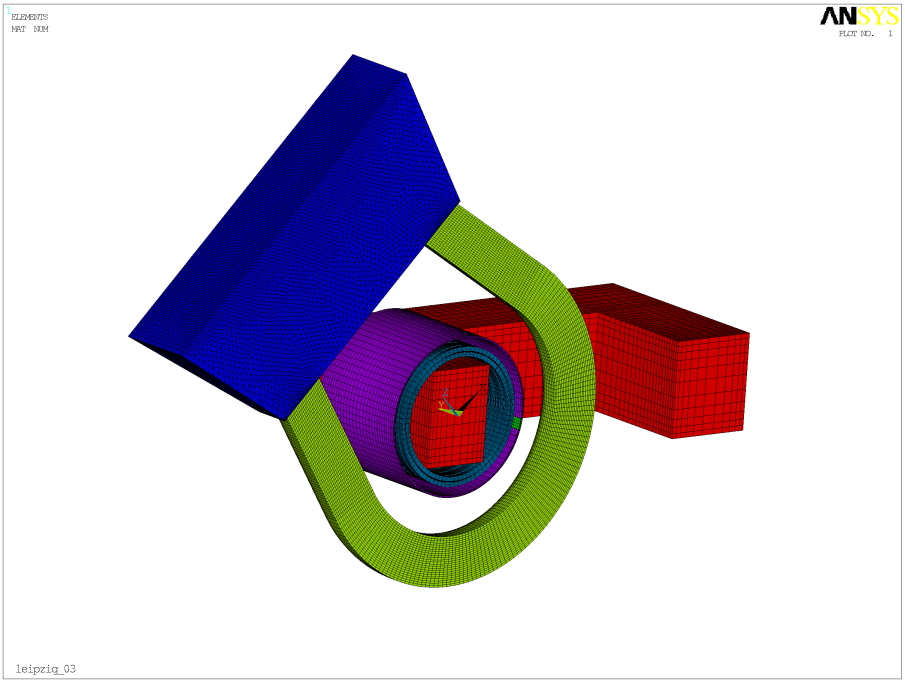

(a) Parts & mesh

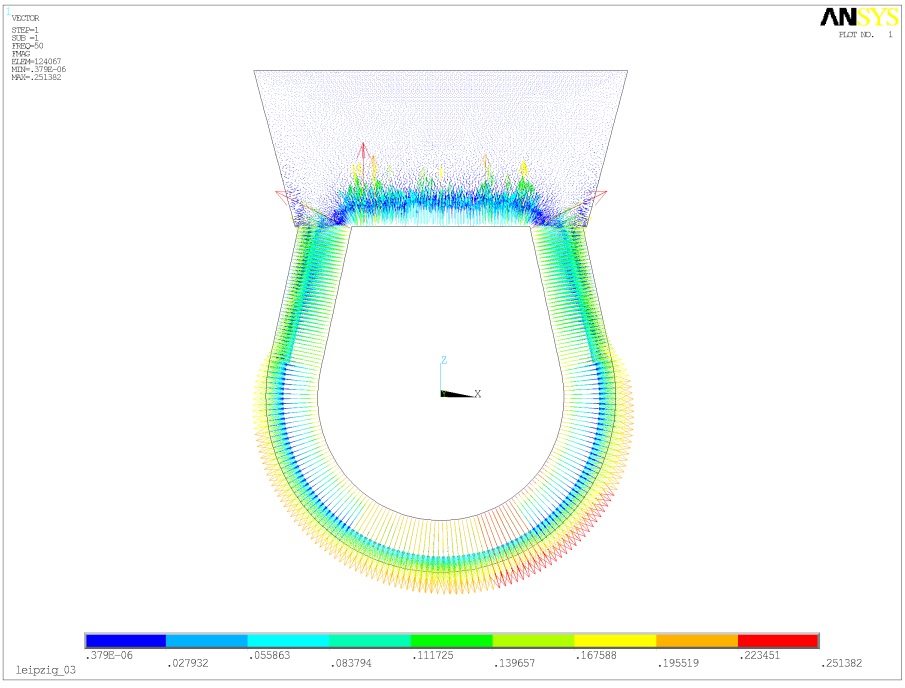

(b) EM forces

Figure 7.8: Parts, mesh and Lorentz force distribution in Leipzig EM ANSYS model, $I_A = 1621$ A, $f = 50$ Hz.

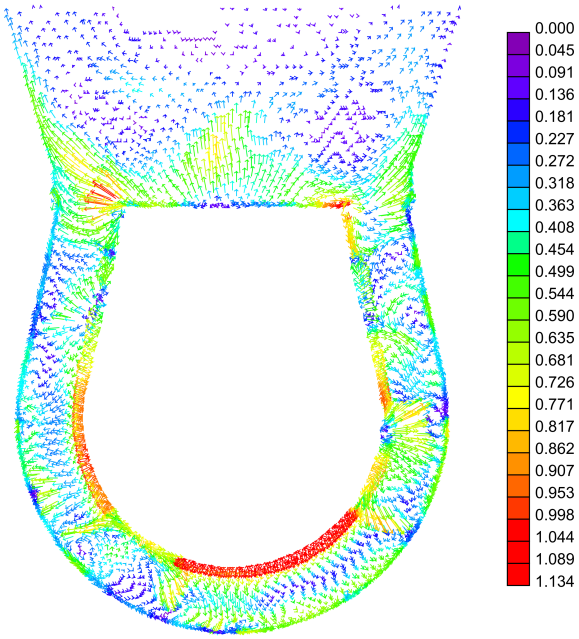

(a) Side view $y = 0$, velocity

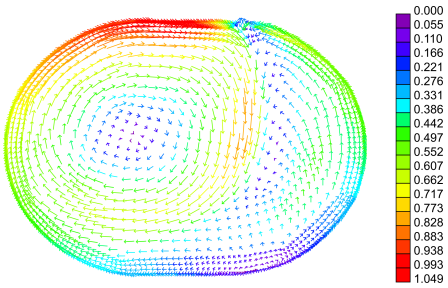

(b) Channel view $x = 0$, velocity

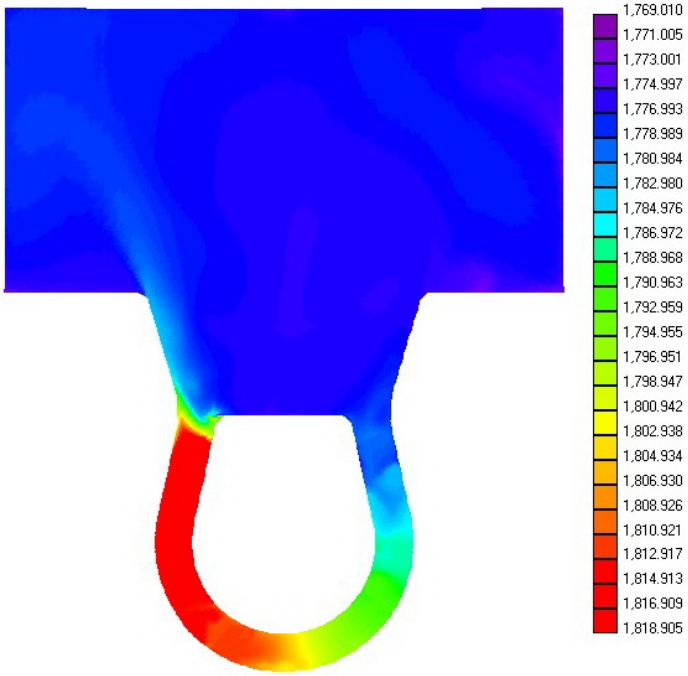

(c) Side view $y = 0$, temperature

Figure 7.9: SST calculated initial velocity and temperature distributions for Leipzig furnace.

Hydrodynamical boundary conditions included no-slip for all solid walls and free-slip for the free boundary. The gravity was collinear to z axis. Thermal boundary conditions were as follows:

- Channel, neck, bath walls: heat transfer $k = 6$ W/(m^2·K) to 330 K;
- Flange: heat transfer $k = 60$ W/(m^2·K) to 330 K;
- Top surface: radiation heat flux $T_{ref} = 1600$ K, $\varepsilon = 0.15$, $Q = -\varepsilon\sigma_B(T^4 - T_{ref}^4)$ ($\sigma_B = 5.67 \cdot 10^{-8}$ W/(m^2·K^4));

Steady $k-\omega$ SST solution was obtained for LES initial conditions (figure 7.9). Strong upward flow can be noticed near the channel exits and just above the inductor at the symmetry plane $y = 0$ (figure 7.9(a)). The maximal flow intensity there is about 1 m/s but it rapidly decays in the bath with the growing distance from the neck bottom. Clean radial flow in the channel can be noticed, but the channel flow mainly is formed by the turbulent vortices with characteristic velocities about 0.5 m/s.

Flow in the channel cross-section (figure 7.9(b)) usually is presented by two recirculating vortices, which rotation axis is directed along the channel at different time moments. Flow structure substantially changes in the channel exit to the neck, where eddy rotation axis becomes orthogonal to the previous direction and flow intensity decreases. Maximal flow velocities are noticed near the channel wall and this steady solution can be unstable.

Temperature distribution in the bath is very homogeneous (figure 7.9(c)). A little hotter region is formed above the neck, where heat from the channel is transported to the bath by the near-wall upward flow. Bath bottom corners are colder and slag formations can occur there. Temperature maximum in the channel has wide localization from one channel side. Temperature gradient between the temperature maximum and the bath is about 40 K and temperature changes very rapidly near the channel exit where its maximum is located.

LES was started from the described SST solution and 70 s of the flow were calculated with 0.005 s time step. The latest 60 s were averaged. Instantaneous velocity patterns introduce turbulent chaotic flow in the channel and in the neck

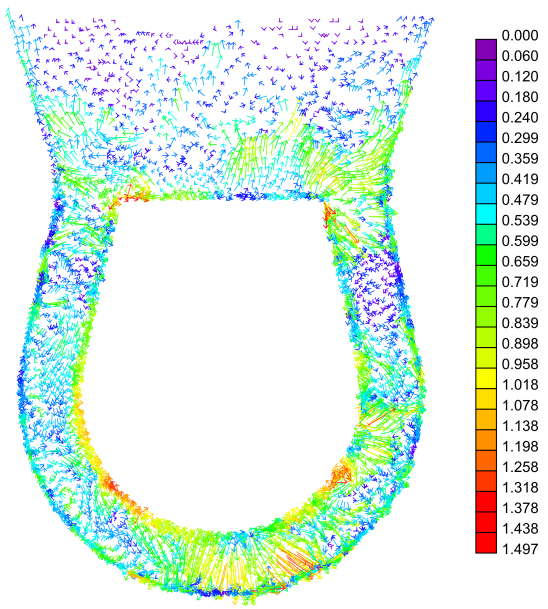

(a) $t = 70$ s, side $y = 0$

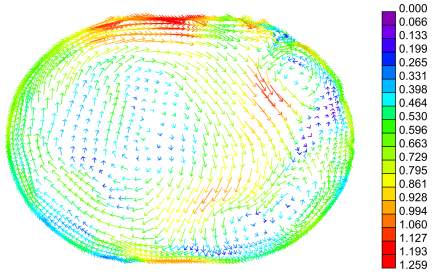

(b) $t = 20$ s, channel $x = 0$

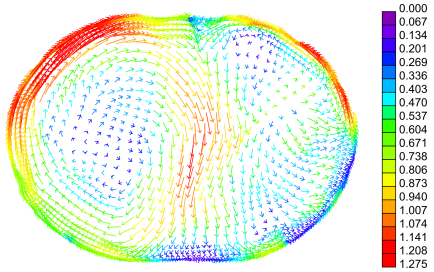

(c) $t = 70$ s, channel $x = 0$

Figure 7.10: LES instantaneous velocity distributions.

(figure 7.13) with maximal velocity values below 1.5 m/s. Two vortex structure in the channel cross-section seems to present almost all the time. Recirculating vortex sizes are different depending on time moment.

Velocity averaging (figure 7.11) introduce strong upward flow from the neck bottom at $y = 0$. This flow seems to be common for this design of the channel furnaces. The maximal flow velocities are noticed again near the channel exits (≈ 0.6 m/s) and near the inner channel wall (≈ 0.75 m/s). Average velocities in the straight channel part near the channel exits seems to be relatively small, which means strong vortical interaction between neck and channel flows there. Characteristic average velocities in the channel are about $0.35 \div 0.50$ m/s (figure 7.11(b)). One of the averaged vortices in the channel cross-section seems to be very suppressed, which means that flow pattern is often presented by one vortex structure.

Temperature evolution in time shows migration of the maximum location to the middle of the channel (figures 7.12(a) and 7.12(b)). Possibly 70 s of flow

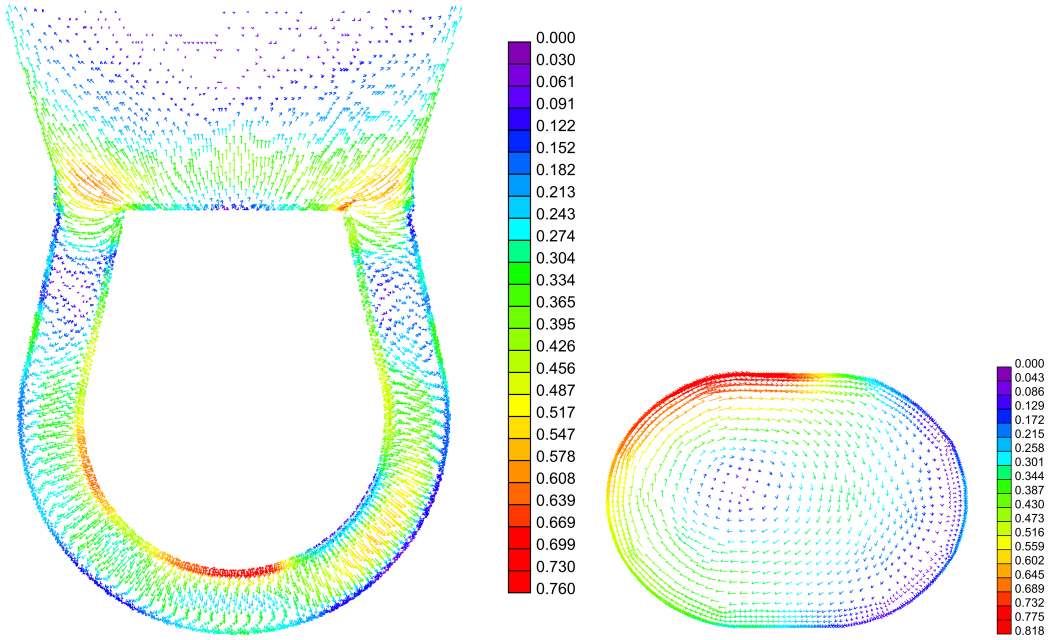

(a) Side view, $y = 0$ (b) Channel view, $x = 0$

Figure 7.11: LES averaged velocity distribution for Leipzig furnace.

development are not enough to estimate tendencies in temperature maximum movements certainly because it has been seen that the temperature maximum can move back from other industrial channel furnace simulations. However, maximal melt temperature and temperature distribution in the bath remain approximately the same during this transition.

Time dependent temperature charts (figure 7.13(a)) are taken at the next channel points: $x \approx -0.34$ m, $z \approx 0$ (left); $x \approx 0$, $z \approx -0.34$ m (center); $x \approx 0.34$ m, $z \approx 0$ (right). The chart illustrates moving of the temperature maximum to the other side of the channel. All temperatures are decreasing till $t = 25$ s. Then temperature in the left side of the channel (where the maximum was placed) continue to decrease, but temperature in the channel center and at the right side are growing almost linearly. Some large period temperature oscillations are noticed only at $25 < t < 50$ s. High frequency oscillations have amplitude about 2.5 K.

Averaged temperature distribution (figure 7.12(c)) still have temperature max-

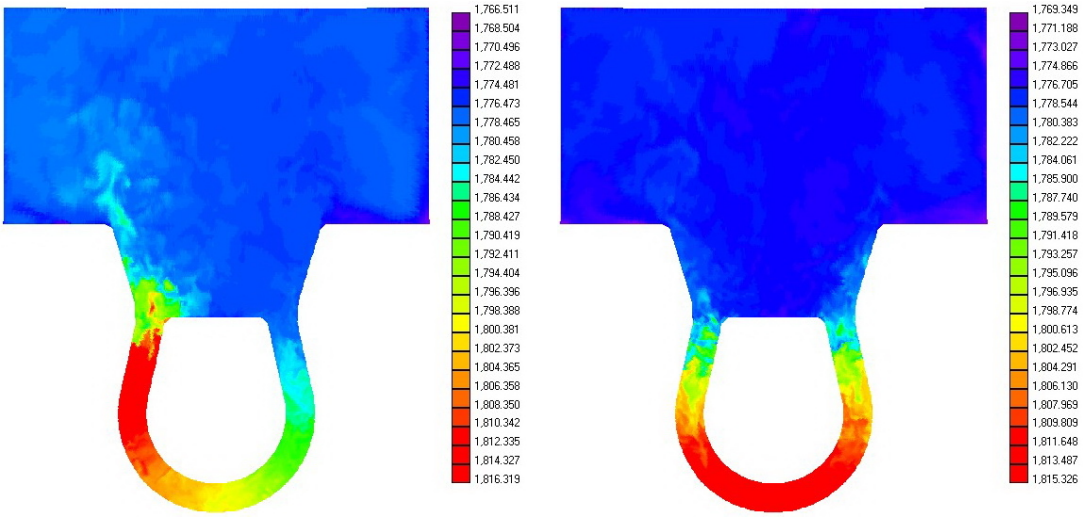

(a) $t = 20$ s

(b) $t = 70$ s

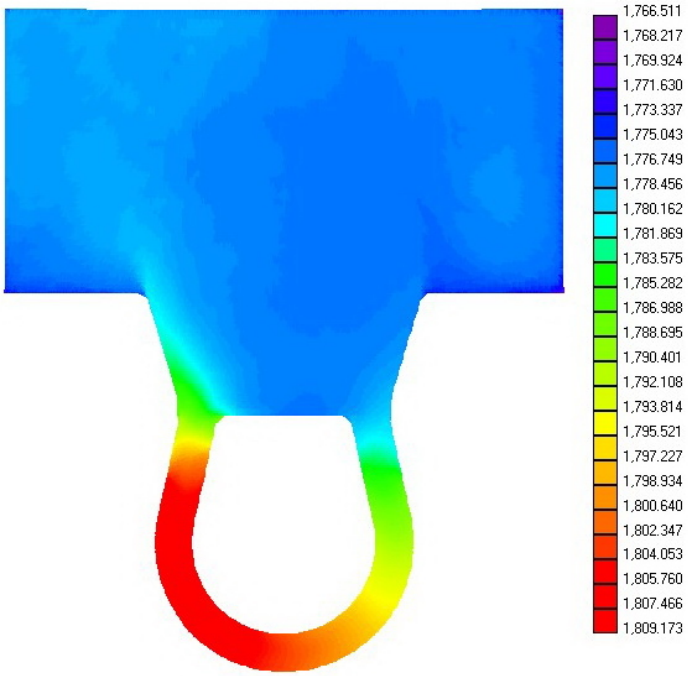

(c) Averaged

Figure 7.12: LES instantaneous and averaged temperature distributions.

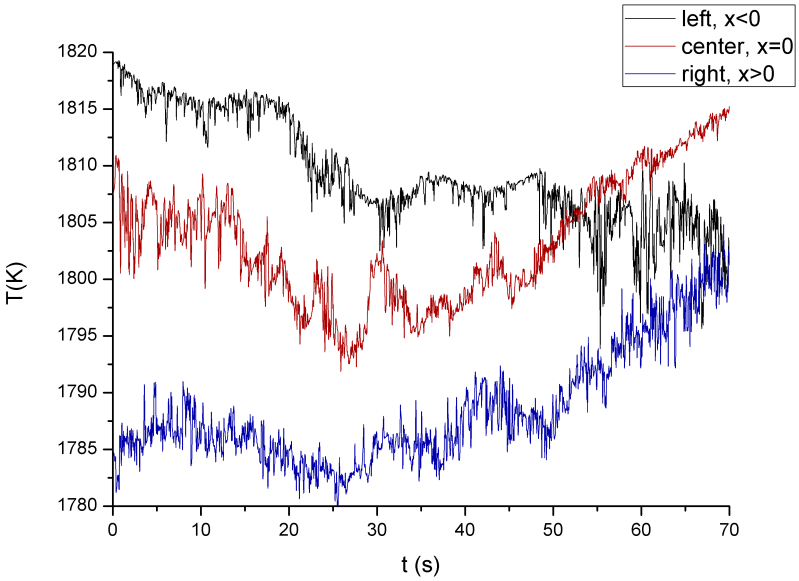

(a) Temperature evolution in time

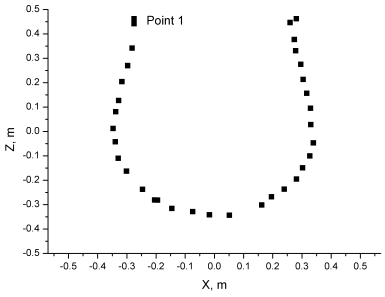

(b) Points in the channel

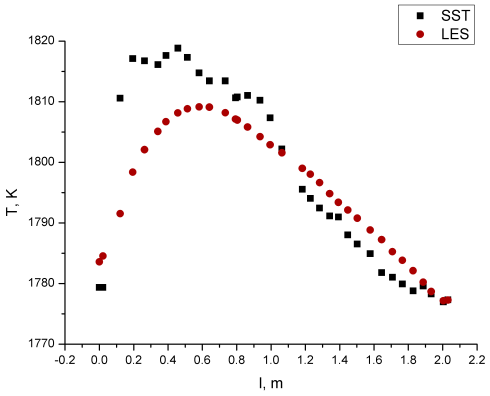

(c) SST and averaged LES along the channel

Figure 7.13: Time dependent and averaged temperatures in the channel.

Table 7.4: Thermal losses in kW through different model boundaries.

	Channel	Neck	Flange	Bath walls	Bath top	Total	Input	Diff
SST	-46.1	-37.8	-4.1	-61.6	-67.4	-216.9	217.1	0.2
LES $t = 20$ s	-46.0	-37.7	-4.0	-61.6	-62.7	-211.9	217.1	5.1
LES $t = 70$ s	-46.2	-37.7	-4.0	-61.6	-62.6	-212.1	217.1	4.9

imum on the one side of the channel. Such location and pronounced temperature gradients near the channel exits indicate existence of the transit flow. The LES averaged temperature difference in the channel is just above 30 K (figure 7.13), which is comparable to the experimental data on Wood's melt laboratory furnace. Temperature distribution along the channel calculated with SST and averaged LES is shown for selected points (figure 7.13(b)), which location is chosen just with a mouse on a display. SST result is not very smooth, due to solution oscillations. It also has larger temperature differences above 40 K and more expressed maximum plateau. Power balance is good through the all calculations (table 7.4). Five kilowatt energy profit indicates that temperature still can grow a little higher, but for transient simulation balance seems to be very good.

7.2.3 Turbulent kinetic energy

Turbulent kinetic energy maps were created from *FLUENT* profile files. The turbulent energy maximums are placed in the round part of the channel at symmetry plane $y = 0$. The maximal turbulent energy values are near 0.3 J/kg in y energy component (figure 7.14(b)). X and z energy components (figures 7.14(a) and 7.14(c)) have approximately equal maximal values, which are one order of magnitude smaller comparing to y component. Both components also have local maximums in the neck above the channel and near the channel exits. y turbulent energy maximums are placed mainly in the inner channel radius at $y = 0$ where two recirculating channel vortices collapse. In general y energy component is analogous to the axial turbulent energy component for the cylindrical induction furnace, which also is larger comparing to other both components.

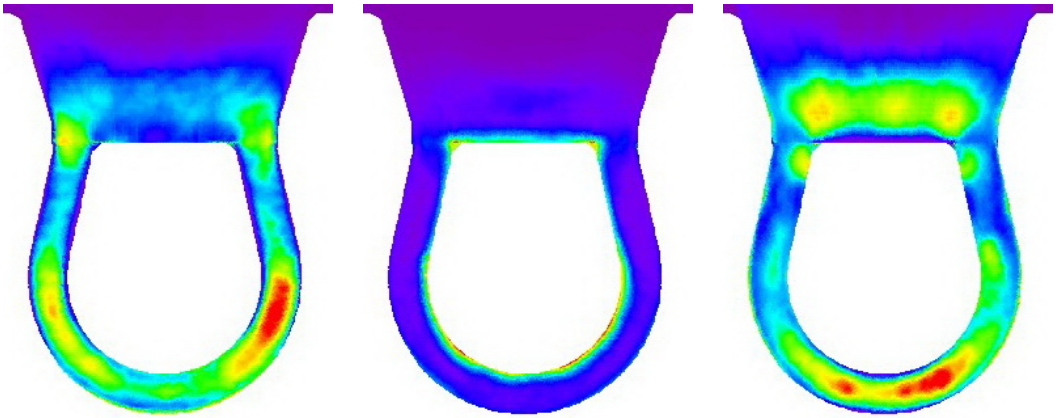

(a) $(0.5v'_x v'_x)_{max} = 0.08$ J/kg, $y = 0$ (b) $(0.5v'_y v'_y)_{max} = 0.30$ J/kg, $y = 0$ (c) $(0.5v'_z v'_z)_{max} = 0.08$ J/kg, $y = 0$

Figure 7.14: Turbulent kinetic energy.

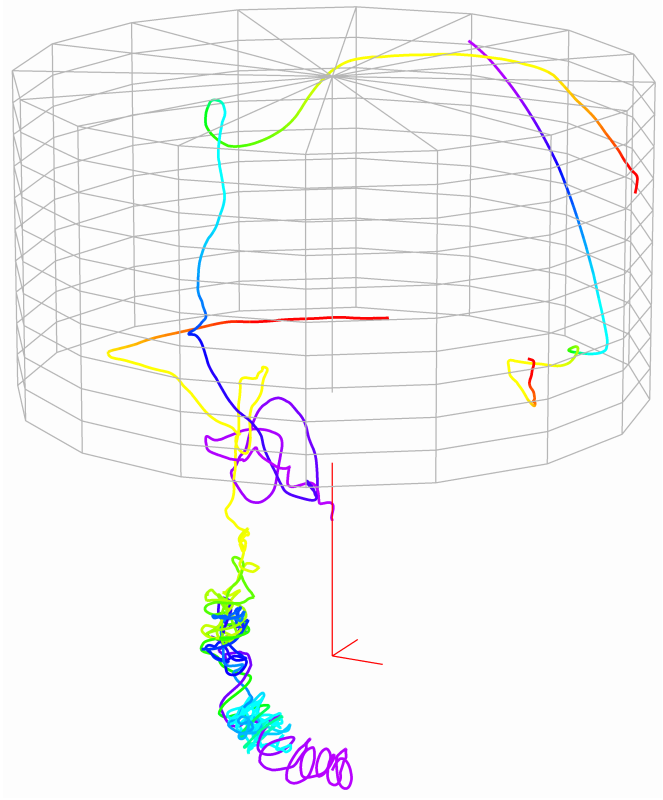

Figure 7.15: LES calculated 60 s particle tracks ($d_p = 0.2$ mm, $\sigma_p = 0$, $\rho_p = 5250$ kg/m$^3 \approx 0.75\rho$).

7.2.4 Particle tracking

Lagrangian particle tracking was performed on this model of industrial induction channel furnace for cast Iron. This tracking also included EM particle force, so $\sigma_p = 0$. Several 0.2 mm particles with $\rho_p = 5250$ kg/m^3 $\approx 0.75\rho$ are released in the different ICF parts, five of them – near the bottom central point in the channel. Their trajectories (figure 7.15) show presence of the mainly thermally determined transit melt flow in the channel, which intensity is much smaller than the intensity of turbulent dominating vortices. Particles tracks represent the previously mentioned properties of vortices near the channel exits. Particles tracing allows to estimate this transit flow velocity, which in this case is near 7 cm/s, while the average particle velocity is above 50 cm/s.

8 Conclusions and future work

Large Eddy Simulations (LES) and flow velocity measurement experiments have been used to study the flow and turbulence structure in a cylindrical crucible under the influence of EM driving force. Experimental results were used to verify numerical simulation of the studied phenomena. Additional numerical study was performed on the near-wall particle accumulation depending on different particle Stokes numbers and physical properties. As a result a comprehensive set of pre- and post-processing tools was created, which was also tested on a mathematical model of the large scale channel induction furnace.

The experiments were performed on a laboratory induction furnace with a Wood's melt using high precision analog-digital amplifier-converter, which are used in medicine. Flow velocities were measured in selected points inside the melt with several permanent magnet probes. Measurements have been made with with the probes, calibrated using the old experimental data and possibly they should be repeated in the future with higher precision. However, these measurements have confirmed the existence of low-frequency velocity oscillations, which introduce maximum of turbulent kinetic energy in the central zone of the melt near the crucible wall. As a result heat and mass exchange between the "main" eddies in the flow is dramatically improved and it can be characteristic for other hydrodynamic system with several turbulent recirculating eddies. Experiments have also shown large influence of the furnace geometry and inductor parameters on the flow structure and characteristic velocities. The smaller melt height and unsymmetrical coil placement increase the maximal flow velocities and intensify turbulent exchange in the melt.

The mathematical model was created in two CFD codes: *FLUENT* and *ANSYS CFX*. Both codes have shown similar numerical results: average velocities were $10 \div 15\%$ less than in experiments, however extreme values of the instan-

taneous velocities were very close. Transient 3D models also have presented low-frequency velocity oscillations like in experiments.

Lagrangian particle tracing has shown preferential accumulation of large particles in the near-wall crucible region. Particle density differences, boundary conditions and EM field can lead to collection of almost all 1 mm particles in the near-wall melt layer. Particles concentrate there in the top, middle or bottom half depending on density ratio ρ_p/ρ. Boundary conditions influence angular homogenization of the particle volume fraction and EM field can completely break the particle motion.

The same numerical technique was used for LES investigation of the channel induction furnace. Calculated results have presented good quantitative agreement with experimental data in both velocity and temperature distributions. The presence of small transit flow, which was found in experiments with symmetrical channel furnace, was confirmed numerically with steady and transient 3D models. Transit flow velocity was found to be not more than 5 cm/s for laboratory CIF. As a result temperature maximum in the channel is shifted to the right or left side. Intensive flow vortices near the channel exits play an important role for the heat transport to the bath. These vortices are analogues to the "main" recirculated vortices in the cylindrical induction furnace.

The proposed numerical simulation technique was applied to investigation of heat and mass transport in industrial size CIF with cast iron and in IFCC with TiAl melt. Both models introduced possibility of LES usage for engineering applications.

Future work will include deeper theoretical investigation of the flow in a cylindrical geometry with a linear stability analysis and new experimental measurements of the flow velocity for different induction furnace configurations. Experimental results will be used for creation of 3D numerical models, which also will account for free surface deformations and melt solidification. Several channel induction furnaces will be studied with the described approach in the future and their geometry will be optimized for better heat exchange between the channel and the bath.

References

[1] *FLUENT 6.2 User's Guide*. Fluent Inc., Lebanon, January 2005. 32

[2] Yu. Gelfgat A. Bojarevics, V. Bojarevics and K. Pericleous. Liquid metal turbulent flow dynamics in a cylindrical container with free surface: experiment and numerical analysis. *Magnitnaya Gidrodinamika*, 35(3):258–277, 1999. 41

[3] Yu. Gelfgat A. Bojarevičs, A. Cramer and G. Gerbeth. Experiments on the magnetic damping of an inductively stirred liquid metal flow. *Experiments in Fluids*, 40:257–266, 2005. 2, 39, 41

[4] Th. Gundrum A. Cramer, K. Varshney and G. Gerbeth. Experimental study on the sensitivity and accuracy of electric potential local flow measurements. *Flow Measurement and Instrumentation*, 17:1–11, 2006. 40

[5] B. Nacke A. Jakovics A. Umbrashko, E. Baake and M. Kirpo. Analysis of th effectiveness of the melting process in the cold crucible using 3d modelling. In *2007 International Symposium on Liquid Metal Processing and Casting*, pages 273–277, Nancy, France, 2007. 7, 170

[6] S.A. Argyropoulos. Measuring velocity in high-temperature liquid metals: a review. *Scandinavian Journal of Metallurgy*, 30(5):273–285, 2000. 36

[7] M.Y. Levina M.Y. Stolov V.I. Sharamkin A.V. Arefjev, I.E. Bucenieks and E.V. Scherbinin. *Heat and Mass Transfer Intensification in Induction Channel Furnaces (preprint, in Russian)*. Inst. of Physics, Latvian SSR Academy of Sciences, Salaspils, 1981. 134

[8] E. Baake. *Grenzleistungs- und Aufkohlungsverhalten von Induktions-Tiegelöfen*. PhD thesis, Universität Hannover, Fakultät für Maschinenwesen, Düsseldorf, 1994. vii, 40, 47, 48, 53

[9] I.E. Barton. Comparison of SIMPLE- and PISO-type algorithms for transient flows. *Int. J. for Numerical Methods in Fluids*, 26(4):459–483, 1998. 70

[10] G.J. Brereton and A. Kodal. An adaptive turbulence filter for decomposition of organized turbulent flow. *Phys. Fluids*, 6, 1994. 57

[11] A. Muiznieks G. Raming A. Mhlbauer Ch. Stenzel C. Gross, W. Assmus. Power consumption of skull melting, part i: Analytical aspects and experiments. *Cryst. Res. Technol.*, 34(3):319–328, 199. 163

[12] Clayton T. Crowe, editor. *Multiphase flow handbook*. CRC Press, 2006. ISBN 0-8493-1280-9. vii, 31, 32, 33

[13] I. Daubechies. The wavelet transform, time-frequency localization and signal analysis. *IEEE Trans. Information Theory*, 36(5):961–1005, 1990. 64

[14] P.A. Davidson. *An Introduction to Magnetohydrodynamics*. Cambridge University Press, 2001. 12, 13, 42, 45

[15] J.W. Deardorff. A numerical study of three-dimensional turbulent channel flow at large reynolds numbers. *J. Fluid Mech.*, 41:453–480, 1970. 26

[16] N.I. Dragunkina and L.L. Tir. Experimental investigation of similarity conditions in the motion of molten metal in an induction furnace. *Magnetohydrodynamics*, 2(1):81–84, 1966. 37

[17] A. Jakovics E. Baake, B. Nacke and A. Umbrashko. Heat and mass transfer in turbulent flows with several recirculated flow eddies. *Magnetohydrodynamics*, 37(1–2). 71

[18] A. Umbrashko E. Baake, B. Nacke and A. Jakovics. Turbulent flow dynamics, heat transfer and mass exchange in the melt of induction funaces. In *Heating by Internal Sources*, pages 47–53, Padova, Italy, 2001. 57

[19] A. Umbrashko E. Baake, B. Nacke and A. Jakovics. Large eddy simulation modeling of heat and mass transfer in turbulent recirculated flows. *Magnetohydrodynamics*, 39:291–298, 2003. 2

[20] J. Miķelsons E. Šilters, G. Sermons. *Electrodynamics (in Latvian)*. Zvaigzne, Rīga, 1986. 15

[21] J.K. Eaton and J.R. Fessler. Preferential concentrations of particles by turbulence. *Int. J. Multiphase Flow*, 20:169–209, 1994. 30, 31

[22] A. Eggers. *Untersuchungen der Schmelzenströmung und des Wärmetrasports im Induktions-Rinnenöfen*. PhD thesis, Universität Hannover, Fakultät für Maschinenwesen, Düsseldorf, 1993. xiii, 137, 139, 159, 160, 161

[23] Y. Du Terrail F. Felten, Y. Fautrelle and O. Metais. Numerical modelling of electromagnetically-driven turbulent flows using LES methods. *Applied Mathematical Modelling*, 28:15–27, 2004. 14, 63, 79

[24] M. Zuccarini E. Takeuchi M.'Tani F. Negrini, M. Fabbri. Electromagnetic control of the meniscus shape during casting in a high frequency magnetic field. *Energy Conversion & Management*, 41:1687–1701, 2000. 164

[25] Y. Fautrelle. Analytical and numerical aspects of the electromagnetic stirring by alternating magnetic fields. *J. Fluid Mech.*, 102:405–430, 1981. 17

[26] K. Fujisaki and T. Ueyama. Magnetohydrodynamic calculation for free surfaces. *J. Applied Phys.*, 83(11):6356–6358, 1998. 94

[27] A. Silberberg G. Segré. Behaviour of macroscopic rigid spheres in Poiseuille flow. Part 2. Experimental results and interpretation. *J. Fluid Mech.*, 14: 136–157, 1962. 34

[28] J. Galpin and Y. Fautrelle. Liquid–metal flows induced by low–frequency alternating magnetic fields. *J. Fluid Mech.*, 239:383–408, 1992. 14

[29] G.Z. Gershuni and E.M. Zhukhovitskii. *Convective Instability of Incompressible Fluid (in Russian)*. Nauka Press, Moscow, 1972. 17

[30] J. Ghojel. Modelling of electromagnetically excited turbulent flow of molten metal in a twin-channel induction furnace. *Progress in Computational Fluid Dynamics*, 6(7):435–445, 2006. 138, 139

[31] J. Ghojel and R. Ibrahim. Computer simulation of the thermal regime of double-loop channel induction furnaces. *Journal of Materials Processing Technology*, 155–156:2093–2098, 2004. 138

[32] J.-L. Guermond and S. Prudhomme. On the construction of suitable solutions to the navier-stokes equations and questions regarding the definition of large eddy simulation. *Physica D*, 207(1–2):64–78, 2005. 26

[33] L.L. Tir G.Ya. Kochetkova, M.Ya. Stolov and P.M. Chaikin. The circulation of metal in an induction furnace. *Magnetohydrodynamics*, 2(2):85–87, 1966. 37

[34] G. Hawkes. Modeling an RF cold crucible induction heated melter with subsidence. In *2004 ASME Heat Transfer/Fluids Engineering Summer Conference*, Charlotte, North Carolina, USA, 2004. 7

[35] M.Y. Stolov I.E. Bucenieks, M.Y. Levina and E.V. Scherbinin. *Physical Grounds of MHD and Heat Phenomena in Induction Channel Furnaces (preprint, in Russian).* Inst. of Physics, Latvian SSR Academy of Sciences, Salaspils, 1980. 132, 134, 158

[36] R.I. Issa. Solution of the implicitly discretised fluid flow equations by operator-splitting. *J. Comput. Phys.*, 62(1):40–65, 1986. 70

[37] C.W. Chang J. Szekely and R.E. Ryan. The measurement and prediction of the melt velocities in aturbulent,electromagnetically driven recirculating low melting alloy system. *Metallurgical Transactions B*, 8:333–338, March 1977. 37

[38] K. Wajima K. Fujisaki and M. Ohki. 3d magnetohydrodynamics analysis method for free surface moltenmetal. *IEEE Trans. Magn.*, 36(4):1325–1328, 2000. 94

[39] Y. Nihei K. Nadaoka and H. Yagi. Grid-averaged lagrangian LES model for multiphase turbulent flow. *Int. J. Multiphase Flow*, 25(8):1619–1643, 1999. 30

[40] G. Djambazov R.A. Harding M. Wickins K. Pericleous, V. Bojarevics. Experimental and numerical study of the cold crucible melting process. *Applied Mathematical Modelling*, 30:1262–1280, 2006. 163

[41] A.N. Kolmogorov. The local structure in incompressible viscous fluids for very large reynolds numbers. *C. R. Acad. Sci. U.S.S.R.*, 30:301, 1941. 23

[42] A. Krauze. *Mathematical modelling of turbulent melt flow under the influence of AC and DC magnetic fields in CZ crystal growth system.* PhD thesis, University of Latvia, Faculty of Physics and Mathematics, Riga, 2005. 2, 71

[43] A. Eggers L. Buligins and A. Mühlbauer. Magnetohydrodynamic thermally driven flows in a channel-induction furnace (in Russian). *Magnetohydrodynamics*, 30(3):312–326, 1994. 135

[44] L.D. Landau and E.M. Lifshitz. *Hydrodynamics (in Russian).* Fizmatlit, Moscow, 2001. 18, 22

[45] B.E. Launder and D.B. Spalding. *Lectures in Mathematical Models of Turbulence.* Academic Press, London, 1972. ISBN 0-12-438050-6. 25

[46] J.D. Lavers and A.M. Ramadan. A boundary element method to predict the shape of a molten metal free surface in electromagnetic confinement field. *IEEE Trans. Magn.*, 24(6):2521–2523, 1988. 94

[47] D. Lennov and A. Kolin. Theory of electromagnetophoresis. I. Magnetohydrodynamic forces experienced by spherical and symmetrically oriented cylindrical particles. *Journal of Chemical Physics*, 22(4):683–689, 1954. 34, 100

[48] B.P. Leonard. A stable and accurate modelling procedure based on quadratic interpolation. *Comput. Methods Appl. Mech. Engrg.*, 19:58–98, 1979. 70

[49] M. Lesieur and O. Métais. New trends in large-eddy simulations of turbulence. *Annu. Rev. Fluid Mech.*, 28:45–82, 1996. 26, 28, 29

[50] D.C. Lillicrap and D.J. Moore. Electromagnetic stirring in coreless induction furnaces. In *Electroheat for Metals*, pages 3.2.1–3.2.12., Cambridge, England, 1982. 37

[51] D.K. Lilly. The representation of small-scale turbulence in numerical simulation experiments. In H. H. Goldstine, editor, *IBM Scientific Computing Symp. on Environmental Sciences*, pages 195–210, 1967. 26, 29

[52] M.Ya. Stolov L.L. Tir. *Electromagnetic Devices for Melt Circulation Control in Electric Furnaces (in Russian)*. Metallurgiya, Moscow, 1975. 16

[53] E. Loth. Numerical approaches for motion of dispersed particles, droplets and bubbles. *Progress in Energy and Combustion Science*, 26, June 2000. 101, 102

[54] T.D. Burton L.P. Wang, M.R. Maxey and D.E. Stock. Chaotic dynamics of particle dispersion in fluids. *Phys. of Fluids A*, 4(8):1789–1804, 1992. 31

[55] O. Simonin M. Boivin and K.D. Squires. Direct numerical simulation of turbulence modulation by particles in isotropic turbulence. *J. Fluid Mech.*, 375:235–263, 1998. 101

[56] K. Yokoji I. Matsumoto K. Kubo Y. Wada M. Enokizono, T. Todaka. Experiment and analysis of levitation-melting method of induction furnace. *IEEE Transactions on Magnetics*, 31(6):4205–4207, 1995. 162

[57] P. Moin W.H. Cabot M. Germano, U. Piomelli. A dynamic subgrid-scale eddy viscosity model. *Phys. of Fluids A*, 3(7):1760–1765, 1991. 29

[58] M.R. Maxey and J.J. Riley. Equation of motion for a small rigid sphere in a nonuniform flow. *Phys. Fluids*, 26(4):883–889, 1983. 32

[59] J.B. McLaughlin. Aerosol particle deposition in numerically simulated channel flow. *Phys. of Fluids A*, 1(7):1211–1224, 1989. 33, 35

[60] B. Melissary and S.A. Argyropoulos. Measurement of magnitude and direction of velocity in high-temperature liquid metals. part i: Mathematical modeling. *Metallurgical and Materials Transactions B*, 36B:691–700, 2005. 38

[61] B. Melissary and S.A. Argyropoulos. Measurement of magnitude and direction of velocity in high-temperature liquid metals. part ii: Experimental measurements. *Metallurgical and Materials Transactions B*, 36B:691–700, 2005. 38

[62] C. Meneveau and J. Katz. Scale-invariance and turbulence models for large-eddy simulation. *Annu. Rev. Fluid Mech.*, 32:1–32, 2000. 26

[63] A. Mestel. On the flow in a channel induction furnace. *J. Fluid Mech.*, 147: 431–447, 1984. 136

[64] D.J. Moore and J.C.R. Hunt. Flow, turbulence and unsteadiness in coreless induction furnaces. In M. R. E. Proctor H. K. Moffatt, editor, *Metallurgical Applications of Magnetohydrodynamics*, pages 93–107, Cambridge, England, 1984. 37

[65] S.A. Morsi and A.J. Alexander. An investigation of particle trajectories in two-phase flow systems. *J. Fluid Mech.*, 55(2):193–208, 1972. 32

[66] E. Taberlet N. El-Kaddah, J. Szekely and Y. Fautrelle. Turbulent recirculating flow in induction furnaces: a comparison of measurements with predictions over a range of operating conditions. *Metallurgical Transactions B*, 17B:687–693, 1986. 53

[67] H. Nagaoka. Inductance of circular solenoidal current sheet. *J. College of Science*, 27(6):18–33, 1909. 55

[68] C.W. Oseen. Uber den goltigkeitsbereich der stokesschen widerstandsformel. *Ark. Mat. Astron. Fysik.*, 9(19), 1913. 32

[69] S.V. Patankar and D.B. Spalding. A calculation procedure for heat, mass and momentum transfer in three-dimensional parabolic flows. *Int. J. of Heat Mass Transfer*, 15:1787, 1972. 70

[70] Stephen B. Pope. *Turbulent Flows.* Cambridge University Press, 2003. ISBN 0-521-59886-9. (Have a photocopy). 7, 23, 24, 26, 27, 88, 90

[71] J.M. Wallace P.S. Bernard. *Turbulent Flow. Analysis, Measurement, and Prediction.* John Wiley & Sons, Inc., Moscow, 2002. ISBN 0-471-33219-4. 23

[72] J.R. Grace R. Clift and M.E. Weber. *Bubbles, Drops and Particles.* Academic Press, New York, 1978. 33

[73] A. Mühlbauer R. Drewek, A. Jakovics and B. Nacke. Experimental and numerical investigations of the melt flow in channel-induction furnaces (in russian). *Magnetohydrodynamics*, 32(4):433–442, 1996. 137, 138

[74] G.D. Raithby and G.E. Schneider. Numerical solution of problems in incompressible fluid flow: treatment of the velocity-pressure coupling. *Numer. Heat Transfer*, 2:417–440, 1979. 70

[75] O. Reynolds. An experimental investigation of the circumstances which determine whether the motion of water shall be direct or sinuous, and the law of resistance in parallel channels. *Philos. Trans. R. Soc. London*, 174: 935–982, 1883. 2

[76] K.R. Beshay R.I. Issa, B. Ahmadi-Befrui and A.D. Gosman. Solution of the implicitly discretized reacting flow equations by operator-splitting. *J. Comput. Phys.*, 93(2):388–410, 1986. 70

[77] R. Ricou and C. Vives. Local velocity and mass transfer measurements in molten metals using an incorporated magnet probe. *Int. J. of Heat Mass Transfer*, 25:1579–1588, 1982. 38, 39, 137

[78] T. Robinson and K. Larsson. An experimental investigation of a magnetically driven rotating liquid-metal flow. *J. Fluid Mech.*, 60:641–664, 1973. 37

[79] G. Gerbeth S. Eckert and V.I. Melnikov. Velocity measurements at high temperatures by ultrasound doppler velocimetry using an acoustic wave guide. *Experiments in Fluids*, 35:381–388, 2003. 38

[80] Matthew N. O. Sadiku. *Numerical Techniques in Electromagnetics*. CRC Press, 2000. ISBN 0-84-931395-3. 15

[81] P.G. Saffman. The lift on a small sphere in a slow shear flow. *J. Fluid Mech.*, 22:385–400, 1965. 30, 34

[82] Pierre Sagaut. *Large eddy simulation for incompressible flows*. Springer-Verlag, Berlin, 2nd edition, 2002. ISBN 3-540-43753-3. 25

[83] L. Schiller and Z. Naumann. Uber die grundlegenden berechnungen bei der schwerkraftaufbereitung. *Ver. Deut. Ing.*, 77:318–320, 1933. 33

[84] H. Schlichting. *Boundary-Layer Theory*. McGraw-Hill, New York, NY, 7th edition, 1979. 50

[85] R. Schwarze. Unsteady RANS simulation of oscillating mould flows. *Int. J. for Numerical Methods in Fluids*, 52(8):883–902, 2006. 57

[86] R. Schwarze and F. Obermeier. Modelling of unsteady electromagnetically driven recirculating melt flows. *Modelling and Simulation in Materials Science and Engineering*, 12:985–993, 2004. 57

[87] A. Sellier. Migration of a solid conducting sphere immersed in a liquid metal near a plane conducting solid wall under the action of uniform ambient electric and magnetic fields. *Magnetohydrodynamics*, 42:317–326, 2006. 101

[88] J.A. Shercliff. Magnetic shaping of molten metal columns. *Proc. R. Soc. London A, Math. Phys. Sc.*, 375(1763):455–473, 1981. 94

[89] A.J. Meir S.I. Bakhtiyarov, R.A. Overfelt and P.G. Schmidt. Experimental measurements of velocity, potential, and temperature distributions in liquid aluminum during electromagnetic stirring. *J. Applied Mech.*, 70(3):351–358, 2003. 40

[90] J. Smagorinsky. General circulation experiments with the primitive equations. *Mon. Wea. Rev.*, 91:99–164, 1963. 26, 28

[91] N.K. Smolencev. *Introduction to wavelets. Wavelets in MATLAB (in Russian)*. DMK Press, Moscow, 2005. ISBN 5-94074-122-3. 64

[92] W.D. Smyth and J.N. Moum. Anisotropy of turbulence in stably stratified mixing layers. *Phys. Fluids*, 12(6):1343–1362, 2000. 88

[93] A.W. Cramb S.S. Roy and J.F. Hoburg. Magnetic shaping of columns of liquid sodium. *Metallurgical and Materials Transactions B*, 26(1):1191–1197, 1995. 94

[94] T. Kume T. Morisue, T. Yajima and S. Fujimora. Analysis of electromagnetic force for shaping the free surface of amolten metal in a cold crucible. *IEEE Trans. Magn.*, 29(2):1562–1565, 1993. 94

[95] A. Kuroda T. Tanaka, K. Kurita. Liquid metal flow with heat transferin in a cold orucible confined by a free surface and a solidification front. *ISIJ International*, 31(12):1416–1423, 1991. 164

[96] E. Taberlet and Y. Fautrelle. Turbulent stirring in an experimental induction furnace. *J. Fluid Mech.*, 159:409–431, 1985. 37, 55, 57

[97] K. Takahashi and S. Taniguchi. Electromagnetic separation of nonmetallic inclusion from liquid metal by imposition of high frequency magnetic field. *ISIJ International*, 43:820–827, 2003. 100

[98] Y. Takeda. Measurement of velocity profile of mercury flow by ultrasound doppler shift method. *Nucl. Technol.*, 79:120–124, 1987. 38

[99] E. Tarapore and J. Evans. Fluid velocities in induction melting furnaces: part1. theory and laboratory experiments. *Metallurgical Transactions B*, 17B:343–351, 1986. 53

[100] H. Tennekes and J.L. Lumley. *A First Course in Turbulence*. MIT Press, Cambridge, MA, 1972. 22, 23, 63

[101] F. Stefani Th. Gundrum, G. Gerbeth and M. Xu. Experimental aspects of contactless inductive flow tomography. *Magnetohydrodynamics*, 42, 2006. 38

[102] A. Muhlbauer Y. Gelfgat L. Gorbunov J. Virbulis E. Tomzig Th. Wetzel, A. Muiznieks and W.V. Ammon. Numerical model of turbulent CZ melt flow in the presence of ac and cusp magnetic fields and its verification in a laboratory facility. *Journal of Crystal Growth*, 230:81–91, 2001. 41

[103] B.G. Thomas. The importance of computational models for further improvements of the continuous casting process. In *Voest Alpine Conference on Continuous Casting*, Linz, 2000. Voest Alpine AG. 2

[104] K. Pericleous V. Bojarevics and R. Brooks. Dynamic model for metal cleanness evaluation by melting in cold crucible. In *2007 International Symposium on Liquid Metal Processing and Casting*, Nancy, France, 2007. 100

[105] E.I. Shilov V. Bojarevičs, J.A. Freibergs and E.V. Shcherbinin. *Electrically Induced Vortical Flows*. Kluwer Academic Publishers, Dordreht, 1989. 100

[106] K. Pericleous V. Bojarevičs. Modelling electromagnetically levitated liquid droplet oscillations. *ISIJ International*, 43(6):890–898, 2003. 162

[107] H.K. Versteeg and W. Malalasekera. *An Introduction to Computational Fluid Dynamics. The Finite Volume Method*. Longman Scientific & Technical, Harlow, 1995. ISBN 0-582-21884-5. 69

[108] A.A. Oksman G.R. Lurin'sh A.I. Chaikovskii A.Yu. Chudnovskii V.G. Zhilin, Yu.P. Ivochkin and E.V. Shcherbinin. An experimental investigation of the velocity field in an axisymmetric electrovortical flow in a cylindrical container (*i*n russian). *Magnetohydrodynamics*, 22(3), 1986. 37

[109] C. Vives and R. Ricou. Magnetohydrodynamic flows in a channel-induction furnace. *Metallurgical Transactions B*, 22B:193–209, 1991. 137, 142

[110] T. von Weissenfluh. Probes for local velocity and temperature measurements in liquid metal flow. *Int. J. of Heat Mass Transfer*, 28(8):1563–1574, 1985. 39

[111] E.E. Lomonova V.V. Osiko, M.A. Borik. Crucible-free methods of growing oxide crystals from the melt. *Ann. Rev. Mater. Sci.*, 17:101–122, 1987. 162

[112] F. Menter W. Vieser, T. Esch. *Heat Transfer Predictions Using Advanced Two-equation Turbulence Models.* CFX Validation Report CFX-VAL10/1002, 2002. 25

[113] A.-M. Walther. *Computersimulation der Schmelzenströmung in Induktions-Rinnenöfen.* PhD thesis, Universität Hannover, Fakultät für Maschinenwesen. 137

[114] David C. Wilcox. *Turbulence Modeling for CFD.* DCW Industries, 1993. ISBN 0-9636051-0-0. 25, 83

[115] D. Perrier Y. Fautrelle and J. Etay. Free surface controlled by magnetic fields. *ISIJ Int.*, 43(6):801–806, 2003. 94

[116] S. Shimasaki Y. Kanno, S. Taniguchi and N. Yoshikawa. Fabrication of metal-matrix composites locally reinforced with ceramic particles by using intermittent AC magnetic field. In *Electromagnetic Processing of Materials*, pages 444–448, Sendai, Japan, 2006. 100

[117] B. Young and A. Leeming. A theory of particle deposition in turbulent pipe flow. *J. Fluid Mech.*, 340:129–159, 1997. 32